Bridge deck aerodynamics:
A case study in full-scale

Nicolò Daniotti

University of Stavanger

Faculty of Science and Technology
Department of Mechanical and Structural Engineering and Materials Science
2022

Year: 2022
Title: Bridge deck aerodynamics: A case study in full-scale
Author: Nicolò Daniotti

Preface

This thesis is submitted in partial fulfilment of the requirements for the degree of Doctor of Philosophy (PhD) at the University of Stavanger (UiS), Norway. The research work was carried out at the Faculty of Science and Technology, Department of Mechanical and Structural Engineering and Material Science, in the period from May 2018 to December 2021. The main supervisor was Prof. Jasna Bogunović Jakobsen and the co-supervisors were Prof. Jónas Thór Snæbjörnsson and Dr. Etienne Cheynet. The study was funded by the University of Stavanger, i.e. the Norwegian Ministry of Education and Research, and supported by the Norwegian Public Road Administration. All the compulsory courses in the PhD study were offered at the UiS. As a part of the research activity, I spent four months at Svend Ole Hansen ApS in København, Denmark, working with field measurements on cable-supported bridges.

The thesis is presented as a monograph, addressing aspects of bridge deck aerodynamics in full-scale.

The Faculty of Science and Technology at UiS appointed the following Assessment Committee: Dr. Guy L. Larose, Senior Technical Director at Rowan Williams Davies and Irwin Inc. and Adjunct Research Professor at Carleton University, Canada; Dr. Andrew D. Quinn, Reader of Atmospheric Science and Engineering at the University of Birmingham, UK and Assoc. Prof. Yanyan Sha, University of Stavanger, Norway.

Throughout my PhD study, I have participated in various research activities focusing on bridge wind-induced vibrations and bridge stay cable vibrations. The corresponding research outputs are reported in journal and

conference publications listed in Appendix C but not discussed herein.

Stavanger, Norway
January 2022

Nicolò Daniotti

Acknowledgements

A view of the Lysefjord Bridge, 10 May 2021. Photo by N. Daniotti.

Abstract

One of the key aspects of bridge deck aerodynamics is the transformation of the incident wind flow into fluctuating surface pressures around a bridge deck. The atmospheric turbulence generates fluctuating loads on bridge decks, i.e. the buffeting wind action. The state-of-the-art knowledge about bridge deck aerodynamics, as well as the bases for the design of long-span bridges, relies primarily on wind-tunnel testing. By contrast, full-scale studies concentrating on the surface pressure distributions around bridge girders are rare. The central thrust of this work is to develop an experimental setup to investigate the aerodynamics of a closed-box girder bridge deck in full-scale.

A bespoke pressure measuring system is designed and developed to monitor wind-induced surface pressures around three chords of the Lysefjord Bridge in Norway, previously instrumented by a number of wind and vibration sensors. The one- and two-point statistics of the undisturbed turbulence are simultaneously measured, thereby facilitating the study of the spatial structure of the gust loading in the atmosphere. The experimental setup is aided by 3D sonic anemometers placed within the disturbed flow regions, upstream of the bridge deck nose and in the near wake.

The overall distortion of the atmospheric turbulence induced by the bridge deck body is examined, as well as the related vortex shedding process. In particular, the flow in the near-wake region of the bridge deck is investigated, in both model- and full-scale. For skewed incident winds, the near-wake flow exhibits highly three-dimensional features, including a significant axial flow on the leeward side of the full-scale bridge deck. Also, the frequency-dependent energy redistribution within the near wake is examined with emphasis on wavelengths associated with the periodic formation of vortex structures. The Strouhal number associated with the deck cross-section studied is found to be similar in both full- and model-scale. The turbulence level in the inflow is found to impact significantly the value of the non-dimensional vortex shed-

ding frequency in full-scale. Specifically, the higher the turbulence intensity, the higher the Strouhal number. Lastly, the "anatomy" of the vortex shedding process is described based on the surface pressure measurements undertaken on the trailing edges of the deck.

Investigating the gust loading generation in full-scale is central to this research. Fluctuating drag, lift and twisting moment are estimated on three chord-wise strips, based on a limited number of pressure sensing points. The analysis of the monitored surface pressures underpins the limits of the strip assumption in modelling the correlation along the bridge span of the lift and moment. Specifically, the span-wise coherence of the turbulence-driven lift and moment is observed to be higher than the span-wise coherence of the incident vertical velocity fluctuations. This result, which is deemed original given its full-scale framework, is in an overall agreement with the wind tunnel studies focusing on the gust loading on motionless section models of closed-box girder bridge decks. Also, a pronounced amplification of the vertical velocity fluctuations is observed upstream of the bridge deck nose, thereby providing a link between the undisturbed turbulence and the resulting gust loading on the deck.

Contents

Nomenclature

Roman symbols

$\bar{u}$ Mean wind speed

$\bar{u}_0$ Reference or nominally undisturbed mean wind speed

$\ddot{r}_{x,z,\theta}$ Lateral (x), vertical (z) and torsional (θ) bridge deck acceleration

$\mathscr{L}_{u,v,w}$ Wave length of longitudinal (u), transversal (v) and vertical (w) turbulence component associated with the peak of the normalized velocity spectra

$\bar{p}_0$ Mean barometric pressure of air

$\bar{q}$ Mean dynamic wind pressure

$a_{u,v,w}$ Coefficient of the one-point velocity spectrum model for longitudinal (u), transversal (v) and vertical (w) turbulence component

$b_{u,v,w}$ Coefficient of the one-point velocity spectrum model for longitudinal (u), transversal (v) and vertical (w) turbulence component

C_L' Lift derivative with respect to the angle of attack

C_M' Moment derivative with respect to the angle of attack

C_D Time-averaged drag coefficient based on D

C_L Time-averaged lift coefficient based on B

C_M Time-averaged moment coefficient based on B^2

C_p Pressure coefficient

C_{uw} One-point co-spectrum between longitudinal (u) and vertical (w) turbulence component

$c_{y1}^{u,v,w}$ Coefficient of the co-coherence for longitudinal (u), transversal (v) and vertical (w) turbulence components

$c_{y2}^{u,v,w}$ Coefficient of the co-coherence for longitudinal (u), transversal (v) and vertical (w) turbulence components

coh_{jk} Root coherence

f Frequency

F_D Drag force per unit length

F_L Lift force per unit length

F_M Moment per unit length

f_n Eigenfrequency

f_r Reduced frequency $f_r = fB/\bar{u}$

f_s Sampling frequency

f_v Vortex shedding frequency

F_x Horizontal force per unit length

F_z Vertical force per unit length

g Gravitational acceleration

$I_{u,v,w}$ Longitudinal (u), transversal (v) and vertical (w) turbulence intensity

k $= 2\pi f/\bar{u}$, wave number

$L_{u,v,w}^{X}$ Longitudinal (u), transversal (v) and vertical (w) integral length scale along the streamwise direction X

m Linear mass

n Reduced frequency $n = fz/\bar{u}(z)$

p Differential surface pressure

p_s Atmospheric static pressure

$p_{\mathrm{max},l}$ Maximum pressure before the transition to turbulence

q Wind dynamic pressure

R_j Autocovariance

$r_{x,z,\theta}$ Lateral (x), vertical (z) and torsional (θ) bridge deck displacement

Re Reynolds number

S_j Auto spectral density function

S_{jk} Cross spectral density function

$S_{u,v,w}$ One-point spectrum of the longitudinal (u), transversal (v) and vertical (w) turbulence component

Sc Mass-damping parameter

St Strouhal number

u Along-wind component of wind velocity

u_* Friction velocity

u_r Reduced velocity

v Cross-wind component of wind velocity

v_x Cross-wise component of wind velocity

v_y Span-wise component of wind velocity

v_z Vertical component of wind velocity

V_{rel} Instantaneous relative wind velocity

w Vertical component of wind velocity

X Along-wind direction

x Horizontal direction normal to the bridge axis

Y Across-wind direction

y Horizontal direction along to the bridge axis

Z Vertical direction

z Vertical direction

z/L Non-dimensional stability parameter

$|J(f_r)|^2$ Joint acceptance function

B   Width of the bridge deck

D   Depth of the bridge deck

Greek symbols

α Angle of wind incidence

β Yaw angle

γ_3 Skewness

γ_4 Kurtosis

γ_{jk} Co-coherence

κ von Kármán constant

μ Dynamic viscosity of the fluid

ν Kinematic viscosity of the fluid

$\phi_{z,j}(y)$ $j-th$ vertical eigenmode shape

ρ Density of air

ρ_{jk} Quad-coherence

θ_v Virtual potential temperature

ζ Structural damping ratio

$|\chi(f_r)|^2$ Aerodynamic admittance function (AAF)

Acronyms

A/D   Analogue-to-digital conversion

ABL   Atmospheric boundary layer

DAQ   Data acquisition system

FL   Full scale of the differential pressure transducer

i.d.   Internal diameter

IP   Independence principle

LIH   Local isotropy hypothesis

QST   Quasi-steady theory

std   Standard deviation

TI   Turbulence intensity

VIV   Vortex-induced vibrations

WASHMS Wind And Structural Health Monitoring system

Operators

$\bar{x}$ Time-averaged value of x

σ_x Standard deviation of x

Chapter 1

Introduction

The objective of the work is to provide a full-scale perspective of the aerodynamics of a closed-box girder bridge deck. Specifically, the wind buffeting load generation and the vortex shedding process are of primary interest. The study is performed utilizing a full-scale outdoor laboratory, with an established array of sensors for studying wind turbulence and bridge vibrations. The monitoring system now integrates simultaneous measurements of wind-induced surface pressures around the bridge girder.

Wind tunnel testing on a bridge section model represents the most established technique to quantify the fundamental aerodynamic properties of a bridge deck cross-section. Measurements of the surface pressures along the periphery of the body are typically undertaken to examine in detail the underlying fluid-structure interaction. This for example concerns the study of the gust loading on a stationary bridge deck section model in a turbulent boundary layer flow. Extending experiments of this type to full-scale cable-supported bridges is tempting. Yet, only a few field studies dealing with surface pressure measurements on bridge girders have been performed. However, the full-scale aspect is important for various reasons as will be briefly explained in the following paragraphs.

As emphasised by Davenport [35], full-scale experiments in the field of wind engineering are of vital importance. Firstly, they contribute to the validation of theories and modelling for wind loading. Secondly, full-scale testing may offer valuable clues needed for the development of new theories.

In the outlook of Larsen and Larose [105] describing the wind buffeting action on a long-span bridge, the following observation is made: "*Despite the many practical applications of buffeting theory, surprisingly little research*

are carried out on the transformation of atmospheric turbulent fluctuations into pressure fluctuations on the bridge deck. The general trend and empirical correlations for certain deck types are known, but the underlying physics are still not well understood and cannot be predicted from first principles - a shortcoming that deserves scientific attention."

A full-scale experiment addressing explicitly the wind-induced surface pressures around a bridge deck is called for; an experiment, that would inherently deal with the true atmospheric turbulence and where the Reynolds number effects linked to model-scale experiments would be absent. Such full-scale testing, albeit challenging in nature, may provide valuable insight into the gust loading process, thereby contributing towards a more accurate prediction of the buffeting response.

One of the key parameters influencing the flow around a body is the Reynolds number. The aerodynamics of a circular cylinder in cross-flow is well known across a wide range of Reynolds numbers, see e.g. Zdravkovich [209, 210]. For sharp-edged bodies, it is often assumed that the Reynolds scaling inequality, which typically stems from the model-scale testing, is associated with a less severe sensitivity to changes in aerodynamics. In other words, flow separation is postulated to occur at the edges. However, the experimental evidence suggests that the characteristics of the shear layers around sharp-edged bluff bodies are also Reynolds number dependent [172; 170; 97; 171; 66; 119]. Hence, the Strouhal number associated with closed-box girder bridge decks is, in principle, also a function of the Reynolds number. Again, a full-scale experiment is needed to address this matter.

When a circular cylinder is yawed/inclined, the flow in the near-wake can be highly three-dimensional, thereby affecting its aerodynamics compared to the cross-flow configuration [209; 210]. To the author's knowledge, a detailed study on the characteristics of the near-wake turbulence past a yawed bridge deck is not yet documented. On the other hand, a non-zero yaw angle can often be associated with the predominant flow direction for a prototype bridge. Therefore, the performed full- and model-scale experiments, at non-zero yaw angles, are also relevant for a more general orientation of the deck to the inflow, than the cross-flow condition. The disturbed flow characteristics, in the deck near wake, reflect the significance of the yaw angle, the turbulence intensity levels in the incident flow and, lastly, the Reynolds number.

This work explores the aerodynamics of the Lysefjord Bridge (Norway), a suspension bridge with a closed-box girder bridge deck, located in highly

complex terrain at the inlet of the Lysefjord. In the past, this bridge has been an object of thorough investigations addressing and validating the buffeting theory [22; 25; 24]. In that respect, this thesis attempts to be complementary, focusing on selected aspects of aerodynamics. To fulfil these objectives, in 2020, two 3D sonic anemometers were installed upstream of the deck nose and in the near-wake region. Thereafter, three chord-wise strips partially equipped with pressure taps were strapped around the bridge deck in 2021. The novel instrumentation allows not only a single bridge deck section study, but also a description of the spatial structure of the wind buffeting forces. The core of this thesis is concentrated on the presentation of the potential of the dataset acquired, along with selected aspects of the aerodynamics of the bridge deck cross-section.

1.1   Research questions

This study addresses the following general research question: *How does the incident wind turbulence transform into fluctuating surface pressures around a bridge deck in full-scale?*

In particular, the underlying research subjects can be outlined through the following questions:

1. *How to instrument a closed-box bridge girder with pressure sensors and sonic anemometry to study the fluid-structure interaction?* This question lays the foundation for the analysis to follow. Monitoring systems tailored to study the one- and two-point statistics of the incident wind turbulence, along with the surface pressures around the bridge girder in service, are rarely documented in the literature. This is why the measurement methodology is included as a part of the research focus.

2. *What are the flow characteristics upstream and downstream of a bridge deck exposed to atmospheric turbulence?* The knowledge of the turbulence structure ahead of the bridge deck nose provides a link between the incident undisturbed flow and the generation of the buffeting forces. Correspondingly, wind velocity measurements undertaken in the near-wake region allow the examination of the vortex shedding process and the deck signature turbulence, in relation to the underlying characteristics of the approaching flow.

3. *How adequate is the strip assumption in modelling the spatial structure of the buffeting forces measured in full-scale? Namely, how does the span-wise coherence of lift and twisting moment compare to the one characterising the oncoming flow?* The relationship between the correlation of the incident velocity fluctuations and the correlation of the resulting buffeting forces acting on a bridge deck is fundamental for the prediction of the bridge dynamic response to gusty winds. Providing a full-scale perspective on the knowledge of turbulence-driven loads on bridge decks is therefore central to this research.

1.2   Synopsis

This study deals with the aerodynamics of a closed-box girder bridge deck in full-scale, which is supplemented by model-scale data. A pressure measuring system is developed to acquire wind-induced surface pressures around the bottom side of the Lysefjord Bridge deck cross-section. Three chords are instrumented, thereby allowing for an investigation of the full-scale span-wise coherence of wind-induced surface pressures. Simultaneous wind velocity measurements are provided by 3D sonic anemometers, 6 m above the girder and 2 m upstream and downstream of the bridge deck nose. The measurements of wind turbulence above as well as upstream of the bridge deck complement the description of the gust loading on the bridge deck in the atmospheric turbulence. Based on the available data, the near-wake turbulence is characterised in both full- and model-scale. Also, potential Reynolds number effects on the vortex shedding process are examined.

The thesis is organized as follows (Figure 1.1):

Chapter 2: The chapter provides first an overview of the past field studies dealing with surface pressure measurements on cable-supported bridges. Thereafter, the conceptual framework for studying wind turbulence as well as wind effects on long-span bridges is given. The emphasis is on the fundamental characteristics of the wind buffeting action and the vortex shedding process.

Chapter 3: The full-scale experiment is described. The necessary details about the experimental setup are given, namely: (a) the sonic anemometry; (b) the accelerometers; (c) the pressure measuring system. In

```
                    ┌─────────────────────────┐
                    │      Chapter 2:         │
                    │    Fundamentals of      │
                    │  bluff body aerodynamics│
                    └────────────┬────────────┘
                                 │
                    ┌────────────▼────────────┐
                    │      Chapter 3:         │
                    │  The full-scale experiment │
                    └────────────┬────────────┘
                                 │
```
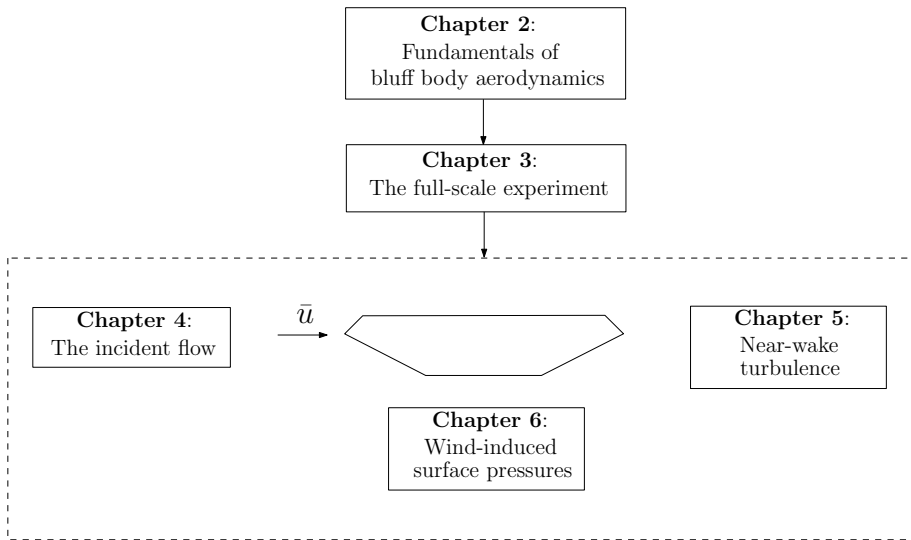
Figure 1.1: Layout of the thesis.

particular, the chapter aims to describe the main features of the system tailored to measure surface pressures around the bridge deck, including the challenges and limitations inherently involved. To the author's knowledge, very few campaigns have been designed to undertake long-term continuous monitoring of surface pressures on a cable-supported bridge in service. Thus, the description of the experimental setup is an important part of the present work.

Chapter 4: The fourth chapter studies the approaching wind turbulence. One year of velocity records for north-northeasterly flows compares the wind turbulence measured 6 m above the bridge deck, on the upwind side, and the wind turbulence seen 2 m ahead of the bridge deck nose. The goal is to quantify the deck-induced distortion of turbulence along with its implications for anemometry instrumentation and gust loading modelling.

Chapter 5: The chapter focuses on the near-wake turbulence, based on velocity measurements undertaken in full-scale and in the wind tunnel. The objective is twofold. Firstly, to directly estimate the non-dimensional vortex shedding frequency, i.e. the Strouhal number, and potential Reynolds number effects. Secondly, to explore the impact of a non-zero yaw angle on the near-wake flow, providing new information

of the three-dimensional structure of the flow developing past a bridge deck in a general orientation to the flow.

Chapter 6: The chapter presents selected findings based on the field measurements of surface pressures around the deck of the Lysefjord Bridge. The analysis primarily revolves around the fluctuating wind buffeting forces and the vortex shedding process. Two primary questions are raised: (a) How does the span-wise coherence of lift and moment compare to the span-wise coherence of the vertical turbulence component? (b) Can the measured trailing edge surface pressures partly explain the lack of observed vortex-induced vibrations? Even though the discussion is based on selected monitoring periods, the results attempt to provide a first insight into some fundamental aspects of the aerodynamics of a bridge deck in the atmospheric turbulence and full-scale Reynolds numbers.

Chapter 7: The conclusions of the thesis are outlined, highlighting the main findings and the contributions which are deemed original. The potential of the datasets acquired is summarised. Lastly, some steps to further develop this particular field of research are presented.

Chapter 2

Background

2.1 Field measurements of wind-induced surface pressures on a bridge deck: an overview

Instrumenting cable-supported bridges with Wind And Structural Health Monitoring systems (WASHMS) has become increasingly popular since the 2000s [206]. The validation of the classical buffeting theory [31; 168; 57] shall be based on a WASHMS consisting of (a) a set of accelerometers to measure the bridge deck response, allowing for the identification of the modal parameters, i.e. eigenfrequencies, mode shapes and structural damping; (b) an array of 3D sonic anemometers to estimate the one- and two-point statistics of the ideally undisturbed wind turbulence. Examples of such WASHMS are numerous, see e.g. Bietry et al. [13]; Cheynet et al. [25, 26]; Fenerci et al. [47]; Andersen et al. [5]. To minimize potential deck-induced flow distortion in the velocity measurements, the wind sensors should be mounted on both sides of the bridge deck [26], a detail which sometimes is overlooked.

The aerodynamic performance of a bridge deck can only be studied indirectly based on a "traditional" WASHMS. For example, the Strouhal (St) number can only be estimated if the prototype bridge exhibits vortex-induced vibrations, see e.g. Macdonald et al. [126]. The experimental investigation of the fluid-structure interaction is typically undertaken in the wind tunnel by measuring the wind-induced surface pressures along the body periphery. However, reported studies on full-scale measurements of wind-induced surface pressures around a bridge deck are rare. This fact reflects the inherent technical challenges involved. Besides the use of pressure sensors, the recent

development of synchronized continuous-wave Doppler wind lidars to e.g. monitor the flow around a bridge deck [27], is a promising addition, but still in infancy, that can provide information previously unattainable in full-scale.

To the author's knowledge, the first estimate of lateral coherence of the leading edge wind-induced surface pressures on a prototype bridge deck was reported in 1988 by Melbourne [137] for the West Gate Bridge (Australia). Pressures at 0.1B (where B is the chord width) from the leading edge were found to be better correlated than the approaching velocity fluctuations: the decay coefficient of the Davenport coherence model [32] was 16 and 4 for the along-wind turbulence component and surface pressures, respectively. The full-scale observation was also supported by a 1:150 section model test in a grid-generated turbulence.

In 1997, another important monitoring campaign was carried out on the Ikara Bridge (Japan) for one week while the midspan was closed to traffic [93; 94; 143]. Surface pressures were measured along the top part of the deck. Time-averaged and fluctuating pressure distributions agreed reasonably well with section model tests [93; 143]. For span-wise separations of $0.7B$ and $1.5B$, the co-coherence of the surface pressures at the windward fairings was observed to be higher than the one of the along-wind and vertical turbulence components, in the frequency range between 0.06 Hz and 0.60 Hz. By performing wind tunnel tests on a motionless section model at scales 1:121, 1:40 and 1:20, the Reynolds number effects on the Strouhal number were also investigated [94].

Frandsen [49] performed simultaneous measurements of wind turbulence, deck acceleration response as well as wind-induced pressures on the main span of the Storebælt East Bridge (Denmark) before it was opened to traffic in 1998. The study provided a full-scale insight into the vortex shedding at lock-in.

A thorough field investigation of vortex shedding was conducted by Li et al. [112, 113] on the twin-box girder of the Xihoumen Bridge (China) from 2009 to 2013. The characteristics of the cross-sectional buffeting forces on the same bridge were also investigated in both full- and model-scale [124]. Nevertheless, a discussion on the span-wise structure of the gust loading was not given. The surface pressure distributions and the aerodynamic admittance functions were characterised in full-scale for the Su-tong Bridge (China) under construction [123].

From 2018 to 2021, Svend Ole Hansen ApS, in collaboration with the

Norwegian Public Roads Administration, conducted an extensive monitoring campaign on the Gjemnessund Bridge (Norway) [4; 5; 3]. The bridge was equipped in 2008 with a system to measure wind-induced surface pressures around its deck [76]. In the more recent experiment, the bridge was instrumented with six pressure strips, thereby allowing a detailed study of the span-wise structure of the gust loading. Andersen et al. [5] showed that the span-wise cross-correlation coefficients of the lift were higher than along-wind and vertical turbulence components. To the author's knowledge, this is the first full-scale evidence showing that the estimated lift force acting on a bridge deck can be better correlated than the incident wind turbulence.

Note that a prototype bridge deck oscillates under gusty winds. Hence, the measured span-wise correlation of the surface pressures may be altered to some extent by the deck motion. In addition to the vibration amplitudes, the turbulence intensity and length scales of the incident flow are parameters influencing the span-wise correlation of the buffeting forces [56].

Although the gust loading on bridge decks is an object of ongoing research in the wind engineering community [105], this overview suggests that full-scale experiments dealing with surface pressures monitored around the bridge girder are a rarity. This thesis attempts to complement and add to previous full-scale studies to provide further insight into various relevant matters.

2.1.1   Pressure measuring systems: challenges

This section aims to highlight some of the challenges associated with field measurements of surface pressures around a bridge deck. Certain technical considerations outlined herein have been the basis for the design of the pressure measuring system for the Lysefjord Bridge deck, the details of which are given in Section 3.4.

This type of experiment poses different, often practical challenges, which may significantly influence the design of the measurement layout. Firstly, it is not always allowed by the authorities to drill holes (in a wind tunnel fashion) through the steel girder to install tapping points, which was the approach adopted in Isaksen [76]; Bastos [7]; Andersen et al. [5] for example. This method is admittedly the most efficient, as both the tubing system and pressure transducers can then be located inside the girder. If this approach cannot be pursued, the pressure taps, together with the corresponding tubing system and, possibly, the electronics, need to be installed on the outer side of

the bridge girder. Tubing length, waterproofing, sun exposure, condensation and electronic noise in the signal cables are some of the technicalities that must be dealt with. It is clear that the design of such a system can easily become more complex. Secondly, unless the field measurements are carried out before the bridge opening to traffic [49], during the construction stage of the bridge [123] or while the bridge is closed to traffic [143], it is difficult to perform pressure measurements on the top side of the bridge girder [188]. Lastly, the design of a pressure measuring system should also account for its maintenance, thereby allowing accessibility and minimizing any interruption of traffic across the bridge.

2.2   Description of wind turbulence

The wind turbulence components are referred to as u, v and w for the along-wind (X-axis), across-wind (Y-axis) and vertical components (positive Z-axis), respectively. Ideally, the undisturbed turbulence is assumed to be a stationary ergodic Gaussian random process with mean and fluctuating components denoted as $\bar{k}$ and k', respectively, where $k = u, v, w$. The velocity fluctuations are assumed homogeneous in the horizontal plane, which is reasonable here given the modest lateral separations considered. In the wind-based coordinate system (X, Y, Z), i.e. in a Cartesian reference frame aligned with the mean (local) streamline, the velocity components are defined as:

$$u = \bar{u} + u' \tag{2.1}$$

$$v = v' \tag{2.2}$$

$$w = w' \tag{2.3}$$

It is implied that $\bar{v} = \bar{w} = 0$. The double-rotation technique [79; 203] is applied to transform the velocity components from the sonic anemometer reference frame to a wind-based reference frame (Figure 2.1). In micro-meteorology, the turbulence characteristics are generally studied in a wind-based coordinate system [79]. The underlying assumption in Equations (2.1) to (2.3) is stationarity, which clearly depends on the averaging time [79].

In wind engineering, the yaw angle β is defined as the azimuth angle between the mean horizontal wind velocity and the normal to the main axis of the bridge deck, which is designated as y, as shown in Figure 2.2. Hence,
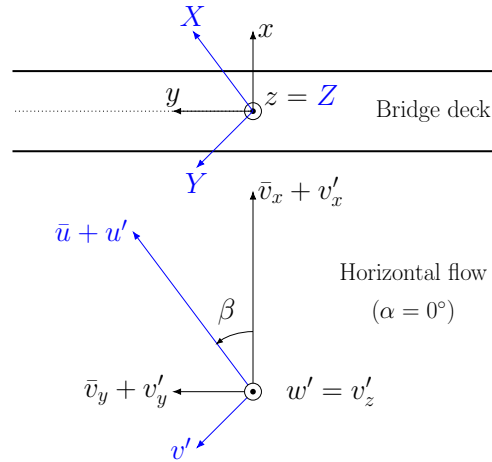
Figure 2.1: The deck-based (x, y, z) and wind-based coordinate systems (X, Y, Z) and the corresponding velocity vector (v_x, v_y, v_z), (u, v, w) for an horizontal flow ($\alpha = 0°$). The axis $z = Z$ points upwards.
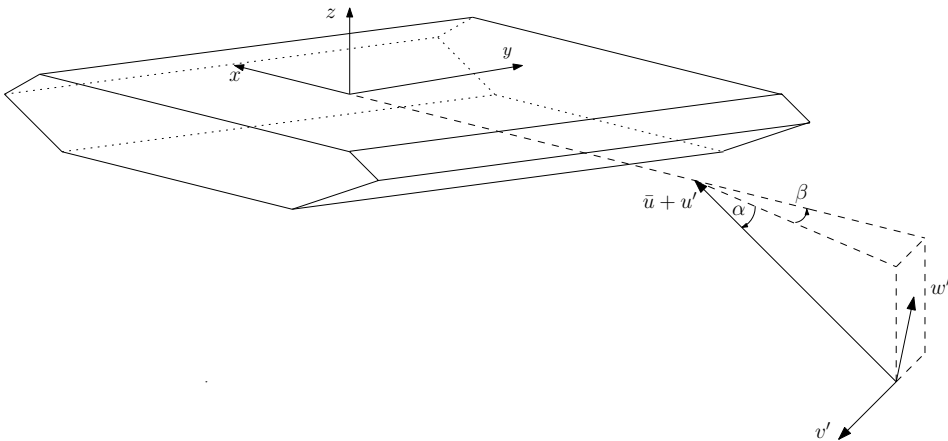
Figure 2.2: Definition of the yaw angle β and the angle of wind incidence α.

$\beta = 0°$ and $\beta = 90°$ correspond to cross and axial flows, respectively. When $\beta \neq 0$, the wind flow is typically defined as "skewed". The wind angle of incidence, which is often called the angle of attack, is computed as:

$$\alpha = \tan^{-1}\left(\frac{v_z}{\sqrt{v_x^2 + v_y^2}}\right) \tag{2.4}$$

where v_j ($j = x, y, z$) are the wind velocity components projected onto

the deck-based reference system (Figure 2.1), namely v_x (x-axis) and v_y (y-axis), which are the across- and along-deck component, respectively. Such a reference frame is commonly utilized for modelling fluctuating wind loads on a bridge deck, see for example Xie et al. [205]; Kimura and Tanaka [84]. In this study, the deck-based reference system is employed to characterise the near-wake turbulence monitored in full-scale.

The turbulence intensities (TI) I_k, where $k = u, v, w$, are defined as:

$$I_k = \frac{\sigma_k}{\bar{u}} \qquad\qquad k = u, v, w \qquad\qquad (2.5)$$

where σ_k is the standard deviation of the velocity component k.

For each turbulence component, the integral length scales in the streamwise direction are computed as:

$$L_k^X = \bar{u} \int_0^{+\infty} R_k(\tau) d\tau \qquad\qquad (2.6)$$

where $k = u, v, w$; $\bar{u}$ is the mean wind speed; $R_k(\tau)$ is the one-sided auto-covariance function and τ is the time lag. The integration is performed fitting an exponential function to $R_k(\tau)$, see e.g. Lenschow et al. [107].

2.2.1 Atmospheric stability

The thermal stratification of the atmosphere is assessed using the non-dimensional stability parameter [79]:

$$z/L = -\frac{zg\kappa\overline{w'\theta_v'}}{\overline{\theta_v}u_*^3} \qquad\qquad (2.7)$$

where z is the height above the surface; g is the gravitational acceleration ($9.81 \, \mathrm{m\,s^{-2}}$); κ is the von Kármán constant (≈ 0.4) [79]; $\overline{w'\theta_v'}$ is the flux of virtual potential temperature estimated at the sensor height z; $\overline{\theta_v}$ is the time-averaged virtual potential temperature at the sensor height z; u_* is the friction velocity, which is estimated as follows:

$$u_* = (\overline{u'w'}^2 + \overline{v'w'}^2)^{1/4} \qquad\qquad (2.8)$$

This definition, which is suggested by Weber [200], is employed due to the complex terrain surrounding the measurement site, where the shear stress $-\rho\overline{v'w'}$ may not be negligible compared to $-\rho\overline{u'w'}$.

2.2.2   One-point velocity spectra

To study the one-point velocity spectra of the neutral atmospheric surface layer, the Kaimal spectral model [80] is the adopted reference for the turbulence components u and v:

$$\frac{fS_u}{u_*^2} = \frac{105n}{(1+33n)^{5/3}} \tag{2.9}$$

$$\frac{fS_v}{u_*^2} = \frac{17n}{(1+9.5n)^{5/3}} \tag{2.10}$$

where n is the reduced frequency defined as

$$n = \frac{fz}{\bar{u}(z)} \tag{2.11}$$

and u_* is the friction velocity and $\bar{u}(z)$ is the mean wind speed at the height z.

For the vertical component, w, the Busch-Panofsky spectrum [19] is chosen as a reference one-point spectrum:

$$\frac{fS_w}{u_*^2} = \frac{3.36n}{1+10n^{5/3}} \tag{2.12}$$

This study focuses on velocity records acquired in complex topography, i.e. the Norwegian fjords, where the turbulence characteristics may differ from those usually estimated for a smooth uniform flat terrain [26; 138]. Hence, the "blunt" and "pointed" spectral models [148; 192; 158] are adopted to match the one-point velocity spectra observed on-site, for the horizontal and vertical turbulence components, respectively:

$$\frac{fS_u}{u_*^2} = \frac{a_u n}{(1+b_u n)^{5/3}} \tag{2.13}$$

$$\frac{fS_v}{u_*^2} = \frac{a_v n}{(1+b_v n)^{5/3}} \tag{2.14}$$

$$\frac{fS_w}{u_*^2} = \frac{a_w n}{1+b_w n^{5/3}} \tag{2.15}$$

where the coefficients a_i and b_i, with $i = \{u, v, w\}$, are estimated in a least-square sense based on the measured velocity spectra. A relationship between

the coefficients can be established based on the local isotropy hypothesis (LIH) in the inertial sub-range [87], as reported in Tieleman [192] for example. Following Kaimal and Finnigan [79], who assumed the von Kármán constant $\kappa = 0.4$ and the Kolmogorov spectral constant equal to 0.55, $b_u = (a_u/0.3)^{3/5}$, $b_v = (a_v/0.4)^{3/5}$ and $b_w = a_w/0.4$.

The inertial sub-range laws introduced by Kolmogorov [87] for locally isotropic turbulence are expressed in terms of wave numbers, i.e. the velocity spectra follow $\propto \varepsilon^{2/3}k^{-5/3}$, where ε is the dissipation rate of the turbulent kinetic energy and k is the wave number, which is defined as:

$$k = \frac{2\pi f}{\bar{u}} \tag{2.16}$$

where f is the frequency and $\bar{u}$ is the mean wind speed, thereby invoking the hypothesis of frozen turbulence [189]. In this study, the discussion regarding the $-5/3$ power law for the inertial sub-range is interchangeably based on wave number (k), frequency (f) or reduced frequency (either $fz/\bar{u}$ or $fD/\bar{u}$).

The co-spectrum, i.e. the real part of the cross-spectrum, between u and w components is modelled following Kaimal et al. [80]:

$$-\frac{fC_{uw}}{u_*^2} = \frac{14n}{(1+9.6n)^{7/3}} \tag{2.17}$$

An example of velocity spectra estimated on the Lysefjord Bridge is given in Figure 2.3, for a remarkably stationary 3 h-long time series acquired on 03/10/2020. The wind was blowing from north-northeast with $\bar{u} = 13.2\,\mathrm{m\,s^{-1}}$ and the atmospheric stability was near neutral. The turbulence intensities, which were estimated on the upwind side of the bridge deck, were $I_u = 0.29$, $I_v = 0.23$ and $I_w = 0.22$. In Figure 2.3, Equations (2.9), (2.10), (2.12) and (2.17) along with the fitted ones, i.e. Equations (2.13) to (2.15), are superimposed to the measured velocity spectra.

Kaimal's spectral models were derived based on velocity fluctuations above a flat and homogeneous terrain [80]. Nevertheless, Figure 2.3 suggests that the models adequately describe S_u and S_w for north-northeasterly flows at the bridge site, which are associated with high turbulence intensities level rarely documented in the scientific literature.

Following Larose [101], the adopted characteristic length scale of turbulence is the wavelength associated with the peak of the normalized velocity
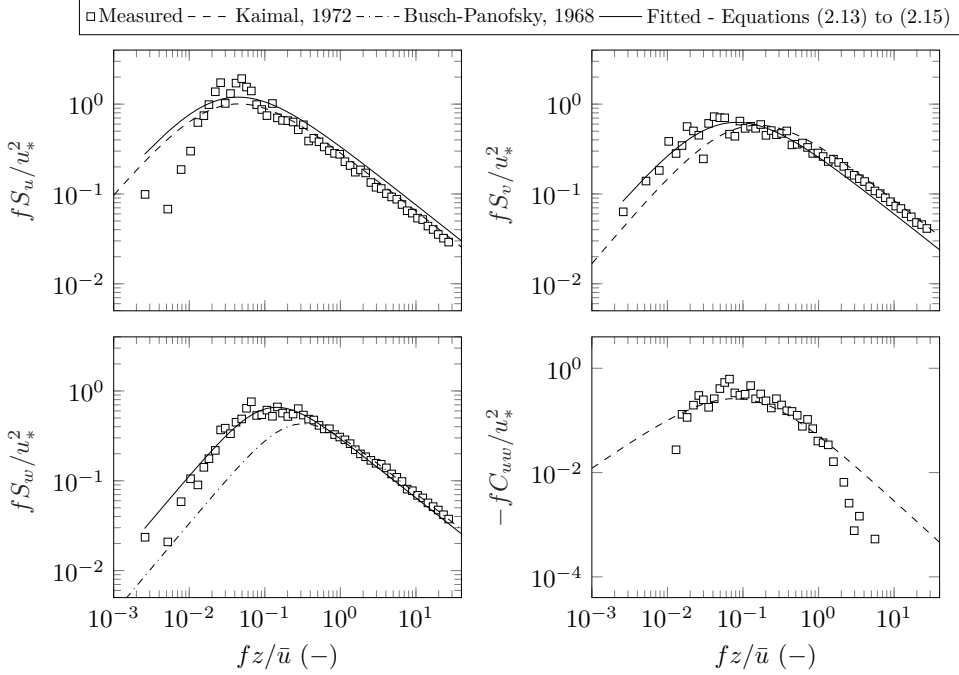
Figure 2.3: One-point velocity spectra S_i, with $i = u, v, w$, and co-spectrum C_{uw} estimated on the Lysefjord Bridge (H08E) from 19:00 to 22:00 UTC on 03/10/2020. The wind direction was 19°, $\bar{u} = 13.2 \, \text{m s}^{-1}$ and $z/L = -0.01$.

spectrum, as graphically represented in Figure 2.4 for fS_w/u_*^2. Here the normalized velocity spectrum is expressed as a function of the wave number k. The wavelengths are designated as $\mathscr{L}_j$ with $j = u, v, w$. They are computed based on the fitted one-point spectra using Equations (2.13) to (2.15) and the following relationships [192]:

$$\mathscr{L}_u = \frac{z}{2\pi} b_u \tag{2.18}$$

$$\mathscr{L}_v = \frac{z}{2\pi} b_v \tag{2.19}$$

$$\mathscr{L}_w = \frac{z}{2\pi} \left(\frac{b_w}{1.5} \right)^{3/5} \tag{2.20}$$

Specifically, the quantity $\mathscr{L}_w$ is used in Section 6.5 for a direct comparison with the results from Larose [101].
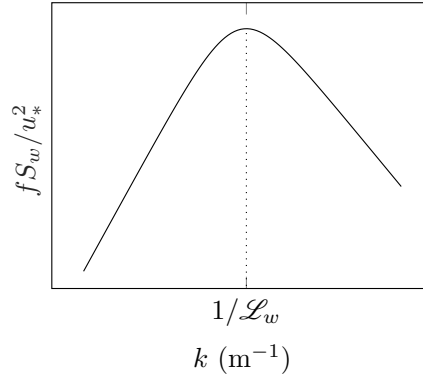
Figure 2.4: Schematic for the calculation of the wavelength $\mathscr{L}_w$ associated with the peak of the normalized spectrum fS_w/u_*^2.

2.2.3   Horizontal coherence

The estimation of the coherence of wind velocity fluctuations along the span of a cable-supported bridge is fundamental to compute the fluctuating wind loads [34]. Hence, the horizontal coherence is of particular interest.

The root-coherence is the square root of the coherence function. The coherence quantifies the correlation between two signals in the frequency space [161]. When the two signals, e.g. velocity fluctuations, are separated in space, the coherence provides a measure of the spatial correlation of the Fourier components [161]. The root-coherence between two stationary random processes j and k is a complex-valued function defined as:

$$coh_{jk}(f, \boldsymbol{x}_j, \boldsymbol{x}_k) = \frac{S_{jk}(f, \boldsymbol{x}_j, \boldsymbol{x}_k)}{\sqrt{S_j(f, \boldsymbol{x}_j)S_k(f, \boldsymbol{x}_k)}} \tag{2.21}$$

where $S_{jk}(f, \boldsymbol{x}_j, \boldsymbol{x}_k)$ is the two-point cross-spectrum between j and k, the spatial coordinates of which are $\boldsymbol{x}_j = [x_j, y_j, z_j]$ and $\boldsymbol{x}_k = [x_k, y_k, z_k]$; $S_j(f, \boldsymbol{x}_j)$ and $S_k(f, \boldsymbol{x}_k)$ are the one-point auto-spectrum of the processes j and k, respectively.

The root-coherence can be expressed as the sum of a real (in-phase) and imaginary (out-of-phase) component:

$$coh_{jk}(f, \boldsymbol{x}_j, \boldsymbol{x}_k) = \gamma_{jk}(f, \boldsymbol{x}_j, \boldsymbol{x}_k) + i\rho_{jk}(f, \boldsymbol{x}_j, \boldsymbol{x}_k) \tag{2.22}$$

where $\gamma_{jk}(f, \boldsymbol{x}_j, \boldsymbol{x}_k)$ is called co-coherence (real part) and $\rho_{jk}(f, \boldsymbol{x}_j, \boldsymbol{x}_k)$ is called quad-coherence (imaginary part).

Based on the horizontally homogeneous turbulence assumption, which is suitable for the present study, the horizontal root-coherence is a function of the spatial separations only. Hence, Equation (2.21) can be rewritten as:

$$coh_{jk}(f, \boldsymbol{x}_j, \boldsymbol{x}_k) \approx coh_{jk}(f, \Delta X, \Delta Y) \tag{2.23}$$

where ΔX and ΔY are the along- and across-wind separations, respectively.

By definition, the cross-spectrum $S_{jk}(f, \Delta X, \Delta Y)$ depends on the angle between the wind vector and the path of the measurement array. Therefore, whenever $\Delta X \neq 0$, a phase shift arises between the two velocity fluctuations [140]. Such a phase shift can be modelled invoking TaylorâĂŹs hypothesis of frozen turbulence [189], namely assuming that the advection time of a frozen eddy is equal to $\Delta X / \bar{u}$. This is generally applicable when the mean lifetime of the turbulence structure is large compared to $\Delta X / \bar{u}$, e.g. at low wave numbers [91; 72].

The model adopted to describe the lateral coherence of the velocity fluctuations is a modified Davenport co-coherence model [32], inspired by the studies of Hjorth-Hansen et al. [62]; Jakobsen [78]; Krenk [90]:

$$\gamma_{kk}(f, \Delta X, \Delta Y) = \exp\left\{ -\frac{1}{\bar{u}}\sqrt{(c_{y1}^k f \Delta Y)^2 + (c_{y2}^k \Delta Y)^2} \right\} \cos\left(\frac{2\pi f \Delta X}{\bar{u}} \right) \tag{2.24}$$

where $k = \{u, v, w\}$; ΔX and ΔY are the cross-wind and along wind separations; c_{y1}^k is a dimensionless coefficient reflecting the Davenport coherence model [32]; c_{y2}^k is a dimensional coefficient (s^{-1}) describing a scale of turbulence [62]. The coefficient c_{y2}^k models the lack of full correlation for eddies having wavelengths similar or smaller than the lateral separation between the measurement array [91; 72]. When $c_{y2}^k = 0$ and the flow is normal to measurement array, i.e. $\Delta X = 0$, Equation (2.24) is reduced to the Davenport coherence model [32].

2.3   Fundamentals of bluff body aerodynamics

This section aims to present some fundamental concepts revolving around the aerodynamics of a bluff body. Here, the term "bluff body" encompasses the cross-sections for which the shear layers separate and the friction drag is negligible compared to the form drag.

2.3.1   The flow around a bluff body

A circular cylinder in a cross-flow is adopted as a reference bluff body since the flow regimes are well understood, see e.g. Zdravkovich [209, 210].

The main features of a 2D flow around a circular cylinder are described in Figure 2.5. The free flow, i.e. the flow undistorted by the presence of the body, is designated as $\bar{u}_0$. Along the stagnation streamline, there is an adverse pressure gradient as the flow decelerates until it reaches the stagnation point. Symmetrically with respect to the stagnation line, there is a region where $u > \bar{u}_0$ and the flow is distorted by the presence of the cylinder. A thin boundary layer is formed along the perimeter of the body, with the flow being attached as long as the pressure gradient is favourable. The boundary layer can be laminar or turbulent depending on the Reynolds number. Flow separation occurs at the points denoted S in Figure 2.5. The separating thin shear layers roll up in vortices which are eventually shed. The interaction between the two shear layers is called vortex shedding. The flow region past the body, enveloped by the shear layers, is termed near-wake. Here, the flow is unsteady. As the vortex shedding is initiated, the body experiences a corresponding time-varying variation of surface pressures, which, in turn, governs the fluctuating aerodynamic forces.

The flow regime for a smooth-surfaced 2D circular cylinder in smooth flow depends on the Reynolds number. The term "flow regime" describes the boundary layer state, the angular position of the separation point and the transition from laminar to turbulent flow. Both time-averaged and fluctuating forces acting on the body can change significantly with the Reynolds number. The surface roughness [1], the turbulence in the incident flow [21; 95; 145] and the cross-flow oscillation amplitudes [153] are among the different parameters influencing the flow around a single circular cylinder.

The flow around a sharp-edged body like a bridge deck cross-section can be described in a similar fashion as outlined above for the circular cylinder.
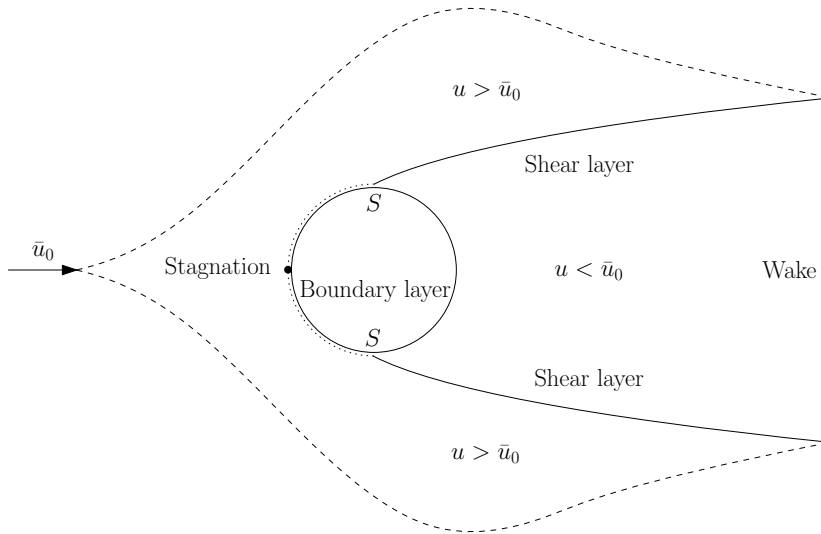
Figure 2.5: Schematic of the flow around a circular cylinder in cross-flow, based on Zdravkovich [209].

In particular, the location of the transition to turbulence can be adopted as a parameter to characterise the flow topology, as described in Schewe [170]. Nevertheless, two main differences from the circular cylinder shall be highlighted: (a) the presence of sharp edges advances the flow separation; (b) the after-body dimension allows for the development of a separation bubble within the separating shear layers, on top and bottom sides of the girder. The character of both the time-averaged and fluctuating aerodynamic forces depends strongly on these flow regions. For a given deck geometry and angle of wind incidence, the *Re* number and the wind turbulence are among the parameters having an impact on the separating shear layers, the spatial extent of the separation bubbles and the location of transition to turbulence.

The fluctuating surface pressures in the separated flow regions are fundamental for the generation of the aerodynamic forces on sharp-edged bodies like a bridge deck. The free-stream turbulence, in terms of intensity and length scale, has pronounced effects on the chord-wise and span-wise characteristics of the surface pressures within the separation bubbles, see e.g. Larose [101] for a thorough overview on the topic.

2.3.2   The governing parameters

Some parameters governing the flow characteristics around a body are out-
lined in this subsection.

Reynolds number

The Reynolds number (Re) quantifies the ratio between inertia and viscous
forces of a fluid particle. It is expressed as:

$$Re = \frac{\rho \bar{u} D}{\mu} = \frac{\bar{u} D}{\nu} \tag{2.25}$$

where D is the across-wind dimension of the body; $\bar{u}$ is the mean speed
of the flow; ρ defines the density of the fluid; μ is the dynamic viscosity of
the fluid whereas ν is the kinematic viscosity.

The forces on a body immersed in a fluid flow depend on the Re number,
see e.g. Zdravkovich [209]. For a circular cylinder, its similitude is funda-
mental when a geometric scaling is introduced, for example during wind
tunnel testing. Cables are typically tested based on 1:1 rigid model to respect
the Re number similitude. For bodies characterised by sharp edges (e.g. a
bridge deck), defined here "sharp-edged bodies", the Re number similarity
requirement is generally relaxed to a certain extent, since the flow separation
is postulated to occur at the sharp edges. A more detailed discussion on this
topic is given in Section 2.3.4.

Reduced velocity

The reduced wind velocity u_r is defined as:

$$u_r = \frac{\bar{u}}{fD} \tag{2.26}$$

where $\bar{u}$ is the free-stream wind velocity; f is the vibration frequency; D is
the across-wind dimension of the body. The reduced velocity quantifies the
ratio between the oscillation period and the time needed for a fluid particle to
travel past the body. The reduced frequency is also used, that is $f_r = 1/u_r$.

Strouhal number

The non-dimensional vortex shedding frequency is defined as Strouhal number (St) [185]:

$$St = \frac{f_v D}{\bar{u}} \tag{2.27}$$

where f_v is the vortex shedding frequency; D is the across-flow dimension of the body; $\bar{u}$ is the free-stream velocity. For a given stationary body geometry, incidence of the flow and surface roughness, the St number is in general function of the Re number:

$$St = St(Re) \tag{2.28}$$

When the vortex shedding frequency (f_v) becomes close to or equal to the eigenfrequency of the body (f_n), vortex-induced vibrations can manifest. The term "lock-in" describes the situation in which f_v is controlled by the body motion, over a certain range of $\bar{u}$. This synchronization range depends in general on the body geometry.

Scruton number

The Scruton number is a non-dimensional mass-damping parameter, defined here as:

$$Sc = \frac{m\zeta}{\rho D^2} \tag{2.29}$$

where m is the mass per unit length; ζ is the structural damping ratio; ρ is the air density; D is the diameter in the case of a circular cylinder.

2.3.3 Vortex shedding for sharp-edged bodies

Vortices shedding past the trailing edges of a sharp-edged body are described by the frequency f_v (Equation (2.27)). Accordingly, for a given Re number and a stationary body, the relationship between the incident flow $\bar{u}$ and the vortex shedding frequency f_v is linear. The flow separates at the upwind

corners and partly reattaches along the horizontal panels, with unstable shear layers forming vortices along the horizontal surfaces [174]. The shear layers separate at the downwind knuckle lines. Their entrainment determines the alternating vortex shedding process. The vortex shedding is associated with a time-varying distribution of the surface pressures, which, in turn, contribute to the generation of the aerodynamic forces. The relative dimension of the coherent vortex structures forming above and below the bridge deck nose depends on the deck geometry. Trapezoidal closed-box girder bridge decks are commonly designed with the horizontal bottom plate shorter than the top one. Thus, larger vortices are expected to be shed below the deck nose, as shown in Figure 2.6 based on a schematic illustration.

The vibrations at lock-in, often called vortex-induced vibrations (VIV), are generally self-limited in amplitude, with the structural [126] and aero-dynamic damping being among the governing parameters, see e.g. Vickery and Basu [198]. The phenomenon of VIVs is non-linear, as the deck motion regulates both the magnitude and phase of the cross-flow force. Note that the span-wise correlation of the induced lift increases when the body is oscillating in cross-flow [146].

Turbulence generally has significant effects on the vortex shedding process. Firstly, vortex shedding tends to be less narrow-banded if the incident flow is turbulent [198]. Secondly, small-scale turbulence influences the transition of the boundary layer over a circular cylinder and delays the flow separation [21; 95]. Similar effects can be observed for the shear layers separating from the front corner of sharp-edged bodies, see e.g. Laneville et al. [96] for the rectangular cylinder. Small-scale turbulence along the stagnation line is significantly distorted as it approaches the body and is subsequently fed into the shear layer, advancing the mixing and entrainment [96]. Thus, the static force coefficients are consequently affected. Analogous considerations
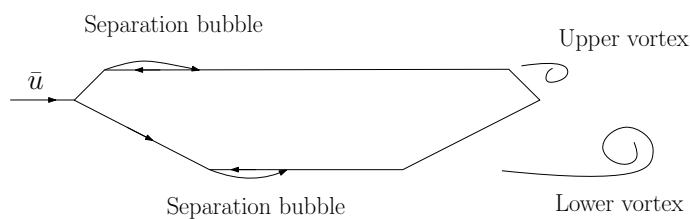
Figure 2.6: Basic schematic of the vortex shedding process for a trapezoidal closed-box girder bridge deck without the railings.

may apply to the shear layers at the trailing edge of a bridge deck.

Any turbulence in the incident flow tends to reduce the span-wise correlation of the vortex shedding process, for e.g. both stationary and vibrating circular cylinders [146]. The way turbulence in the free flow tends to inhibit VIVs depends on the structural damping, see e.g. the study on the Second Severn Crossing cable-stayed bridge [126]. Lastly, the geometry and porosity of the railing is another variable influencing the significance of turbulence for the onset of VIVs [132]. Thus, when testing the sensitivity of a deck section model to VIVs, it is clear that the turbulence should be adequately scaled [75] to simulate its effect at the cross-section level but also along the bridge span.

The full-scale studies generally report VIVs for a flow almost perpendicular to the bridge deck [104; 49; 126]. This suggests that, for non-zero yaw angles, the vortex formation past the trailing edges may be affected by the three-dimensionality of the near-wake flow, similarly to the case of a yawed/inclined circular cylinder [174; 133]. Yet, detailed studies focusing on the structure of the near-wake flow past a yawed bridge deck are scarce.

For trapezoidal closed-box girder bridge decks, the use of guide vanes at the bottom knuckle lines is generally efficient in inhibiting VIVs. A retrofitting based on guide-vanes was applied to e.g. the Storebælt East Bridge (Denmark) [104], the Osterøy Bridge (Norway) [77] and the Gjemnessund Bridge (Norway) [58]. Also, the slope of the downwind inclined bottom panel in the girder affects the formation of the lower coherent vortex structure. Larsen and Wall [106] demonstrated the effectiveness of using an angle around 15° based on dynamic tests of section models of trapezoidal closed-box girder bridge decks, equipped with road furniture. The heave VIVs were largely suppressed, as the separation of the shear layer at such a shallow angle is partly reduced and the vortex roll-up is "delayed" further downstream.

2.3.4   Reynolds number effects on sharp-edged bodies

It is well known that the aerodynamic characteristics of a circular cylinder in cross-flow are dependent on the *Re* number flow regime [210]. For sharp edged bluff bodies, a less severe dependence on the *Re* number is generally expected since flow separations generally occur in the vicinity of the edges. Thus, a relaxation of the *Re* number similitude between model-scale and prototype is normally adopted for wind engineering applications in wind tunnels, where a mismatch of one or two orders of magnitude is to be expected.

With this assumption, it is also tacitly assumed that changes in the *Re* number do not impact significantly the separated flow regions or the state of the boundary layer around the periphery of the body, namely the location of the transition to turbulence.

However, depending on the flow re-attachment, whether and to which extent it occurs, the aerodynamic characteristics of bluff bodies with sharp edges may suffer from *Re* number effects [66; 172; 170; 97; 171; 119]. Some examples of experiments pertaining to a closed-box bridge deck are the approach span of Storebælt East Bridge (Denmark) [172; 170], the Ikara Bridge (Japan) [94], a streamlined single box girder with an aspect ratio of 6.2 [58] and the Gjemnessund Bridge (Norway) [3].

A schematic is given in Figure 2.7, where the interpretation of the flow field across different *Re* number regimes, together with the drawing itself, are inspired by Schewe and Larsen [172]; Schewe [170]. The classification of the flow regimes by Roshko [162] for a circular cylinder was essentially extended by Schewe [170] in relation to more-or-less bluff bodies. In Figure 2.7, the flow over the bottom side of the bridge deck governs the *Re* number dependence. Note that, in general, the presence of railings may impact, to a certain degree, the sensitivity of the flow to the *Re* number. Care must be taken when scaling the railings in model scale to ensure correspondence with the aerodynamic effect on the prototype bridge. Lastly, it is worth stressing that a *Re* number dependence on the aerodynamics of trapezoidal bridge deck cross-sections is not always pronounced and an accurate prediction of the *St* can be obtained in the wind tunnel, see e.g. the main span of the Storebælt East Bridge, with $B/D = 7.8$ [97]. As suggested by Larose and DâĂŹauteuil [97], the aspect ratio is among the governing factors.

For the case of a rectangular cylinder, the parameters governing the degree of *Re* number effects on the aerodynamics are primarily [97; 171]: (a) the aspect ratio, which essentially determines the after-body length available for the flow to reattach; (b) the angle of wind incidence; (c) the sharpness of the corners; (d) the turbulence in the free-stream.

Given the different parameters governing potential *Re* number effects on the flow around sharp-edged bodies, a case by case approach is generally deemed appropriate. The present work attempts to add to previous studies on this topic, focusing on the *St* number estimated based on near-wake velocity measurements undertaken in model- and full-scale.
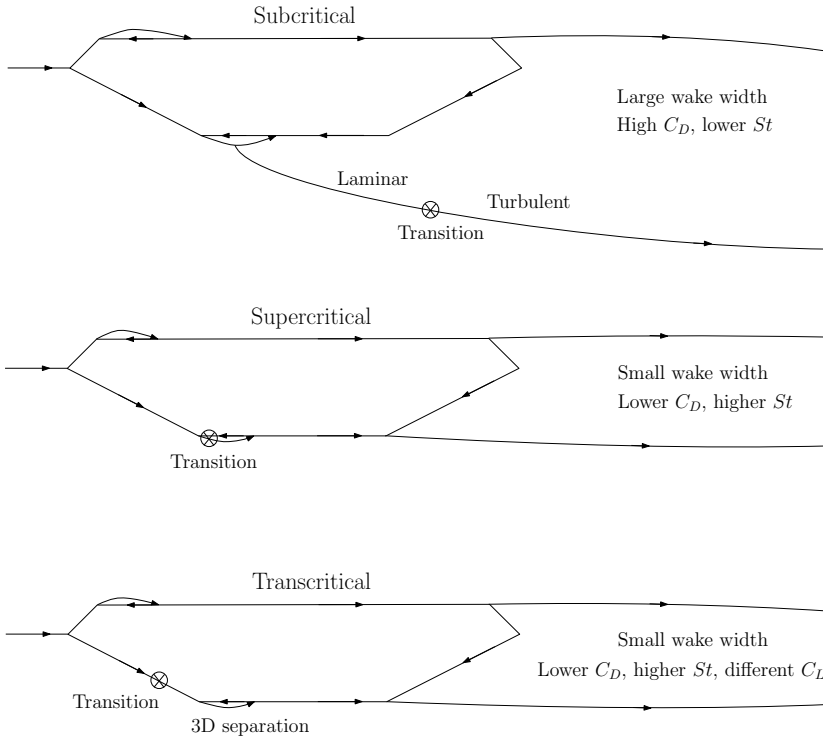
Figure 2.7: Schematic of the flow topologies for different *Re* numbers. The interpretation shown here for the Lysefjord Bridge cross-section is reproduced from Schewe and Larsen [172]; Schewe [170], where the approach span of Storebælt East Bridge (Denmark) was investigated. The cross represents the transition from laminar to turbulent flow.

2.3.5   Flow around a yawed line-like structure

When a generic line-like structure is at an angle to the flow, the aerodynamic forces may, in principle, change compared to the cross-flow configuration. In fact, the flow around the body can exhibit significant three-dimensional characteristics. For a yawed/inclined circular cylinder, the so-called "independence principle" (IP), or "cosine rule", is often employed. Accordingly, the incident flow is decomposed as follows (see Figure 2.8):

$$\bar{v}_x = \bar{u} \cdot \cos(\beta) \tag{2.30}$$
$$\bar{v}_y = \bar{u} \cdot \sin(\beta) \tag{2.31}$$
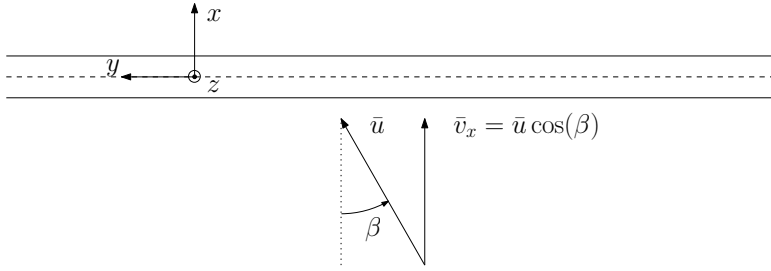
Figure 2.8: Schematic of a yawed cylinder.

where $\bar{v}_x$ and $\bar{v}_y$ are the normal and axial velocity components, respectively; β is the yaw angle. According to the independence principle, $\bar{v}_x$ and $\bar{v}_y$ can be considered separately and the aerodynamic forces are governed by the velocity component normal to the cylinder axis. Thus, the yawed case is linked back to the normal incidence, i.e. $\beta = 0°$. However, Zdravkovich [210] pointed out that: (a) the IP does not apply to separated flows; (b) the axial velocity components affects the flow separation. Thus, the IP principle is not always appropriate. Its applicability strongly depends on the yaw angle magnitude [18].

For example, this approach can be checked against the static force coefficients and wake characteristics, see e.g. Ramberg [153], with the *Re* number and the cross-flow oscillations (either stationary cylinder or vibrating cylinder) being the two fundamental variables. It is experimentally verified in terms of *St* number [59; 186; 89; 195; 153] for yawed/inclined stationary circular cylinders in the sub-critical range of *Re* number when $\beta \leq 40°$. Nevertheless, for larger yaw angles [153] or higher *Re* number [18] the IP is not justified, even to simply predict the *St* number.

For sharp-edged bodies, e.g. a bridge deck, the near-wake flow structure when $\beta \neq 0°$ has not been much investigated. A detailed study can be found in Lou et al. [120], where the wake pattern was characterised for a yawed square cylinder, at $Re = 3600$. The IP was found to describe the observed *St* number for $\beta \leq 40°$. However, bridge decks are generally more slender than square cylinders. Even if separation is assumed to occur at the edge location, the axial velocity component $\bar{u}_A$ can affect the separation bubble and the reattachment point, thereby influencing its aerodynamic characteristics. In addition, the slenderness of a sharp-edged body influences the sensitivity to the *Re* number [97]. When discussing the *St* number for a yawed bridge deck cross-section, the applicability of the IP is, thus, not justified a-priori.

When a smooth-surfaced circular cylinder is inclined/yaw, the so-called "axial flow" develops in the near wake [175]. It has been demonstrated to be relevant for the inclined cable aerodynamics [130], as it interacts with the vortex shedding [175; 131; 133]. When testing an inclined ($\beta = 45°$) cable model with helical fillets, Kleissl and Georgakis [86] did not report evidence of an axial flow based on near-wake flow visualization. To which extent an axial flow develops in the near wake of a bridge deck cross-section has not been explored yet. The present study attempts to provide some insights into this topic.

2.4   Quasi-steady aerodynamics of bridge decks

In general, the aerodynamic forces acting on a cable-supported bridge deck are due to [177]:

- The mean wind speed;

- The atmospheric wind turbulence, i.e. the so-called wind buffeting;

- The motion of the bridge deck cross-section in its three-degree-of-freedom (i.e. self-excited forces) and potential aerodynamic instabilities;

- The shedding of vortices in the near wake of the deck cross-section;

This study focuses primarily on the fluctuating wind buffeting loading. The modelling of vortex-induced vibrations and motion-dependent forces was not attempted. The reader shall refer to e.g. Simiu and Scanlan [177]; Dyrbye and Hansen [41] for a comprehensive overview on the aeroelasticity of cable-supported bridges.

The buffeting response is the dynamic motion of a structure excited by wind turbulence, which is modelled as an external random time-dependent loading. The buffeting action on a bridge deck originates from the wind-induced fluctuating surface pressures around the deck periphery. Here, the buffeting theory is addressed in the frequency domain, i.e. the so-called "spectral approach" is utilized. The buffeting problem of aircraft wings was first studied by Liepmann [117] in 1952. The application of the buffeting theory to cable-supported bridges is due to the seminal work of Davenport [33, 34] and Scanlan [168].
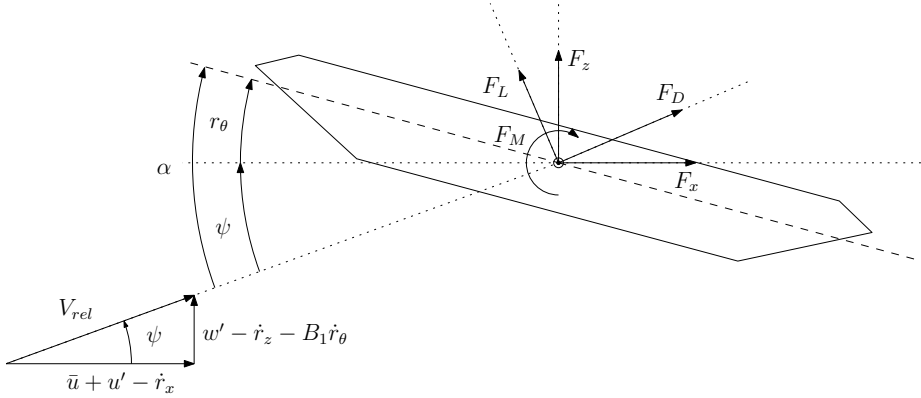
Figure 2.9: Notation for the cross-sectional aerodynamic forces (case of a zero yaw angle).

The framework of the buffeting theory addressed herein hinges on the following assumptions:

1. Quasi-steadiness, e.g. for the lift force per unit length (see Figure 2.9):

$$F_L = \frac{1}{2}\rho V_{rel}^2 B C_L(\alpha) \tag{2.32}$$

where V_{rel} is the relative velocity; α is the instantaneous relative angle of attack; B is the deck width; $C_L(\alpha)$ is the steady lift coefficient. The quasi-steady theory (QST) is generally most appropriate for low reduced frequencies $f_r = fB/\bar{u}$.

2. Linearity. Assuming small displacement and velocities:

$$V_{rel}^2 = \bar{u}^2 + 2\bar{u}u' - 2\bar{u}\dot{r}_x \tag{2.33}$$

$$\alpha = r_\theta + \psi = r_\theta + \frac{w' - \dot{r}_z - B_1\dot{r}_\theta}{\bar{u} + u' - \dot{r}_x} \tag{2.34}$$

$$C_L(\alpha) = C_L(\alpha_0) + \alpha C_L'(\alpha_0) \tag{2.35}$$

Note that the term B_1, which was first introduced by Irwin [74], accounts for aerodynamic damping contributions given by the torsional motion of the deck. In fact, it describes the distance of the so-called

aerodynamic centre from the shear centre, i.e. the arm by which the lift force generates the overturning moment. In principle, the value of B_1 depends on f_r and can be estimated based on the knowledge of the aerodynamic derivatives [38]. If not available, the value $B_1 = 0.25$ is generally assumed based on thin airfoil theory.

3. The fluctuating buffeting forces are assumed to be stationary random processes [117].

4. The real part of the one-point cross spectrum S_{uw} is assumed negligible. In the frequency domain, this is supported by Cheynet [22]; Øiseth et al. [147], who highlighted a negligible impact of S_{uw} on the computed vertical buffeting response of the Lysefjord Bridge and the Sotra Bridge, respectively.

5. The span-wise coherence of the oncoming turbulence is equal to the span-wise coherence of the buffeting forces, i.e. "the strip assumption", which was adopted first by Liepmann [117]. Its validity depends on the ratio between the length scale of turbulence and the characteristic length of the body, as outlined by Davenport [34]. The assumption may not be accurate in describing the gust loading for lift and twisting moment, for which the length scale associated with w ($\mathscr{L}_w$) may be of similar size as the deck width [101]. In this case, the wind turbulence is distorted as it is advected past the deck and a secondary span-wise cross-flow is augmented. This, together with the turbulence effect on the separated flow regions, favours an increase in the span-wise correlation of the lift force and the twisting moment [101].

6. The geometry of the bridge deck cross-section is constant along the span.

7. The yaw angle is $0°$.

It is worth noting that the linear framework employed to model the wind buffeting forces may not be appropriate when the oscillations of the relative angle of attack, driven by the wind turbulence, become significant. On the Lysefjord Bridge, a turbulence intensity $I_w \approx 0.17$ is generally observed for north-northeasterly flows [26]. This value can be interpreted as a dynamic angle of attack $\approx 10°$, which goes beyond the range of angles where the

linearisation of Equation (2.35) is adequate for the cross-section studied (see Figure B.2). For large low-frequency fluctuations of the angle of attack, a non-linear approach to model the aerodynamic forces is generally more accurate, see e.g. Diana and Omarini [39]; Argentini et al. [6].

   The computation of the buffeting response is out of the scope of the present study. Here the emphasis is primarily on the generation of the forces due to the full-scale wind turbulence. Validation of the buffeting theory applied to the Lysefjord Bridge can be found in Cheynet [22]; Cheynet et al. [25]. Nevertheless, it is clear that the present research ultimately aims at a more accurate prediction of the bridge buffeting response.

2.4.1   Cross-sectional buffeting forces

The power spectrum of the cross-sectional buffeting matrix at a given strip is defined as follows:

$$
\begin{bmatrix} S_{F_x}(f_r) \\ S_{F_z}(f_r) \\ S_{F_\theta}(f_r) \end{bmatrix} = \left(\frac{1}{2}\rho B \bar{u} \right)^2 \boldsymbol{B} \begin{bmatrix} S_u(f_r) \\ S_w(f_r) \end{bmatrix}
\tag{2.36}
$$

$$
\boldsymbol{B} = \begin{bmatrix} \left(2\frac{D}{B}C_D\right)^2 \cdot |\chi_{u,x}(f_r)|^2 & \left(\frac{D}{B}C_D' - C_L\right)^2 \cdot |\chi_{w,x}(f_r)|^2 \\ (2C_L)^2 \cdot |\chi_{u,z}(f_r)|^2 & \left(C_L' + \frac{D}{B}C_D\right)^2 \cdot |\chi_{w,z}(f_r)|^2 \\ (2BC_M)^2 \cdot |\chi_{u,\theta}(f_r)|^2 & \left(BC_M'\right)^2 \cdot |\chi_{w,\theta}(f_r)|^2 \end{bmatrix}
\tag{2.37}
$$

where $f_r = fB/\bar{u}$ is the reduced frequency; $S_{F_k}(f_r)$, with $k = x, z, \theta$, is the the auto-spectrum of the horizontal force, vertical force and moment per unit length, respectively; $|\chi_{j,k}(f_r)|^2$, with $j = u, w$ and $k = x, z, \theta$, are the aerodynamic admittances; $S_u(f_r)$ and $S_w(f_r)$ are the one-point auto-spectrum of the horizontal (u) and vertical (w) turbulence components, respectively.

   The aerodynamic admittance functions of a bridge deck cross-section are typically obtained from: (a) wind tunnel studies on motion-less section models in turbulent flow [100; 165; 101; 115] or in sinusoidal gusts [37]; (b) analytical models [98; 116]; (c) numerical simulation methods [154; 60]; (d) albeit very seldom, full-scale experiments [123; 124].

Unless an active turbulence generation is employed in the wind tunnel [37], it is often challenging to isolate the effect of either u or w on the admittances [101]. Hence, it is assumed:

$$|\chi_{u,x}(f_r)|^2 = |\chi_{w,x}(f_r)|^2 = |\chi_x(f_r)|^2 \tag{2.38}$$

$$|\chi_{u,z}(f_r)|^2 = |\chi_{w,z}(f_r)|^2 = |\chi_z(f_r)|^2 \tag{2.39}$$

$$|\chi_{u,\theta}(f_r)|^2 = |\chi_{w,\theta}(f_r)|^2 = |\chi_\theta(f_r)|^2 \tag{2.40}$$

Thus, the cross-sectional buffeting forces described in Equation (2.36) can be re-written as:

$$S_{F_x}(f_r) = (\frac{1}{2}\rho\bar{u}B)^2|\chi_x(f_r)|^2[(2\frac{D}{B}C_D)^2 S_u(f_r) + (\frac{D}{B}C_D' - C_L)^2 S_w(f_r)] \tag{2.41}$$

$$S_{F_z}(f_r) = (\frac{1}{2}\rho\bar{u}B)^2|\chi_z(f_r)|^2[4C_L^2 S_u(f_r) + (C_L' + \frac{D}{B}C_D)^2 S_w(f_r)] \tag{2.42}$$

$$S_{F_\theta}(f_r) = (\frac{1}{2}\rho\bar{u}B)^2|\chi_\theta(f_r)|^2[4B^2 C_M^2 S_u(f_r) + B^2 C_M'^2 S_w(f_r)] \tag{2.43}$$

From Equations (2.42) and (2.43), the cross-sectional admittance function for the lift ($|\chi_z(f_r)|^2$) and moment ($|\chi_\theta(f_r)|^2$) can be computed as follows:

$$|\chi_z(f_r)|^2 = \frac{S_{F_z}(f_r)}{(\frac{1}{2}\rho B\bar{u})^2[4C_L^2 S_u(f_r) + (C_L' + D/BC_D)^2 S_w(f_r)]} \tag{2.44}$$

$$|\chi_\theta(f_r)|^2 = \frac{S_{F_\theta}(f_r)}{(\frac{1}{2}\rho\bar{u}B)^2[4B^2 C_M^2 S_u(f_r) + B^2 C_M'^2 S_w(f_r)]} \tag{2.45}$$

2.4.2 Modal buffeting forces

Following Davenport [33, 34], the modal loads are computed using the joint acceptance functions. The lift forces are addressed hereinafter. Likewise, similar expressions can be derived for the drag force and the overturning moment.

For the $j-th$ vertical eigenmode $\phi_{z,j}(y)$, the corresponding joint acceptance function $|J_{z,j}(f_r)|^2$ is defined as follows:

$$|J_{z,j}(f_r)|^2 = \int_0^L \int_0^L \phi_{z,j}(y_1)\gamma_{F_zF_z}(f_r,\Delta y)\phi_{z,j}(y_2)dy_1dy_2 \qquad (2.46)$$

where $\gamma_{F_zF_z}(f_r,\Delta y)$ is the co-coherence (Equation (2.22)) of the vertical forces, the span-wise separation of which is Δy. Equation (2.46) describes the lack of full correlation of the vertical buffeting forces along the bridge span, weighted by a given eigenmode shape.

The spectrum of the modal lift force associated with $\phi_{z,j}(y)$ can be thus expressed as:

$$S_{Q_{z,j}}(f_r) = S_{F_z}(f_r)\,|J_{z,j}(f_r)|^2 \qquad (2.47)$$

If the strip assumption is invoked, e.g. for the lift force:

$$\gamma_{F_zF_z}(f_r,\Delta y) \approx \gamma_{ww}(f_r,\Delta y) \qquad (2.48)$$

Equation (2.46) then becomes:

$$|J_{z,j}(f_r)|^2 = \int_0^L \int_0^L \phi_{z,j}(y_1)\gamma_{ww}(f_r,\Delta y)\phi_{z,j}(y_2)dy_1dy_2 \qquad (2.49)$$

Here, $|J_{z,j}(f_r)|^2$ is computed based on the co-coherence of the oncoming vertical turbulence component. Equation (2.49) is commonly adopted in the computation of the buffeting loads primarily because an accurate knowledge of $\gamma_{F_zF_z}(f_r,\Delta y)$ is not always readily available. However, there is experimental evidence that the strip assumption (Equation (2.48)) may not always be applicable for lift and moment on bridge decks, see e.g. Larose [100, 101]; Jakobsen [78]. For example, the span-wise correlation of the lift acting on a closed-box girder bridge deck can be higher than the span-wise correlation of the vertical velocity fluctuations [100; 101; 78]. Consequently, using Equation (2.49) may lead to an underestimation of the modal lift force, for a given aerodynamic admittance function defined as in Equation (2.44).

2.4.3   The aerodynamic admittance function

The aerodynamic admittance function (AAF) relates the incoming turbulence to the unsteady gust loading on a line-like structure. It is a transfer function

that quantifies the efficiency of a body to generate e.g. the lift across different wave numbers, thereby accounting for the size of the eddies and their spatial characteristics as they are distorted and travel past the body. In the following, the AAF associated with the lift force is addressed.

The concept of AAF was first introduced by Sears [173] to compute the unsteady lift on a 2D thin symmetrical airfoil under a fully correlated sinusoidal vertical gust. Liepmann [117] suggested the following approximation to the Sears functions:

$$|\chi_z(f_r)|^2 = \frac{1}{1 + 2\pi^2 f_r} \tag{2.50}$$

where the reduced frequency f_r is based on the chord dimension. Equation (2.50) provides a relatively simple, yet practical, formula which is generally employed for comparison. Note that Equation (2.50) essentially describes a two-dimensional AAF as the incident flow is 2D and, thus, it is based on the chord-wise wave number only. Liepmann [118] extended the formulation for airfoils to the span-wise wave number to include the 3D effect of the oncoming turbulence. Later on, the lift-surface theory was employed by Graham [52, 53] to provide a numerical solution to the problem of the lift on a thin airfoil with infinite span considering the span-wise variation of turbulence, i.e. arbitrary yawed gusts. A close form solution can be found in Mugridge [142] for example. More recently, a generalized approach to compute the two-wave number lift AAF of a thin airfoil was developed by Li et al. [116].

As opposed to a thin airfoil, flow separation typically occurs on bridge decks. In addition, the width of the deck can be comparable or even larger than the typical length scales associated with the vertical velocity fluctuations. The application of the AAF to the buffeting problem of long-span bridges was initiated by Davenport [33]. The gust loading is typically modelled based on the chord-wise number using the strip assumption [33; 168]. The framework of its validity was outlined by Davenport [33] and Vickery [197]: the strip assumption is generally adequate when the turbulence length scales are much larger than the characteristic body dimension, the drag force being a good example. When that is not the case, the buffeting forces can be better correlated than the incoming velocity fluctuations, see e.g. Larose [100, 102]; Larose and Mann [98]; Larose et al. [99]; Sankaran and Jancauskas [166]; Kimura et al. [83]; Jakobsen [78]; Li et al. [115]. This is due to the 3D character of the incident turbulence and its distortion as it travels past the body

[101]. Consequently, a 3D analytical model was developed by Larose and Mann [98] to address the influence of the incident turbulence on the measured AAF as well as the span-wise structure of the gust loading. Based on Li et al. [116], a further generalization of the gust load modelling was proposed in Li et al. [115] employing a two-wavenumber 3D AAF in which the gust-independent (effects of the body geometry) and gust-dependent (effects of turbulence) contribution were explicitly defined.

In this study, the AAF is studied using Equations (2.44) and (2.45). Following the nomenclature used by Li et al. [115], they can be designated as 3D one-wavenumber AAF.

Chapter 3

The full-scale experiment

3.1 The Lysefjord Bridge

The study focuses on the full-scale measurements carried out on the Lysefjord Bridge (Figure 3.1), a suspension bridge crossing the inlet of Lysefjord, a narrow fjord in the south-western part of Norway (58.9237°N 6.0985°E). The bridge has a main span of 446 m (Figure 3.2), with its midspan located 55 m above the mean sea level. Its longitudinal axis is oriented with an azimuth angle of $-42°$ (Figure 3.3). The bridge location is characterised by complex topography, with surrounding steep hills and mountains which influence significantly the prevailing wind direction and the turbulence characteristics. Flows from north-northeast (from the inside of the fjord) or south-southwest (from the inlet of the fjord) are predominantly observed at the site [26].

The cross-section of the bridge deck is a hexagonal closed-box steel girder (see Figure 3.4) with a width-to-depth ratio of $B/D = 4.6$, where B = 12.3 m and D = 2.7 m. The angle between the bottom plate and the lower side panel of the bridge deck is 27°. Whereas, the top inclined panels have an inclination of 45°. The bridge has a two-lane road. The cycle/pedestrian lane and corresponding median divider are located on the west side of the deck.

3.2 Overview of the experimental setup

Since November 2013, the Lysefjord Bridge has been equipped with a Wind and Structural Health Monitoring system [25] which currently comprises 3D sonic anemometers, tri-axial accelerometers and a Real-Time Kinematic-

Figure 3.1: A view of the Lysefjord Bridge from the south-west (Photo by N. Daniotti - UiS).
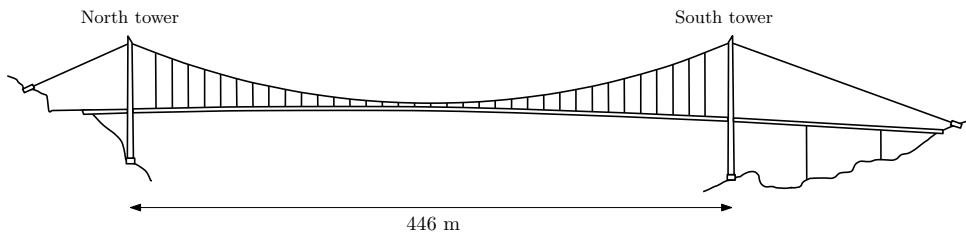
Figure 3.2: Overview of the Lysefjord Bridge.

Global Positioning system (RTK-GPS) [178].

To minimize the deck-induced flow distortion when studying the turbulence characteristics [26], the instrumentation layout was updated in 2017 by mounting 3D sonic anemometers on both sides of the bridge deck. In August 2020, two 3D sonic anemometers with a horizontal head for lower flow distortion from the transducers and probe supports were installed at the deck level. The primary objective of these additional sensors is to study the turbulence structure and vortex formation in the near wake region. An overview of the system for continuous long-term monitoring of wind turbulence and bridge deck acceleration response is given in Figure 3.5.

To gain further insight into the aerodynamics of a bridge deck at full-scale *Re* numbers in a turbulent atmosphere, a tailor-made pressure measurement system was installed in June 2021. The design and development process of this system is challenging and will be further discussed in Section 3.4.
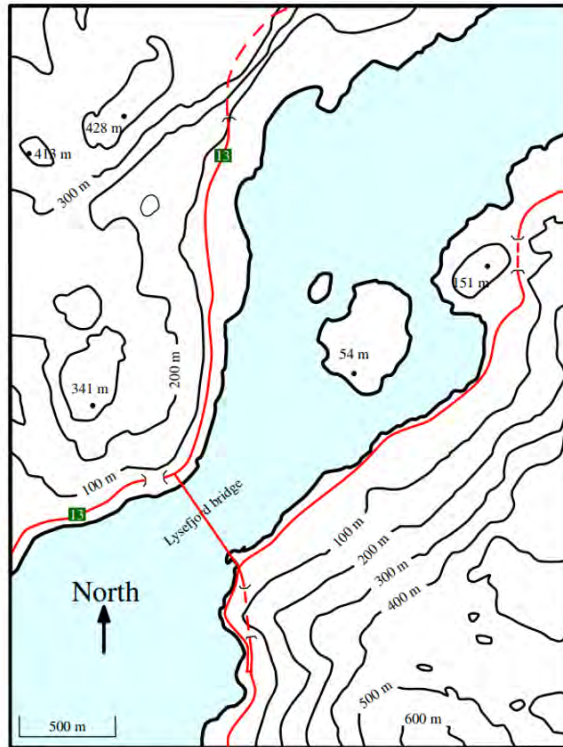
Figure 3.3: Topographic map of the area around the Lysefjord Bridge, from Cheynet et al. [26].
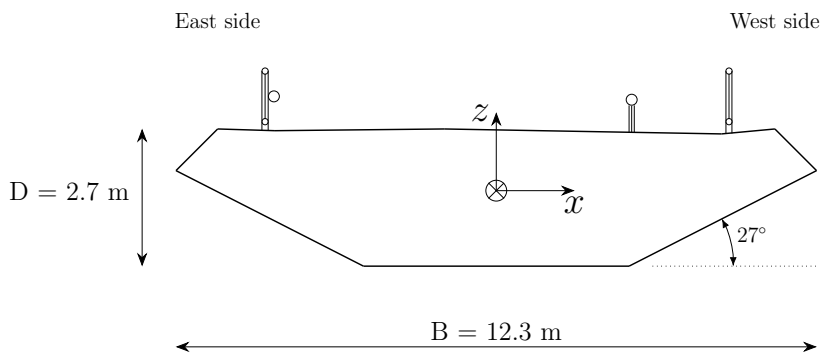
Figure 3.4: Schematic of the deck cross-section of the Lysefjord Bridge.

Wind-induced surface pressures are now measured along three cross-sectional strips along the main span of the bridge, between hangers H-08 and H-10. A list of the complete instrumentation system is given in Table 3.1.

Table 3.1: Summary of the instrumentation setup for monitoring wind turbulence, surface pressures and bridge deck acceleration response. The span-wise distance from the north tower is designated as y.

Sensor ID	Description	Location	y (m)
H08E	3-D WindMaster Pro	Hanger H-08, 6 m above the deck, East	103
H08Wb	3-D WindMaster Pro	Hanger H-08, 6 m above the deck, West	103
H08Wt	3-D WindMaster Pro	Hanger H-08, 10 m above the deck, West	103
P08Et	Static pressure probe	Hanger H-08, 4 m above the deck, East	103
P08Wt	Static pressure probe	Hanger H-08, 4 m above the deck, West	103
D08E	3-D WindMaster HS	Deck level, 2 m from deck edge, East	105
D08W	3-D WindMaster HS	Deck level, 2 m from deck edge, Wast	105
P08E	Static pressure probe	Deck level, deck nose, East	105
P08W	Static pressure probe	Deck level, deck nose, West	105
PSA	Pressure strip A	-	109
PSB	Pressure strip B	-	114
A_H09E	Tri-axial accelerometer	Hanger H-09, East	115
A_H09W	Tri-axial accelerometer	Hanger H-09, West	115
PSC	Pressure strip C	-	126
H10E	3-D WindMaster Pro	Hanger H-10, 6 m above the deck, East	127
H10W	Vaisala WXT520	Hanger H-10, 6 m above the deck, West	127
H18E	3-D WindMaster Pro	Hanger H-18, 6 m above the deck, East	223
H18W	3-D WindMaster Pro	Hanger H-18, 6 m above the deck, West	223
A_H18E	Tri-axial accelerometer	Hanger H-18, East	223
A_H18W	Tri-axial accelerometer	Hanger H-18, West	223
H20W	3-D WindMaster Pro	Hanger H-20, 6 m above the deck, West	247
H24W	3-D WindMaster Pro	Hanger H-24, 6 m above the deck, West	295
A_H24E	Tri-axial accelerometer	Hanger H-24, East	295
A_H24W	Tri-axial accelerometer	Hanger H-24, West	295
A_H30E	Tri-axial accelerometer	Hanger H-30, East	367
A_H30W	Tri-axial accelerometer	Hanger H-30, West	367
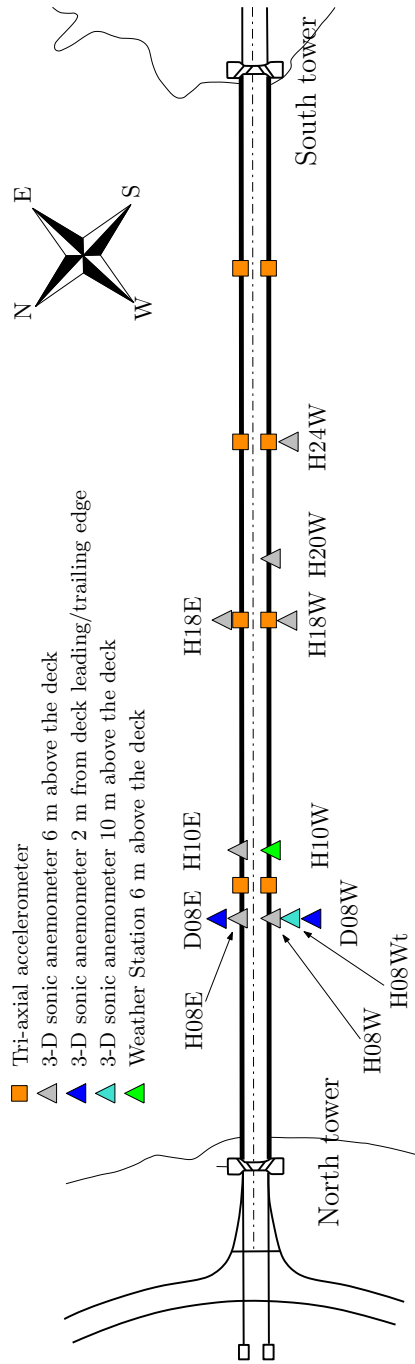
Figure 3.5: Overview of the instrumentation for wind turbulence and bridge deck response study. The distance between two neighbouring hangers is 12 m.

3.3 Detailed bridge instrumentations

3.3.1 Accelerometers

Four pairs of tri-axial accelerometers are located on the diaphragms inside the bridge girder to monitor the bridge response. The main focus is on the translational response in vertical and lateral directions as well as the rotation around the bridge axis. The sensors are located in the vicinity of hangers H-09, H-18, H-24 and H-30 (see Figure 3.5). The accelerometers are CUSP-3D from Canterbury Seismic Instruments (tri-axial MEMs servo silicon accelerometers), with a ± 4g range and a maximum output rate of 200 Hz. The linearity of the sensor is $< \pm 0.1\%$. Within the temperature range $-10\,°C$ to $50\,°C$, the offset and gain errors are $< \pm 0.02\%$ and $< \pm 0.08\%$, respectively.

3.3.2 Sonic anemometers above the bridge deck

The wind turbulence is monitored using simultaneous 3D sonic anemometers installed on the upwind and downwind sides of the bridge deck. The wind sensors are designated in accordance with their spatial location utilizing the text string HXY, where X identifies the hanger number and Y specifies the west (W) or east (E) side of the deck (see Figure 3.5). The notation follows the one introduced in Cheynet et al. [26] for the sake of consistency.
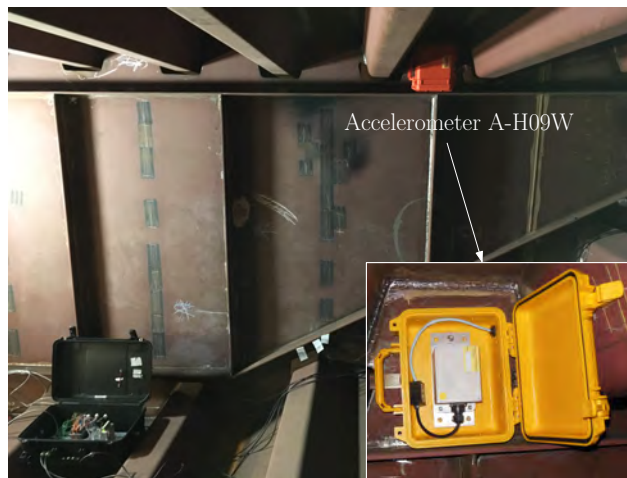
Figure 3.6: A view of the accelerometer A_H09W and its location within the bridge girder (Photo by J.T. Snæbjörnsson - UiS).

Seven anemometers are located at 6 m height above the deck. At hanger H-08 on the west side, an additional anemometer (H08Wt) is positioned at 10 m height above the road level. The fixtures of the instruments are such that the horizontal location of the sonic measurement volume is approximately at the leading/trailing edge of the bridge girder. The distance between each neighbouring hanger is 12 m. Therefore, the span-wise separation between the sonic anemometers ranges from 24 m up to 120 m and from 24 m up to 192 m on the east and west side of the deck, respectively. The sonic anemometers mounted above the bridge deck are 3-D WindMaster Pro manufactured by Gill Instruments. The instrument provides wind measurement data along three-axis with an output sampling rate up to 32 Hz.

A weather transmitter (WXT530 from Vaisala) is mounted on hanger H10, west side of the deck, to monitor the micro-meteorological data in terms of the horizontal wind components, relative humidity, barometric pressure, absolute air temperature and rain intensity. The sensor can operate with a sampling frequency of up to 4 Hz.

3.3.3   Sonic anemometers at the bridge deck level

The near wake turbulence of the bridge deck is studied based on simultaneous measurements performed by two 3D sonic anemometers positioned at the deck level, both upstream and downstream of the deck along a single cross-sectional strip. The latter is located in the vicinity of hanger H-08, 2.1 m towards the middle of the span. The sensors are identified using the text strings D08W and D08E, for the west and east side, respectively. A schematic of locations of the sonic measurement volume for the different sonic anemometers at hanger H-08 is shown in Figure 3.7. The supporting brackets for anemometers D08W and D08E are designed to achieve a distance between the measurement volume and the bridge deck nose of approximately 2.00 m and 0.14 m along the horizontal and vertical planes, respectively. Figure 3.7 illustrates the instrumentation setup designed to provide unique simultaneous measurements of undisturbed turbulence above the deck, as well as near deck turbulence at nose height, both upstream and downstream.

The fluctuations of the vertical velocity component in the near-wake region, close to its expected centreline, are of primary interest. Hence, the choice of the anemometer geometry for this specific application becomes essential. The 3D sonic anemometers utilized are the Gill WindMaster HS,
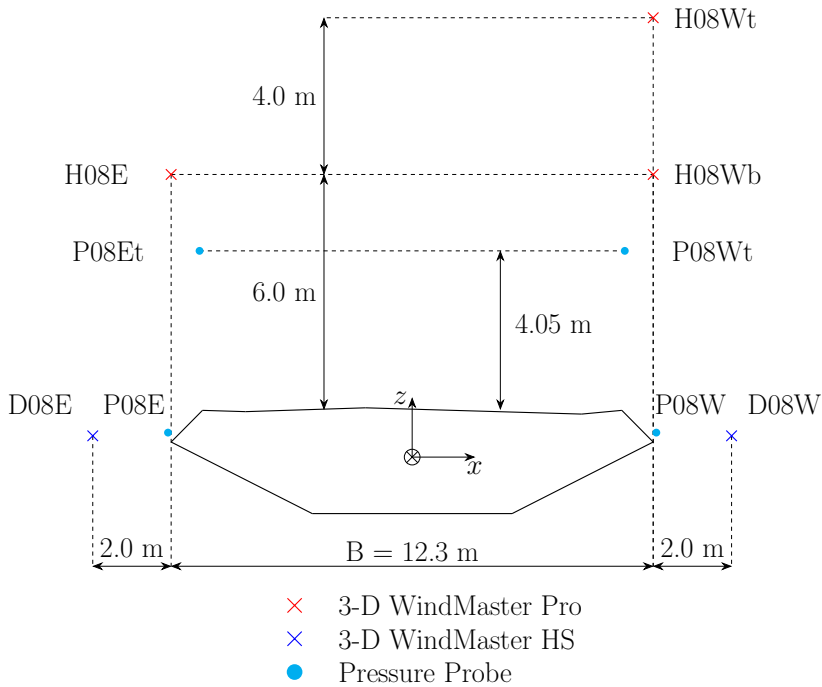
Figure 3.7: Scheme of the instrumentation for wind flow measurements within a cross-section strip at hanger H-08 (120 m from midspan).

manufactured by Gill Instruments (see left panel of Figure 3.8). This sensor is designed with a horizontal head to minimize the anemometer body-induced distortion of the vertical turbulence component, allowing for accurate flow measurements over a wide range of angles of attack, especially when the head faces the flow. The instrument outputs 3-axis wind speed and sonic temperature data with an internal sampling rate up to 32 Hz. The length of the sonic path is 150 mm and the diameter of the transducers is 11 mm [134]. A close-up of the anemometers is reported in Figure 3.8. The anemometers are mounted with a tilt angle within $\pm 1°$ from the horizontal plane, thereby ensuring accurate measurements of the angle of attack both for upstream and downstream flows. When the supporting bracket is on the upwind side of the sonic paths (wake measurements), the reading of the horizontal velocity components may be partly affected by shadowing effects from the bracket.

The supporting bracket for the anemometers was designed based on specific aspects. Firstly, it was crucial to perform flow measurements in the vicinity of the near wake centreline, e.g. close to the bridge deck nose.

Figure 3.8: A view of the sonic anemometers D08W and H08Wb (left panel) and a close-up on the bracket supporting sonic anemometer D08E (right panel). Photos by N. Daniotti - UiS.

This facilitates the investigation of the potential presence of an axial flow developing on the leeward side of the bridge. Secondly, the layout of the frame had to be designed to minimize the flow distortion induced by the supporting structure itself. The response of the anemometer is obviously not omnidirectional in the sense that a larger flow distortion is expected when the anemometer is positioned downstream the bridge deck, i.e. for near-wake flow measurements. However, in this region, the flow is, anyway, severely distorted by the deck signature turbulence and dominated by the formation of vortex structures, which likely overshadow the additional flow distortion induced by the boom/anemometer system. Thirdly, adequate robustness of the structure was required to withstand a wide range of weather conditions, avoiding unwanted structural vibrations under gusty winds.

Two views of the bracket supporting the anemometers D08W and D08E are shown in Figure 3.8. The frame consists primarily of aluminium strut profiles manufactured by Bosch Rexroth. It was fixed in two points onto the railing, namely the bottom pipe and the vertical rods. Figure 3.9 shows a drawing of the supporting brackets as built.
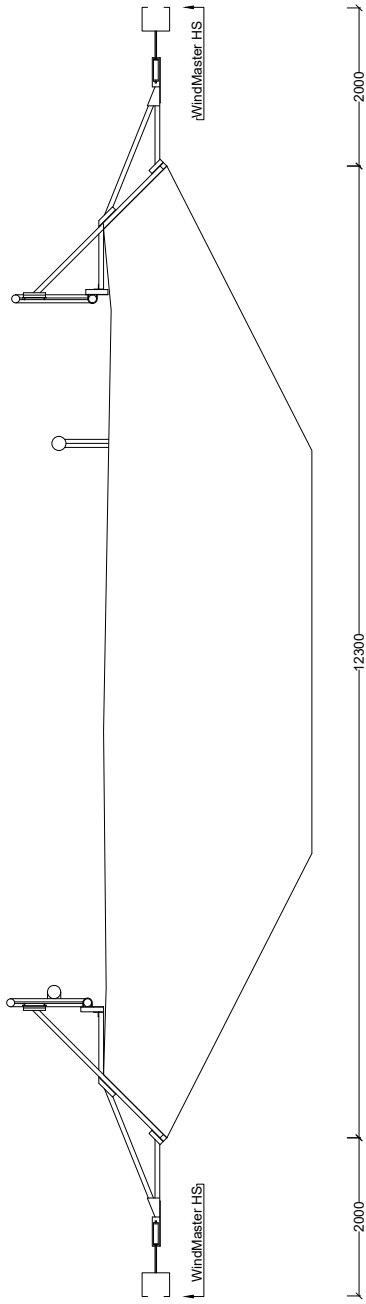
Figure 3.9: A drawing of the brackets supporting the 3-D Sonic Anemometer WindMater HS by Gill Instruments, tailored for turbulence measurement in the near wake. Dimensions are in (mm).

3.3.4   Data acquisition

The digital signals (RS422 communication format) of the wind and acceleration sensors are acquired utilizing five data acquisition units (DAQs), which serve 18 separate instruments. The timing synchronization of the units is based on GPS time. A master logging unit groups the UTC synchronized data stream from each DAQ unit and locally records 10 min-long data-sets, containing data from all sampled channels. Thereafter, the data is automatically transferred and stored in a server located at the University of Stavanger by utilizing a 4G router communication. The DAQ units are CUSP-Ms manufactured by Canterbury Seismic Instruments. The data acquisition system is set to operate in a continuous sampling mode, with a sampling frequency of 50 Hz for all the channels. An in-depth description of the measurement system for continuous monitoring of wind and structural response can be found in Snæbjörnsson et al. [178].

3.4   Pressure measuring system

3.4.1   Overview

The pressure measuring system comprises 36 pressure taps, distributed along three pressure strips, which are placed along the bottom perimeter of the bridge girder. The objective is to monitor the wind-induced surface pressure distribution around the bridge deck but also to study their span-wise coherence. A simplified schematic of the instrumentation setup adopted is given in Figure 3.10. Each pressure tap is monitored using an analogue differential pressure transducer (ePressure V2.0 sensor from SVMtec GmbH). The reference static pressure for the sensors is obtained from a controlled air volume located inside the bridge girder. Fluctuations of the atmospheric static pressures are monitored using two omni-directional static pressure probes [141] installed 4 m above the bridge deck at hanger H-08 (see Figure 3.7). Two additional pressure probes are mounted at the nose on each side of the deck (Figure 3.7). The pressure sensors are housed in transducer boxes, which are fixed to the railing in the vicinity of the pressure strips. Signal cables are conveyed from the transducer boxes to the interior of the bridge girder. The A/D conversion is performed and the data acquisition is handled by DAQ units from NI that are operated using the LabVIEW software.
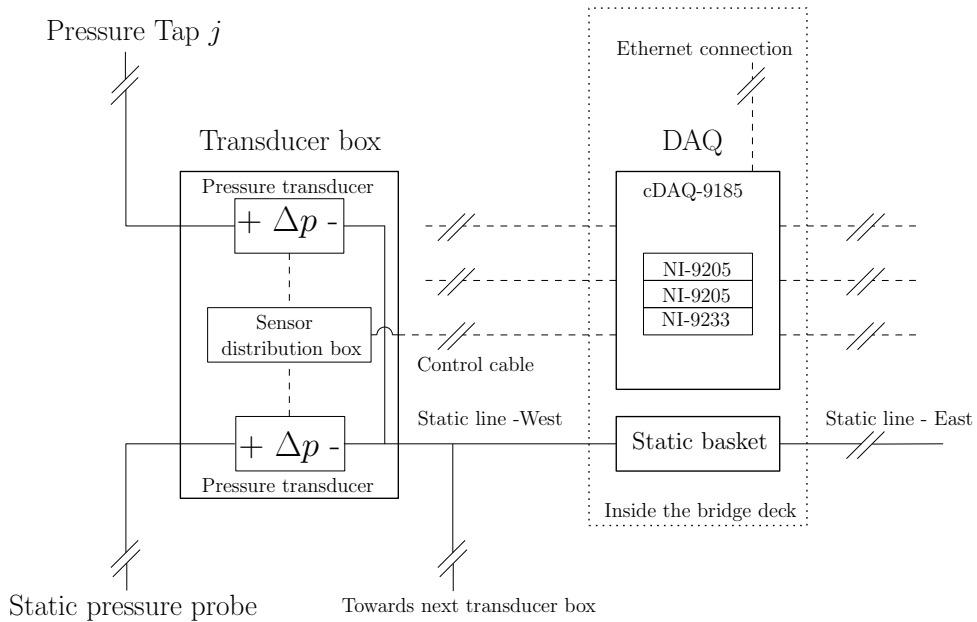
Figure 3.10: A schematic of the pressure measurement system. For the sake of clarity, a single transducer box, containing two differential pressure transducers, is used here to represent six transducer boxes with six pressure transducers each. The dotted lines indicate signal cables whereas the thin continuous lines indicate the tubing to the pressure transducers.

The installation of the pressure measuring system was completed on 11-12 June 2021. Since then, the system has been operated with only minor interventions for maintenance and without major changes in the layout or electronics.

An initial measurement setup consisting of three pressure probes ("Hoxey probes" developed by Moran and Hoxey [141]) was installed on the bridge in July 2020. The goal of that pilot study was to test the pressure sensors and the data acquisition system, as well as investigate the wind-induced pressures at the leading and trailing edge of the deck. One pressure probe was fixed to the hanger H-08 on the west side, at 3.4 m height above road level, to monitor the atmospheric static pressure. The other two pressure probes were positioned on the mounting bracket supporting the deck side sonic anemometers D08E and D08W. The corresponding pressure sensing locations are reported in Figure 3.7. All three probes had a common reference pressure from a pneumatic static bottle (from the Scanivalve Corporation)

located inside the bridge deck. This measurement setup was operated until the complete pressure measuring system was installed in June 2021.

3.4.2   Surface pressure

Fluctuating surface pressures are monitored on the portion of the deck between hanger H-08 and hanger H-10. This is also the part of the bridge that is densely instrumented with sonic anemometers (see Figures 3.5 and 3.7). The surface pressures are monitored along three chord-wise strips, that are stretched around the bridge deck. Each strip has 12 tapping points. The layout of the pressure taps per strip, which is reported in Figure 3.11, is based on the positions where the larger variance of surface pressure is expected to occur for a typical closed-box girder bridge deck of a similar width-to-depth ratio [101]. The pressure strips are referred to as Strip A, Strip B and Strip C. Strip A is positioned 5.8 m from hanger H-08, towards the middle of the main span. The normalized span-wise separations between the strips are $\Delta y/B = 0.41$, $\Delta y/B = 0.98$ and $\Delta y/B = 1.38$, as shown in Figure 3.12. These distances were chosen mainly based on wind tunnel studies that investigated the span-wise correlation of fluctuating lift and overturning moment due to the buffeting wind action, in a simulated atmospheric boundary layer flow [101; 99; 98], based on spire-generated turbulence.

The pressure taps are identified using the character string XY, where $X = \{A,B,C\}$ traces the chord-wise pressure strip; $Y = \{1,2,...,12\}$ denotes the location of the tapping point within a given chord-wise strip (see Figure 3.11). The numbering scheme of the taps follows an anti-clockwise direction starting from the pressure tap located on the top inclined surface of the girder, on the east side.
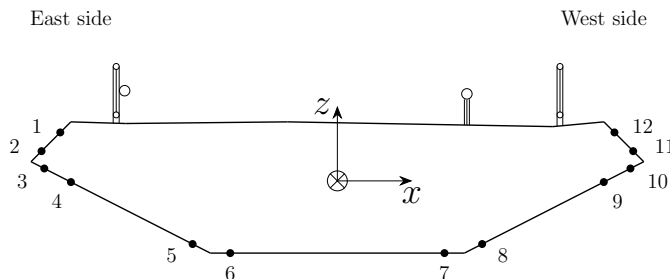
Figure 3.11: Pressure taps distribution for pressure strips A, B and C.
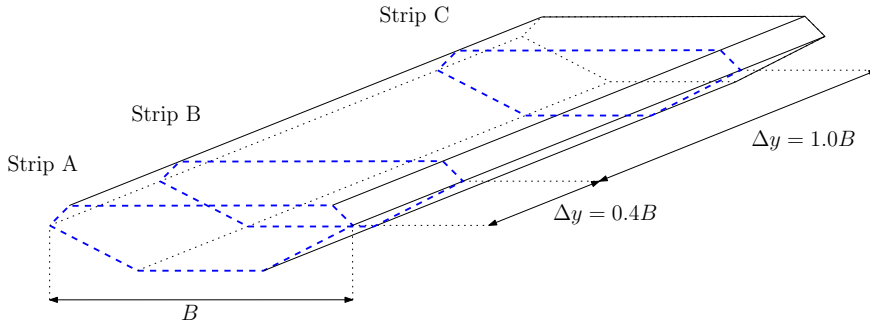
Figure 3.12: Span-wise separation of the pressure strips. Pressure strip A is located 5.8 m from the hanger H-08 cross-section, towards the mid-span.

The along-span position of the pressure strips in relation to the first 4 eigenmode shapes is illustrated in Figure 3.13. Here, the eigenmodes are identified using the character string *abn*, where $a = H, V, T$ represents the lateral (H), vertical (V) and torsional (T) bridge motion; $b = S, A$ is the symmetric (S) or asymmetric (A) mode shape; *n* is the mode number. In the same figure, the eigenfrequencies are also reported. The modal analysis is performed using the simplified bridge model described in Cheynet et al. [25].

The chord-wise pressure strips essentially consist of custom-made straps, which were developed in collaboration with Seilmaker Mathiesen AS, Stavanger (Norway). The design concept is based on the pressure taps being embedded in a strap, which is tensioned around the lower and inclined surfaces of the bridge deck up to the railings. The strap needs to be double skinned, so that surface pressure measurements can be performed at tapping points on the outer skin, approximately 20 mm from the steel deck surface, while the bottom skin, the strap itself, supports the tension applied and protects the tubing in-between the two layers. The objective is to create a pressure measurement concept that could be implemented without any damage to the bridge structure, such as drilling holes through the steel skin of the girder. The solution achieved, is deemed a fairly natural and successful first step in potential further development, although not without some complications as can be expected.

Selected views of the pressure strip during the assembly stage are reported in Figure 3.14. The total nominal length of the main body, i.e. a lashing belt made of polyester, is 15.98 m whereas its width is 75 mm. It is equipped with an overlaying net running along the portions of the belt where the tapping
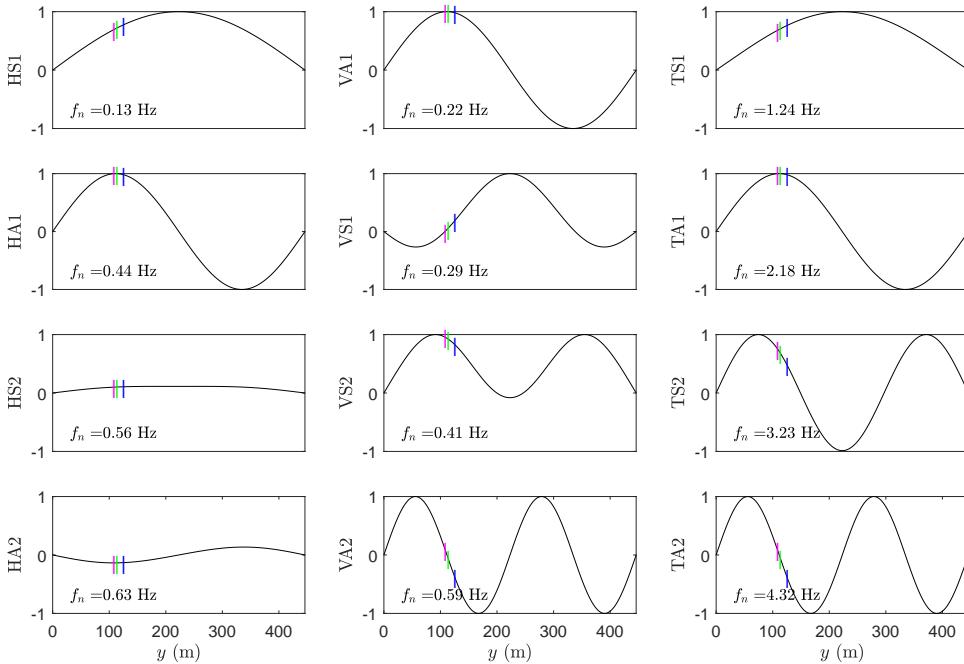
Figure 3.13: The location of the pressure strip A (|), B (|) and C (|) with respect to the first 4 horizontal (left panels), vertical (mid panels) and torsional (right panels) eigenmode shapes.

points are deployed. One side of the overlay is stitched to the lashing belt whereas the other is equipped with a Velcro strap which serves as a securing system.

The tapping points consist of thread-to-barb fixed elbow fittings (ELB50-3/8 manufactured by Pneumadyne), with a thread size of 3/8 NPT (M) and a barb accommodating tubing size of 5 mm internal diameter (i.d.). A view is given in Figure 3.14. The tapping hole size is 6 mm in diameter. Such a dimension was found adequate to prevent a complete blocking of the sensing hole due to dust particles and raindrops during rainfalls. The threaded end protrudes through the overlaying net, onto which a thin carbon fibre fixing plate (100 mm in length and 60 mm in width) is installed. This provides a relatively flat surface around the tapping hole, which is essential when performing surface pressure measurements. The 90° elbow is eventually fixed using a compatible locking nut (see Figure 3.14), which also acts as a droplet stopper for water running down, along the strap. The pressure signal is conveyed to the pressure transducers using flexible clear tubing with 5 mm
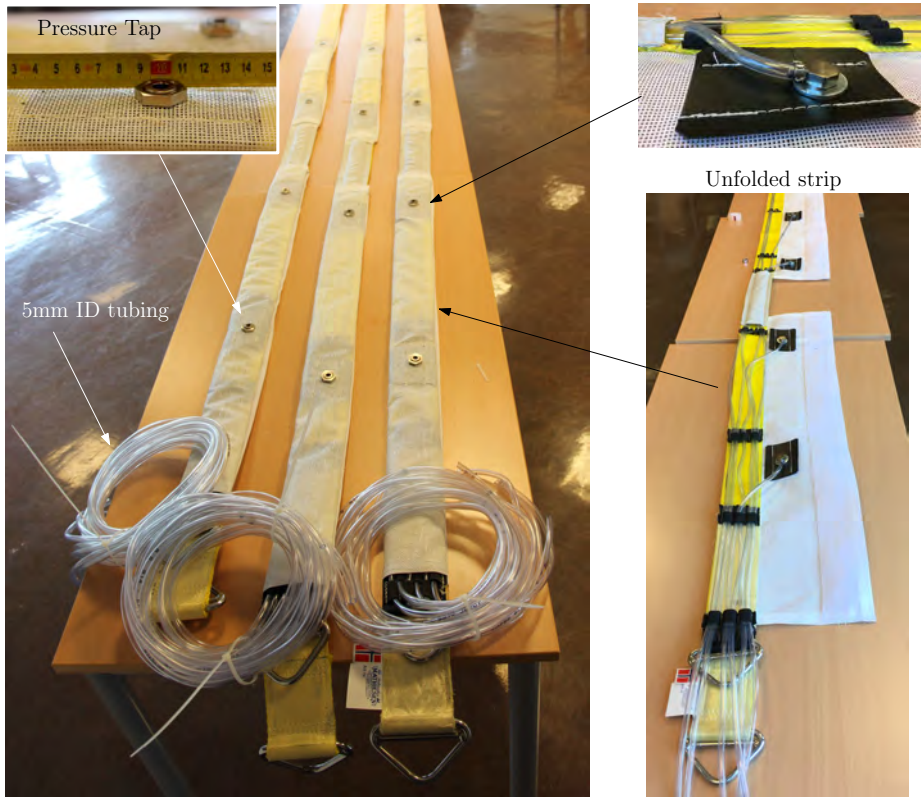
Figure 3.14: Selected views showing the essential features of the pressure strip. Photos by N. Daniotti - UiS.

i.d., which runs along the strap, between the inner and outer skin. Such a value of internal diameter should minimize condensation-induced problems [109] which may distort the pressure signals. Undesired movements of the tubing system are prevented utilizing stitched guiding loops along the belt. The length of the tubing varies depending on the location of the pressure tap. The shortest length is 2.30 m (pressure taps 01 and 12) whereas the longest is 7.57 m (pressure taps 6 and 7). The distortion effects on the pressure signals induced by the tubing system are corrected in the frequency domain [73] utilizing a frequency response function estimated based on the theoretical formulation described in Bergh and Tijdeman [12]. The design of the tubing system, in terms of length and i.d., also considers the transition to turbulent flow, which is not compliant with the assumptions that the theory of Bergh and Tijdeman [12] was derived for. Following Kaspersen and Krogstad [81], the maximum amplitude of pressure associated with laminar flow within the

Figure 3.15: The pressure strips as seen from the base of the North tower (left panel) and a side view of one end of the strap and corresponding anchoring elements, showing also two tapping points (right panel). Photos by J.T. Snæbjörnsson - UiS.

tubing is computed as a function of frequency and axial coordinate along the tube length, for all tapping points. The performance of the tubing system is found adequate to ensure a reliable estimate of the corresponding transfer functions to correct the pressure signals. Outside the overlaying net of the pressure strip, the tubing system is protected from direct sun exposure and intrusion of foreign objects by using braided expandable plastic sleeves, as shown in Figure 3.16.

At critical locations along the strap, such as corners of the bridge girder, Aramid tape is utilized on the side facing the steel deck to ensure adequate strength as well as flexible and lightweight reinforcement. The same Aramid tape reinforcement is employed at the two ends of the belt. EPDM foam sheets are installed at discrete locations along the bottom inclined surface of the bridge deck, at gaps between the strap and the girder surface, to prevent unwanted vibrations of the belt to occur. The overlay offers porosity of the protection for the tubing system as well as a uniform surface roughness along the pressure strip length. The porosity of the overlaying net also facilitates water drainage. A view of the pressure strips from the base on the north tower is given in the left panel of Figure 3.15.
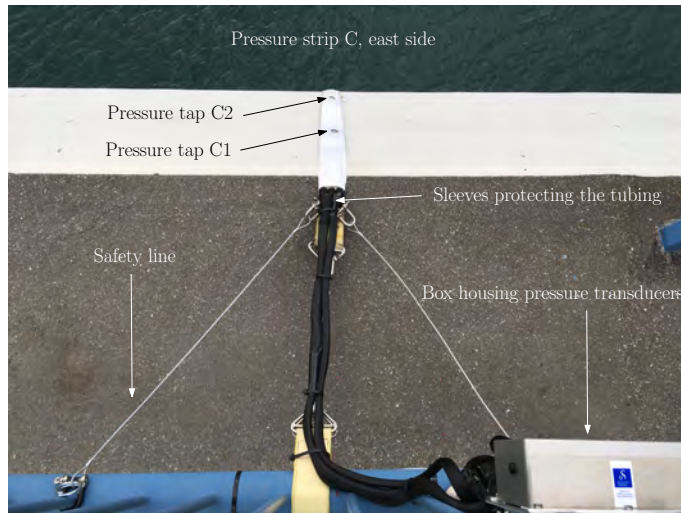
Figure 3.16: A top view of pressure strip C on the bridge deck. Photo by N. Daniotti - UiS.

Two stainless steel triangle delta rings are fitted to the ends of the strip to serve as fixing points, as shown in Figures 3.14 and 3.16. A stainless steel turnbuckle connects (see right panel of Figure 3.15) the pressure strip to a lashing belt reinforced with Aramid tape, which is fixed to the bottom pipe of the railings (Figure 3.16). Two ratchet lashing belts were utilized to achieve the targeted tension of the pressure strap. Periodic inspections are undertaken to ensure the tension of the pressure strip.

Rainfall may pose some practical challenges for the acquisition of valuable surface pressure data around a bridge deck in a wet state, as also reported by Isaksen [76]. For the pressure taps $\{03, ..., 10\}$, the drainage of possible rainwater intrusion is facilitated by gravity as well as the orientation of the tapping hole itself, i.e. the tapping holes are not directly exposed to rain. The slope of the tubing also contributes to preventing the tubing from being waterlogged along the measurement line. The pressure taps on the bottom part of the deck generally provide adequate monitoring of wind-induced pressures also during rainfalls. On the other hand, the pressure taps located on top inclined surfaces of the girder, i.e. taps $\{1, 2, 11, 12\}$, are directly exposed to raindrops and, therefore, they are not fully operational when the rain intensity is significant. However, valuable pressure signals can generally be obtained under drizzle, as the tapping point is not flush with the strap surface due to the presence of the locking nut, which prevents rainwater travelling

downwards along the deck slope from entering the tapping hole. Once the tubing gets waterlogged despite the gravity drainage, it generally takes 3 to 5 days to re-establish a pressure signal undistorted by water intrusion and/or condensation, depending on the wind conditions, air temperature fluctuations and sun exposure. Inspection and, if needed, manual purging of the pneumatic lines are undertaken periodically.

3.4.3   Reference pressure system

When performing (low-amplitude) differential measurements of wind-induced surface pressures in full-scale, it is essential to have adequate control of the reference pressure [109]. The design and implementation of the reference pressure system are fundamental aspects to minimize the bias in the pressure data. For example, the famous Aylesbury comparative experiment [176] highlighted a lack of accuracy in the reference pressure, when comparing mean pressure coefficients for the very same 1:100 scale low-rise building, which was tested across seventeen wind tunnels worldwide. As pointed out by Levitan [109] for the field of building aerodynamics, adopting a suitably (mechanically) low-pass filtered atmospheric static pressure as reference pressure is the most advantageous approach. The source of the atmospheric static pressure could be either a ground tapping, consisting of a manhole or buried tank equipped with a small hole [111; 110; 68], or a static pressure probe mounted at a reference height [69; 159; 67]. Due to the inherent fluctuations of the atmospheric (static) pressure, a suitable pneumatic average with a restrictor tube is generally used as a mechanical low-pass filter [109]. The positioning of the pressure probe poses a further challenge, especially in complex terrain. Placing the reference static pressure probe within the static fields of the monitored structure or neighbouring (bluff) bodies shall, therefore, be avoided.

The so-called "hybrid" [109] reference pressure system, an implementation of which can be found in e.g. Snæbjörnsson [179], is utilized for the present experiment. The source of the reference pressure is a suitably insulated air tank, providing the backing pressure for all the differential pressure measurements. The atmospheric static pressure, which is sensed by a pressure probe described in Section 3.4.4, is measured separately against the selected backing pressure, in the same way as the surface pressure at the taps. After digital low-pass filtering, its signal can be subtracted from the external surface
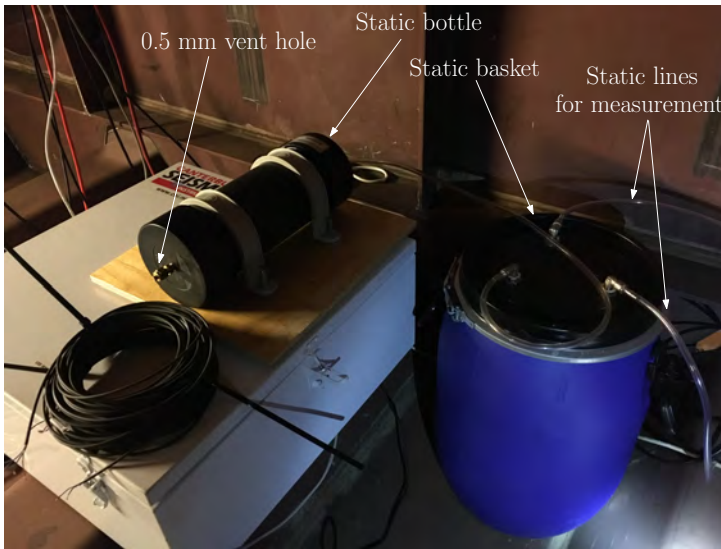
Figure 3.17: System for ambient reference pressure serving the static lines connected to the differential pressure transducers. Photo by N. Daniotti - UiS.

pressure signal of interest to incorporate the low-frequency fluctuations of the atmospheric static pressure. Thus, an overall versatile reference pressure system can be achieved (see Figure 3.10).

The differential pressure transducers are all referenced to the internal pressure within a pressure static bottle (manufactured by Scanivalve), which is connected in series to a pressure static basket of larger volume to serve a large number of pressure sensors in the measurement chain. This reference pressure system is located inside the bridge deck in the vicinity of hanger H-08, as depicted in Figure 3.17. The static pressure bottle has an internal volume of approximately $3.2 \cdot 10^{-3}$ m^3 filled with non-corrosive expanded mesh, which helps to damp potential pressure waves within the volume. One end is equipped with a vent hole of 0.5 mm in diameter, which governs the leakage rate in order to allow for low-frequency changes of the internal pressure due to temperature, ventilation and humidity variations inside the bridge girder. The other end is connected to the pressure static basket via a 1 m-long flexible tubing with 5 mm i.d.. Following a design by Scanivalve, the static pressure basket, which consists of polyethene drum with a volume of 30 L, is equipped with open and cleaned aluminium cans and is airtight apart from input and output. The static basket outputs two reference (static) pressure lines for differential measurements, namely one for the east side of the deck

and one for the west side. The above-described (static) reference pressure system provides an adequately reliable and stable ambient backing pressure, which is essential for low-amplitude differential pressure measurements.

The backing pressure is transmitted to the differential pressure transducers by using a 5.0 mm i.d. clear PVC tubing, with 10 m length (inside the bridge deck), which transitions to a 6.3 mm inner diameter reinforced PVC clear tubing (outside the bridge deck), with a total length of 22 m. Tubing having an inner diameter larger than 4 mm should minimize condensation problems [109], which could have a fatal effect on the final differential pressure reading. Outside, the reference line is embedded in a plastic conduit, which is fixed to the bottom pipe of the railings, to protect it from direct sun exposure, thereby limiting a potential source of relatively fast temperature changes. In the vicinity of each pressure strip, a single 0.5 m-long and 5.0 mm i.d. clear PVC tubing brings the backing pressure signal to the inside of the transducer box (see also Section 3.4.5). A bulged tube connector manufactured by Scanivalve is used to transition to a 1.5 mm i.d. Tygon clear tubing, which serves all the reference ports of the differential pressure transducers using "T" or "X" tube connectors manufactured by Pneumadyne together with short feeder lines (approximately 60 mm long). The layout of the backing pressure tubing system is identical for both the east and west sides of the bridge deck.

An inherent challenge for such a reference system is the sensitivity to temperature changes, which, even if relatively small in magnitude, can induce relatively large pressure changes relative to a given dynamic pressure [109]. However, since both the reference volume and static lines are located within the same environment, the pressure drift induced by a temperature drift should be minimum. Moreover, a low-pass filtered version of the atmospheric static pressure is subtracted from the acquired surface pressure signals (see Section 3.4.4). This should more or less cancel out potential drift driven by temperature changes. The inside of the bridge deck is nominally sealed from the outside environment due to the operation of a dehumidification system inside the bridge. This contributes to minimizing any high-frequency ambient pressure fluctuations inside the bridge girder.

Periodically, the tubing system conveying the reference pressure is inspected to ensure that no inadvertent critical damage and/or leaking affects the output of the differential pressure transducers.

3.4.4   Atmospheric static pressure

The knowledge of the atmospheric static pressure is essential when performing full-scale experiments on bridge aerodynamics utilizing a differential pressure measuring system. Therefore, it is crucial to consider the location of the pressure probe in relation to the static pressure field surrounding the bridge deck. Obviously, the reference pressure probe shall be positioned where the body-induced effects on the static pressure field of the turbulent flow are minimum [30; 109]. Mean wind speed, wind direction, angle of incidence of the flow, turbulence intensity and length scales are among the factors likely influencing both the time-averaged and fluctuating component of the static pressure at a given location around the deck. The adoption of two pressure probes located on each side, well above the bridge deck was, therefore, a fairly natural choice to ensure a representative measure of the static pressure for the oncoming flow.

The atmospheric static pressure is studied using simultaneous measurements of the shroud-type static pressure probes described in Moran and Hoxey [141]. The probes are installed at 4.05 m height above the deck on the upwind and downwind sides at hanger H-08, as shown in Figure 3.18. The text strings P08Wt and P08Et (see also Figure 3.7) identify the pressure probe located on the west and east side of the deck, respectively. Performance specifications of the pressure probe can be found in Moran and Hoxey [141]; Hoxey et al. [68] as well as in the review paper of Nishiyama and Bedard Jr [144]. The probe is omni-directional with respect to the yaw angle and is operational also during rainy and adverse weather conditions. The shroud-collar gap of the probe [141] is set to 5.5 mm. An 11.7 m-long clear flexible tubing with 5 mm i.d. transmits the pressure signal to the box housing the differential pressure transducers (Section 3.4.5). As for the pressure taps distributed around the bridge deck (section 3.4.3), tubing-induced distortions of the pressure signals are corrected in the frequency domain [73] utilizing a frequency response function estimated based on the theoretical formulation described in Bergh and Tijdeman [12].

Since its original development in 1979 [141], the static pressure probe has been utilized for a variety of full-scale applications such as wind-induced loads on buildings [160; 159; 65], sensing the pressure field around a full-scale building [67], boundary-layer meteorology [68], the aerodynamics of trains [152; 184] and reference (static) pressure for studies on building aerodynamics [159; 67; 179].
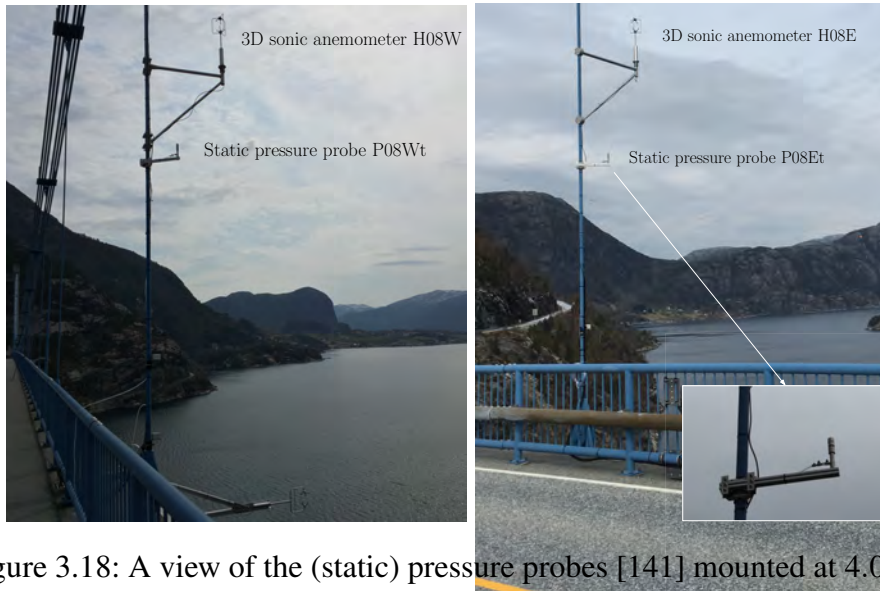
Figure 3.18: A view of the (static) pressure probes [141] mounted at 4.05 m height above the bridge deck at hanger H-08, on the west side (left panel) and east side (right panel). Photos by N. Daniotti - UiS.

Wind tunnel tests were conducted at Svend Ole Hansen ApS (Copenhagen, Denmark) to assess the capabilities of the probe in sensing the first moment of the static pressure for both (nominally) smooth and turbulent flows (spire-generated turbulence with $I_u \simeq 0.10$). The details of the experimental setup adopted and essential results can be found in Appendix A. In spire-generated turbulence with $I_u \simeq 0.10$, the probe measures the mean static pressure with an error between -0.03 and $+0.03$ the wind dynamic pressure, for angles of wind incidence in the range $-10° \leq \alpha \leq 10°$. In summary, the probe response is nearly omni-directional with respect to the yaw angle and associated with suitably small errors for changes in the angle of attack. Therefore, the probe is ideally suited for the present full-scale experiment.

3.4.5   Data acquisition

Thirty-six individual differential pressure transducers (ePressure V2.1 from SVMtec GmbH) are utilized. The pressure transducers have a full-scale (FS) range of ± 2500 Pa and a rated accuracy of maximum 0.25% FS (typically 0.05% FS). The signal output is analogue voltage, within the range 2.25 ± 2 V. The output voltage is temperature-compensated for values of air temperature ranging from 5°C to 50°C. A frequency resolution up to 1 kHz is possible.
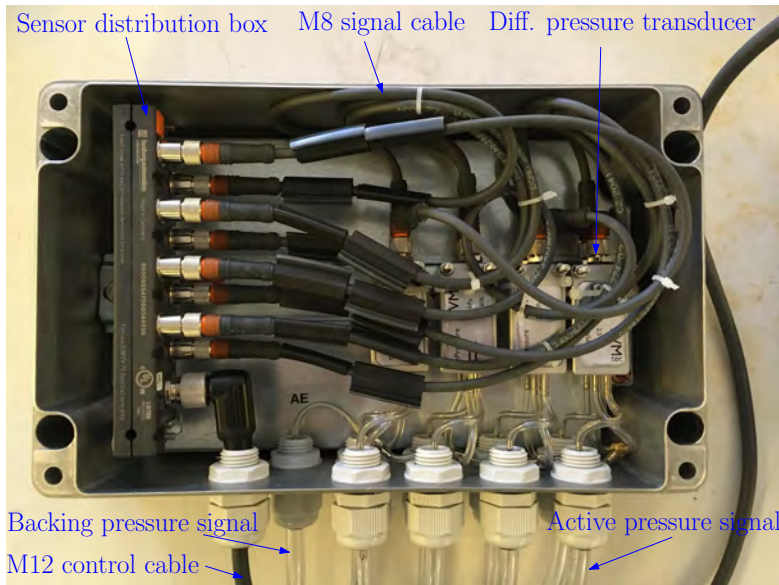
Figure 3.19: A transducer box including eight differential pressure transducers
(ePressure V2.1 from SVMtec GmbH) and a sensor distribution box.

The pressure transducers are housed in the so-called transducer boxes,
the inside of which is shown in Figure 3.19. For each pressure measurement
strip, two transducer boxes, adjacent to either end of the strap, collect the
pressure signals, one from the east side and the other from the west side.
Each pressure transducer is connected to a miniature sensor distribution box.
The sensor distribution box is equipped with 8 ports for M8 3-pole cables
and a M12 connection for the control cable from the transducer box to the
DAQ units inside the bridge. The latter allows for a shared power supply for
the pressure transducers as well as a junction for the different signal wires,
thereby minimizing the number of signal cables entering the bridge deck.
The transducer box is rated IP 68 and is equipped with two protective vents
(PolyVent High Airflow, manufactured by Gore) to reduce condensation,
minimize the temperature increase and balance the pressure within the sealed
enclosure. As mentioned in Sections 3.4.2 and 3.4.4, the pressure signals
from the tapping points as well as the pressure probes are transmitted to
the transducer box using 5 mm i.d. flexible clear tubing. A transition to a
60 mm-long 1.5 mm i.d. Tygon clear tubing, which eventually connects the
active side of the pressure transducer, occurs within a cable gland fitted to the
side of the box, as shown in Figure 3.19. The transition consists of a bulged

Figure 3.20: A view of two transducer boxes on the east side of the bridge deck (left panel) and a close-up showing their fixture (right panel).

tube connector manufactured by Scanivalve.

A total of six transducer boxes are installed on the bridge, three on each side, in the vicinity of each pressure strip monitored. A view of two transducer boxes installed on the east side of the deck is given in Figure 3.20. These boxes are fixed to the vertical rods of the railings (see right panel of Figure 3.20) in such a way that the additional air-flow blocking is minimized, thereby reducing potential induced flow distortion for the adjacent pressure taps. For the typical frequency range of interest in full-scale bridge aerodynamics, this effect is considered negligible.

The logging system consists of a CompactDAQ Ethernet chassis (cDAQ-9185 manufactured by NI) equipped with three Voltage Input modules (two NI-9205 and one NI-9233, manufactured by NI). A view of the data acquisition unit is given in Figure 3.21. The CompactDAQ controls the connectivity, timing, synchronization and data acquisition. Each NI-9205 module can perform 16 differential or 32 single-ended analogue inputs using a programmable input range, with a 16-Bit A/D (analog-to-digital converter). All the channels are multiplexed to the A/D, with a conversion time of 8 μs. To minimize the electrical noise present in the input signals, and, in general, attain more accurate measurements, a differential measurement approach is utilized. The NI-9233 module features 4 input channels with a $\pm$ 5 V range and a 24-Bit resolution for the A/D. Based on the adopted pressure transducers, the analog-to-digital conversions provide pressure resolutions of 0.0763 Pa and 0.0003 Pa for NI-9205 and NI-9233 modules, respectively.
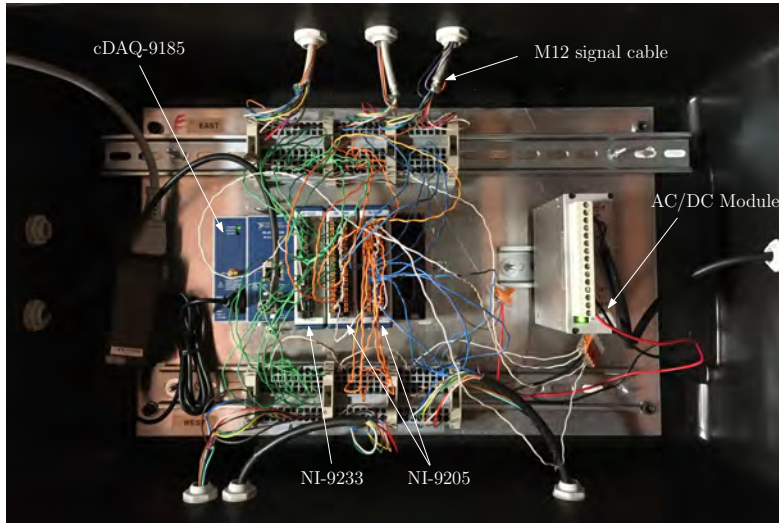
Figure 3.21: Internals of the data acquisition box for pressure measurements.

The data acquisition unit (CompactDAQ) is connected to the central computer via the local area network (LAN) using a TCP/IP protocol. The computer runs a dedicated logging routine written in LabVIEW, a visual programming language from NI. The synchronized pressure data is gathered in a single text file every 10 min and stored locally on the hard drive of the central computer. Thereafter, the data is transferred to a server at the University of Stavanger via the mobile network by means of a 4G router. The data acquisition unit operates in a continuous sampling mode, with a sampling frequency set to 50 Hz for all monitored channels. Given the adopted conversion time per channel, namely 8 µs/16 for the NI-9205 module, the inherent constant delay between the output of subsequent channels is negligible for the adopted sampling frequency. Hence, a digital time shift correction for such an asynchrony is not applied.

Quality checks are undertaken to ensure that the pressure measuring system outputs valuable signals. A dedicated preliminary analysis of the data is essential to identify potential issues stemming from rainwater and/or foreign object intrusion in the tapping points, electrical noise in the DAQ system, leaks in the tubing system or, in general, a non-operational component in the measurement chain which cannot be easily identified during visual inspections.

Chapter 4

The approaching turbulent flow

4.1 Introduction

The primary objective sought in this chapter is twofold. Firstly, a site-specific statistical description of wind turbulence is addressed as it is essential when studying wind-induced effects on line-like structures [34]. The case of cable-supported bridges located in complex terrain environments may also require ad hoc studies, since the turbulence characteristics differ from those encountered in a flat and homogeneous terrain [91; 28; 47; 26; 138; 139]. Therefore, wind turbulence modelling is here addressed as a basis for the topics discussed in the subsequent chapters, namely near-wake turbulence (Chapter 5) and wind buffeting loads (Chapter 6). Secondly, the deck-induced distortion of the approaching wind turbulence is studied, focusing on a potential relationship with the generation of the gust loading, as well as its (often practical) implications regarding the anemometry instrumentation on cable-supported bridges. In that respect, the chapter attempts a natural continuation of the analysis of the deck-induced flow distortion described in Cheynet et al. [26] for the Lysefjord Bridge.

The layout of the chapter is as follows: after presenting an overview of the wind conditions on-site (Section 4.2), the processing of the velocity data utilized for subsequent computation is given in Section 4.3. Thereafter, the one-point turbulence characteristics for north-northeasterly flows are discussed, since this wind exposure is treated further in Chapters 5 and 6. The emphasis is on the comparison between the wind turbulence seen at 6 m height above the deck, on the upwind side, and the wind turbulence 2 m

upstream the bridge deck nose (Section 4.4). Lastly, Section 4.5 discusses the modelling of the wind turbulence in terms of one-point velocity spectra and lateral co-coherence.

4.2   Wind conditions: an overview

Figure 4.1 reports the wind rose estimated based on 10 min-long stationary records, acquired from 01/08/2020 to 01/08/2021. The velocity records are from sonic anemometer H08E, which is located on the east side of the deck at 6 m-height above the road level, which corresponds to 62 m above the mean sea level. In the figure, the bridge axis is represented by the black thick line with an azimuth angle of $-42°$. Due to the local topography [26; 29], two primary directional sectors can be identified: flows from inside the fjord (north-northeast exposure) and from the inlet of the fjord (south-southwest exposure). The largest wind velocities, i.e. $\bar{u} \geq 15\,\mathrm{m\,s^{-1}}$, are recorded for the south-southwesterly flows, namely from the sub-sector centred around $220°$, which is also generally characterised by turbulence intensities between 10% and 15% [25]. The mean wind speed associated with north-northeast winds does not exceed the value of $15\,\mathrm{m\,s^{-1}}$. Figure 4.1 also shows that wind seldom blows normal to the bridge axis.

As already described in Cheynet et al. [25, 26] and reported in Figure 4.2 for I_w, the turbulence intensity (TI) recorded on-site depends on the wind
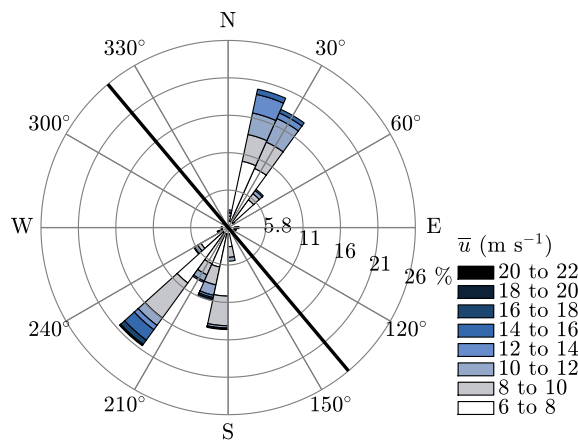
Figure 4.1: Mean wind speed recorded by H08E, based on 10 min-long stationary records with $u \geq 6\,\mathrm{m\,s^{-1}}$, acquired from 01/08/2020 to 01/08/2021.
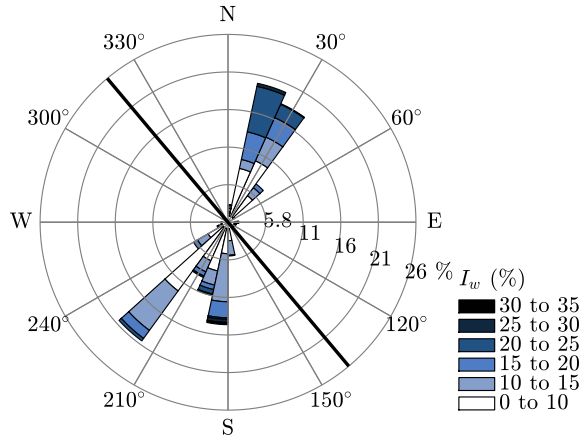
Figure 4.2: Vertical turbulence intensity (I_w) recorded by H08E, based on 10 min-long stationary records with $u \geq 6\,\mathrm{m\,s}^{-1}$, acquired from 01/08/2020 to 01/08/2021.

exposure. A larger TI is generally found for the north-northeast exposures, with values up to $I_w = 0.26$ likely due to the influence of the highly complex terrain upstream of the bridge [29]. Nevertheless, flows associated with exceptionally low TI and stable thermal stratification of the atmosphere may also be, albeit rarely, recorded, as described in Cheynet et al. [27]. The observed TI for south-southwesterly flows is generally slightly larger for the sub-sector centred around 190°. Note that for SSW flows, I_w is generally underestimated when using velocity records acquired on the downwind side (H08E) due to the deck-induced flow distortion [26].

4.3   Data collection and processing

4.3.1   Dataset

The dataset comprises velocity records acquired from 01/08/2020 to 01/08/2021. Due to a failure of some GPS receivers providing the time synchronization for data sampling, velocity records acquired by sonic anemometers H08Wb and H08Wt were only available starting from 21/12/2020 and onwards. Cheynet et al. [26] demonstrated that the deck-induced flow distortion affects the velocity measurements undertaken on the downwind side of the Lysefjord Bridge deck, at 6 m height from the road level. Thus, to ensure a statistical
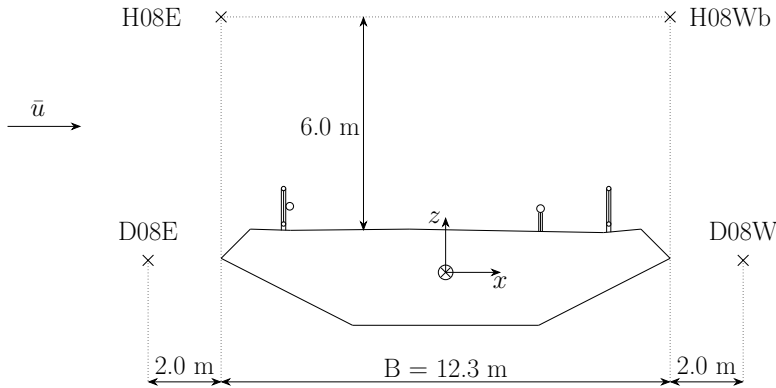
Figure 4.3: Schematic of the sonic anemometers layout at hanger H08.

significance of the results presented herein, the NNE wind exposure is prioritized. Similarly, Chapter 5 addresses the near-wake turbulence for NNE flows. Nevertheless, selected records associated with SSW winds are utilized throughout this work, e.g. in Section 4.5.2 to discuss the lateral coherence and in Section 6.6 to explore the vortex shedding process.

The reference sonic anemometer is H08E (see Figure 4.3), which is located at 6 m height above the deck, on the upwind side of the girder for north-northeasterly winds. Throughout the chapter, the symbol $()_0$ denotes a quantity computed based on H08E. For example, $(\bar{u})_0$ is the mean wind speed at the reference sonic anemometer H08E. It is assumed that H08E samples the undistorted (by the bridge deck) approaching wind turbulence. This is supported by the results discussed hereinafter but also in Cheynet et al. [26]. Note that some minor transducer-induced flow distortion may arise, especially for the one-point cross-spectra involving w. For turbulence measurements upstream of the deck, the sonic anemometer D08E is utilized. The sonic volume is located 2 m ahead of the bridge deck nose, as shown in Figure 4.3. The span-wise separation between the two sonic anemometers H08E and D08E is 2.15 m.

4.3.2   Data processing

The present section summarizes the processing of the data to study the first- and second-order statistics of wind turbulence, including the velocity spectra in the local wind coordinate system (Section 2.2). The term "local" refers herein to the point of measurement, i.e. the location of the sonic anemometer

considered, as different levels of mean flow distortion are expected along and across the bridge deck. An averaging time of 20 min is utilized, with the underlying assumption of stationarity of the time series for that duration. The double-rotation technique [79; 203] is adopted to project the recorded three velocity components onto the wind coordinate system u, v, w. Prior to the pre-processing, the velocity records are low-pass filtered and down-sampled to 25 Hz.

The correction proposed in the keynote series number KN1508 by Gill Instruments [51] is utilized to correct the "bug" affecting the vertical velocity component readings for the sonic anemometers H08Wb, H08Wt, H18E, H18W, H20W and H24W, which are of the older WindMaster Pro type. Note that no correction is needed for the newer sonic anemometers H08E, H10E, D08E and D08W. No correction to account for probe-induced flow distortion effects (see e.g. Peña et al. [151]) is attempted either.

For the ease of interpretation as well as implementation, the second-order stationarity of the velocity fluctuations u, v and w is addressed following Cheynet et al. [26]. A centred-unweighted moving standard deviation filter with an averaging time of 5 min is utilized. The tested 20 min blocks for u, v and w are rejected if any instantaneous averaged value has a relative difference larger than 40%.

Heavy rain or snow is often the cause of noisy data from sonic anemometers. If the instruments can not evaluate the velocity data, they report a 999 value, which needs to be removed from the data set, during the pre-processing. The precipitation data from the weather station H10W can be used to flag those samples. The velocity records are de-spiked and the resulting NaN values linearly interpolated [36] for subsequent processing provided that the percentage of NaN's is lower than 1%. In addition, the skewness and kurtosis of u, v, w for each 20 min of 25 Hz data segment are computed. Samples associated with a value of skewness outside the range (-2,2) or a kurtosis larger than 8 [196] are disregarded for further processing.

Prior to the calculations of the second-order statistics of turbulence, any linear trend is removed. Only samples with mean wind speed $\bar{u} \geq 6\,\mathrm{m\,s}^{-1}$ and $|z/L| < 0.1$ are considered for further computations. The atmospheric stability parameter, z/L, is assessed using Equation (2.7), based on the sonic anemometer H08E. Furthermore, the accepted yaw angle is limited to $-45° \leq \beta \leq 45°$ whereas for the mean angle of wind incidence the range is $-10° \leq \alpha \leq 10°$. Samples associated with turbulence intensity $I_u \leq 0.01$ or $I_u \geq 0.40$

are also disregarded. The total number of 20 min-long samples included in post-processing is eventually 219 for the NNE wind sector, to be addressed hereinafter.

Power spectral density function

Each spectrum is computed based on 20 min-long stationary time series using the Thomson [191] multi-taper method, with a time-halfbandwidth product of 4, and subsequently smoothed over 100 frequency windows, the centre of which is equally spaced along a logarithmic axis. The lowest resolved frequency is $1.7 \cdot 10^{-3}$ Hz. Thomson's method [191] applies orthogonal tapering functions to the full-length time series, thereby estimating uncorrelated power spectral densities, which are averaged to obtain the final output. The multitaper spectrum estimation method is well suited to estimate the power spectra characterised by a power-law behaviour [136].

Eventually, the ensemble average of the normalized power spectral densities is performed using the median operator for each normalized frequency bin. Here, the reduced frequency is $n = fz/\bar{u}$ (Equation (2.11)), where f is the frequency, z is the measurement height above the sea level and $\bar{u}$ is the mean wind speed estimated at H08E.

4.4   Analysis of the approaching wind flow

Herein the one-point turbulence characteristics for north-northeasterly approaching flows are discussed, with emphasis on the comparison between the wind turbulence seen at 6 m height above the deck, on the upwind side, and the wind turbulence 2 m upstream the bridge deck nose.

4.4.1   First-order statistics

Figure 4.4 quantifies the relationship between the mean wind speed $\bar{u}$, the mean yaw angle β and the mean angle of wind incidence α recorded at H08E and D08E. On D08E, 2 m upstream of the deck leading edge, the mean velocity parallel to the (local) streamline is found to decrease by 9%. This represents the blocking effect of the bridge deck as the flow approaches the stagnation region, where the adverse pressure gradient is expected to be
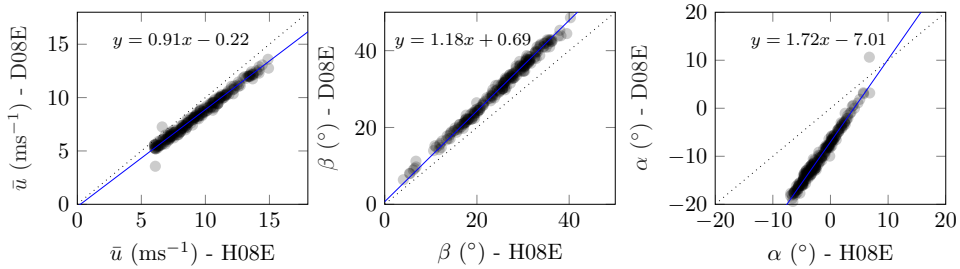
Figure 4.4: Relationship between mean wind speed $\bar{u}$ (left panel), mean yaw angle β (mid panel) and mean angle of wind incidence α (right panel) recorded by H08E and D08E (upstream the deck); 219 20 min-long records with $u \geq 6\,\mathrm{m\,s^{-1}}$ and $|z/L| \leq 0.1$, from 01/08/2020 to 01/08/2021.

relatively strong [11]. Due to the asymmetry of the cross-section, the ratio $\bar{u}$(D08E)/$\bar{u}$(H08E) increases slightly as α decreases.

The mean flow approaching the deck appears to be distorted also in terms of yaw angle β. The latter exhibits a systematic increase with respect to the yaw angle estimated at H08E, thereby indicating that for $\beta \neq 0°$, the velocity component along the bridge axis increases locally. In other words, when the flow is at an angle, the streamlines deflect slightly towards the bridge axis as the stagnation region is approached. This behaviour is well documented for the three-dimensional flow around a yawed/inclined ($\beta \leq 45°$) circular cylinder, see e.g. Shirakashi et al. [175]; Kozakiewicz et al. [89] for the sub-critical Re number regime. In fact, flow visualizations showed that streamlines generally bend along the cylinder axis before going past it at an angle of $\beta \approx 0°$.

The flow 2 m upstream of the leading edge of the deck is deflected downwards, as shown in Figure 4.4. When $\alpha = 0°$ at H08E, the mean angle of wind incidence at D08E is $-7°$.

Field measurements of wind turbulence on cable-supported bridges are commonly undertaken with sensors mounted above the bridge deck, see e.g. Kristensen and Jensen [91]; Sacré and Delaunay [164]; Brownjohn et al. [17]; Bietry et al. [13]; Fenerci et al. [47]; Cheynet et al. [26]. In general, the measured mean angle of wind incidence likely depends on the surrounding terrain characteristics as well as the height of the sonic volume above the bridge girder and placement relative to the deck width. The impact of the

sensor position on the measured angle of attack is also a function of the deck geometry, its aspect ratio and the railing transparency/geometry. Unless ad hoc wind tunnel studies [93] or CFD calculations [123] are additionally performed, it is often challenging to isolate and quantify the contribution given by the deck-induced flow distortion. To the author knowledge, only two examples of sonic anemometers mounted on horizontal booms at the deck level are documented in the literature: the Tsing Ma Suspension Bridge in Hong Kong [207] and the Gjemnessund Bridge in Norway [5]. For the latter, a bias in the mean angle of incidence was found when comparing flow measurements 2.7D upstream of the leading edge and above the bridge deck, on the upwind side. The estimated bias was on average $-5°$ for a horizontal flow [5], which reflects the distortion of the streamlines induced by the bridge deck.

Albeit being an "extreme" case, as the measurements here presented are undertaken only 2 m ahead of the leading edge, Figure 4.4 provides a first insight into the level of the distortion of the mean flow characteristics estimated upstream of a bridge deck nose. Why is that important? Firstly, if a prediction of the buffeting response is attempted, the values of $\bar{u}$ and α need to be accurately estimated. Secondly, the level of distortion for the mean values may indicate that the fluctuating velocity components, e.g. velocity spectra, are also affected by the blocking effect created by the girder, as shown in the following sections. This aspect is, perhaps, overlooked in some field studies, where "corrections" are applied only to $\bar{u}$ and α, thereby neglecting the potential distortion of the recorded velocity spectra, which is then subsequently used for buffeting calculations.

4.4.2   Integral turbulence characteristics

The one-point turbulence characteristics estimated at H08E and D08E are given in Tables 4.1 and 4.2 for the north-northeasterly flows. Each quantity is expressed as $a \pm b$, where a is the ensemble-averaged value based on the median operator and b is the corresponding standard deviation.

The significant turbulence intensity levels recorded by H08E reflect a wind flow in a complex terrain environment. For example, $\sigma_w/\sigma_u = 0.74 \pm 0.08$, is much larger than the value generally associated with flat homogeneous terrain and $|z/L| \leq 0.1$, e.g. $\sigma_w/\sigma_u = 0.5$ [183]. The estimated values are in overall agreement with those reported in Cheynet et al. [26], who considered

Table 4.1: Turbulence intensities and integral length scales of turbulence for NNE flows; 219 20 min-long records with $u \geq 6\,\mathrm{m\,s^{-1}}$ and $|z/L| \leq 0.1$, from 01/08/2020 to 01/08/2021. The notation $\pm$ indicates the standard deviation of a quantity.

Sensor	I_u	I_v	I_w	L_v^X/L_u^X	L_w^X/L_u^X
H08E	0.26 ± 0.07	0.22 ± 0.06	0.19 ± 0.05	0.81 ± 0.43	0.41 ± 0.15
D08E	0.27 ± 0.08	0.25 ± 0.08	0.34 ± 0.09	0.78 ± 0.59	0.47 ± 0.21

Table 4.2: Estimated turbulence characteristics for NNE flows; 219 20 min-long records with $u \geq 6\,\mathrm{m\,s^{-1}}$ and $|z/L| \leq 0.1$, from 01/08/2020 to 01/08/2021. The notation $\pm$ indicates the standard deviation of a quantity.

Sensor	σ_v/σ_u	σ_w/σ_u	σ_u/u_*	σ_v/u_*	σ_w/u_*
H08E	0.85 ± 0.13	0.74 ± 0.08	1.94 ± 0.30	1.72 ± 0.37	1.41 ± 0.23
D08E	0.96 ± 0.15	1.28 ± 0.15	1.65 ± 0.43	1.60 ± 0.42	2.10 ± 0.53

only samples $u \geq 10\,\mathrm{m\,s^{-1}}$ and $|z/L| \leq 0.1$ to reduce the uncertainties in the estimates. Table 4.1 shows that the estimation of L_v^X/L_u^X is associated with a fairly large dispersion due to the low-frequency velocity fluctuations in the natural wind. A lower dispersion is attained for L_w^X/L_u^X since S_w is characterised by less energy at $n < 0.1$ [150].

Upstream of the bridge deck nose, the local turbulence intensities, I_v and I_w, exhibit a significant increase on D08E compared to H08E. Specifically, $I_w = 0.34 \pm 0.09$. Instead, the local I_u did not change significantly. However, for a body-distorted flow approaching the stagnation region as in D08E, local turbulence intensities are inherently affected by the attenuation of the local mean wind speed. Thus, the relationship between the standard deviation of u, v, w recorded at H08E and D08E is explored in Figure 4.5 to better interpret the results. The along-wind component rms attenuate by 9%, which, interestingly enough, coincides with the attenuation of $\bar{u}$. Along the across-wind direction, velocity fluctuations ahead of stagnation are not particularly affected in terms of their variance. Instead, the vertical velocity component experiences a strong amplification, namely a 53% increase.

The results shown in Figure 4.5 can be interpreted based on the theory developed by Hunt [70] to describe the distortion of isotropic turbulence
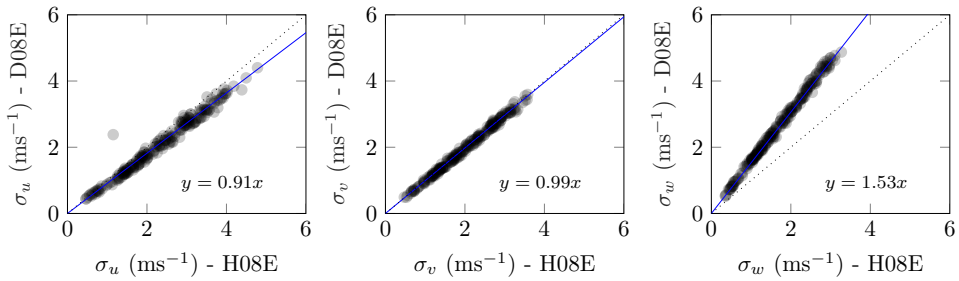
Figure 4.5: Relationship between σ_u (left panel), σ_v (mid panel) and σ_w (right panel) recorded by H08E and D08E (upstream the deck); 219 20 min-long records with $u \geq 6\,\mathrm{m\,s}^{-1}$ and $|z/L| \leq 0.1$, from 01/08/2020 to 01/08/2021.

approaching and past any symmetrical body. The along-wind rms value, σ_u, can be reduced by the blocking generated by the body whereas it can be amplified by the distortion of turbulence due to the mean velocity [70; 10; 11]. Their relative contribution largely depends on the ratio L_u^X/D. When the length scale of turbulence is much larger than the body characteristic dimension ($L_u^X/D \gg 1$), like in the present study, σ_u is expected to reduce as $\bar{u}$ [70], which is in agreement with the ratios $(\bar{u})_{D08E}/(\bar{u})_{H08E} = 0.91$ and $(\sigma_u)_{D08E}/(\sigma_u)_{H08E} = 0.91$. This is due to the blocking by the body, which is larger than the vorticity distortion for $L_u^x/D \gg 1$ [11; 16]. Conversely, σ_w is expected to increase ahead of the body [70], as is observed here (see Figure 4.5).

Intuitively, the relative importance of blocking and vorticity distortion can be also investigated in terms of velocity spectra, thereby showing any amplification or attenuation of the velocity fluctuations approaching a body as a function of the wave number [16]. This matter is investigated in the following section.

4.4.3   Velocity spectra

The one-point velocity spectra are shown in Figure 4.6 as a function of $fz/\bar{u}$, where $\bar{u}$ is estimated based on H08E. Spectra are calculated as described in Section 4.3. The normalization is based on the variance at H08E, i.e. $(\sigma_k^2)_0$, with $k = u, v, w$. Hence, an amplification or attenuation of the spectral energy can be easily identified. For comparison, the semi-empirical velocity spectra Equations (2.9), (2.10), (2.12) and (2.17) are superimposed in the same figure.
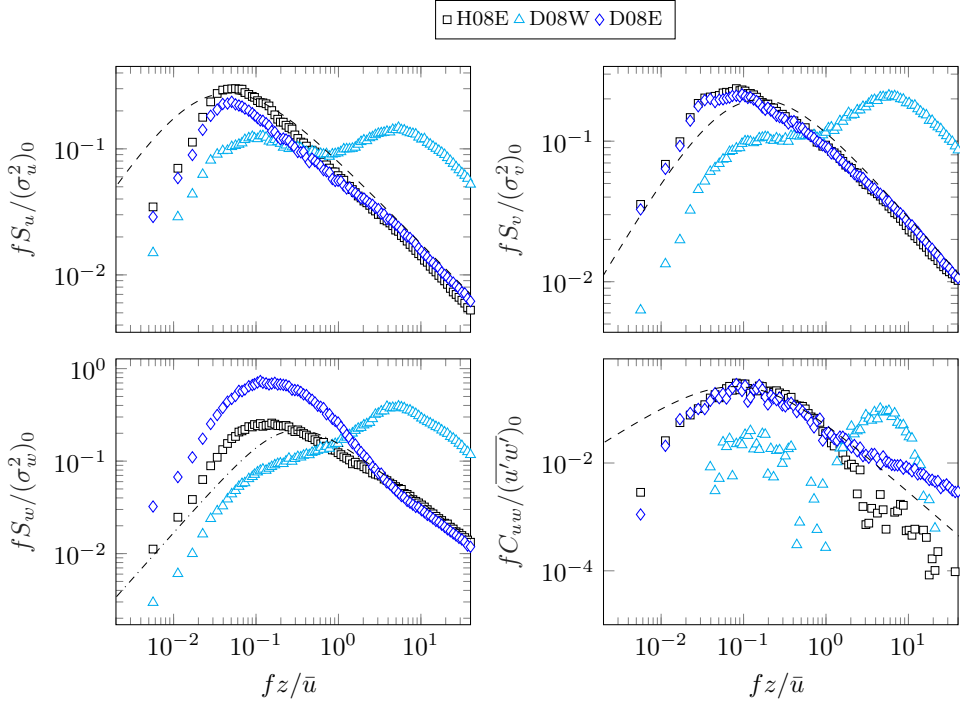
Figure 4.6: Ensemble-averaged one-point velocity spectra for NNE flows; 219 20 min-long records with $u \geq 6\,\mathrm{m\,s^{-1}}$ and $|z/L| \leq 0.1$, from 01/08/2020 to 01/08/2021.

The velocity spectrum estimated in the near wake (D08W) are also included for the sake of clarity. However, a dedicated discussion on the near-wake turbulence will be given in Chapter 5.

At H08E, the spectral content of S_u is lower than predicted by Equation (2.9) for $n = fz/\bar{u} \leq 0.04$. However, the spectral peak of fS_u is adequately captured. At low reduced frequencies, the slope of the spectrum appears to be steeper than $\propto f^1$. This may be ascribed to the filtering effects of the neighbouring hills and mountains, especially when side valley flows interact and mix with the main valley flows, along the fjord for the NNE wind sector [23]. In other words, the complex topography, together with a relatively short fetch, work as a "high-pass filter", thereby partly suppressing the spectral energy for low wave numbers. Equation (2.12) captures adequately S_w only for $fz/\bar{u} \geq 0.3$, with a mismatch in the spectral peak, which is found at a lower reduced frequency, namely $fz/\bar{u} \approx 0.15$. An overall agreement is found between the estimated S_v and Equation (2.10). The real part of

the cross-power spectral estimates (C_{uw}) exhibits lower spectral content for $fz/\bar{u} \leq 0.08$ than predicted by Equation (2.17).

Within the inertial sub-range, which is here identified for $fz/\bar{u} \geq 4$, the roll-off slope of S_u, S_v and S_w follows the prediction by Kolmogorov [87], i.e. $\propto f^{-5/3}$. On the other hand, for $Re(C_{uw})$ the decay is steeper than $\propto f^{-7/3}$.

Figure 4.6 shows that the along-wind fluctuations measured ahead of the deck are slightly attenuated for the majority of energy-containing eddies, i.e. at low reduced frequencies. The across-wind component v instead, does not experience a significant distortion. As anticipated in Figure 4.5, the largest amplification is observed for the vertical turbulence component w. The spectral shape of fS_w is also greatly affected by the deck blocking effect, with its width being spread across a wider band of frequency. Two noteworthy observations can be made:

(a) for $fz/\bar{u} \leq 0.05$, fS_w at D08E follows the slope estimated at H08E, with a simple increase in power.

(b) for $0.8 \leq fz/\bar{u} \leq 3$, S_w at D08E exhibits a decay faster than $\propto f^{-5/3}$.

In section 6.5.2, it will be shown that the monitored turbulence-driven twisting moment follows the slopes of S_w at D08E, thereby suggesting that the approaching turbulence distorted by the deck can partly describe the generation of the cross-sectional buffeting forces.

The distortion of turbulence 2 m ahead of the deck leading edge is better quantified in Figure 4.7, where the spectral ratios $(S_j)_{D08E}(n)/(S_j)_{H08E}(n)$, with $j = u, v, w$, are computed. When $(S_j)_{D08E}(n)/(S_j)_{H08E}(n) > 1$, the corresponding velocity fluctuations approaching the girder are amplified for a given reduced frequency. If $(S_j)_{D08E}(n)/(S_j)_{H08E}(n) < 1$, an attenuation is attained.

Figure 4.7 suggests that $fz/\bar{u}$ is a fundamental parameter when characterising the distortion of the turbulence 2 m upstream of the Lysefjord Bridge deck. In particular, the distortion effect is clearly frequency-dependent: for $fz/\bar{u} < 3$, S_w is amplified whereas S_u is slightly suppressed; for $fz/\bar{u} > 3$ S_w is attenuated and, instead, S_u and S_v experience an energy increase. These results are in overall agreement with the studies on the distortion of the turbulence ahead of a symmetric 2D body, see Hunt [70]; Bearman [10, 11]. The reduced frequency at "cut-off" appears to be the same for all three velocity components. The corresponding wavelength is around $(z/2\pi)/3 = 3.3$ m,
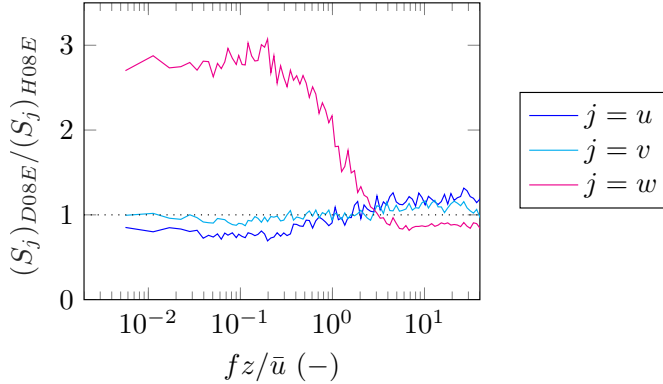
Figure 4.7: The distortion of turbulence $2\,\mathrm{m}$ upstream the bridge deck for NNE flows; 219 20 min-long records with $u \geq 6\,\mathrm{m\,s^{-1}}$ and $|z/L| \leq 0.1$, from 01/08/2020 to 01/08/2021.

which is of the same order of magnitude as the deck height ($D =2.7\,\mathrm{m}$). This value of wavelength likely changes depending on the horizontal separation from the body [10; 11].

According to Bearman [10], for $L_u^X/D \gg 1$ and no distortion of turbulence due to vortex stretching, S_u along the stagnation line of a symmetric body is given by:

$$(S_u)_l = (S_u)_0 \cdot \frac{(\bar{u}^2)_l}{(\bar{u}^2)_0} \tag{4.1}$$

where the notation $()_l$ identifies the approaching turbulence.

For the case at hand, $(\bar{u})_l/(\bar{u})_0 = 0.91$. Thus, the expected ratio should read $(S_u)_l/(S_u)_0 = 0.83$, which describes reasonably well the magnitude documented in Figure 4.7 for $fz/\bar{u} < 0.3$, e.g. wavelengths larger than 33 m ($2.7B$).

Interestingly, the wavelengths associated with the upper plateau of the spectral ratio $S_w(D08E)/S_w(H08E)$ in Figure 4.7 are compliant with the constant portion of the aerodynamic admittance functions for lift and moment, which is estimated for frequencies lower than $fB/\bar{u} = 0.1$ (see Section 6.5.2). A distortion of the turbulence ahead of a body may play role in the admittance of a square plate [10] but also partly influence the span-wise correlation of the wind buffeting forces, as suggested by Larose [101]. Figure 4.7 may indicate that the pronounced distortion of the vertical turbulence component
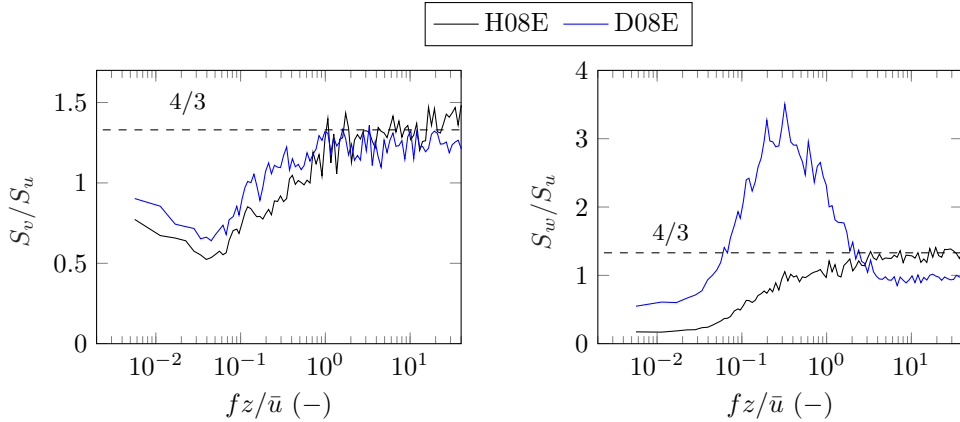
Figure 4.8: The spectral ratio S_v/S_u (left panel) and S_w/S_u (right panel), for NNE flows; 219 20 min-long records with $u \geq 6\,\mathrm{m\,s^{-1}}$ and $|z/L| \leq 0.1$, from 01/08/2020 to 01/08/2021.

for low reduced frequencies partly contribute to the observed larger span-wise coherence of the lift/moment (see Section 6.5) in the same range of frequencies.

The spectral ratios S_v/S_u and S_w/S_u estimated at H08E and D08E are given in Figure 4.8 as a function of $fz/\bar{u}$.

For the "undisturbed" flow at 6 m height above the deck, on the upwind side, the value of 4/3 predicted for local isotropy [87] is reached. In the range of reduced frequencies $4 < fz/\bar{u} < 20$ belonging to the inertial sub-range, the estimated median spectral ratios are 1.31 ± 0.03 and 1.26 ± 0.03 for S_v/S_u and S_w/S_u, respectively at H08E. A lower value estimated for S_w/S_u may suggest a minor flow distortion induced by the sonic anemometer itself [151]. For the case at hand, the transducer-induced flow distortion on H08E data appears to be limited, at least from the viewpoint of the spectral ratio S_w/S_u.

For the approaching flow at D08E, it is found that $S_v/S_u \approx 1.20$ in the reduced frequency range of $4 < fz/\bar{u} < 20$, whereas $S_w/S_u \approx 0.95$, which indicates anisotropy. This was somehow anticipated given the straining of the turbulence along a dominant direction [54]. Note that at D08E the flow is strongly sheared and, thus, the double-rotation technique may not be fully appropriate to compute u, v, w.

4.5 Spectral modelling of turbulence

4.5.1 One-point velocity spectra

The one-point spectra of u, v and w, previously shown in Figure 4.6, are now presented in Figure 4.9 normalized using the friction velocity estimated at H08E $(u_*^2)_0$. Equations (2.13) to (2.15) are also superimposed the measured S_u, S_v and S_w respectively. The corresponding coefficients, which are esti-
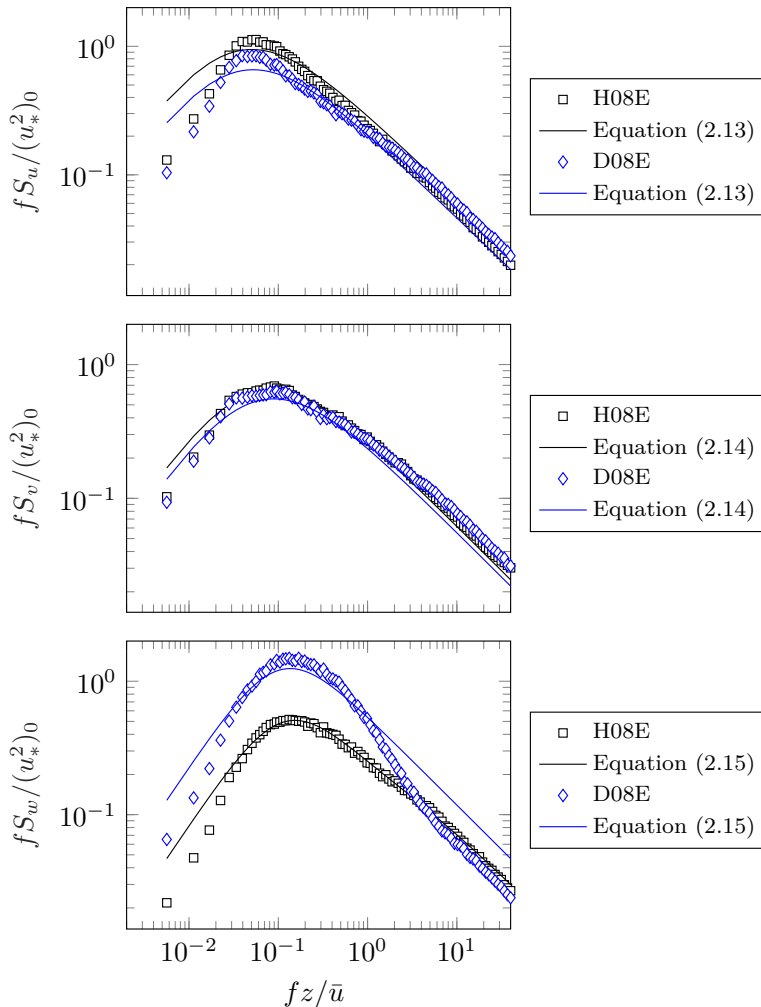
Figure 4.9: The fitted and estimated one-point velocity spectra for NNE flows; 219 20 min-long records with $u \geq 6\,\mathrm{m\,s^{-1}}$ and $|z/L| \leq 0.1$, from 01/08/2020 to 01/08/2021.

Table 4.3: The estimated coefficients for the one-point velocity spectra (Equations (2.13) to (2.15)) for NNE flows; 219 20 min-long records with $u \geq 6\,\mathrm{m\,s^{-1}}$ and $|z/L| \leq 0.1$, from 01/08/2020 to 01/08/2021.

Sensor	Turbulence component j	a_j	b_j
	u	86	30
H08E	v	35	18
	w	8	32
	u	58	29
D08E	v	29	17
	w	23	42

mated in a least-square sense considering the range $0.006 \leq fz/\bar{u} \leq 40$, are reported in Table 4.3. The coefficients a_j and b_j are estimated independently based on each equation.

For all turbulence components, the spectral peaks are reasonably well captured by the fitted spectra, both in terms of magnitude and location along the reduced frequency axes. Fo S_u and S_w, the fitted spectra systematically overestimate the spectral energy for $fz/\bar{u} \leq 0.04$. As previously mentioned, this effect may reflect the high-pass filtering due to surrounding complex terrain, which breaks down the eddies with the largest wavelengths. Note that the relationship between a_j and b_j in the inertial sub-range agrees fairly well with the predictions for u and v, see e.g. Kaimal and Finnigan [79]. On the other hand, a_w and b_w do not follow the relationship $b_w = a_w/0.4$. If a one-parameter fitting is attempted using $b_w = a_w/0.4$, the spectral peak of fS_w would shift towards high reduced frequencies, thereby underestimating the low-frequency spectral content. This justifies the choice of a 2-parameter fitting to model adequately S_w.

The length scales of the turbulence relative to the bridge deck dimension are parameters that govern the wind buffeting loads [34]. In particular, the ratio $\mathscr{L}_w/B$ is fundamental to discuss the cross-sectional admittance function of lift and moment as well as their span-wise correlation [101]. Based on the fitted spectrum of w, $\mathscr{L}_w = 61\,\mathrm{m}$ and, thus, $\mathscr{L}_w/B = 5$ on average for north-northeasterly flows.

4.5.2 Lateral co-coherence

The wind records acquired on 09/04/2021 from 00:20 to 00:50 UTC are utilized to discuss an example of co-coherence modelling for the approaching wind flow. The wind was blowing from SSW. The fundamental wind characteristics estimated at H08Wt are summarised in Table 4.4.

The coherence is based on the measurement array consisting of sonic anemometers H18W, H20W and H24W, which are located on the upwind side of the bridge deck for the case at hand. The co-coherence is calculated utilizing Welch's algorithm [201], with a segment duration of 180 s and 50% overlapping. The fitting of the co-coherence model in Equation (2.24) to the estimates is done for reduced frequencies $fB/\bar{u} \leq 0.3$. This range is found adequate to avoid noise-induced distortion of the co-coherence at higher frequencies that might introduce a bias during the fitting.

The measured and fitted co-coherence of u, v, w are shown in Figure 4.10 as a function of the frequency f, for three lateral separations. The fitted coefficients of Equation (2.24) are given in the same figure. The model describes adequately well the observed co-coherence, especially for the horizontal turbulence components u and v. For $f \leq 0.1$ Hz, γ_{ww} is significantly lower than unity for the two largest separations, which is captured by the coefficient $c_{y2}^w = 0.02$ s^{-1}. This reflects the attenuation of correlation for eddies having wavelengths of similar size or even shorter than the cross-wind separation [72; 91; 167]. In other words, the Davenport coherence model is generally adequate when $L_Y/\Delta Y \gg 1$, where L_Y is a characteristic length scale of turbulence in the across-wind direction.

The same co-coherence shown in Figure 4.10 is presented in Figure 4.11 as a function of $f\Delta Y/\bar{u}$. The measured γ_{uu} and γ_{vv} collapse more or less into a curve, thereby suggesting that Davenport's similarity applies for the horizontal turbulence components. Here, Davenport's similarity means that the co-coherence estimate collapses on the same curve when expressed as a function of $f\Delta Y/\bar{u}$. On the other hand, for the vertical velocity component,

Table 4.4: Turbulence characteristics on 09/04/2021 from 00:20 to 00:50 UTC, sonic anemometer H08Wt.

Dir (°)	$\bar{u}$ (m s^{-1})	$\bar{\alpha}$ (°)	u_* (m s^{-1})	z/L	I_u	I_v	I_w	$\mathcal{L}_w$ (m)
214	13.6	1.5	0.85	0.08	0.14	0.14	0.10	42
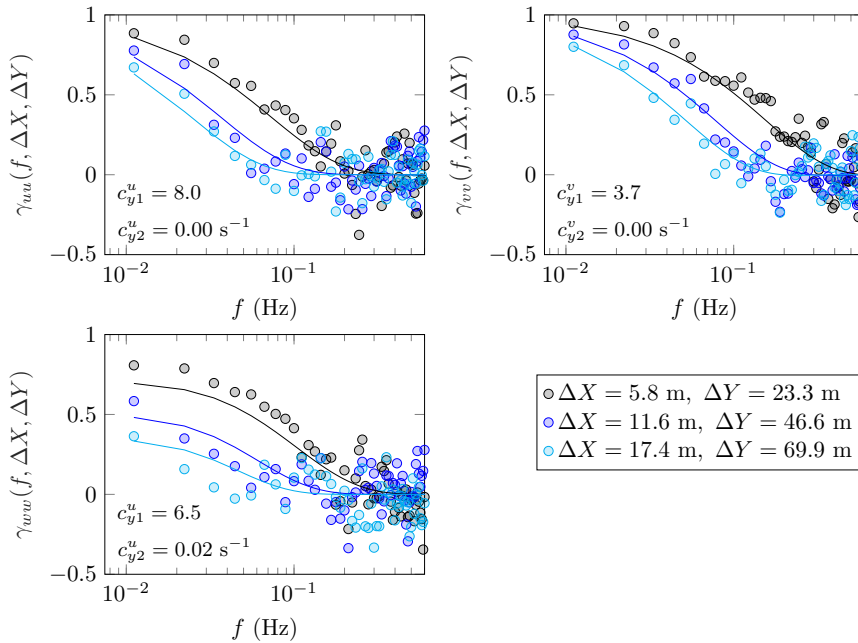
Figure 4.10: Horizontal co-coherence of velocity fluctuations u, v and w as a function of frequency, for a SSW flow, recorded on 09/04/2021 from 00:20 to 00:50 UTC. The wind direction was $214°$ and $\bar{u} = 13.6$ m s^{-1}.

Davenport's similarity does not apply here. This may be due to: (a) the lack of full correlation of w in the low-frequency range, which is modelled using c_{y2}^w in Equation (2.24); (b) the potential dependence of c_{y1}^w on $\Delta Y / z$.

When the lateral separations are relatively large, it appears it may be challenging to fit adequately γ_{ww} with the adopted co-coherence model (Equation (2.24)). This may be attributed to the dependence of the decay coefficient c_{y1}^w on $\Delta Y / z$, as pointed out by Kristensen et al. [92] for the longitudinal fluctuations and discussed further in Bowen et al. [15]. An example of implementation can be found in Sacré and Delaunay [164], where the lateral coherence for the Pont de Saint-Nazaire (France) was studied including the effect of $\Delta Y / z$ on the root-coherence.

4.6   Summary

One- and two-point statistics of the incident flow represent a fundamental input for the prediction of the buffeting response of a line-like structure,
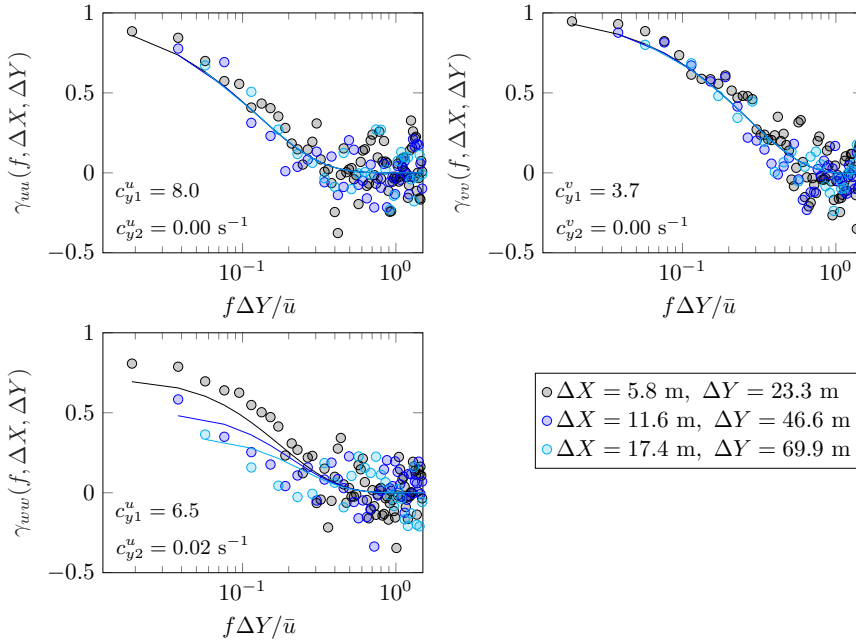
Figure 4.11: Horizontal co-coherence of velocity fluctuations u, v and w, as a function of $f\Delta Y/\bar{u}$; SSW flow, recorded on 09/04/2021 from 00:20 to 00:50 (UTC). The wind direction was $214°$ and $\bar{u} = 13.6$ m s^{-1}.

e.g. a long-span bridge. This chapter studied north-northeasterly flows for near-neutral stratification of the atmosphere at the Lysefjord Bridge site. The discussion focused on velocity records acquired over a one year period and provides the basis for the analysis that will follow in Chapters 5 and 6.

The incident wind turbulence was studied at 6 m height above the bridge deck, on the upwind side, and 2 m ahead of the bridge deck nose. One of the objectives was to describe how the bridge deck distorts the approaching turbulence and its potential significance for the generation of the gust loading. Secondly, spectral modelling of turbulence was discussed, highlighting some fundamental features stemming from the complex terrain environment.

At the measurement station upstream of the bridge deck, the flow is deflected downwards, e.g. when the incident, nominally undisturbed, flow is horizontal ($\alpha = 0°$), the angle of attack measured ahead of the girder is $-7°$. The mean flow is also attenuated by 9%, similarly to the standard deviation of the along-wind component. On the other hand, the vertical velocity fluctuations were found to experience a pronounced amplification. The distortion

of the turbulence observed 2 m upstream of the deck is frequency-dependent. For $fz/\bar{u} < 3$, the spectral energy of S_w is 2.7 times larger in the disturbed flow region 2 m in front of the deck nose, than in the undisturbed flow 6 m above the deck. The overall increase in rms values is 53%. Conversely, S_u and S_v attenuate slightly in the disturbed flow region.

In general, the results discussed attempt to present an original overview of the flow distortion experienced by atmospheric turbulence ahead of a bridge deck. Two perspectives can be outlined: (a) given the level of flow distortion observed, it is unfeasible to utilize sonic anemometry ahead of the bridge deck to monitor undisturbed turbulence. Horizontal booms can definitely be designed longer than those adopted here. On the other hand, increase flexibility become a potential issue. Nevertheless, it is believed that reaching an adequately undisturbed measurement station far enough in front of the deck will be cumbersome in practice. (b) The distortion of the wind turbulence observed upstream of the bridge deck can be interpreted as an intermediate link between the incident undisturbed flow and the gust loading mechanism. In fact, eddies are distorted as they approach the stagnation region and, subsequently, travel past the bridge deck. Following Larose [101], it is proposed that the significant distortion of S_w in particular, can be, at least partly, related to the spatial structure of the lift and moment acting on a bridge deck (see e.g. Section 6.5.2).

Chapter 5

Near-wake turbulence

5.1 Introduction

This chapter focuses on the turbulence characteristics in the near wake of the Lysefjord Bridge deck, in both full- and model-scale. The term "near wake" is adopted herein following Kiya and Matsumura [85]. According to them, the near wake encompasses downstream separations of $x/D < 5$ for a circular cylinder in cross-flow and sub-critical Reynolds (Re) number regime.

When vortex-induced vibrations are not clearly detected, an accurate estimation of the Strouhal (St) number in full-scale is deemed possible, in principle, utilizing surface pressure measurements around the bridge girder [49; 112; 5]. A system of synchronized continuous-wave Doppler wind lidar instruments can also be employed to study the flow around a bridge deck [27], as well as sonic anemometry [5], which is particularly well suited for long-term continuous monitoring.

In this chapter, the capabilities of sonic anemometry to capture the formation of eddies on the leeward side of the deck are explored. Furthermore, possible Re number effects on the St number, which may also be present for sharp-edged bodies [66; 97; 171; 170], are studied. Such a potential dependence is investigated herein based on velocity measurements undertaken in the near wake of a stationary section model, tested in a wind tunnel (see Appendix B). A primary objective is to quantify the Re number effects, if any, on the St number and the significance of turbulence, namely its intensity, in the approaching flow. In fact, the free-stream turbulence impacts significantly the flow transition, from laminar to turbulent, in the disturbed flow region of

a circular cylinder for example [209].

The overall alteration of the atmospheric turbulence by the bridge deck obstacle is examined, as well as the related vortex shedding process. To further investigate the aerodynamic characteristics of the bridge deck for skewed flows in a controlled environment, wind tunnel tests on a section model of the Lysefjord Bridge were designed. The emphasis is primarily on mapping the near-wake turbulence based on hot-wire measurements, including all three velocity components. A particular feature of the wind tunnel experiments is the inclusion of a yawed model configuration ($\beta = 25°$), in both smooth and turbulent flows. In particular, the wind tunnel experiments were designed to document the wake turbulence case of a yawed section model, which reflects the wind conditions generally encountered on-site [26]. The objective is twofold. Firstly, the hot-wire measurements attempt to highlight the different features of the near-wake turbulence, including the vortex shedding frequency, when the bridge is yawed to the flow. Secondly, the signature of an axial flow developing along the leeward side of the bridge axis is sought after. For the aerodynamics of yawed/inclined cables, the presence of the axial flow along the cylinder axis is known to interact with the vortex formation in the near wake [133]. Thus, the chapter raises the following question: how and to what extent an axial flow can develop on the leeward side of a full-scale bridge deck for a non-zero yaw angle? Finally, the results presented in this chapter attempt to corroborate the lack of clear vortex-induced vibrations recorded.

The analyses presented herein are based on the underlying assumption of a stationary bridge deck, which is compliant with the wind tunnel tests performed on a 1:50 stationary section model (Appendix B.1). In full-scale, such an assumption does not hold strictly. Nevertheless, at the bridge quarter span, which is close to the measuring chord, and for a mean wind speed around $\bar{u} = 15\,\mathrm{m\,s^{-1}}$, the 95th percentile of the (normalized) heave motion standard deviation estimated is $\sigma_{r_z}/D = 0.013$. Such a limited magnitude of heave motion should not generate significant motion-induced vortices in the near wake. Vertical eigenmodes VA1 (first asymmetric) and VS2 (second symmetric) are the primary contributors to the vertical motion of the deck around the chord where the velocity measurements are undertaken, i.e. hanger H-08.

The chapter is organized as follows. Section 5.2 introduces some fundamental characteristics of near-wake turbulence in full-scale using a selected 30 min-long monitoring period. Thereafter, in Section 5.3, the (full-scale)

mean flow and integral turbulence characteristics in the near-wake region are presented and compared to those associated with a nominally undisturbed incoming flow, for a neutral atmospheric stratification. The velocity spectrum of the vertical turbulence component is studied with emphasis on the interaction between the free-stream turbulence and the vortex shedding process, for full-scale Re numbers. Some fundamental findings based on velocity measurements in the near wake of a 1:50 scale stationary section model are summarised in Section 5.4. Section 5.5 discusses the St number estimated based on model and full-scale testing, attempting to provide insight into the Re number scaling effects, if any, for the case at hand.

5.2   Wake flow characteristics in stable atmosphere

A 30 min-long run associated with a stationary flow and a stable atmospheric stratification is exploited herein to present some fundamental features of wind turbulence in the near wake of the bridge deck. A stably stratified wind flow is often associated with low turbulence intensities, as turbulence mixing is partly inhibited [79]. Thus, the corresponding effect of turbulence on the deck aerodynamics should be limited considering the Re numbers range of this full-scale experiment. Table 5.1 reports the fundamental turbulence characteristics for the stationary data run acquired on 26/08/2021 02:40 UTC by the sonic anemometer H08E, which is located on the upwind side of the deck. A north-northeasterly wind is blowing with, $\bar{u} = 8.1 \, \mathrm{m\,s^{-1}}$ and $u_* = 0.29 \, \mathrm{m\,s^{-1}}$. The non-dimensional stability parameter is $z/L = 0.58$, i.e. stable atmospheric stability, which justifies the relatively low turbulence intensities measured. A value such as $I_w = 0.08$ is rarely encountered on-site for the NNE wind sector [27]. A positive mean angle of wind incidence, namely $\bar{\alpha} = 2.6°$, is recorded. Skewness and kurtosis estimated for the vertical component w are 0.16 and 3.58, respectively.

The time histories of the three velocity components in the near wake

Table 5.1: Turbulence characteristics on 26/08/2020 02:40 UTC, 30 min-long records from sonic anemometer H08E.

Dir (°)	$\bar{u}$ (ms^{-1})	$\bar{\alpha}$ (°)	u_* (ms^{-1})	z/L	I_u	I_v	I_w	L_w^X (m)
39	8.1	2.6	0.29	0.58	0.09	0.10	0.08	48
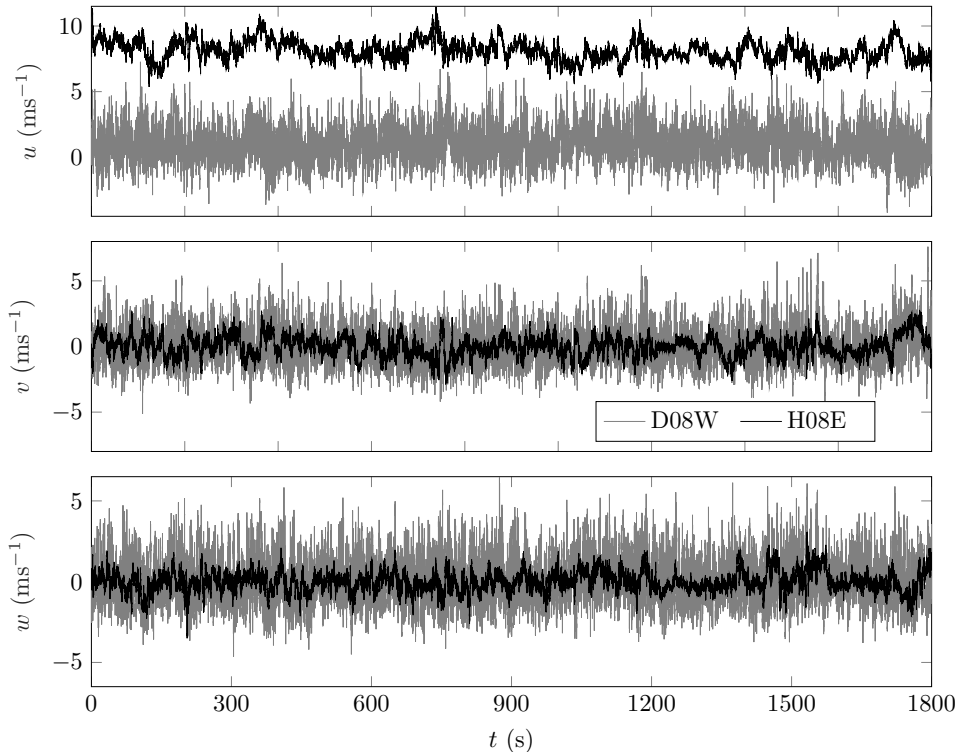
Figure 5.1: Wind velocity components acquired at 6 m height above the deck (H08E-black) and in the near wake (D08W-grey), 26/08/2020 02:40 UTC.

(D08W) are given in Figure 5.1, together with the components associated with incoming turbulence (H08E). The velocity components are expressed in the local wind coordinate system. As expected, the ratio $(\bar{u})_{wake}/\bar{u}_0$, which is estimated at $0.74D$ from the trailing edge, is low, namely 0.12. In fact, the sonic measurement volume is positioned close to the expected centre-line of the near wake, i.e. the nose deck level, where the velocity defect is expected to reach its maximum for a given stream-wise location. The difference in terms of the standard deviation of the velocity components is also remarkable, especially for the w component, which is characterised by a ratio between variances $(\sigma_w^2)_{wake}/(\sigma_w^2)_0 = 2.15$, where the notation $()_0$ refers to the reference value based on H08E. For the other two components, the ratios are $(\sigma_u^2)_{wake}/(\sigma_u^2)_0 = 1.68$ and $(\sigma_v^2)_{wake}/(\sigma_v^2)_0 = 1.62$. This suggests that the monitored near-wake is highly turbulent and three-dimensional, thereby indicating the development of coherent flow structures. For the undisturbed turbulence, $\overline{u'w'} = -0.03\,\mathrm{m^2\,s^{-2}}$ whereas in the near wake $\overline{u'w'} =$
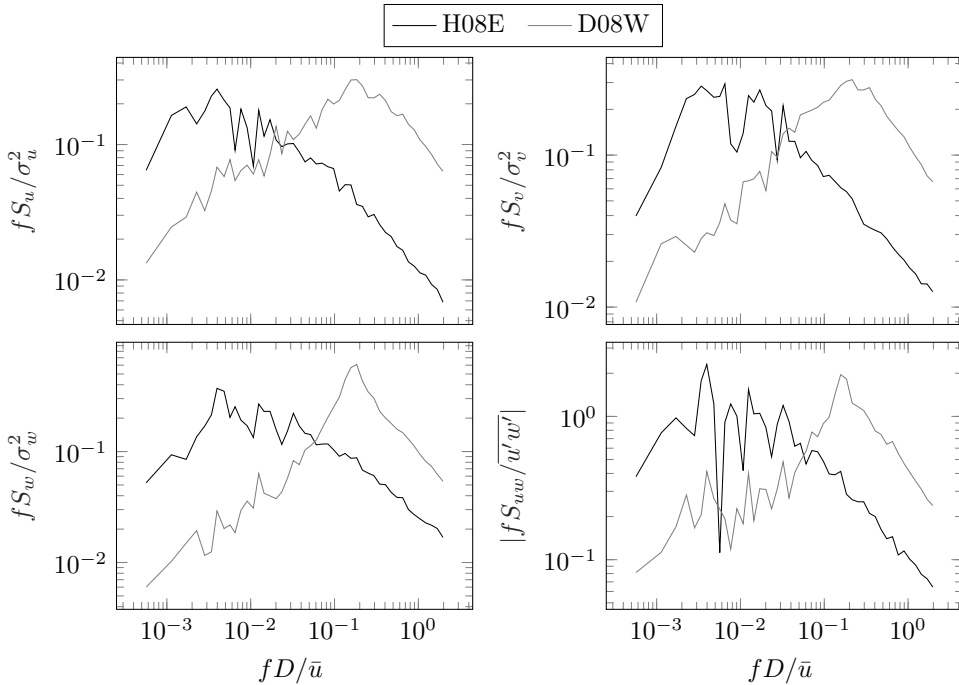
Figure 5.2: One-point velocity spectra estimated at 6 m height above the deck (H08E-black) and in the near wake (D08W-grey), based on 30 min-long time series acquired on 26/08/2020 02:40 UTC.

$0.12\,\mathrm{m^2\,s^{-2}}$. The sign of the latter depends on the relative position between the sonic measurement volume and the wake centreline, which, intuitively, varies as a function of the mean angle of wind incidence. Yet, asymmetries in the wake topology may arise due to bridge deck asymmetry, as Section 5.4 attempts to clarify. For the time series at hand, $\bar{\alpha} = 2.6°$ and, thus, the measurement volume is displaced towards the lower region of the near wake, thereby suggesting a consistently positive value of the Reynolds shear stress in the monitored near wake.

By inspecting Figure 5.1, it is also possible to note how the velocity fluctuations in the near wake are modulated, in amplitude, by the low-frequency fluctuations of the background turbulence. The quasi-periodic high-frequency fluctuations, on the other hand, reflect a more organized flow structure associated with the eddies formation in the near-wake region. This can be appreciated by examining Figure 5.2, which displays the corresponding one-point velocity spectra as a function of the reduced frequency $fD/\bar{u}$, where
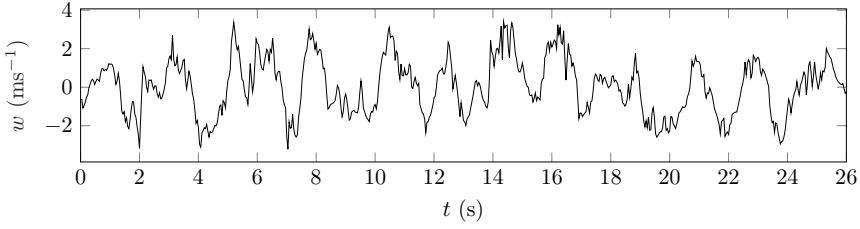
Figure 5.3: Segment of the (unfiltered) vertical velocity fluctuations w measured in the near wake (D08W), acquired from 26/08/2020 02:40 UTC.

$\bar{u}$ is the mean wind speed of the incoming flow. The spectra are normalized based on the local variances, e.g. based on either H08E or D08W sonic anemometer data. Figure 5.2 describes the turbulence structure in the near wake. The bridge deck inhibits eddies having larger wavelengths and the turbulence kinetic energy is shifted towards higher reduced frequencies. In the near wake, all one-point velocity spectra fS_j with $j = u, v, w$ peak at $fD/\bar{u} = 0.174$, which corresponds to the non-dimensional vortex shedding frequency for the case at hand. A segment of time series showing the vertical velocity fluctuations in the near-wake region is given in Figure 5.3. The velocity record is not high-pass filtered beforehand. Despite the expected incoherent high-frequency fluctuations and low-frequency random modulation, both in amplitude and frequency, driven by the background turbulence, a clear signature of a coherent motion can be detected visually.

Compared to the other velocity spectra shown in Figure 5.2, S_w exhibits a relatively narrow band-width centred around the St number, thereby indicating a less noisy detection of coherent flow structures, at least at the sonic measurement location. For the horizontal components, the influence of the background turbulence is more evident for $fD/\bar{u} \leq 0.10$, given the different sized eddies involved. The roll-off slope for $fD/\bar{u} \ll St$ is approximately $\propto f^{1/2}$ and $\propto f^{3/4}$ for fS_u - fS_v and fS_w, respectively. The spectral levels of the three velocity components in the near wake become higher than those characterising undisturbed turbulence for $fD/\bar{u} > 0.02$ approximately. The spectral ratios, between the near-wake and undisturbed velocity components, at the vortex shedding frequency, are defined as:

$$\frac{(S_k(fD/\bar{u} = St))_{wake}}{(S_k(fD/\bar{u} = St))_0}, \qquad k = u, v, w \qquad (5.1)$$

The computed values are 24, 23 and 36 for u, v and w components, respectively.

Despite the stably stratified condition of the atmosphere (Table 5.1), which is known to delay the isotropic conditions towards higher wave numbers [20], the undisturbed turbulence isotropy is reached in the inertial subrange at about $fD/\bar{u} \approx 0.3$ for the case at hand. This is checked following Kaimal and Finnigan [79], namely by checking within the inertial subrange: (a) $f^{-5/3}$ slope of the velocity spectra; (b) $S_v/S_u = 4/3$ and $S_w/S_u = 4/3$; (c) $C_{uw} \approx 0$. Interestingly, all one-point velocity-spectra in the near-wake region exhibit a $\propto f^{-5/3}$ power law for $fD/\bar{u} \geq 0.4$. Also, C_{uw} is found to scale $\propto f^{-7/3}$, as predicted under isotropic conditions for the co-spectrum [121]. However, the spectral ratios S_v/S_u and S_w/S_u are limited to 1.10 and 1.08, respectively. A higher sampling rate together with a smaller sonic measurement volume would be needed to further investigate isotropy in near-wake turbulence.

In principle, velocity measurements undertaken in the near wake may inherently suffer from potential probe- and supporting bracket-induced flow distortion (see Section 3.3.3), especially for the horizontal turbulence components. However, the deck-generated turbulence and vortex formation in the near-wake region likely overshadow the above-mentioned flow distortion, which is considered here to have a secondary effect on the recorded velocity data.

5.3   Wake flow statistics in neutral atmosphere

The dataset utilized in this section comprises velocity records acquired from 01/08/2020 to 01/08/2020. North-north easterly flows are prioritized, given their larger probability of occurrence for the selected period. In addition, wake flow measurements in the wind tunnel were undertaken with a cycling/pedestrian lane positioned on the downwind side of the deck, which simulates a NNE wind exposure. Thus, a full-scale comparison for the same configuration is deemed natural in terms of e.g. St number (see Section 5.5). Another reason for choosing this wind exposure is that sub-meso atmospheric motions seem to be filtered out by the fjord in the NNE wind sector [23].

For the selection of the dataset, the chosen reference sonic anemometer is H08E (see Figure 3.7), which is located on the upwind side of the bridge deck 6 m above the road level. The averaging time employed to compute statistics is 20 min, which is assumed to be appropriate to reduce the uncertainties in

the estimates for both undisturbed and near-wake turbulence. The velocity records are de-spiked and the resulting NaN values linearly interpolated [36] for subsequent processing provided that the percentage of NaN is lower than 1%. Only time series associated with $\bar{u} \geq 6\,\mathrm{m\,s^{-1}}$ are chosen. This is adequate for the analysis of pressure data (Chapter 6), which disregards records associated with a mean dynamic wind pressure lower than $20\,\mathrm{Pa}$. Furthermore, the analysis focuses on near-neutral stratification of the atmosphere only ($|z/L| \leq 0.1$). The yaw angle is constrained to the range $-45° \leq \beta \leq 45°$. The records used are 20 min-long. Their stationarity is checked for the velocity fluctuations u, v and w following Cheynet et al. [26], i.e. by employing a centred-unweighted moving standard deviation filter, with an averaging time of 5 min. If any instantaneous averaged value has a relative difference larger than 40%, the entire 20 min block is rejected and therefore disregarded for subsequent computations. Finally, samples associated with $I_u \leq 0.01$ or $I_u \geq 0.40$ are disregarded. The total number of 20 min-long samples included in the analysis is 219.

The turbulent flow in the near wake of a bluff body can be highly three-dimensional, depending also on the inclination of the body to the approaching flow. An obvious example is the near wake of a yawed/inclined cable [131; 133; 212]. Due to the pronounced three-dimensionality of the flow expected in the present application, the deck-based coordinate system (Section 2.2) is utilized to characterise near-wake turbulence.

5.3.1 First-order statistics

The time-averaged values of the velocity components v_x, v_y and v_z estimated in the near wake (D08W) are compared to the ones characterising the free-stream (H08E) in Figure 5.4. The cross-wise velocity component $\overline{v_x}$ was significantly attenuated, as expected, given the very near-wake location of the measuring volume, i.e. $3D$ from the shear centre of the cross-section. The median value of $(\overline{v_x})_{wake}/(\overline{v_x})_0$ is 0.15, with a dispersion of ± 0.07 given by the *std* of the ratios. Interestingly, only a mild dependence on the oncoming mean wind speed can be detected. For the velocity components along the bridge axis $\overline{v_y}$, a linear correlation can be established (mid panel of Figure 5.4), with the slope $(\overline{v_y})_{wake}/(\overline{v_y})_0 = 0.77$, which is in overall agreement with a corresponding estimate for a yawed circular cylinder in the sub-critical *Re* number range, see for example Zhao et al. [211]. Finally, the right panel
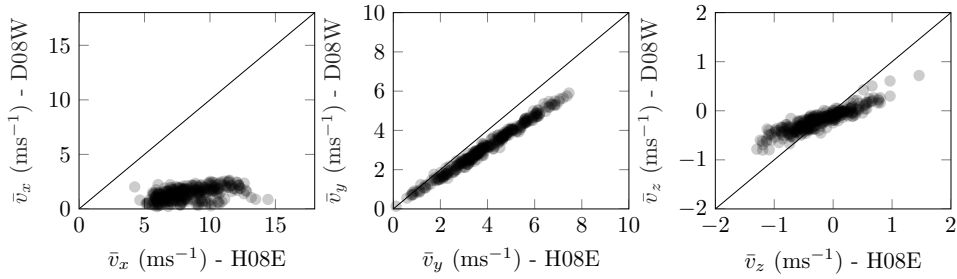
Figure 5.4: Relationship between mean statistics of wind velocities (v_x, v_y, v_z) recorded at 6 m height above the deck (H08E) and in the near wake (D08W), for north-northeasterly flows with $u \geq 6\,\mathrm{m\,s^{-1}}$ and $|z/L| \leq 0.1$, acquired from 01/08/2020 to 01/08/2021.
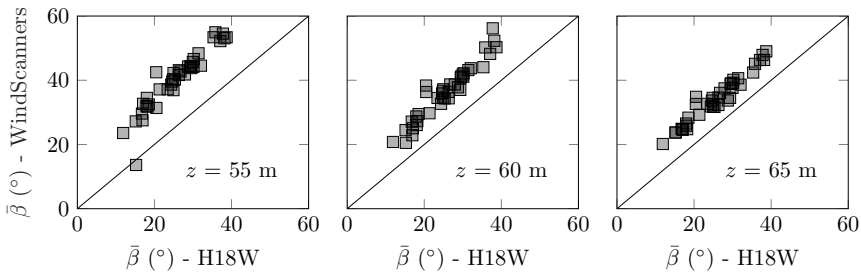
Figure 5.5: Comparison between time-averaged yaw angle measured by sonic anemometer H18W at 60 m and Wind Scanners at 55 m (left panel), 60 m (mid panel) and 65 m (right panel) above sea level and $17D$ downstream the shear centre of the bridge deck; 52 10 min-long samples (the dataset was described in Cheynet et al. [27]).

of Figure 5.4 suggests that flow in the vicinity of the near-wake centreline is more horizontal than the undisturbed one, for both positive and negative angles of (approaching) wind incidence.

In full-scale, the effects of a non-zero yaw angle on the horizontal mean flow in the intermediate wake of the Lysefjord Bridge can also be investigated by revisiting selected velocity measurements based on a system of synchronized continuous-wave Doppler wind lidar instruments [27]. Using the dataset described in [27], Figure 5.5 depicts the differences between the yaw angle associated with the undisturbed flow and the one estimated $17D$ downstream the shear centre of the cross-section. At the deck nose level ($z = 55\,\mathrm{m}$), the mean flow is clearly at an angle, in the horizontal plane, relative to

the free stream. The dataset is provided by Cheynet [23].

Axial flow in the near-wake region

In the field of cable aerodynamics, Shirakashi et al. [175] performed one of the
very first wind tunnel studies documenting the development of a "secondary
flow", i.e. an axial flow along the cylinder axis, on the leeward side of a yawed
($\beta = 30°$) smooth-surfaced cable. Such an axial flow was found to impact
significantly the characteristics of the vortex shedding process. The crucial
role of the axial flow in the aerodynamics of yawed/inclined cables was
studied extensively by Matsumoto et al. [131; 130; 133], who demonstrated
that (unsteady) axial flow can affect and partly inhibit vortex shedding, thereby
influencing the onset of dry inclined cable galloping for certain wind-cable
angles. For an inclined stationary circular cylinder case in the sub-critical
Re number range, the axial velocity component intensifies the degree of
three-dimensionality of the near-wake flow [212; 128; 211]. Experiments
focusing on the aerodynamics of a yawed square cylinder at $Re = 3.6 \cdot 10^3$
also demonstrated the presence of a significant velocity component along the
cylinder axis at $x/D = 10$ in the wake region [120]. Its magnitude, relative to
the free-stream, was larger than the one estimated for a circular cylinder at the
same downstream location and the same yaw angle. Yet, the near-wake flow
structure of a yawed stationary rectangular cylinder, or (single) closed-box
bridge girder is rarely documented.

The aspect-ratio or free end conditions of a section model can influence
axial flow development during wind tunnel experiments of circular cylinders
for example [133]. Although full-scale anemometer measurements are free
from these issues, they are prone to flow distortion from the supporting bracket
or the probe geometry. Figure 5.6 quantifies the so-called secondary flow in
the near wake, in the vicinity of its centreline, both in direction and magnitude.
The left panel of Figure 5.6 suggests that the mean near-wake flow follows the
free-stream wind direction for $-5° \leq \beta \leq 5°$, i.e. is close to being normal to
the bridge deck. Instead, a strong axial velocity component develops as soon
as the free stream yaws with $\beta \geq 15°$. Above this value, the mean yaw angle
estimated in the near wake is scattered around a median value of $\beta \approx 60°$,
without significant dependence on the undisturbed wind direction. The mean
axial velocity component reaches a magnitude of $0.5 \cdot \bar{u}_0$ for $\beta \approx 40°$. That
value agrees reasonably well with axial flow intensity developed along the
leeward inclined smooth-surfaced cable model tested with a wind-cable angle
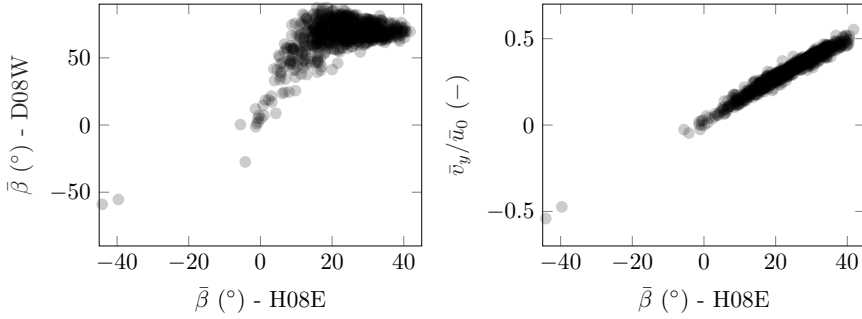
Figure 5.6: Left panel: time-averaged yaw angle recorded at 6 m height above the deck (H08E) and in the near wake (D08W). Right panel: normalized magnitude of the axial velocity component as a function of the yaw angle on H08E. The data selected were for north-northeasterly flows with $u \geq 6\,\mathrm{m\,s^{-1}}$ and $|z/L| \leq 0.1$, acquired from 01/08/2020 to 01/08/2021.

around 45° [133]. Yet, the precise role of the detected axial flow in the bridge deck near wake in (a) the interaction between separated shear layers and (b) the overall vortex shedding process, is not fully understood.

5.3.2 Second-order statistics

The integrated turbulence characteristics in the near wake are studied in terms of standard deviation, as shown in Figure 5.7. When the fluctuations in the incoming flow are relatively small, deck-generated turbulence along with the formation of coherent vortex structures are responsible for a significant energy increase in the near wake, for all velocity components. For increasing levels of turbulence in the free stream, the bridge deck appears to partly inhibit the near-wake turbulence fluctuations along the chord-wise direction, i.e. v_x. Instead, σ_{v_y} is found to be more or less conserved, if not slightly increased, on the leeward side of the girder.

As described in Section 5.2, the formation of coherent vortex structure is better described by the variance of vertical turbulence component v_z. This is confirmed by the right panel in Figure 5.7, which quantifies the remarkable increase of σ_{v_z} in the near-wake region for the entire range of free-stream turbulence intensities and especially within the lower end. This is further appreciated in Figure 5.8, where the variances $\sigma_{v_x}^2$, $\sigma_{v_y}^2$ and $\sigma_{v_z}^2$ are normalized by $\bar{u}_0^2$. No evident dependence of $(\sigma_{v_z}^2)_{wake}/(\sigma_{v_z}^2)_0$ on the free-stream yaw
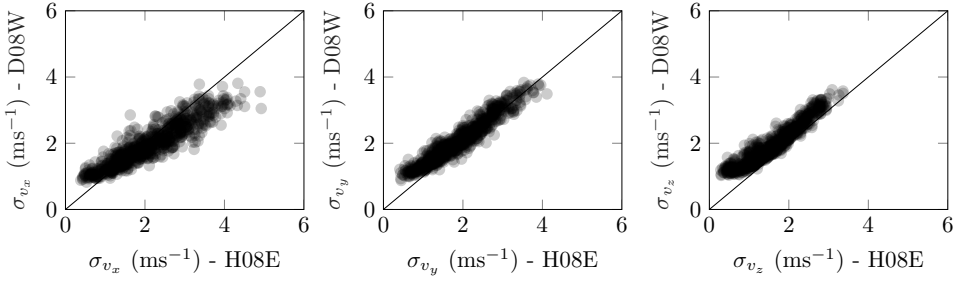
Figure 5.7: Comparison between σ_{v_j}, with $j = x, y, z$ measured at 6 m height above the deck (H08E) and in the near wake (D08W), for north-northeasterly flows with $u \geq 6\,\mathrm{m\,s^{-1}}$ and $|z/L| \leq 0.1$, acquired from 01/08/2020 to 01/08/2021.
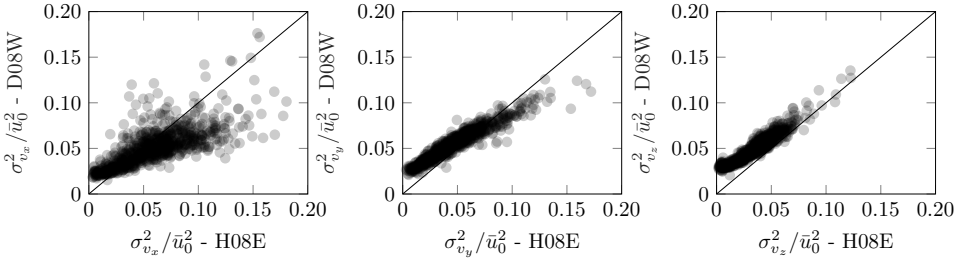
Figure 5.8: Comparison between $\sigma_{v_j}^2/\bar{u}_0^2$, with $j = x, y, z$, measured at 6 m height above the deck (H08E) and in the near wake (D08W), for north-northeasterly flows with $u \geq 6\,\mathrm{m\,s^{-1}}$ and $|z/L| \leq 0.1$, acquired from 01/08/2020 to 01/08/2021.

angle can be established, which could be partly explained by the fact, that the prevailing wind direction on-site is rarely normal to the bridge deck. The adoption of phase-averaging techniques [85; 71] to describe the properties of coherent vortex structures in the near wake may provide an improved insight into the above-mentioned dependence.

The normalized covariance $\overline{v_x' v_z'}/\bar{u}_0^2$ is studied as a function of the mean angle of wind incidence $\overline{\alpha}$ in Figure 5.9. A change of sign of $\overline{v_x' v_z'}/\bar{u}_0^2$ is found to occur around $\bar{\alpha} \approx 0°$, with $\overline{v_x' v_z'} > 0$ for positive angles of attack and $\overline{v_x' v_z'} < 0$ for negative angles of attack. In the present study, the sonic measurement volume is fixed relative to the bridge girder and, thus, $\overline{v_x' v_z'}/\bar{u}_0^2$ is, in principle, anticipated to vary in magnitude and sign as a function of mean angle of wind incidence. Figure 5.9 suggests that, for a horizontal flow, the
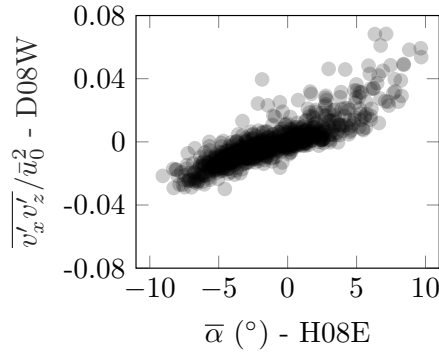
Figure 5.9: Variation of $\overline{v'_x v'_z}/u_0^2$ in the near wake (D08W) with the mean angle of wind incidence $\overline{\alpha}$, for north-northeasterly flows with $u \geq 6\,\mathrm{m\,s^{-1}}$ and $|z/L| \leq 0.1$, acquired from 01/08/2020 to 01/08/2021.

transverse location of the near-wake centreline should be more or less at the deck nose level. For positive angles of attack, the sonic measurement volume is displaced below the (nominal) near-wake centreline and, hence, $\overline{v'_x v'_z}/\bar{u}_0^2 > 0$. The opposite holds for the negative angles of attack. The Reynolds shear stress $\overline{v'_x v'_z}/\bar{u}_0^2$ is expected to have an opposite sign about a wake centreline due to the inherent characteristics of the vortex shedding process, see for example Kiya and Matsumura [85]; Ong and Wallace [149] for the covariance $\overline{v'_x v'_z}/\bar{u}_0^2$ in the wake of a circular cylinder in the sub-critical Re number regime.

Despite the inherent geometric asymmetry of the cross-section, it is perhaps not just a fortuitous coincidence that a dispersion in the values of $\overline{v'_x v'_z}/\bar{u}_0^2 > 0$ starts at around $\bar{\alpha} \approx 7°$. Considering the combined effects of turbulence intensity [97] and Re number [171] on the lift slope characterising sharp-edged bluff bodies, it can be postulated that, in full-scale, the local maximum of the lift coefficient shown in Figure B.2 is likely shifted towards lower values of $\bar{\alpha}$.

5.3.3 One-point velocity spectrum S_{v_z}

The ensemble-averaged normalized velocity spectrum of v_z estimated in the near wake is shown in Figure 5.10. The $f S_{v_z}/\sigma_{v_z}^2$ representative of undisturbed turbulence, i.e. measured by sonic anemometer H08E, and the Busch-Panofsky spectrum [19] (Equation (2.12)) are superimposed for the sake of comparison. Each spectrum is computed based on 20 min-long stationary time
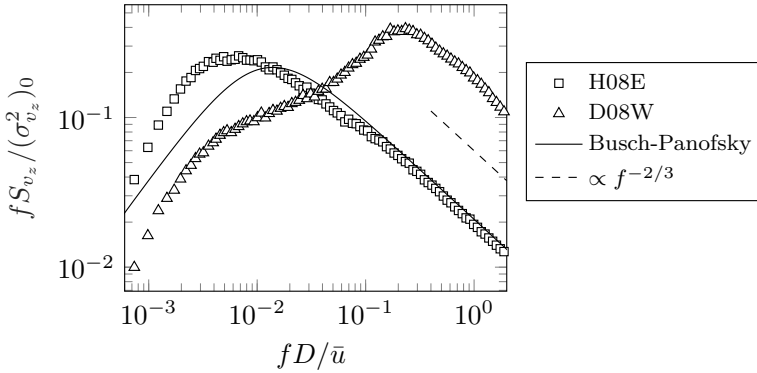
Figure 5.10: Ensemble-averaged one-point velocity spectrum S_{v_z} in the near wake (D08W) for north-northeasterly flows with $u \geq 6\,\mathrm{m\,s}^{-1}$, $|z/L| \leq 0.1$ and $-10^\circ \leq \bar{\alpha} \leq 10^\circ$, acquired from 01/08/2020 to 01/08/2021. The normalization is based on the variance of the (nominally) undisturbed turbulence measured by H08E.

series using Thomson [191] multi-taper method, with a time-halfbandwidth product of 4, and subsequently smoothed over 100 frequency windows, the centre of which is equally spaced along a logarithmic axis. The lowest frequency resolved is $1.7 \cdot 10^{-3}$ Hz. The normalization of each spectrum is based on the variance of the undisturbed turbulence, which is designated as $(\sigma_{v_z}^2)_0$. Eventually, the ensemble average of the normalized power spectral densities is performed using the median operator for each normalized frequency bin.

An interpretation of the spectral shape of S_{v_z} is given as follows. In the low-frequency range, namely for $fD/\bar{u} \leq 5 \cdot 10^{-3}$, the spectral energy is reduced due to the presence of the bridge deck, which acts as a "high-pass filter", e.g. distorting eddies characterised by longer wave lengths. Interestingly, despite the lower energy content, $f \cdot S_{v_z}$ in the near wake exhibited the same falling off slope $\propto f^1$ associated with the velocity spectrum of undisturbed turbulence. An inflection point can be located at around $fD/\bar{u} = 8 \cdot 10^{-3}$. It will later be shown that within this range of reduced frequencies, the spectral shape of S_{v_z} in the near wake is significantly affected by the level of turbulence in the free stream. On average, the spectral energy in the near wake overtakes the undisturbed turbulence at $fD/\bar{u} = 0.04$. At this reduced frequency, the inertial sub-range is not reached yet for the undisturbed turbulence, the vertical spectrum of which falls off with the expected $\propto f^{-5/3}$ slope. In the near wake, fS_{v_z} peaks within a reduced frequency range centred at $fD/\bar{u} =$

0.20, which corresponds to the median non-dimensional vortex shedding frequency, i.e. the St number associated with the studied bridge deck. In this reduced frequency region, e.g. $fz/\bar{u} \approx 4.5$, isotropy is already reached in the undisturbed monitored turbulence. For $fD/\bar{u} \geq 0.40$, the S_{v_z} spectrum follows $\propto f^{-5/3}$, as predicted by Kolmogorov [87] for locally isotropic turbulence. A power law $\propto f^{-5/3}$ in the inertial sub-range is generally reported for the two-dimensional near-wake velocities past a circular cylinder, both experimentally [149] and numerically [125] in the sub-critical Re number regime. Although a power law roll-off indicates the existence of an inertial sub-range, this does not ascertain local isotropy [20]. The latter is further checked by inspecting the spectral ratios S_w/S_u and S_v/S_u, as well as the magnitude of the cross-spectrum Co_{uw} [79]. It can be inferred that for $|z/L| \leq 0.1$, i.e. near-neutral stratification of the atmosphere, local isotropy is not reached in the near-wake turbulence for the case at hand. The reason is that $S_v/S_u \approx 1.15$ for $fD/\bar{u} > 0.5$. On the other hand, S_w/S_u is found to approach a value of around $4/3$ at $fD/\bar{u} \approx 0.5$.

Thus, Figure 5.10, together with the results presented in Figure 5.2 which includes all velocity spectra for a selected case study in a stably stratified flow, suggest that an inertial sub-range in the turbulent near-wake of the studied bridge deck, for full-scale Re number, is generally reached for $fD/\bar{u} \geq 0.50$.

Influence of turbulence intensity

Figure 5.11 illustrates the influence of the free-stream turbulence intensity I_w on the normalized velocity spectra of v_z estimated in the near wake for $|z/L| \leq 0.1$, i.e. near neutral stratification of the atmosphere. It is clear that in the low (reduced) frequency range, namely $fD/\bar{u} \leq 1 \cdot 10^{-2}$, the scatter in the spectral shape is driven by the turbulence intensity (TI). In particular, the higher the turbulence intensity (I_w), the higher energy level in the near wake reflecting the background turbulence. For the larger TI, a shoulder-shaped behaviour can be detected for $fD/\bar{u} \approx 4 \cdot 10^{-3}$, which corresponds approximately to the reduced frequency range at which the undisturbed $f \cdot S_{v_z}$ starts peaking. Instead, a low turbulence intensity affects less strongly the low-end of fS_{v_z}/σ_w^2 in the near wake, as the incident eddies are more easily distorted for low TI.

The influence of I_w on the turbulent near-wake production for $fD/\bar{u} \ll St$ is more or less the same up to $fD/\bar{u} \approx 7 \cdot 10^{-2}$, starting from which the formation of coherent vortex structures is enhanced for lower TI. The spectral
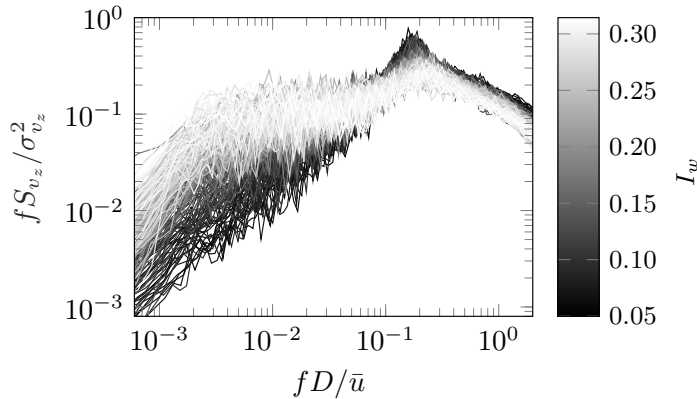
Figure 5.11: Influence of incoming turbulence intensity (I_w) on the one-point velocity spectrum S_{v_z} in the near wake (D08W) for north-northeasterly flows with $u \geq 6\,\mathrm{m\,s}^{-1}$, $|z/L| \leq 0.1$ and $-10° \leq \bar{\alpha} \leq 10°$, acquired from 01/08/2020 to 01/08/2021.

peak associated with the vortex shedding frequency exhibits a dependence on the free-stream turbulence intensity: the corresponding *St* number estimate increases as I_w increases. Furthermore, both the width and prominence of the spectral peak varies with the I_w value. The most energy-containing eddies of atmospheric turbulence have a characteristic length scale much larger than the representative dimension of the bridge deck. Thus, large-scale turbulence can be interpreted as low-frequency fluctuating mean wind speed and the Strouhal relationship in Equation (2.27) outputs vortex shedding frequencies with a frequency band centred at f_v [198]. The higher the turbulence intensity, the wider is the bandwidth [198]. For $fD/\bar{u} > 0.4$, the $\propto f^{-5/3}$ roll-off does not appear to be impacted by the different levels of turbulence in the free stream. The results discussed above are assumed valid for a given length scale-to-depth ratio, which in full-scale is $L_w^X/D \gg 1$ given the nature of atmospheric turbulence and dimensions of the studied bridge cross-section.

5.4   Near-wake features in model-scale

The near-wake turbulence characteristics are now discussed based on the wind tunnel investigations described in Appendix B.3. We shall remind the reader that the velocity measurements are undertaken at a distance of B/2
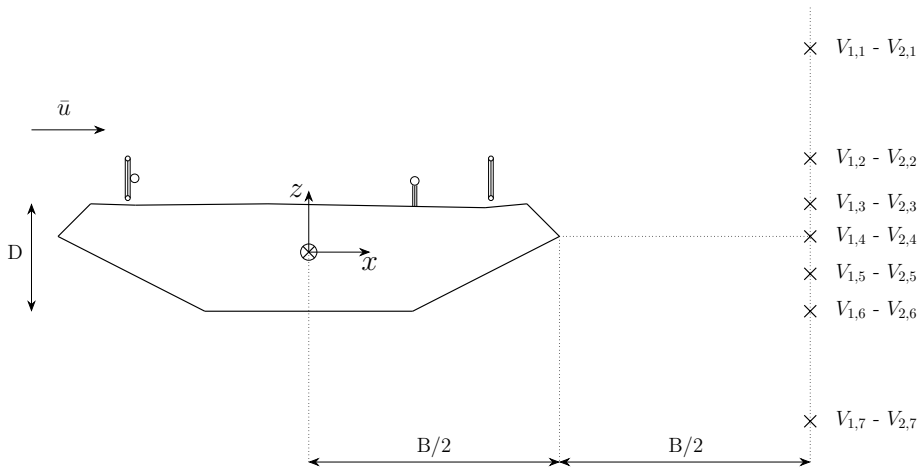
Figure 5.12: Near-wake measurement stations of the X probes. Each ($\times$) indicates a pair of X probes performing simultaneous velocity measurements.

downstream of the trailing edge of the section model, for both non-yawed and yawed ($\beta = 25°$) configuration. The tested Reynolds number is $Re = 3.6 \cdot 10^4$ (based on the across-wind dimension, D). A description of the setup utilized, including the location of the measurement stations and coordinate system, is given in Appendix B.3. The location of the measurement stations is displayed in Figure 5.12 for the sake of clarity. Unless otherwise stated, the one-point statistics are computed based on the hotwire anemometer designated as *X probe* 1 (see Appendix B.3).

5.4.1 First-order statistics

The profiles of the time-averaged values $\bar{u}$, $\bar{v}$ and $\bar{w}$ are shown in Figures 5.13 and 5.14 for non-yawed ($\beta = 0°$) and yawed ($\beta = 25°$) section model, respectively. The coordinate $z = 0\,\text{m}$ corresponds to the location of the shear centre. For $\beta = 0°$ the maximum velocity deficit of the along-wind component is estimated at the measurement point $V_{1,4}$, which corresponds to the trailing edge height. Due to the asymmetry of the deck cross-section around the *x*-axis and the presence of railings, a symmetric distribution of $\bar{u}/\bar{u}_0$ around the wake centreline is not observed. However, one could argue about the definition of the wake centreline for an asymmetric cross-section. The value of the maximum velocity deficit depends on the turbulence of the incoming flow, with $\bar{u}/\bar{u}_0 = 0.27$ and $\bar{u}/\bar{u}_0 = 0.36$ for smooth and turbulent flow, respectively.

Thus, a lower time-averaged drag coefficient is expected for a turbulent flow and $\bar{\alpha} = 0°$ due to the faster wake recovery, see e.g. Bogunovic Jakobsen [14]. For comparison, the ratio $\bar{u}/\bar{u}_0 = 0.34$ was estimated by Mannini et al. [127] 0.4B downstream from the trailing edge of a stationary 5:1 rectangular cylinder tested in turbulent flow ($Re = 1.13 \cdot 10^5$). The half-width of the wake [48], which is defined for both upper and lower sides, is affected by turbulence primarily in the lower side, where it increases by 37% compared to the smooth flow case. As the cross-section is a trapezoidal closed-box girder with a relatively larger dead air volume below the nose line, the formation of vortex structures is expected to stretch over a wider region, i.e. between the bottom plate and the nose axis, which is in agreement with the profile depicted in

Figure 5.13: Distribution of the normalized time-averaged velocity components for $\beta = 0°$, in smooth and turbulent flow ($I_u = 0.10$). The solid and dashed black lines are piecewise cubic interpolations.
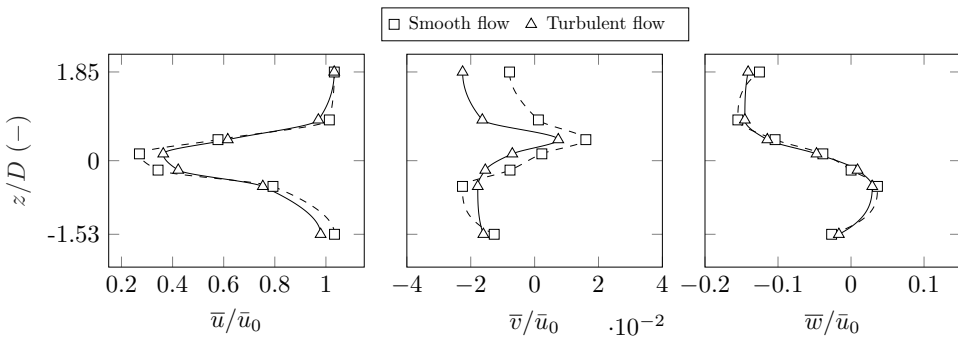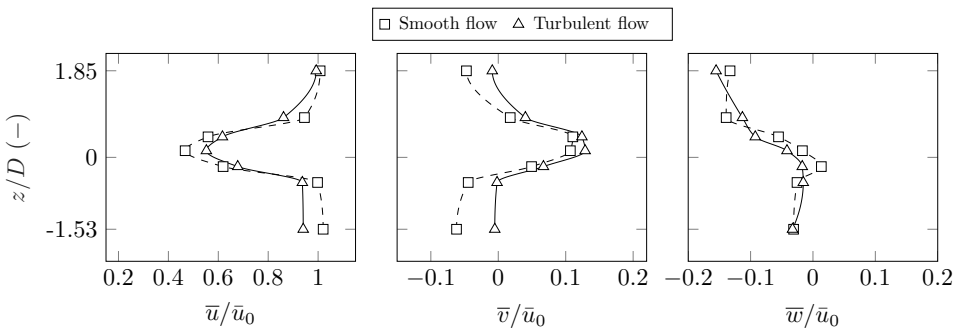

Figure 5.14: Distribution of the normalized time-averaged velocity components for $\beta = 25°$, in smooth and turbulent flow ($I_u = 0.10$). The solid and dashed black lines are piecewise cubic interpolations.

Figures 5.13 and 5.14. The values $\bar{u}/\bar{u}_0$ are slightly larger than 1 for the outer measuring stations and reflect likely the signature of the interaction between the shear layers and the accelerated flow above/below them. For the yawed configuration (Figure 5.14), an increase of the ratio $\bar{u}/\bar{u}_0$ is observed, namely $\bar{u}/\bar{u}_0 = 0.47$ and $\bar{u}/\bar{u}_0 = 0.55$ for smooth and turbulent flow, respectively. The behaviour corresponds to a weaker velocity deficit for $\beta = 25°$. This can somehow be anticipated from the decrease of drag coefficient for increasing yaw angle, which is generally documented during wind tunnel tests of bridge deck section models [40; 213]. A non-zero yaw angle appears to increase slightly the upper half-width of the wake. On the other hand, a non-zero yaw angle favours a decrease of the lower half-width of the wake. For example, Zhou et al. [212] observed a decrease of the half-width of the wake for a circular cylinder in the sub-critical regime, at $x/D = 10$, for increasing yaw angle.

The variation of the across-wind component $\bar{v}/\bar{u}_0$ with z/D quantifies the degree of (time-averaged) three-dimensionality of the near-wake flow [153; 128]. When $\beta = 0°$, the near-wake is, as expected, fairly two-dimensional for both smooth and turbulent flows (Figure 5.13), as $-2.5\% \leq \bar{v}/\bar{u}_0 \leq 2.5\%$, e.g. $\bar{v}$ is close to zero. For $\beta = 25°$, a significant increase of $\bar{v}/\bar{u}_0$ is observed along the four centrally located measurement stations, thereby quantifying a strongly three-dimensional flow in that region. Shape-wise, the vertical profile of $\bar{v}/\bar{u}_0$ is consistent with the one estimated for $\bar{u}/\bar{u}_0$. The maximum value $\bar{v}/\bar{u}_0 = 0.13$ is reached at the trailing edge height in turbulent flow conditions. The corresponding value of the span-wise component, i.e. along the bridge deck axis, is $0.35 \cdot \bar{u}_0$. It is postulated that it is a signature of the organized axial flow structure developing on the leeward side of the bridge deck section model. Furthermore, for a yawed/inclined circular cylinder in the sub-critical flow regime, vortices are shed in alignment with the cylinder for $\beta \leq 30°$ [153; 190] and a three-dimensionality of the wake can be detected up to $x/D = 40$ downstream the model [199]. Despite the different geometry of the bridge deck studied herein, a similar three-dimensional development of the wake is expected along the stream-wise direction.

The axial flow quantified in full-scale using sonic anemometry (Section 5.3.1) was further investigated in the wind tunnel undertaking basic flow visualizations using wool tufts. Figure 5.15, which shows a view from downstream the model, confirms the presence of a strong flow developing along the axis of the section model, on its leeward side.

Figure 5.15: A snapshot of the flow visualizations for yawed section model ($\beta = 25°$) in smooth flow, showing a signature of the axial flow in the near wake. The photo is from SOH Wind Engineering LLC [182].

For both non-yawed and yawed configurations, the distribution of $\bar{w}/\bar{u}_0$ suggests that the mean streamlines are deflected downwards in the upper near wake. Instead, within the portion of the wake located below the trailing edge of the girder, the mean flow exhibits a more horizontal character.

5.4.2   Second-order statistics

The distributions of $\overline{u'^2}/\overline{u}_0^2$, $\overline{v'^2}/\overline{u}_0^2$ and $\overline{w'^2}/\overline{u}_0^2$ are given in Figures 5.16 and 5.17 for non-yawed ($\beta = 0°$) and yawed ($\beta = 25°$) section model, respectively. Statistics are computed based on unfiltered signals. For the along-wind component u' in a non-yawed setup, the variance peaks at two locations along z, which correspond to the lower bottom side of the section model and the upper side of the railings. This is likely associated with the convected upper and lower free shear layers originating from the model. In fact, the maximum velocity fluctuations in the near wake are expected to occur in the vicinity of the vortex centre [169; 9]. The vertical velocity component is more affected by the eddies formation in the near wake. Nevertheless, both background turbulence and coherent quasi-periodic flow structures are included in the variance estimates presented in Figure 5.16. The velocity spectra discussed in section 5.4.4 will clarify the impact of turbulence in the undisturbed flow on the near-wake velocity fluctuations across different reduced frequency ranges. Despite the different wake half-width stemming from the wake stream-wise evolution, the profile of $\overline{u'^2}/\overline{u}_0^2$ for the turbulent flow configuration is
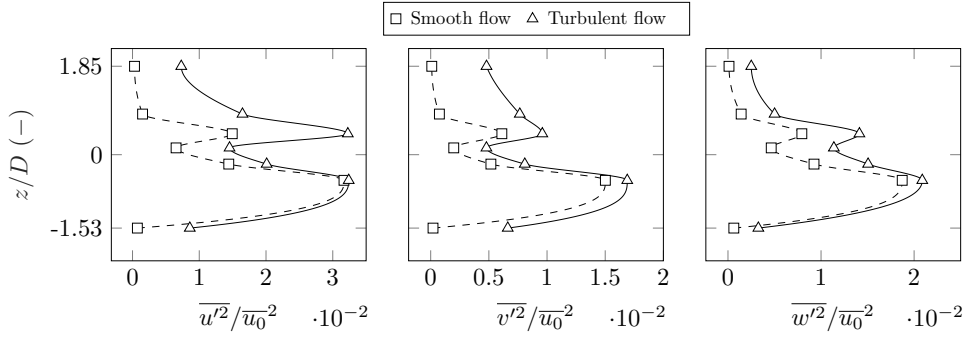
Figure 5.16: Distribution of the normalized variances of the velocity components for $\beta = 0°$, in smooth and turbulent flow ($I_u = 0.10$). The solid and dashed black lines are piecewise cubic interpolations.
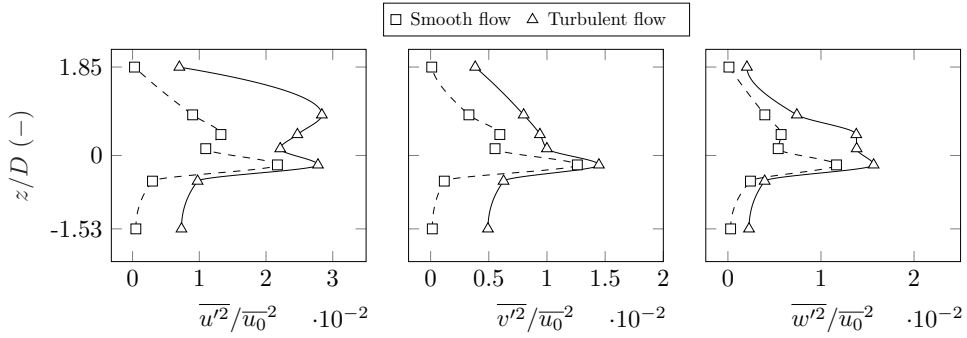
Figure 5.17: Distribution of the normalized variances of the velocity components for $\beta = 25°$, in smooth and turbulent flow ($I_u = 0.10$). The solid and dashed black lines are piecewise cubic interpolations.

in qualitative agreement with the profile estimated by Cheynet et al. [27] at $40\,\text{m}$ (3.25B) from the trailing edge using two synchronized short-range dual-Doppler wind lidars.

With $\beta = 25°$, the distribution of $\overline{u'^2}$ changes significantly. In the lower part of the near wake, $\overline{u'^2}$ peaks at a height closer to $z = 0\,\text{m}$ compared to the runs with $\beta = 0°$. This is the case for both smooth and turbulent flows, and is consistent with the decreased lower wake half-width observed for the non-zero yaw angle, see Section 5.4.1. In smooth flow, the magnitude of $\overline{u'^2}$ is strongly reduced when $\beta = 25°$, as generally observed for a circular cylinder when increasing the yaw angle up to $45°$ [212].

Similarly to the along-wind component, the vertical variations of $\overline{v'^2}$ and
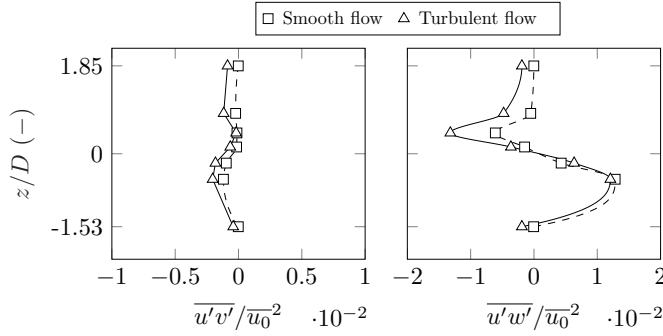
Figure 5.18: Reynolds shear stresses profiles for $\beta = 0°$, in smooth and turbulent flow ($I_u = 0.10$). The solid and dashed black lines are piecewise cubic interpolations.
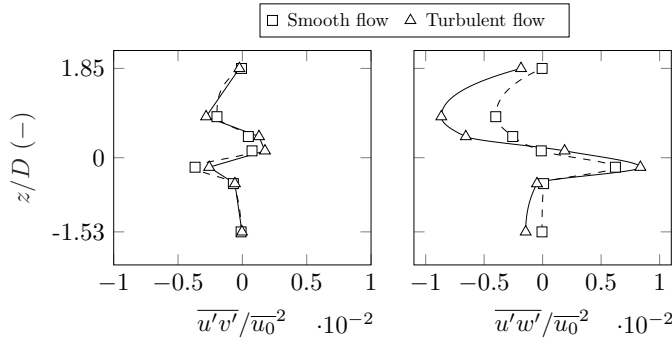
Figure 5.19: Reynolds shear stresses profiles for $\beta = 25°$, in smooth and turbulent flow ($I_u = 0.10$). The solid and dashed black lines are piecewise cubic interpolations.

$\overline{w'^2}$ are influenced by the yaw angle in terms of shape as well as magnitude.

Finally, the normalized covariances $\overline{u'w'}/\overline{u_0}^2$ and $\overline{u'v'}/\overline{u_0}^2$ are shown in Figures 5.18 and 5.19 for $\beta = 0°$ and $\beta = 25°$, respectively. The largest values of $\overline{u'w'}/\overline{u_0}^2$ occur in correspondence with the largest $\overline{u'^2}/\overline{u_0}^2$, which is consistent with the observations on the near wake of a circular cylinder [85; 149]. A non-zero yaw angle is associated with a decrease, in magnitude, of the Reynolds shear stress $\overline{u'w'}/\overline{u_0}^2$. Interestingly, $\overline{u'w'}/\overline{u_0}^2 \approx 0$ at the deck nose level ($V_{1,4}$ or $V_{2,4}$), as observed from the full-scale measurements, see Section 5.3.2. The increase, in absolute value, of the normalized covariance $\overline{u'v'}/\overline{u_0}^2$ for the innermost monitored points when $\beta = 25°$ is likely associated with the 3D character of the near wake for a non-zero yaw.
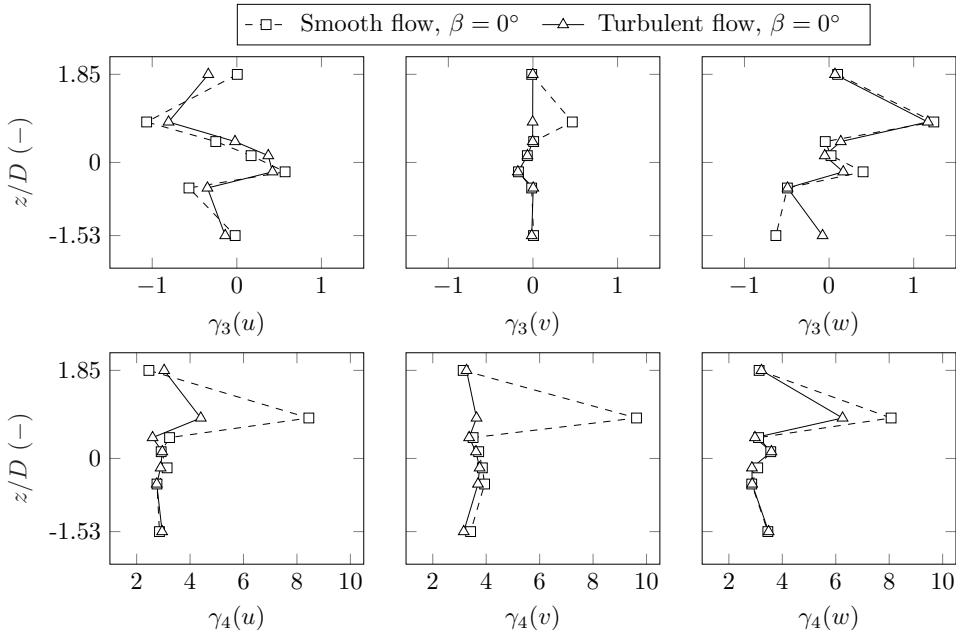
Figure 5.20: Profiles of skewness (γ_3) and kurtosis (γ_4) for $\beta = 0°$, in smooth and turbulent flow ($I_u = 0.10$).

5.4.3 Higher-order statistics

The profiles of skewness (γ_3) and kurtosis (γ_4) are given in Figure 5.20 for $\beta = 0°$. For the along-wind component u, the largest departure from a Gaussian behaviour is observed for the point $V_{1,2}$. This is likely due to the flow intermittency at the edge of the wake [46], as observed also by Mannini et al. [127] in the near wake of a 5:1 stationary rectangular cylinder. In the inner region of the near wake, namely points $V_{1,4}$ and $V_{1,5}$, the along-wind velocity fluctuations are positively skewed. The outermost measurement stations $V_{1,1}$ and $V_{1,7}$ generally exhibit a Gaussian behaviour. The profile of skewness for the vertical component should be antisymmetric with respect to the wake centreline [46; 149], which is more or less confirmed in the present study as well.

5.4.4 One-point velocity spectra

The one-point velocity spectra estimated at location $V_{1,6}$ for $\beta = 0°$ in turbulent flow are presented in Figure 5.21 as a function of the reduced frequency
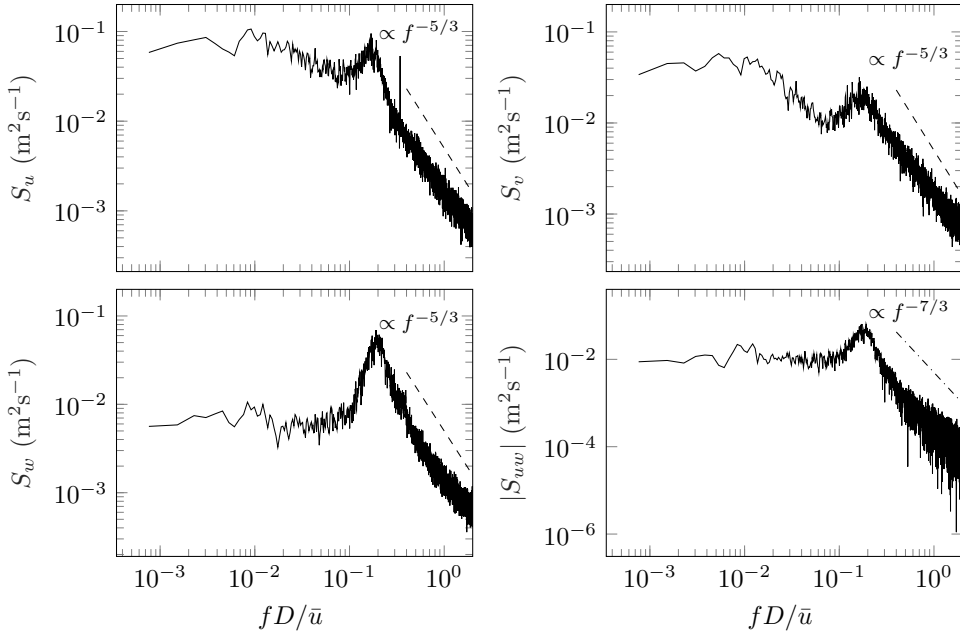
Figure 5.21: Single-point velocity spectra at location $V_{1,6}$ in the near wake for $\beta = 0°$ and turbulent flow ($I_u = 0.10$).

$fD/\bar{u}$. A clear peak at $fD/\bar{u} = 0.190$ can be identified especially in the spectrum of the vertical velocity component (S_w). As expected, the vortex shedding process is less dominant in the spectra of the velocity components u and v, for the monitored locations in the near wake. However, a peak can still be detected at $fD/\bar{u} = 0.190$. The distinct harmonic at $fD/\bar{u} = 0.35$ for S_u is considered to be associated with the (aliased) harmonics of the wind tunnel system engine. Despite the anticipated (nominally) two-dimensional character of the near wake, for $\beta = 0°$, it is interesting to note that the across-wind component is also affected by the vortex shedding process, thereby suggesting the presence of a three-dimensional organized flow structure. In this case, turbulence in the flow appears to enhance the vortex shedding peak in S_v for $\beta = 0°$.

Kolmogorov [87] predicts that there exists a frequency range where turbulence is proportional to a -5/3 power law (the inertial subrange). Figure 5.21 suggests that S_u and S_w do follow a decay approximately $\propto f^{-5/3}$ for $0.40 \leq fD/\bar{u} \leq 1$. Instead, S_v appears to decay at a slightly slower rate. The median values of the corresponding spectral ratios are $S_v/S_u = 0.98$ and
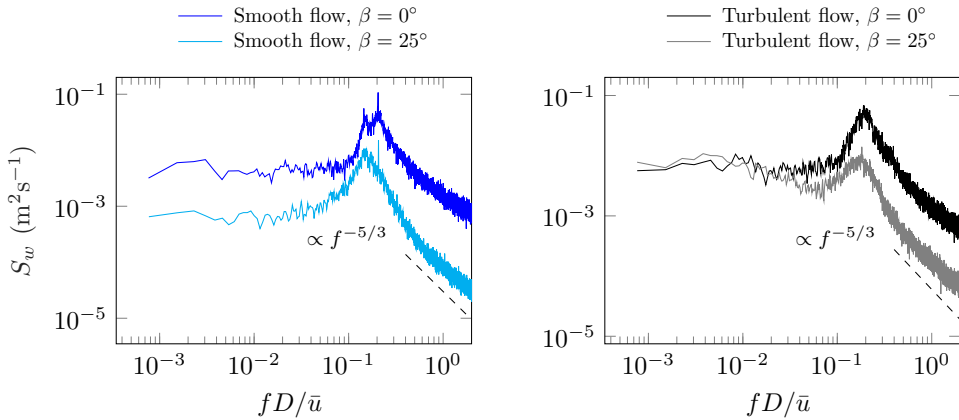
Figure 5.22: Comparison of the single-point velocity spectrum S_w at location $V_{1,6}$ for different flow conditions and yaw angles tested.

$S_w/S_u = 0.88$, for reduced frequencies within $0.40 \leq fD/\bar{u} \leq 1$. Thus, local isotropy is not reached yet. It is worth noting that in the outermost monitored stations of the near-wake spectral ratios of approximately $4/3$ are reached for the turbulent flow and zero yaw angle.

The effects of a non-zero yaw angle ($\beta = 25°$) and turbulence in the flow on S_w is synthesised in Figure 5.22 for the monitored location $V6$ as an example. The frequency is normalized based on the undisturbed mean wind speed $\bar{u}$ since the applicability of the independence principle (IP) is not justified a priori for the tested cross-section. Firstly, for $\beta = 25°$, the magnitude of the spectral peak associated with vortex shedding is attenuated and its width broadens, suggesting a weaker formation of vortices in the near wake when the section model is yawed. Secondly, for both smooth and turbulent flows, S_w peaks at lower reduced frequencies when $\beta = 25°$, which is in agreement with the independence principle. In fact, if the velocity component normal to the bridge axis $\bar{u}_N = \bar{u} \cdot \cos(\beta)$ is utilized in the normalization, the spectral peaks would occur at approximately the same reduced frequency $fD/\bar{u}_N$ for $\beta = 0°$ and $\beta = 25°$. Further discussion on the matter is presented in Section 5.5.

The turbulent flow within the very near-wake region is very sensitive to the dynamic behaviour of the two shear layers developing on either side of the bridge deck along with the vortex shedding. Thus, the measured velocity spectra across transverse direction are expected to be consequently affected in terms of roll-off slopes as well as the extent of the inertial sub-range.
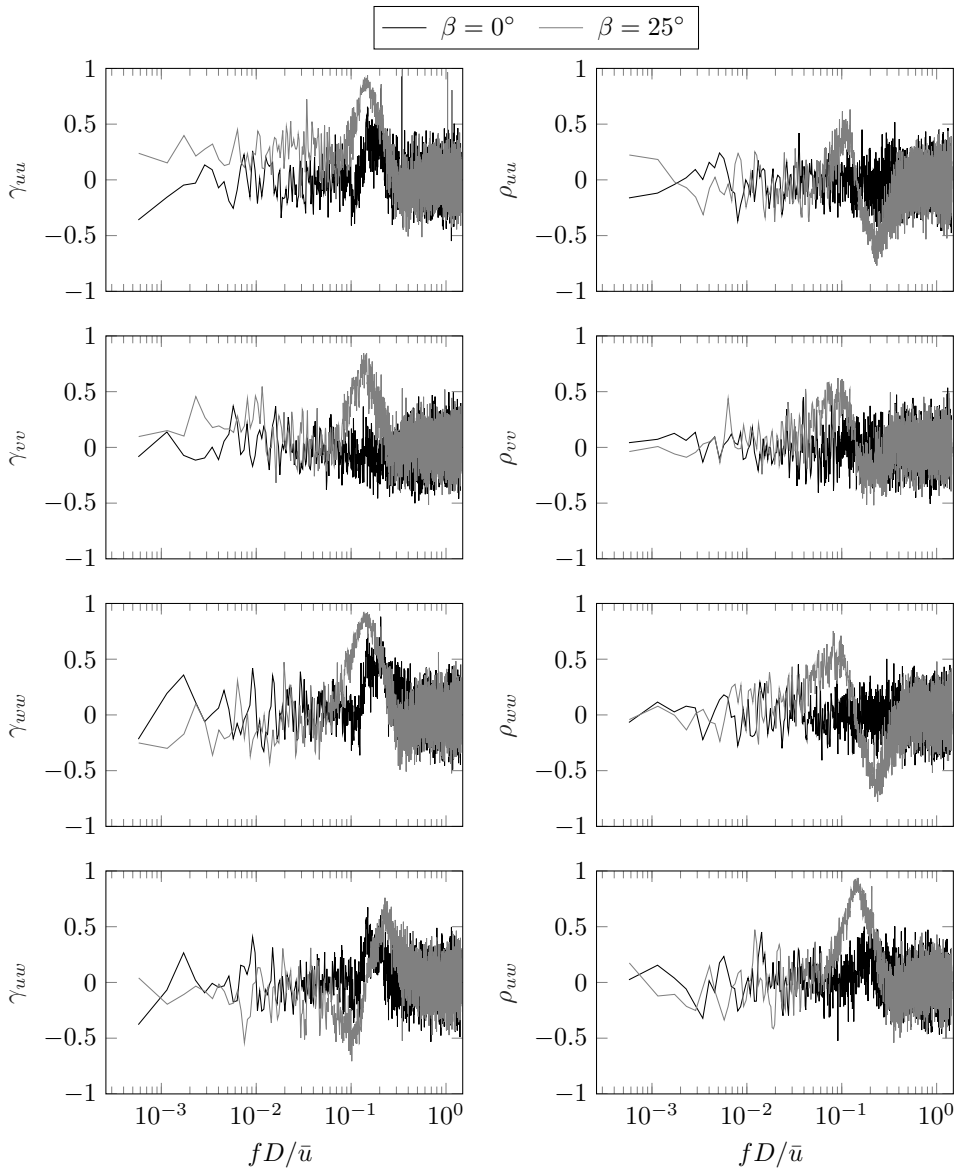
Figure 5.23: Co- and quad-coherence of the three velocity components in the near wake at locations $V_{1,6}$ and $V_{2,6}$, for $\Delta y/B = 0.3$ and smooth flow.

5.4.5 Span-wise coherence

The span-wise co- and quad-coherence (see Equation (2.22)) between the velocity fluctuations at $V_{1,6}$ and $V_{2,6}$ is displayed in Figures 5.23 and 5.24, for smooth and turbulent flow, respectively. The normalized span-wise separa-
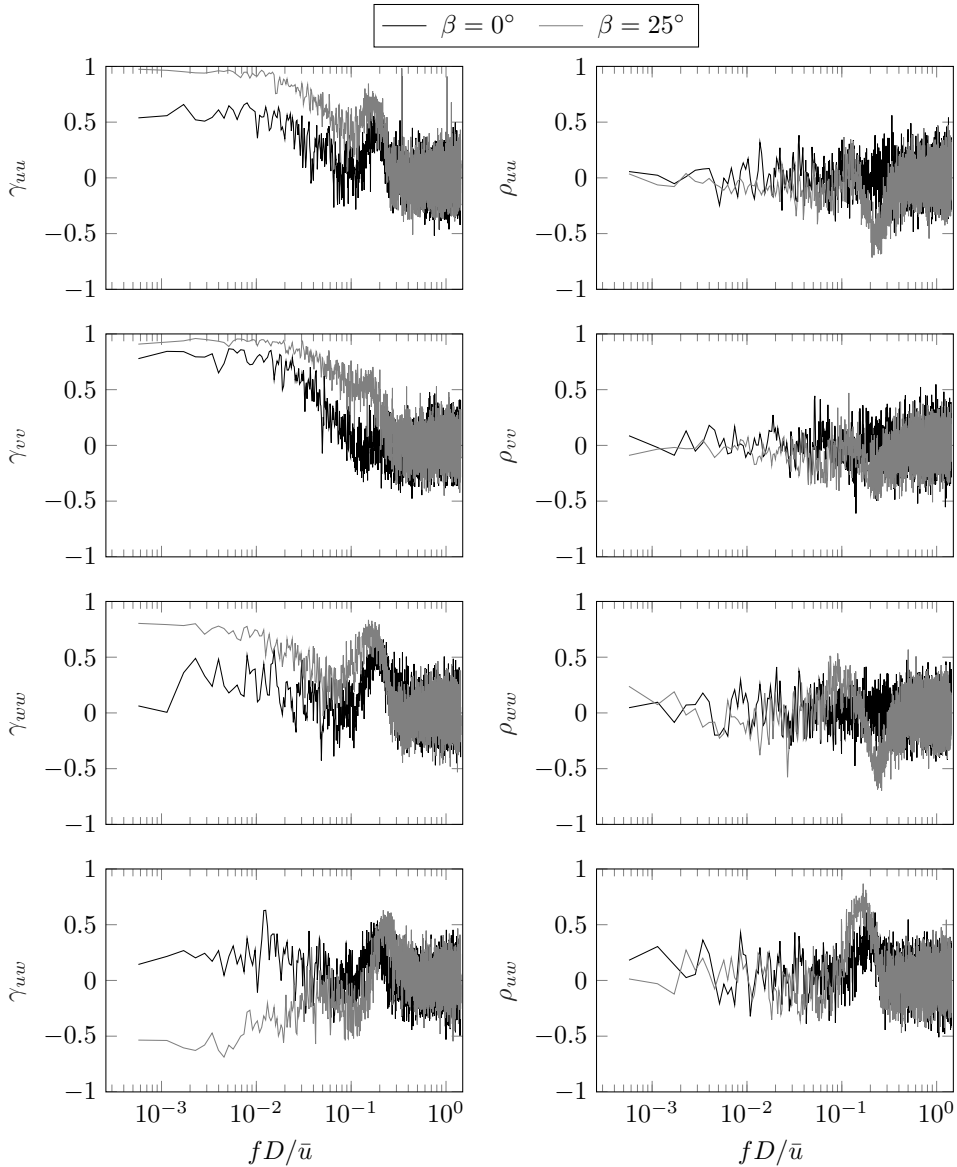
Figure 5.24: Co- and quad-coherence of the three velocity components in the near wake at locations $V_{1,6}$ and $V_{2,6}$, for $\Delta y/B = 0.3$ and turbulent flow.

tion between the measurement stations, which are aligned with the bottom horizontal panel of the girder (see Appendix B.3), is $\Delta y/B = 0.3$.

A non-zero yaw angle is found to have pronounced effects on the co- (γ_{jj}, where $j = u, v, w$) and quad-coherence (ρ_{jj}, where $j = u, v, w$) and for more

or less all velocity components. The magnitude of γ_{jj} at the non-dimensional vortex shedding frequency increases compared to the case of normal incidence of the flow ($\beta = 0°$), in smooth (Figure 5.23) and turbulent flow (Figure 5.24). Also, the frequency bandwidth associated with the formation of coherent (in-phase) vortex structures is slightly wider for $\beta = 25°$. This can be attributed to the strong three-dimensionality of the near-wake flow for the yawed runs. Along the cross-flow direction, $\gamma_{vv} = 0.8$ at the vortex shedding frequency when $\beta = 25°$ whereas no significant correlation is found for $\beta = 0°$, thereby suggesting a more 2D character of the near wake. The relatively strong quad-coherence at $\beta = 25°$ reflects the delay along the bridge axis in the near-wake flow.

The different level of span-wise correlation observed when the flow is skewed also arises from the different wake topology in terms of first- (Section 5.4.1) and second-order (Section 5.4.2) statistics. When $\beta = 25°$, the lower wake half-width was found to decrease and, consequently, velocity fluctuations at the measurements point $V_{1,6}$ and $V_{2,6}$ attenuate. In other words, the average position of the lower vortex core moves upwards towards the wake centreline. Hence, $V_{1,6}$ and $V_{2,6}$ are likely located closer to the separating shear layers at $\beta = 25°$. This may partly explain the slight increase of co-coherence given in Figure 5.23 when the flow is skewed.

Observations along these lines apply also to the turbulent flow case shown in Figure 5.24. Again, the magnitude of the co-coherence at the vortex shedding frequency is larger for $\beta = 25°$. However, turbulence in the incident flow attenuates the lateral correlation of the vortex shedding process. Also, the higher values of γ_{uu}, γ_{vv} and γ_{ww} for $fD/\bar{u} \leq 0.05$ and $\beta = 25°$ are a signature of the faster wake recovery as outlined above.

Note that the non-dimensional vortex shedding frequency is reduced when the flow is skewed in both smooth and turbulent flow. This is in line with the observation based on the one-point velocity spectra (Section 5.4.4).

5.5   Strouhal number

The section outlines the results and observations on the *St* number based on the model- and full-scale investigation. The emphasis is on the sensitivity of the *St* number on the *Re* number, the turbulence level in the approaching flow and the yaw angle.

5.5.1 Model-scale data

The vortex shedding frequency is estimated based on the velocity spectrum of the transverse component w, which is an effective indicator of organized flow structures in the near wake of a body [212], as shown in Section 5.4.4. The corresponding St number is defined as the reduced frequency $fD/\bar{u}$ at which the spectral peak of S_w occurs. The St number estimates are given in Figure 5.25 for both smooth and turbulent flows along with the corresponding predictions based on the independence principle (IP), namely:

$$St(\beta) = St(\beta = 0°)\cos(\beta), \tag{5.2}$$

which is usually experimentally [59; 186; 89; 195; 153] and numerically [128] verified for yawed/inclined stationary circular cylinders in sub-critical range of Re number when $\beta \leq 40°$. Figure 5.25 suggests that the estimated St numbers are in agreement with the independence principle, for the tested yaw angle, Re number and mean angle of wind incidence, in both smooth and turbulent flow.

In turbulent flow conditions, the estimated St number is 9% larger compared to one estimated in a smooth flow (Figure 5.25). This is likely due to the interaction between free stream turbulence and separated shear layers and more narrow wake in turbulent flow. This is in agreement with Mannini et al. [127], who underlined an increase of St with increasing TI (and turbulence length scales) for a stationary 5:1 rectangular cylinder at $\bar{\alpha} = 0°$,
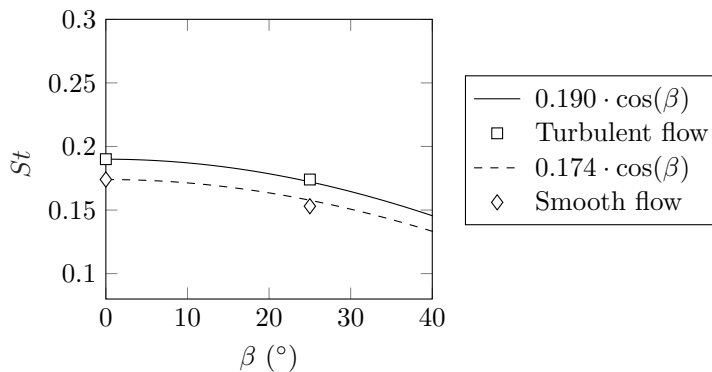
Figure 5.25: Estimates of the Strouhal number St in turbulent and smooth flows, $Re = 3.6 \cdot 10^4$, $\bar{\alpha} = 0°$.

for $5.6 \cdot 10^4 \leq Re \leq 6.0 \cdot 10^4$. The largest estimate reported in Mannini et al. [127] ($St \simeq 0.185$), was based on surface pressure signals, with $I_u = 13.5\%$ and $L_u^x/D = 3.9$. Similar observations apply for a smooth-surfaced circular cylinder in the sub-critical Re number regime, where an increase of turbulent intensity is generally associated with an increase of St number [21]. In fact, free-stream small-scale turbulence is known to influence the transition of the boundary layer over the cylinder surface and delay the flow separation [95].

5.5.2 Full-scale observations

Similarly to the model-scale investigation, the St number is estimated based on the normalized velocity spectrum $f S_w / \sigma_w^2$, using the full-scale dataset described in Section 5.3. The mean angle of wind incidence is limited to the range $-5° \leq \bar{\alpha} \leq 5°$ to minimize the potential dispersion of the estimates. This choice is made considering that for a 5:1 rectangular cylinder, the St number is not significantly affected by angles of attack limited to $\pm 5°$ [127; 171]. It is worth noting that the median and standard deviation of the St number estimates do not significantly change when a range $-10° \leq \bar{\alpha} \leq 10°$ is employed. Figure 5.26 quantifies the dependencies of the estimated St number on yaw angle β and vertical turbulence intensity I_w characterising the undisturbed wind flow. No clear interdependence between normalized shedding frequency and yaw angle can be established, thereby setting the
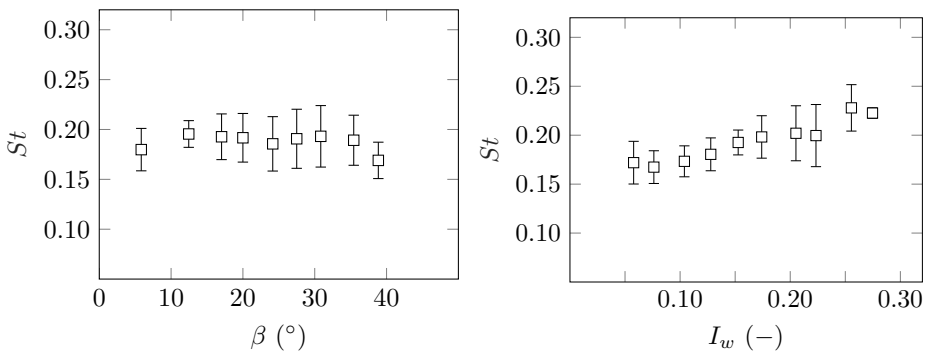
Figure 5.26: Dependence of the Strouhal number St on yaw angle (left panel) and free-stream turbulence intensity (right panel), for north-northeasterly flows with $u \geq 6\,\mathrm{m\,s}^{-1}$, $|z/L| \leq 0.1$ and $-5° \leq \bar{\alpha} \leq 5°$, acquired from 01/08/2020 to 01/08/2021.

full-scale counterpart apart from the validity of the "cosine rule", i.e. the independence principle. On the other hand, the TI was found to influence significantly the *St* number, as anticipated in Section 5.3.3.

5.5.3 Discussion - *Re* number dependence

As described in Section 2.3.4, the flow around sharp-edged bluff bodies may exhibit a certain dependence on *Re* number [172; 170; 97; 171]. The unique set of full- and model-scale velocity records sampled in the near wake of the Lysefjord Bridge permits the investigation of potential *Re* number effects.

Table 5.2 compares the *St* number estimates for the investigated *Re* numbers. The dataset acquired in full-scale is binned based on three different ranges of TI and the stated yaw angles encompass a range $\pm 5°$ to increase the number of available samples and reduce the uncertainties in the comparison with wind tunnel data. Similarly, Figure 5.27 reports a summary of the *St* number estimates as a function of the *Re* number.

No evidence of substantial *Re* number effects can be detected based on the *St* number estimates. Following the interpretation given by Schewe [170] about *Re* number effects on separated flow and wake topology, it is postulated that, below the deck nose line, flow separation occurs at the downwind knuckle lines in both model- and full-scale *Re* number tested. Thus, no significant change would be anticipated in the value of the *St* number (and possibly C_D). Though, it is expected that the laminar-to-turbulent transition occurs earlier in full-scale.

Table 5.2: *St* number estimates based on model- and full-scale velocity measurements in the near wake. In model-scale $\bar{\alpha} = 0°$ whereas in full-scale $-5° \leq \bar{\alpha} \leq 5°$. The cycle/pedestrian lane is on the downwind side of the bridge deck, e.g. N-NE wind exposure.

		$\beta = 0°$	$\beta = 25°$
Model-scale	Smooth flow	0.174	0.153
$Re = 3.6 \cdot 10^4$	$I_w = 0.08$	0.190	0.174
Full-scale	$I_w \leq 0.10$	-	0.168 ± 0.016
	$0.10 \leq I_w \leq 0.20$	0.187 ± 0.023	0.183 ± 0.026
$1.1 \cdot 10^6 \leq Re \leq 2.7 \cdot 10^6$	$0.20 \leq I_w \leq 0.30$	0.210 ± 0.028	0.204 ± 0.038
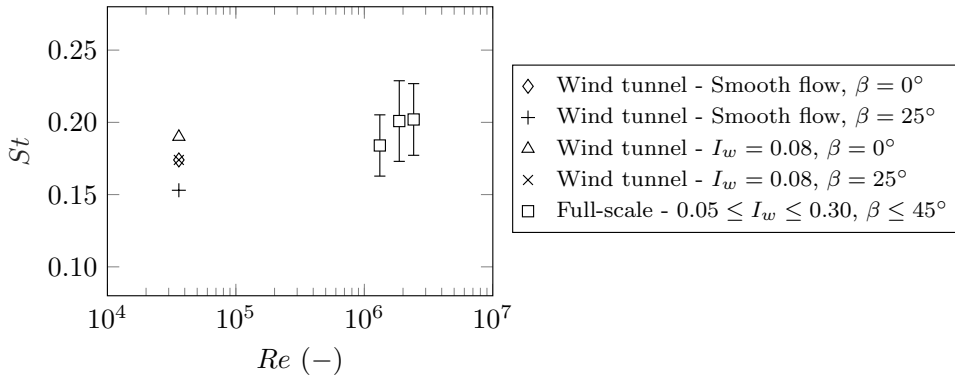
Figure 5.27: Estimates of the Strouhal number St as a function of the Re number. The cycle/pedestrian lane is on the downwind side of the bridge deck.

As pointed out by Larose and DâĂŹauteuil [97], the slenderness of a body is a key parameter for possible dependence of the aerodynamics on the Re number. The Lysefjord Bridge has an aspect ratio of 4.7, which is more streamlined than the approach span of the Storebælt East Bridge ($B/D = 3.7$), the aerodynamics of which (St number and C_D) exhibited a certain sensitivity to the Re number. At the same time, the bridge studied herein is much bluffer than the main span of the Storebælt East Bridge cross-section ($B/D = 7.8$), which did not experience a pronounced Re number sensitivity. Other comparative model- and full-scale experiments on closed-box girder [94; 3] and twin-box girder [113] bridge deck showed a certain dependence of the St on Re number. However, no conclusion can be made as a case by case approach is deemed appropriate, given the different deck geometries and various aspects concerning the scaling in the wind tunnel, such as the degree of sharpness of corners and railings. These are additional factors affecting the potential Re number sensitivity [97].

The Strouhal number of a bare deck can significantly differ from the one associated with a deck equipped with road furniture. An example on the static rig side is the Gjemnessund Bridge deck ($Re = 1.7 \cdot 10^4$), the St number of which was 0.23 and 0.13 for the bare and fully equipped deck, respectively [4]. It was suggested that the modelling of railings is important when the observed Re number effects on the St number estimates are discussed [3]. For the case at hand, the results presented in terms of St number implies that the railings are adequately modelled in the wind tunnel testing using a 1:50

geometric scale.

Here, the results discussed in terms of potential Re number effects hinge on the assumption that no significant change of the St number occurs within the considered range of angle of attack, i.e. $-5° \leq \bar{\alpha} \leq 5°$. In principle, it is possible that the Reynolds number sensitivity is dependent on the angle of attack, see e.g. Matsuda et al. [129]; Schewe [171].

When comparing wind tunnel tests undertaken in turbulent flow to full-scale experiment, it is worth commenting on the turbulence modelling. Small-scale turbulence is known to influence separating shear layers and flow reattachment over sharp-edged bodies [163; 193; 157; 96]. Hence an adequate scaling should be targeted. Nevertheless, the need for testing relatively high Re numbers, without introducing excessive blocking, generally implies limitations in simulating the low-frequency range of the velocity spectra due to tunnel size limitations. Following Irwin [75], an adequate matching of the high-frequency end of the velocity spectrum leads to the following relationship:

$$\frac{I_{u,m}}{I_{u,p}} = \left(\frac{L_{u,m}^x}{L_{u,p}^x}\right)^{1/3} \left(\frac{B_p}{B_m}\right)^{1/3} \tag{5.3}$$

where the subscripts m and p stand for model and prototype, respectively. For example, Macdonald et al. [126] used Equation (5.3) to predict vortex-induced vibrations of the Second Severn Bridge using sectional model testing. An excellent agreement was found with the full-scale observations.

In the present study, $I_{u,m}/I_{u,p} \approx 0.65$. Thus, the equivalent prototype turbulence intensity is $I_{u,p} = 0.15$ and the results presented in Table 5.2 shall be interpreted accordingly. Overall, an adequate agreement between full- and model-scale St number estimates can be established.

5.6   Detecting vortex-induced vibrations

To the author's knowledge, no clear evidence of vortex-induced vibrations has been recorded on Lysefjord Bridge since the installation of the Wind And Structural Health Monitoring system back in 2013. Different factors may contribute in inhibiting the vortex-induced vertical oscillations: (a) turbulence intensities are remarkably high given the complex terrain location; therefore

the span-wise coherence of vortex-induced fluctuating lift is expected to be lower; (b) the local wind conditions are such that yaw angles close to $0°$ are rarely encountered; (c) the development of an axial flow in the leeward side of the bridge girder may affect the span-wise correlation of vortex shedding.

A heave response curve demonstrating the onset of vortex-induced vibrations, like the one shown for the Second Severn Crossing cable-stayed Bridge (UK) by Macdonald et al. [126], cannot be attained for the Lysefjord Bridge. However, it is deemed worthwhile investigating whether a given vertical eigenmode may be prone to a potential increase in the response magnitude in the vicinity of $1/St$, which is now known (section 5.5). For this purpose, one year of response data associated with stationary flows is selected, with a NNE wind exposure, yaw angles limited to $-20° \leq \beta \leq 20°$ and $I_w \leq 0.25$. Furthermore, samples associated with the presence of traffic loading on the bridge are disregarded using the identification procedure described in Cheynet et al. [24]. This is done primarily to remove the influence of traffic loading, which may overshadow the signature, if any, of vertical vortex-induced vibrations. It also guarantees that the bridge deck aerodynamics are not influenced by the presence of vehicles on the bridge.

The ratio between the modal displacement associated with eigenmode VS2 to the one associated with eigenmode VA1 is expressed in Figure 5.28 as a function of the reduced velocity and I_w. A tendency of increasing the modal response ratio can be observed for the lower values of I_w at $\bar{u}/(f_{VS2}D) \approx$
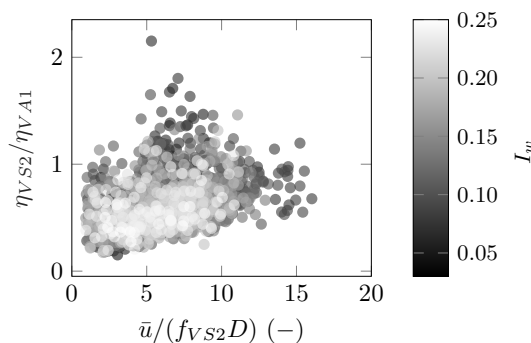
Figure 5.28: Ratio between the $10\,\text{min}$-averaged std of heave modal displacement response associated with eigenmode VS2 over VA1, as a function of the reduced velocity $\bar{u}/(f_{VS2}D)$ and I_w. The dataset is based on one year of records, for $-20° \leq \beta \leq 20°$, NNE wind exposure and no traffic loading.

5.3, where $f_{VS2} = 0.413$ Hz, and lower values of I_w. The corresponding St number would be $St \approx 1/5.3 = 0.19$, which is in agreement with the estimates proposed in Figure 5.27. Figure 5.28 attempts to show that an increase in (relative) vertical modal response magnitude (VS2) can be observed for reduced velocities close to $1/St$ and low levels of I_w.

5.7   Summary

The structure of the wind turbulence in the near wake of the Lysefjord Bridge deck has been characterised in both model- and full-scale. Sonic anemometry was proven to be effective in monitoring the vortex formation on the leeward side of a prototype bridge deck. The complementary hot-wire measurements undertaken in the near wake of a 1:50 stationary sectional model provided an insight into the potential sensitivity to Re number effects, in terms of Strouhal number. The significance of a skewed incident flow on the near-wake topology was also explored. The chapter provides valuable findings relevant to the aerodynamics of yawed line-like sharp-edged bodies.

One-point flow statistics were analysed based on a dataset consisting of one year of velocity measurements from the NNE wind sector, with a near-neutral stratification of the atmosphere. The time-averaged values, which were estimated at 0.74D from the trailing edge, revealed the existence of a pronounced axial flow when the oncoming flow is skewed more than $15°$. Its magnitude can reach $0.5 \cdot \bar{u}_0$ when the yaw angle is $40°$. The vertical velocity fluctuations were proven to be an effective indicator of the vortex shedding process. The St number estimates were found fairly sensitive to the turbulence intensity in the approaching flow. The higher the turbulence intensity, the higher the Strouhal number. The median St value of was found to be 0.20.

The complementary velocity measurements undertaken in the wind tunnel provided an insight into the vertical wake structure at 2.28D from the trailing edge of the bridge deck. Both yaw angles of $0°$ and $25°$ were tested in smooth and turbulent flows. The value of $25°$ was used to mimic the full-scale prevailing yaw angle. A non-zero yaw angle was found to favour a faster recovery of the near wake, with turbulence in the incident flow accelerating this process. Interestingly, the empiricism of the independence principle was found adequate to describe the observed Strouhal numbers in both smooth and turbulent flows in model-scale. Lastly, the lack of a pronounced Re number sensitivity for the case at hand was highlighted and discussed based on the

fundamental parameters governing the flow around sharp-edged bodies.

Chapter 6

Fluctuating wind-induced pressures

6.1   Introduction

The chapter discusses selected fundamental results based on full-scale wind-induced surface pressures measured on the Lysefjord Bridge. The data analysis concentrates primarily on the buffeting wind loading and the vortex shedding process. Selected pressure measurements are analysed to highlight the significance of the dataset recorded for studying the fluid-structure interaction in full-scale. Also, the discussion corroborates the importance of field experiments dealing with surface pressure measurements.

The buffeting theory, commonly applied to predict the bridge dynamic response to gusty winds, typically relies on the "strip assumption" [34]. Accordingly, the span-wise coherence of the wind buffeting loads is assumed equal to the span-wise coherence of the oncoming velocity fluctuations. The validity of this assumption depends on the ratio between the length scale of turbulence (e.g. $\mathscr{L}_w$) and the characteristic dimension of the body. Wind tunnel studies have shown that the unsteady lift and twisting moment acting on a closed-box girder bridge deck are typically better correlated along the bridge deck span than the incident flow, see e.g. Larose [100, 101]; Jakobsen [78]; Li et al. [115]. The few field investigations available (e.g. Melbourne [137]; Niihara et al. [143]; Andersen et al. [5]), point towards the same result. Nevertheless, apart from the results presented in Andersen et al. [5], the span-wise coherence is often discussed in terms of leading edge surface pressures

only. This is due to the technical difficulties in monitoring the complete aerodynamic forces on a bridge deck in service. One of the rationales behind this chapter is to study the gust loading on a bridge deck in the natural environment. Specifically, the objective is to assess the validity of the strip assumption for the monitored lift force and overturning moment, when the characteristic length scale associated with the vertical turbulence component is several times larger than the deck width (e.g. $\mathscr{L}_w/B \approx 4$), which is, to the author's knowledge, rarely tested in wind tunnels.

Characterising the vortex shedding process is another primary objective of the chapter, which complements the discussion on the near-wake turbulence presented in Chapter 5. The surface pressures monitored at the trailing edges provide an insight into the vortex shedding above and below the deck nose, thereby exploring potential effects of the asymmetry of the deck cross-section and the presence of the railings. Also, the significance of the turbulence level in the incident flow along with a non-zero yaw angle are addressed using one- and two-point statistics of the trailing edge pressures.

The pressure dataset is quality checked in several steps. Visual inspection of the time series, cross-checks based on variances, auto-spectra and coherence functions are among the steps performed prior to any detailed analysis of the pressure signals. Note, that these checks and pre-processing of the data is performed shortly after the pressure data is stored. This helps to identify high-quality data sets and keep track of the quality of the data and potential problems, stemming primarily from low wind velocity, rainwater intrusion and/or moisture in the tubing connected to the pressure taps. The pressure probes P08W, P08Wt, P08E and P08Et, as well as the pressure taps located below the deck nose, are found to work dependably. On the other hand, rainwater intrusion represents a common problem for the tapping points above the deck nose, i.e. 01,02, 11 and 12 (see Figure 3.11). Part of the pre-processing is devoted to flagging data samples where the pressure signals are affected by the presence of water in parts of the tubing system. For this study, all samples in which at least one pressure signal does not pass the quality check are disregarded.

The chapter is organized as follows: the basic pre-processing and analysis methods applied to the pressure signals are presented in Section 6.2. The first part of the analysis addresses the static pressure measured 4 m above the bridge deck (Section 6.3). Thereafter, the focus is on the fluctuating wind loads, namely how the atmospheric turbulence transforms into surface pres-

sures around the bridge deck (Section 6.5). Furthermore, an insight into the spatial structure of the lift and twisting moment is given, with emphasis on the validity of the strip assumption for the case at hand. Lastly, the characteristics of the vortex shedding process are explored in Section 6.6.

6.2   Data Processing

6.2.1   Tubing system-induced distortion effects

For an accurate statistical analysis of the fluctuating surface pressures measured in full-scale or in a wind tunnel, it is imperative to have adequate control of the required frequency response of the pressure measuring system [63; 108]. The connecting tubing system described in Section 3.4 is utilized in the present study to transmit the pressure signal from the sensing hole to the port of the pressure transducer. Hence, the measured pressure fluctuations experience frequency-dependent distortions in terms of both amplitude and phase [12], depending on the characteristics of the complete tubing system, including the transducer volume, and some fundamental properties of the air.

In the present study, magnitude and phase distortion effects on the measured pressure signals induced by the tubing system are digitally corrected based on the theoretical formulation described by Bergh and Tijdeman [12]. Different experimental techniques [12; 73; 64; 88] were utilized to validate the theoretical framework developed by Bergh and Tijdeman [12]. An adequate agreement between theory and experiment was generally obtained, which justifies its adoption in several wind tunnel applications. A detailed discussion on the theory, including its assumptions and derived recursion equations, can be found in Bergh and Tijdeman [12]; Holmes and Lewis [64]; Kaspersen and Krogstad [81]; Kovaerk et al. [88]; Isaksen [76].

One of the underlying assumptions of the theory by Bergh and Tijdeman [12] is that the flow is laminar. Following Kaspersen and Krogstad [81], the maximum amplitude of measurable pressure is computed as a function of frequency and position along the tubing length, for each tapping point. This facilitates the estimation of the transition to turbulence within the tubing system. For the most critical pressure taps, i.e. A06 and A07, which have the longest tubing system, the maximum estimated pressure, before the transition to turbulence is reached, is $p_{\mathrm{max},l} = 560\,\mathrm{Pa}$ at the critical frequency of $19\,\mathrm{Hz}$. For frequencies below $5\,\mathrm{Hz}$, $p_{\mathrm{max},l} > 2000\,\mathrm{Pa}$. All the remaining pressure taps
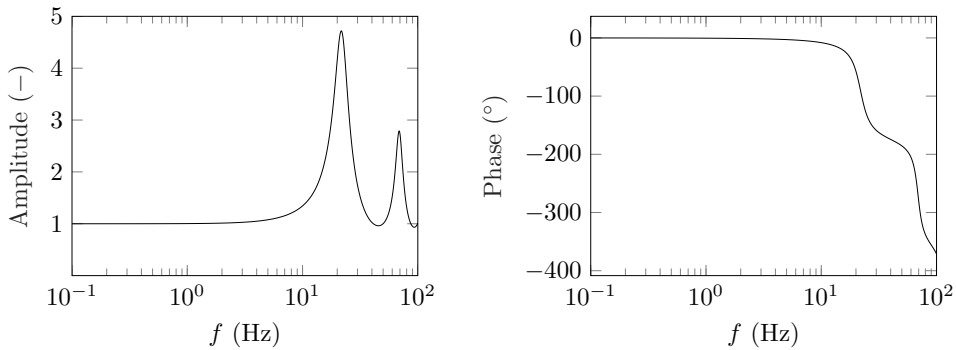
Figure 6.1: Transfer function of a double pressure measuring system, with main tubing of $L = 3.43$ m and 5 mm i.d.; $\overline{T} = 15\,°C$ and $\overline{p}_0 = 101\,325$ Pa.

are characterised by $p_{\mathrm{max},l} > 1000$ Pa for $f \leq 10$ Hz.

The calibration of the distorted pressure signals is carried out in the frequency domain [73] utilizing a frequency response function estimated based on the theory of Bergh and Tijdeman [12]. A dedicated subroutine is implemented in the pre-processing of the pressure data acquired using tapping points and pressure probes, for every 10 min-long sample. The required micro-meteorological data sensed by the weather station H10W installed on the bridge (see Section 3.3.2) are utilized as input for the calculation of the transfer functions. In fact, among the different parameters influencing the dynamic response of a pressure tubing system, the mean barometric pressure of air ($\overline{p}_0$) is generally recognized as having the largest impact [12; 88]. Specifically, an increase in $\overline{p}_0$ corresponds to a higher magnitude of the resonance peak together with a decrease, in absolute value, of the phase. This is particularly relevant for tubing systems commonly adopted in wind tunnel applications, where the scales of both length and especially i.d. of the tubing are smaller compared to a typical full-scale wind-engineering application.

Figure 6.1 shows an example of amplitude and phase response characteristics for a pressure tubing system consisting of a 3.43 m-long 5 mm i.d. flexible tubing, which transitions to a 60 mm-long 1.5 mm i.d. next to the pressure transducer. The increase of transducer volume, which is set to 17.2 mm^3, due to a diaphragm flexibility, is neglected. The adopted air temperature and barometric pressure are $\overline{T} = 15\,°C$ and $\overline{p}_0 = 101\,325$ Pa, respectively. The frequency response function is estimated for frequencies up to 100 Hz, even though the range of interest depends on the adopted sampling frequency,
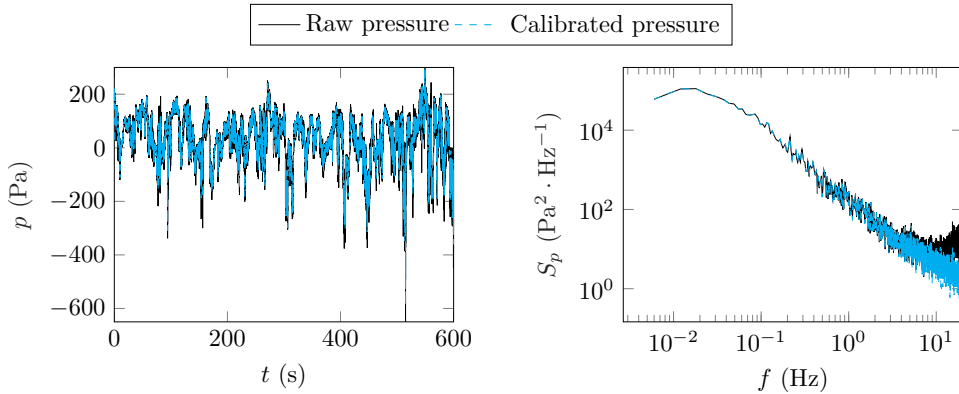
Figure 6.2: 10 min-long time history (left panel) and auto-spectrum (right panel) comparing a pressure signal before and after the calibration accounting for the tubing system distortion. The record was acquired at tap A03 on 06/08/2021 21:30 UTC, for $\bar{u} = 11\,\mathrm{m\,s^{-1}}$ and a wind direction of $17°$.

which was $f_s = 50\,\mathrm{Hz}$ in the present study (Section 3.4.5). Figure 6.1 shows that gain and phase distortion is minimum up to around 6 Hz. The first resonance of the pressure tubing system occurs at around 22 Hz whereas the second one is at 70 Hz.

An example of correction [12; 73] applied to a raw pressure signal is given in Figure 6.2. The surface pressure is acquired on the windward edge of the bridge deck (pressure tap A3, see Section 3.4.2). The surface pressure auto-spectrum, before and after the correction, shows that a consistent decay slope is achieved in the high-frequency range.

6.2.2 Pressure coefficients

In the present chapter, the reference time-varying wind dynamic pressure $q(t)$ is defined as:

$$q(t) = \frac{1}{2}\rho\left(u(t)^2 + v(t)^2 + w(t)^2\right) \tag{6.1}$$

where ρ is the air density; u, v and w are the along-wind, across-wind and vertical velocity components measured at a reference location, respectively. Depending on the turbulence intensity levels, differences arise when computing the mean dynamic pressure based on either the mean square or the squared mean [156]. Here, the mean dynamic pressure $\bar{q}$ is estimated as follows:

$$\bar{q} = \frac{1}{2}\rho \overline{(u(t)^2 + v(t)^2 + w(t)^2)} \tag{6.2}$$

The time-varying pressure coefficient $C_p(t)$ is defined as:

$$C_p(t) = \frac{p(t) - p_r(t)}{\bar{q}} \tag{6.3}$$

where $p(t)$ is the differential pressure at a given tapping point; $p_r(t)$ is the differential reference pressure, which is computed by applying a centred-unweighted moving average filter, with an averaging time of 5 min, to the static pressure $p_s(t)$ measured 4 m above the deck (either P08Wt or P08Et), on the upwind side (see Section 3.4.4); $\bar{q}$ is the mean dynamic pressure. The latter is estimated using the sonic anemometer located on the upwind side of the girder at hanger H08, i.e. either H08E or H08Wb. The computation of the pressure coefficients relies on the assumption of stationary velocity fluctuations, which is checked as described in Chapter 4 and Section 5.3.

6.2.3   Cross-sectional aerodynamic forces

The aerodynamic forces per unit length are obtained by integration of the surface pressure measured along each pressure strip. For example, the vertical force per unit length is computed as follows:

$$F_z(t) = \sum_{j=1}^{N_{pt}} p_j(t) A_{j,F_z} \tag{6.4}$$

where A_{j,F_z} is a tributary area assigned to pressure tap j, ensuring the correct sign convention for the calculation of the force. Horizontal force F_x and twisting moment F_θ are computed in a similar fashion. Note that the structural coordinate system is centred at the shear centre of the cross-section, which is 1.45 m from the bottom plate of the girder.

6.3   Atmospheric static pressure

The wind dynamic pressure $q(t)$ was computed based on the three velocity components recorded by the sonic anemometers H08E and H08Wb, see

Table 6.1: Turbulence characteristics on 06/08/2020 18:30 UTC, 60 min-long record from sonic anemometer H08E.

Dir (°)	$\bar{u}$ (m s^{-1})	$\bar{\alpha}$ (°)	u_* (m s^{-1})	z/L	I_u	I_v	I_w	$\mathcal{L}_w$ (m)
23	10.4	-1.9	1.52	-0.01	0.28	0.25	0.20	49

Equation (6.1). The atmospheric static pressure is the difference between the dynamic velocity pressure and the total atmospheric pressure. This pressure difference is, however, not static by nature, in spite of the name. This section deals with the comparison of the fluctuating part of the static pressure ($p'_s(t)$) with the dynamic wind velocity pressure ($q(t)$) and the vertical wind velocity fluctuations ($w(t)$), recorded by the sonic anemometers above the deck. As described in Section 3.4, the signal of the static pressure is measured by the reference pressures probes P08Wt and P08Et. All the pressure signals are referenced to the pressure inside a controlled air volume, located inside the bridge girder. Prior to the analysis, both the wind velocities and the pressure data were low-pass filtered and, subsequently, decimated by a factor of two, attaining a sampling frequency of $f_s = 25$ Hz. This is found appropriate to compute the statistics of interest for the present section.

A 1 h-long record is chosen to study the static pressure measured simultaneously on the upwind and downwind side of the deck, at 4 m height above the road level (see Figure 3.7). The corresponding turbulence characteristics derived from the sonic anemometer data are reported in Table 6.1. The wind is blowing from NNE and the value of z/L suggests a nearly neutral stratified atmosphere. The recorded I_u agrees well with the values generally estimated for flows approaching the bridge from the fjord [26], which are significantly high at a moderate wind speed. The yaw angle is $\beta = 25°$ and the angle of wind incidence is $-2°$.

The time history of wind dynamic pressure and static pressure measured on the upwind side of the bridge deck is given in Figure 6.3. The fluctuations of static pressure are found to follow the wind gusts, with a slightly negative correlation coefficient, namely $R_{qp_s} = -0.15$. To better visualize the relationships between fluctuating wind velocities and static pressure, a 10 min-long segment of w and $p'_s(t)$ is shown in Figure 6.4. A negative correlation ($R_{wp_s} = -0.53$) can be established, which agrees with the negative value of $p_s - w$ covariance generally found for near-neutral atmospheric stratification,
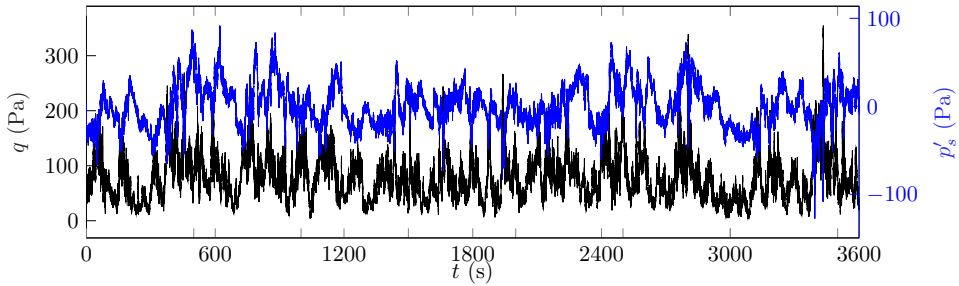
Figure 6.3: Time histories of dynamic wind pressure q and fluctuating static pressure p'_s measured on the upwind side of the bridge deck on 06/08/21 18:30 UTC.
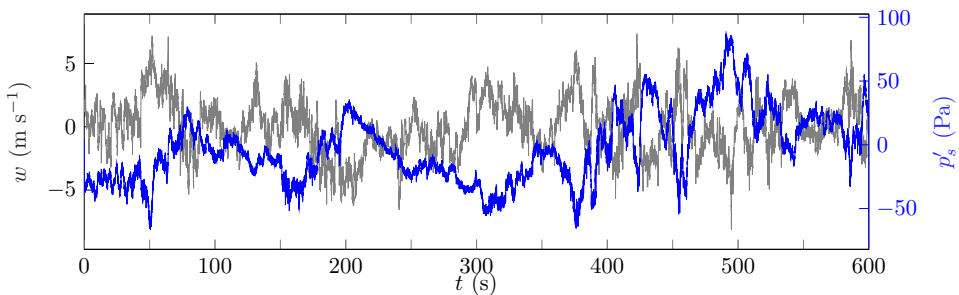
Figure 6.4: Time histories of vertical turbulence component w and fluctuating static pressure p'_s measured on the upwind side of the bridge deck on 06/08/21 18:30 UTC.

at least in the lower part of the ABL [135].

One point-spectra of vertical turbulence component (S_w) and dynamic wind pressure (S_q) are given in Figure 6.5, for measurements undertaken simultaneously on the upwind and downwind side of the deck. The spectra are normalized based on the variance of the corresponding quantity estimated on the upwind side of the girder, which is more representative of free-stream characteristics [26]. The normalized spectra are expressed as a function of the wave number $k = 2\pi f / \bar{u}$ based on the hypothesis of frozen turbulence [189]. For the sensor H08E, which is located upwind, an inertial subrange can be identified for $k \geq 0.1\,\mathrm{m}^{-1}$, as the normalized velocity spectra of the three velocity components and, consequently, the wind dynamic pressure, follow a decay $\propto f^{-2/3}$. Cheynet et al. [26] elaborated on the flow distortion recorded on the downwind side of the Lysefjord Bridge, which is clearly recognisable
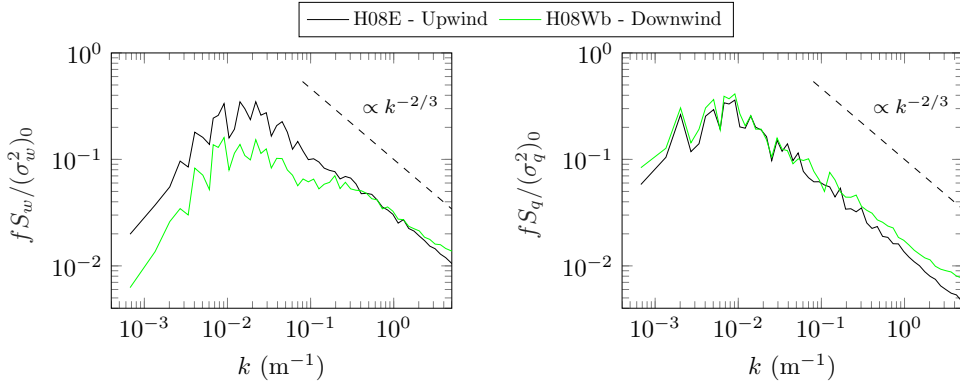
Figure 6.5: One-point normalized spectrum of vertical turbulence component (left panel) and wind dynamic pressure (right panel) recorded on the upwind and downwind side of the deck, 06/08/21 18:30 UTC.

in Figure 6.5 for the vertical velocity component at H08Wb.

It is deemed necessary to establish to which extent the bridge deck may influence the static pressure fluctuations at P08Et, i.e. 4 m-height above the deck ($z =60$ m above the sea level) on the upwind side. Figure 6.6 shows the relationship between the shear stress ρu_*^2 and σ_{p_s}, for 50 10 min-long stationary segments associated with NNE flows and $|z/L| \leq 0.1$. Ideally, if there was no bridge deck, pressure fluctuations should be driven by the boundary layer turbulence only. The slope of the linear fit is 2.95.

According to Elliott [43], who measured the static pressure fluctuations within the first 6 m of the atmospheric boundary layer in relatively flat terrain, the rms pressure should scale as follows:

$$\sigma_{p_s} = 2.6 \cdot \rho u_*^2 \tag{6.5}$$

The slope estimated in Figure 6.6 is not significantly larger than the value 2.6 found in Elliott [43] and from other pressure measurements undertaken in wind tunnels, cf. e.g. Table 2 in Katul et al. [82] or Tsuji et al. [194] assuming $\sigma_u/u_* = 1.95$ for the present study (see Table 4.2). Although not conclusive, this result suggests that the distortion, induced by the deck, of the static pressure fluctuations, is limited for the case at hand. Note that this study refers to wind turbulence in complex terrain, high levels of turbulence intensity and $z = 60$ m. To the author's knowledge, a description of the
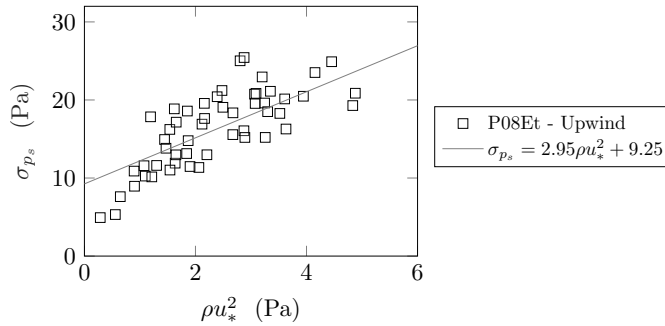
Figure 6.6: The relationship between shear stress and standard deviation of static pressure. 50 10 min-long stationary segments associated with NNE flows and $|z/L| \leq 0.1$.

atmospheric pressure fluctuations in those conditions is not yet available in the scientific literature for comparison.

6.3.1   One-point spectrum

The spectrum of the static pressure measured simultaneously on the upwind and downwind side of the bridge deck is shown in Figure 6.7. The fundamental statistics of the signals are also reported in Table 6.2. The spectrum of the static pressure, denoted S_{p_s}, is characterised by higher spectral content (by a factor of 2) up to $k \approx 0.2\,\mathrm{m}^{-1}$ on the upwind side of the girder than downwind. For larger values of the wave number, the static pressure fluctuations on the downwind side of the cross-section overtake those estimated upwind. The observed behaviour is in line with the bridge-deck flow distortion affecting the vertical turbulence component recorded on the downwind side of the girder, at 6 m height above the road level [26]. The normalized spectrum of the w component (Figure 6.5) exhibits higher energy downwind the deck for

Table 6.2: Characteristics of fluctuating static pressure 4 m above the bridge deck, recorded on 06/08/21 18:30 UTC. $\gamma_3(p_s)$ and $\gamma_4(p_s)$ denote the skewness and kurtosis of p_s, respectively.

Location/Probe	σ_{p_s} (Pa)	$\gamma_3(p_s)$	$\gamma_4(p_s)$	Power-law exponent in inertial subrange
Upwind - P08Et	24	0.28	3.19	-2.05
Downwind - P08Wt	18	-0.02	3.32	-1.62
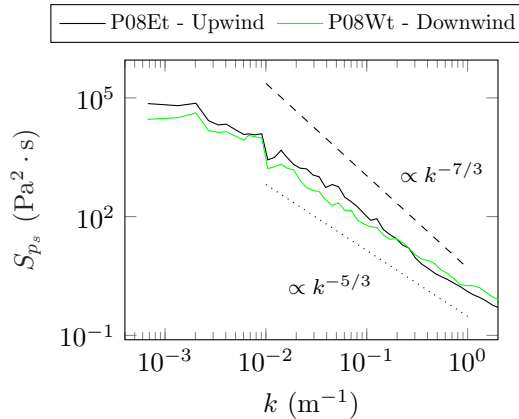
Figure 6.7: One-point spectrum of static pressure recorded at 4 m height on the upwind and downwind side of the deck, 06/08/21 18:30 UTC.

$k \geq 0.4\,\mathrm{m}^{-1}$ whereas for the static pressure this threshold moves towards lower wave numbers ($k \approx 0.2\,\mathrm{m}^{-1}$), possibly because the pressure probes have a smaller vertical separation from the deck level.

The slope of the S_{p_s} auto-spectrum in the inertial subrange is estimated in a least-square sense considering a linear power-law decay within the range $0.1\,\mathrm{m}^{-1} \leq k \leq 2\,\mathrm{m}^{-1}$. For frequency close to the stated upper bound, no attenuation is expected in the response of the pressure probe [68]. The estimates corresponding to the upwind and downwind pressure probes are given in Table 6.2. On the upwind side of the girder, S_{p_s} exhibits a decay rate $\propto k^{-2}$. No dramatic changes are observed in the estimated magnitude of the slope when analysing different records. In particular, the value -2.05 reported in Table 6.2 is slightly larger than the one estimated based on the ensemble-averaged static pressure spectrum, namely -1.81, considering 26 stationary samples with $\bar{u} \geq 6\,\mathrm{m\,s}^{-1}$ and $|z/L| \leq 0.1$.

At P08Wt, i.e. on the downwind side of the girder, the roll-off decay slope is -1.62, which is slower than for the upwind side. This may be attributed to deck-induced distortion of the turbulent flow as it travels past the body. As previously mentioned, this behaviour resembles the one associated with the attenuation of S_w on the downwind side of the girder (see Figure 6.5).

Two main sources may influence the linearity of the roll-off of S_{p_s} in the inertial subrange. Firstly, the horizontal and vertical motion of the bridge deck potentially affects the static pressure field above the deck, to a certain degree. This is supported by the fact that for records associated with low TI levels,

Table 6.3: An overview of the power-law behaviour ($\propto k^c$) of the turbulent pressure auto-spectrum measured within the ABL using probes. The table is partly based on Table 2.1 in Lyons [122]. Note that the power-laws reported were taken from the corresponding reference.

Author	Power-law exponent c	Pressure probe	Comments
Elliott [43, 42]	-1.7	Semi-directional	Flat boundary; $z \leq 6\,\text{m}$
Wilczak et al. [202]	$-2.33^{(a)}, -1.67^{(b)}$	Omni-directional	[a] $f < 0.01\,\text{Hz}$, [b] $f > 1\,\text{Hz}$
Katul et al. [82]	-1	Omni-directional	-
Albertson et al. [2]	-3/2	Omni-directional	$z = 1.5\,\text{m}$
Hoxey et al. [68]	-4/3	Omni-directional	$z \leq 10\,\text{m}$
Present study	-2.05	Omni-directional	$z = 60\,\text{m}$

the signature of vertical eigenmodes VA1 and VS2 can be detected in the static pressure auto-spectrum. Secondly, even if the bridge deck was ideally motionless, the static pressure field at 4 m height above the road level is likely influenced by the presence of the deck itself, thereby not fully representing the undisturbed atmospheric static pressure of the oncoming flow.

According to the inertial sub-range laws introduced by Kolmogorov [87] for locally isotropic turbulence, the auto-spectrum of atmospheric static pressure fluctuations should follow [8]:

$$S_{p_s}(k) \propto \varepsilon^{4/3} k^{-7/3} \tag{6.6}$$

A comparison with available results on turbulent atmospheric pressure (within the flow) dealing with the roll-off of S_{p_s} in the inertial subrange, is given in Table 6.3. The table, which benefited from Table 2.1 in Lyons [122], summarises selected field studies where a pressure probe was employed and the power-law slope of the pressure spectrum ($\propto k^c$, where c is the decay constant and k is the wave number) was reported. Note that (laboratory or field) experiments focusing on turbulent pressure fluctuations at the ground surface are not dealt with. Table 6.3 highlights a significant variation of the slope of $S_{p_s}(k)$ reported in the scientific literature on the atmospheric static pressures in ABL flows. Some potential relevant causes are outlined as follows: (a) the type of pressure probe is of primary importance, since the static pressure output may be influenced by the wind dynamic pressure [50; 155]; (b) a universal power law to scale atmospheric pressure in the inertial sub-range is generally not attained [50], which stems from the different

contributions to the pressure auto-spectrum, i.e. shear-turbulence with $k^{-11/3}$, turbulence-turbulence with $k^{-7/3}$; (c) variation in the atmospheric stability and location across the different field experiments.

6.3.2 Coherence

The velocity fluctuations measured simultaneously on the upwind (H08E) and downwind (H08Wb) side of the deck, along with the static pressure fluctuations, are studied in terms of horizontal coherence. It is worth noting that velocity measurements are undertaken 2 m higher than the static pressure measurements. The real ($\gamma_{ii}(f, \Delta X, \Delta Y)$, $ii = w, p_s$) and imaginary parts ($\rho_{ii}(f, \Delta X, \Delta Y)$, $ii = w, p_s$) of the horizontal coherence are given in Figure 6.8. The negative values of $\gamma_{ww}(f, \Delta X, \Delta Y)$ at around $k = 0.25 \, \text{m}^{-1}$ clearly reflect the phasing between the velocity fluctuations recorded at two points separated by a non-zero along-wind separation ΔX, as described in Cheynet et al. [28]; ESDU 86010 [45] for example. Invoking the hypothesis of frozen turbulence [189] to model the advection time $\Delta X / \bar{u}$, such phase difference can be expressed as:

$$\phi(f, \Delta X) = \cos\left(\frac{2\pi f \Delta X}{\bar{u}}\right) + i \sin\left(\frac{2\pi f \Delta X}{\bar{u}}\right) \tag{6.7}$$

Thus, out-of-phase velocity fluctuations are expected to occur at $k =$
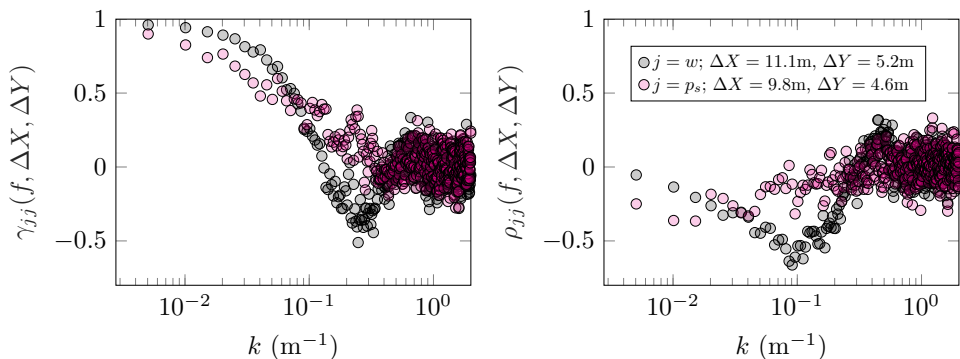

Figure 6.8: Horizontal co- (right panel) and quad-coherence (right panel) of $w - w$ and $p_s - p_s$ recorded on hangers H08E and H08W, 06/08/21 18:30 UTC.

$\pi/\Delta X$, which clearly agrees with the negative values of co- and quad-coherence of w shown in Figure 6.8.

The co-coherence of the static pressure was lower than the one of vertical turbulence component w for $k \leq 8 \cdot 10^{-2}$ m^{-1}. The vertical eigenmodes VA1 ($f =0.225$ Hz) and VS2 ($f =0.413$ Hz) were found to influence $\gamma_{p_s p_s}(f, \Delta X, \Delta Y)$, which exhibits two clear peaks at $k = 0.136$ m^{-1} and $k = 0.243$ m^{-1}. The above-mentioned eigenmode shapes are characterised by anti-nodes in the vicinity of the measuring chord considered herein. The standard deviation of the heave motion measured at H09 is $\sigma_{r_z}/D = 0.012$ for the case at hand. Thus, it appears that the pressure probes are able to capture the fluctuations of the static pressure field generated by the dynamic motion of the deck at 4 m above the road level. Note that this occurs in addition to the deck-induced distortion of the fluctuating static pressure measured on the downwind side of the bridge deck and despite the significant levels of turbulent intensity in the free stream.

The vibrations of the tubing system, induced by the girder motion, are unlikely to be responsible for the peak in the co-coherence estimates of the static pressure. Specifically, the tubing systems for both active and reference pressure experience the same level of vibrations, since they are located in the very same environment. Hence, this effect, i.e. pressure waves travelling within the tubing system, should cancel out in the differential output of the pressure transducers.

The pressure probes (P08Wt and P08Et) and the sonic anemometers (H08Wb and H08E) have a vertical separation of 1.95 m. Yet, valuable information can be attained about the pressure-velocity correlation, and its variation as the turbulent flow is advected over the girder. In particular, the distortion induced by the bridge deck is of interest for studying the fluid-structure interaction. No correction was applied to the pressure signals to account for the spatial phasing introduced in the horizontal plane between the probe and the sonic anemometer. The point-wise co- and quad-coherence are shown in Figure 6.9. Here, the term "point-wise" refers to quantities monitored at stations more or less close to each other. On the upwind side of the deck, the co-coherence was around -0.8 up to $k = 0.07$ m^{-1}, when it starts to decay. This wave number is associated with eddies the wavelengths of which are similar or larger than the deck width.

The pressure-velocity relationship indicates that, in the low reduced frequency range, the pressure fluctuations are out-of-phase compared to the
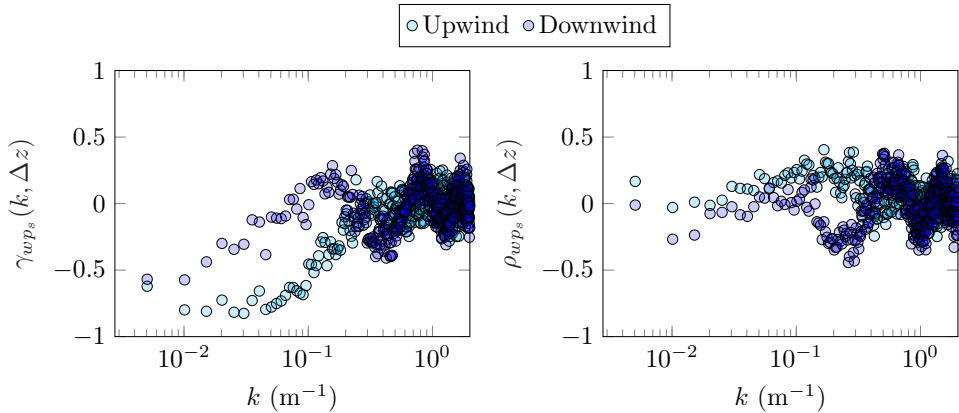
Figure 6.9: "Point-wise" co- (left panel) and quad-coherence (right panel) between w and p_s recorded on the upwind and downwind side of the deck, 06/08/21 18:30 UTC.

fluctuations of the w component, which is in agreement with Elliott [43] and McBean and Elliott [135] for the lower part of the ABL. An eddy moving downward is associated with an increase in static pressure from its time-averaged value. The corresponding correlation coefficient is $R_{wp_s} = -0.53$. The effects of the dynamic pressure on the pressure probe records are unclear but a systematic noise component may be added to the pressure signal [204].

The one-point spectrum of static pressures (see Figure 6.7) already indicates a signature of the deck-induced distortion of the pressure field above the bridge deck. This is further explored in terms of velocity-pressure relationships estimated on the downwind side of the deck, as shown in Figure 6.9. The co-coherence γ_{wp_s} decays faster on the downwind side than upwind. However, for $k \leq 5 \cdot 10^{-2}\,\mathrm{m}^{-1}$, the co-coherence is also negative. Interestingly, the co-coherence exhibits a clear peak at around $k = 0.46\,\mathrm{m}^{-1}$, which corresponds to $fD/\bar{u} = 0.198$. The latter is in overall agreement with the Strouhal number of the Lysefjord cross-section estimated in full-scale (Section 5.5). At these reduced frequencies, the S_w spectrum recorded on the downwind side of the deck exhibits higher spectral levels than upwind, as shown in Figure 6.7 for example, and discussed in Cheynet et al. [26]. Such findings corroborate with the observation that the turbulent flow recorded on the downwind side of a $B/D = 4.6$ deck, at 2.2D above road level, is affected by the blocking of the girder, signature turbulence of the deck as well as vortex shedding.

6.4 Reference control measurements

The chord-wise distribution of the pressure taps employed on the Lysefjord Bridge (see Figure 3.11) does not guarantee comprehensive monitoring of fluctuating lift and overturning moment. Indeed, lower variances are measured due to a coarse layout of the tapping points. Thus, a reference case study in full-scale is utilized to assess to which extent the sectional buffeting forces estimated on the Lysefjord Bridge are adequate for analysing: (a) the aerodynamic admittance functions; (b) the span-wise co-coherence of the wind-induced forces.

The reference field measurements are from the Gjemnessund Bridge (Norway), which was the object of extensive monitoring of wind turbulence, deck response and surface pressures undertaken by Svend Ole Hansen ApS, in collaboration with the Norwegian Public Road Administration [5; 4]. The bridge cross-section consists of a hexagonal closed-box steel girder with a width-to-depth ratio of $B/D = 5.3$ [76]. Apart from a different geometry of the railings and median divider, the main geometric differences (at the cross-sectional level) compared to the Lysefjord Bridge are the slenderness and the presence of the guide vanes at the bottom knuckle lines [5]. Nevertheless, these two details are not believed to impact significantly the results presented in this section. The dataset utilized here was courtesy of Svend Ole Hansen ApS and the Norwegian Public Road Administration.

A subset of tapping points on the Gjemnessund Bridge was chosen to simulate the layout on the Lysefjord Bridge, as shown in Figure 6.10. Such a subset is designated as "dummy pressure strip" (DPS) in the following. The objective is to compare the normalized spectra and span-wise co-coherence of the cross-sectional lift and twisting moment based on the fully instrumented
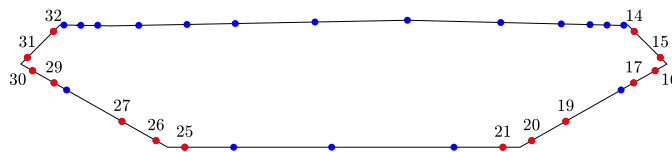
Figure 6.10: Chord-wise distribution of pressure taps on the Gjemnessund Bridge. For details see Andersen et al. [5]. The red dots represent the so-called "dummy pressure strip" (DPS), which simulates the layout utilized on the Lysefjord Bridge.

pressure strip and the pressure strip dummy. Thus, the obtained results should represent a reference in the analysis of buffeting loads derived from the surface pressures acquired on the Lysefjord Bridge.

6.4.1 Fluctuating lift and moment

The normalized power spectral densities of lift and twisting moment on the Gjemnessund Bridge are given in Figure 6.11 for a selected time-interval, during which $\bar{u} = 10.9 \, \text{m s}^{-1}$, $\beta = 7°$, $I_u = 0.14$ and $I_w = 0.11$. It can be inferred that the spectral shapes of F_z and F_θ are more or less preserved when the coarser distribution of pressure tap is employed (DPS). The corresponding attenuation in the variance can be appreciated in Figure 6.12, which displays the associated aerodynamic admittance functions $|\chi_z(f_r)|^2$ and $|\chi_\theta(f_r)|^2$ computed using Equations (2.44) and (2.45). Shown is also the Liepmann approximation to the Sears functions [117] for the sake of comparison. The admittance functions, $|\chi_z(f_r)|^2$ and $|\chi_\theta(f_r)|^2$ appear to be scaled only in magnitude with the finer distribution of pressure taps. The estimated offset is not severely frequency-dependent and, thus, it is reasonable to use a simple constant as the scaling factor. For the case at hand, the scaling constants are found to be 5 and 3 for the lift force and moment aerodynamic admittance functions, respectively.
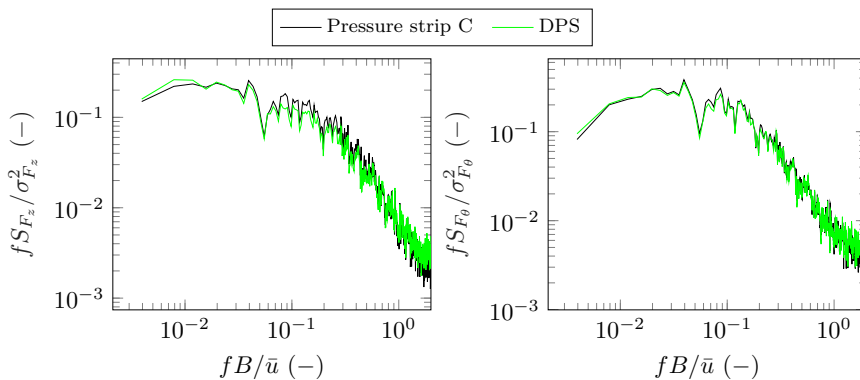
Figure 6.11: Comparison between the cross-sectional lift (left panel) and overturning moment (right panel) normalized spectra using all and a subset of pressure taps. The dataset from the Gjemnessund Bridge is from 01/10/2019, 02:00 to 03:00 UTC. For details see Andersen et al. [5].
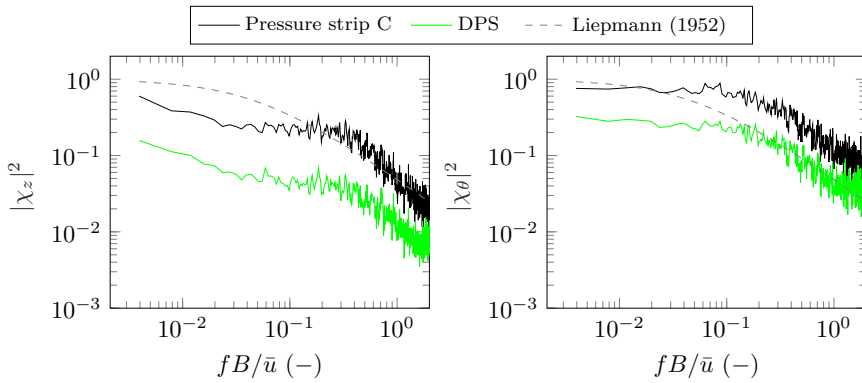
Figure 6.12: Comparison between the aerodynamic admittance functions of lift (left panel) and overturning moment (right panel). The dataset from the Gjemnessund Bridge is from 01/10/2019, 02:00 to 03:00 UTC. For details see Andersen et al. [5].
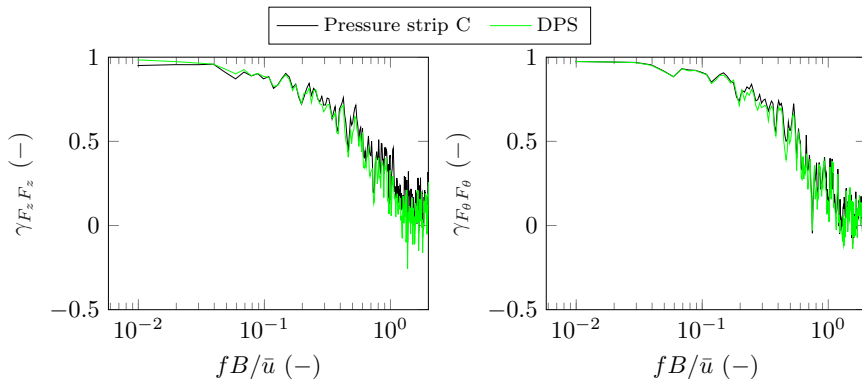
Figure 6.13: Comparison between the span-wise ($\Delta y/B = 0.60$) co-coherence of lift (left panel) and overturning moment (right panel). The dataset from the Gjemnessund Bridge is from 01/10/2019, 02:00 to 03:00 UTC. For details see Andersen et al. [5].

6.4.2   Span-wise co-coherence of lift and moment

The impact of a coarser distribution of pressure taps around the deck periphery on the co-coherence $\gamma_{F_z F_z}$ and $\gamma_{F_\theta F_\theta}$ is quantified in Figure 6.13. Note that the road surface pressures are not included in the estimate. No significant amplification or attenuation of the measured coherence can be observed. Therefore, Figure 6.13 suggests that the layout of pressure taps used on the

Lysefjord Bridge can provide a valuable output in terms of co-coherence of the lift and twisting moment. In other words, the spatial structure of the gust loading on the bridge deck can be studied without significant loss of information.

6.5 Characteristics of the fluctuating buffeting wind forces

A selected monitoring interval is chosen to investigate the fundamental features of the wind buffeting forces. The prerequisites are a relatively large mean wind speed, dry conditions to avoid distortions of different pressure signals and a limited magnitude of both yaw angle and angle of wind incidence. The chosen wind event is the same as studied in Table 6.1 in relation to the study of atmospheric pressure fluctuations. Note that the mean angle of wind incidence was $-1.9°$.

6.5.1 Surface pressure distribution

The distribution of the standard deviation of the pressure coefficient estimated at strip A is given in Figure 6.14. The corresponding values are reported in Tables 6.4 and 6.5. The largest variance is observed on the upwind inclined edges, namely below the bridge deck nose, where the pressure tap A04 exhibits $\sigma_{C_p} = 1.02$. Instead, on both the top and bottom trailing edges of the girder, the surface pressure fluctuations are lower in magnitude. For example, the variance estimated at A12 is approximately 1/3 of the one at A01. While the strong pressure fluctuations at the leading edges (A01 to A04) reflect the
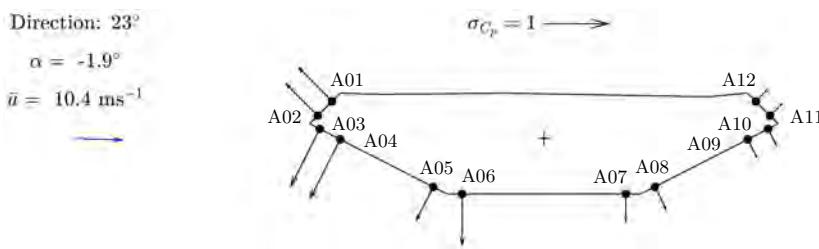
Figure 6.14: Distribution of the standard deviation of the pressure coefficients at strip A; the dataset is from 06/08/2021, from 18:30 to 19:30 UTC.

Table 6.4: Statistics of fluctuating pressure coefficients measured at strips A, B and C on 06/08/2021, from 18:30 to 19:30 UTC. $\gamma_3(C_p)$ and $\gamma_4(C_p)$ denote the skewness and kurtosis of C_p, respectively.

Pressure tap	σ_{C_p}	$\gamma_3(C_p)$	$\gamma_4(C_p)$
A01	0.74	-0.30	4.32
A02	0.69	-0.66	6.30
A03	0.99	-0.55	3.72
A04	1.02	-1.39	6.40
A05	0.56	-0.80	4.48
A06	0.78	-0.69	3.32
A07	0.42	-1.16	6.07
A08	0.39	-1.41	7.80
A09	0.30	-1.00	7.37
A10	0.29	-1.03	8.37
A11	0.26	-0.67	5.83
A12	0.25	-0.71	6.98
P08Et	0.31	0.28	3.19
P08Eb	0.55	-0.09	3.79
P08Wt	0.24	-0.02	3.33
P08Wb	0.23	-0.31	4.59

approaching turbulence, the significant variance at A05 and A06 is likely associated with separating shear layers and the formation of a separation bubble. Also, considering the negative angle of attack for the case at hand ($-1.9°$), A04 may actually be located in a separated flow region. Note, that part of the variance recorded at the leading edge is due to the relatively large turbulence intensity ($I_w = 0.20$) encountered. This, together with the length scale of turbulence relative to the characteristic sharp-edged body dimension, governs the magnitude of pressures forming in separated/reattaching flow regions [163] as well as in the stagnation region [61].

Higher-order statistics are investigated in terms of skewness ($\gamma_3(C_p)$) and kurtosis ($\gamma_4(C_p)$), which are reported in Tables 6.4 and 6.5. A departure from a Gaussian stochastic process is observed for more or less all surface pressures, with a value of skewness up to -1.41 at A08, thereby indicating the occurrence of significant negative pressure fluctuations. The time history of the fluctuating pressure coefficient recorded at A04 (below the deck nose, on the leading edge) is reported in Figure 6.15, as an example. The pressure signal is clearly non-Gaussian ($\gamma_3(C_p) = -1.39$ and $\gamma_4(C_p) = 6.40$) and exhibits

Table 6.5: Continued from Table 6.4.

Pressure tap	σ_{C_p}	$\gamma_3(C_p)$	$\gamma_4(C_p)$
B01	0.64	-0.14	4.55
B02	0.67	-0.56	5.80
B03	0.94	-0.63	4.50
B04	0.91	-1.24	6.15
B05	0.54	-1.21	7.09
B08	0.42	-1.41	7.33
B09	0.29	-1.40	13.20
B10	0.28	-1.12	9.89
B11	0.26	-0.59	5.43
B12	0.26	-0.74	6.77
C01	0.64	-0.20	5.77
C02	0.66	-0.57	5.94
C03	0.94	-0.76	4.60
C04	0.91	-1.34	6.52
C05	0.54	-1.31	7.70
C08	0.41	-1.26	6.39
C09	0.31	-0.80	5.23
C10	0.28	-0.64	4.82
C11	0.27	-0.59	5.58
C12	0.27	-0.82	7.50
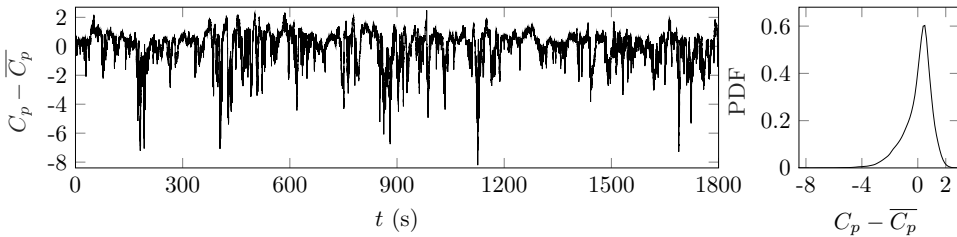
Figure 6.15: Time history of fluctuating pressure coefficient at tap A04 (leading edge) and corresponding probability density function; the dataset is from 06/08/2021, from 18:30 to 19:00 UTC.

several negative peak pressure coefficients below -5. This is quantified by the probability density function (PFD) of $C_p - \overline{C_p}$ reported in Figure 6.15. The magnitudes of skewness and kurtosis of the pressure signals are influenced by the intensity and scale of turbulence (see e.g. Mannini et al. [127]), the degree of which likely depends on the flow region. On the other hand, the velocity

fluctuations are fairly Gaussian for the vertical component, $\gamma_3(w) = 0.07$ and $\gamma_4(w) = 3.30$. Therefore, the strongly skewed probability density functions of surface pressure at the leading edge, shown in Figure 6.15, must arise from the interaction mechanism between the turbulence and the shear layer.
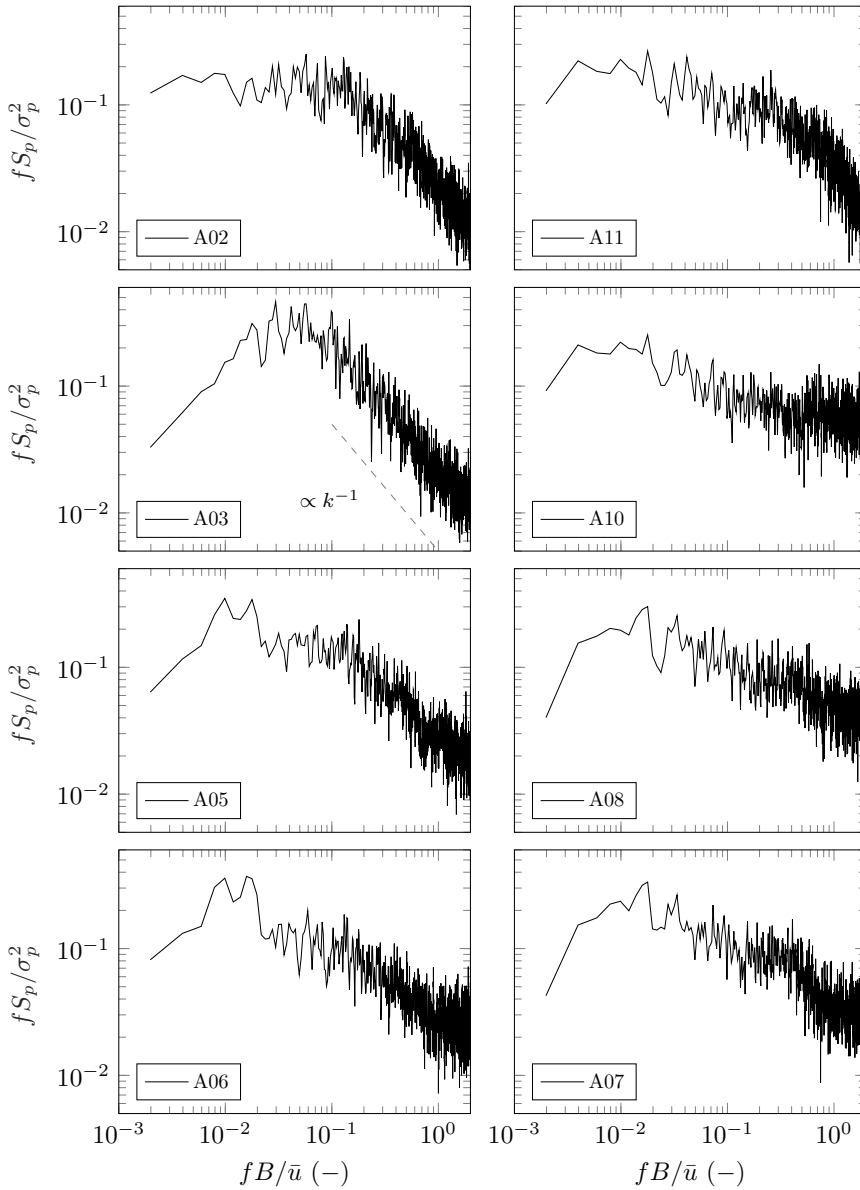
Figure 6.16: Power spectral densities of selected surface pressure signals at strip A; the dataset is from 06/08/2021, from 18:30 to 19:30 UTC.

   The normalized power spectral density estimates of selected surface pressures at chord A are given in Figure 6.16. At the leading edge of the girder, the spectral shape of surface pressure at A02 (A03) follows the spectral shape of S_u (S_w), thereby reflecting quasi-steadiness. In the inertial sub-range, the spectrum S_p at A02 and A03 decays following a power law $\propto f^{-2}$, approximately. The faster roll-off than the ABL turbulence ($S_w \propto f^{-5/3}$) is related to the velocity-pressure admittance. As the flow moves towards the upwind lower corner (tapping points A05 and A06), part of the energy is shifted towards higher reduced frequencies, as flow separation is likely to occur. Nevertheless, the influence of the low-frequency fluctuations in the approaching flow on the pressure auto-spectra can still be detected.

   Before the leeward knuckle lines, i.e. at tapping point A07, a signature of bridge deck vertical motion (eigenmodes VA1 and VS2) can be detected for $0.10 \le fB/\bar{u} \le 0.40$. This slight increase in energy almost disappears as the flow separates past the knuckle line, i.e. at tap A08 in the lower downwind inclined edge of the girder. The presence of a significant axial flow for yaw angles larger than $10°$ (see Section 5.3.1) may have a role in distorting the flow in the near wake region below the deck nose line and, thus, partly inhibit the formation of coherent vortex structures. At pressure tap A10, which is located on the downwind bottom inclined panel, a mild signature of vortex shedding can be ascertained at approximately $fB/\bar{u} = 0.90$. Figure 6.16 shows that the incoming turbulence intensity levels may overshadow vortex formation, as described in Mannini et al. [127] for a stationary 5:1 rectangular cylinder tested with $I_u = 0.14$ and $L_u^x/D = 3.9$.

6.5.2   Cross-sectional wind forces and aerodynamic admittance

In Figure 6.17, the normalized power spectral densities of the horizontal force, vertical force and moment estimated at the chord A are shown as a function of the reduced frequency $fB/\bar{u}$. For the sake of clarity, a separate panel in the same figure includes the normalized velocity spectra estimated at H08E. Lift and twisting moment exhibits a comparable frequency distribution. The frequency-multiplied moment spectrum, fS_{F_θ} peaks at around $fB/\bar{u} = 0.04$, which is close to the region where the pre-multiplied spectrum fS_w also reaches its maximum, at $fB/\bar{u} = 0.03$. Instead, the lift spectrum fS_{F_z} appears to have a slightly broader spectral peak for the case at hand. As mentioned
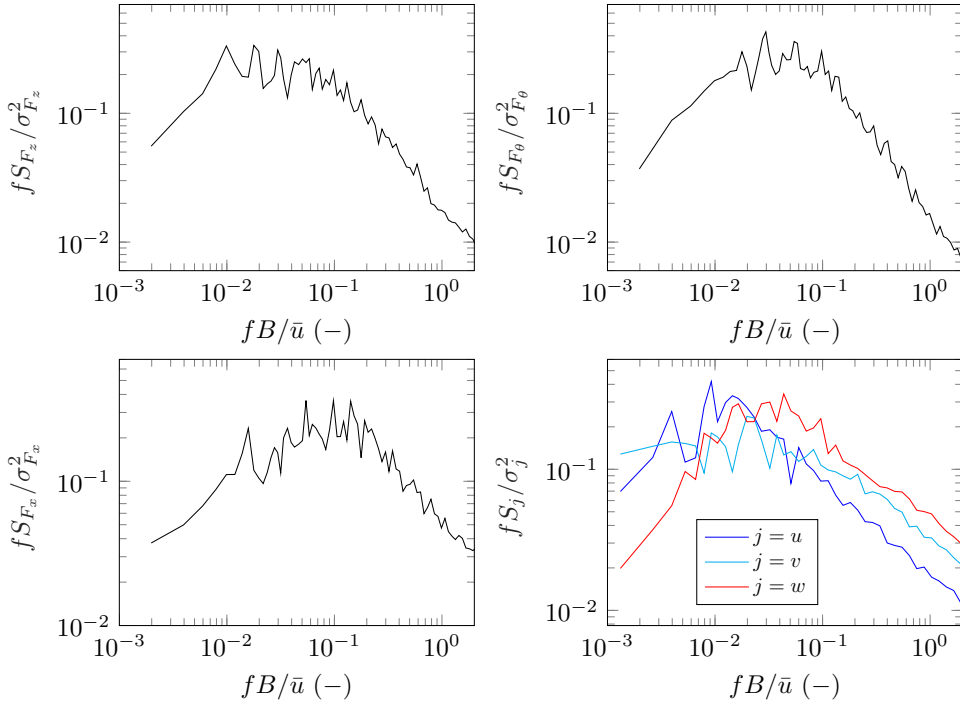
Figure 6.17: Normalized power spectral densities of vertical force (top left panel), overturning moment (top right panel), horizontal force (bottom left panel) and turbulence components at H08E (bottom right panel); the dataset is from 06/08/2021, from 18:30 to 19:30 UTC.

in Section 6.4, the adopted distribution of tapping points is better suited to monitor the twisting moment.

As for the surface-pressure fluctuations, the turbulence-driven force are not Gaussian. Specifically, $\gamma_3(F_z) = -0.79$ and $\gamma_4(F_z) = 3.81$ for the lift whereas $\gamma_3(F_\theta) = -0.39$ and $\gamma_4(F_\theta) = 3.89$ for the moment. Similar values of skewness and kurtosis of the lift force were generally observed also for much lower turbulent intensity levels, e.g. $I_w \approx 0.08$.

An exercise is made attempting to link together the incoming turbulence, the distortion of eddies observed 2 m upstream the bridge deck (see Section 4.4) and the cross-sectional buffeting forces. The pair S_w and S_{F_θ} is chosen. The left panel of Figure 6.18 demonstrates the deck-induced distortion of the vertical turbulence component w approaching the bridge cross-section by comparing the velocity spectra normalized by the variance estimated at the reference sonic. The variance σ_w^2 estimated at sonic D08E, at the deck
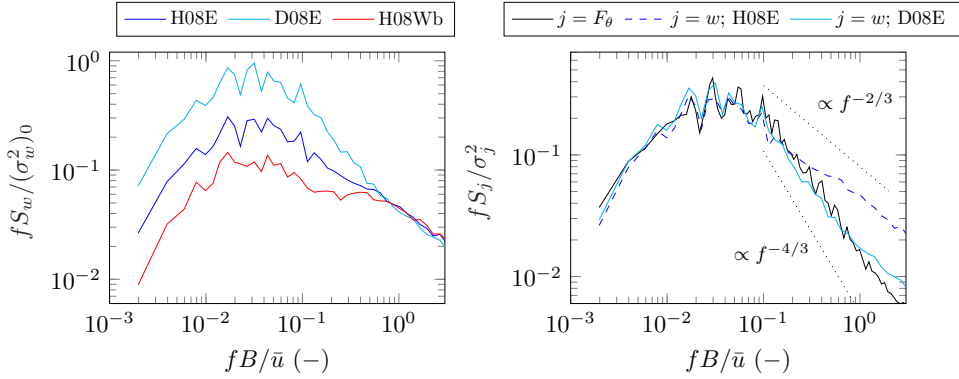
Figure 6.18: Spectrum of the w component recorded at H08E, D08E and H08Wb normalized by the variance at H08E (left panel); normalized spectrum of the overturning moment compared to the S_w normalized based on the variance at each measurement location (right panel); the dataset is from 06/08/2021, from 18:30 to 19:30 UTC. $\mathcal{L}_w/B = 4$ and $I_w = 0.20$.

nose, is 1.56 times the one estimated at sonic H08E, i.e. 6 m above the road level, on the upwind side. The increase in variance is significant for reduced frequencies $fB/\bar{u} < 0.5$. Note that: (a) after the spectral peak, S_w decays much more rapidly upstream of the deck nose in the range $0.1 \leq fB/\bar{u} \leq 0.5$; (b) the $\propto f^{-5/3}$ roll-off in the inertial subrange starts at a much higher reduced frequency at D08E. These are some of the characteristics of the turbulence measured at D08E. The distortion of turbulence observed 2 m ahead of the deck nose is discussed more thoroughly in Chapter 4.

The same exercise is repeated, but now by normalizing the vertical velocity spectra at H08E and D08E, using the local variances at each measurement location and comparing them to the normalized moment spectrum. The results can be seen in the right panel of Figure 6.18. For $fB/\bar{u} \leq 0.7$ the agreement between the spectral shape of fS_{F_θ} and fS_w recorded upstream the deck nose is excellent. Interestingly, the w and F_θ spectra appear to decay following more or less the same power law, which is not too dissimilar from $\propto f^{-7/3}$ for the case at hand. Hence, there is a frequency range where the distorted turbulence approaching the deck decays more rapidly than the nominally undisturbed flow.

Overall, the right panel of Figure 6.18 provides a link between the upstream flow distortion generated by the deck and the generation of an unsteady twisting moment due to wind turbulence. Whether the observed flow distor-
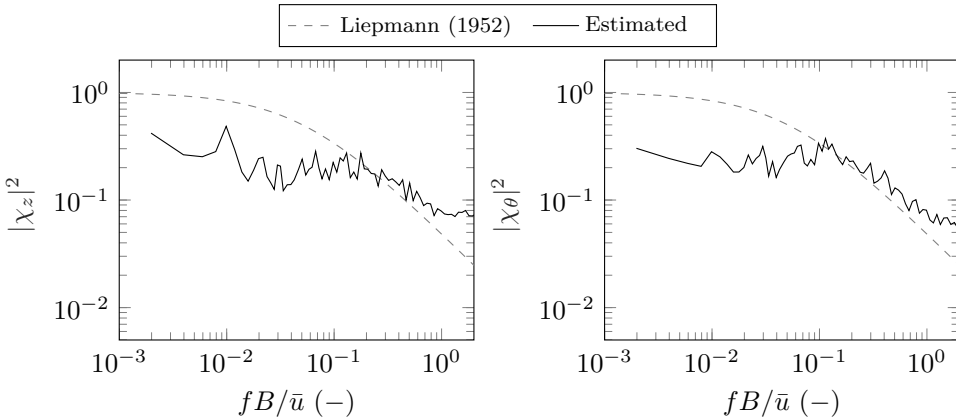
Figure 6.19: Aerodynamic admittance function of vertical force (left panel) and overturning moment (right panel); the dataset is from 06/08/2021, from 18:30 to 19:30 UTC. $\mathcal{L}_w/B = 4$ and $I_w = 0.20$. The correction factors from Section 6.4 were here used.

tion of w can be, at least partly, associated with a 3D effect, namely a larger span-wise coherence of the lift and moment, is still an overly ambitious question for the author at this stage of the research. Nevertheless, the documented distortion of the vertical turbulence component ahead of the girder (see e.g. Figure 4.7) is understood to be one of the features of the three-dimensional interaction between the incident turbulence and the uniform bridge deck obstacle. The attenuation of S_w on the downwind side of the deck (e.g. left panel of Figure 6.18 or Cheynet et al. [26]), together with the augmentation of S_w upstream of the stagnation region (Figure 4.7) are likely associated with the so-called "pillow" effect or "gust buster" effect. These terms were used by Davenport and Larose [103], respectively, to describe the generation of the gust loading on a bridge deck and the concurrent distortion of the turbulence, as it is advected past the body.

The estimated cross-sectional aerodynamic admittance functions of lift and twisting moment are shown in Figure 6.19. For comparison, the Liepmannâ-Źs approximation [117] to the Sears function [173] for thin airfoils is included in the same figure. The functions are determined in a linearised framework as outlined in Section 2.4, i.e. based on the spectra of the cross-sectional aerodynamic forces (see Figure 6.17), the static force coefficients and the velocity spectra. The mean angle of wind incidence is $-1.9°$ and, thus, the values of C_D, C_L and C_M are interpolated based on the static force

coefficients given in Appendix B.2. Lift and moment slopes are taken as $C'_L = 4.696$ and $C'_M = 1.293$, respectively. The computed functions are eventually scaled using the coefficients estimated in Section 6.4, namely 5 for the lift and 3 for the twisting moment. This allows for a more realistic representation of the magnitude of the aerodynamic admittance functions. Note that the shape of the function is not altered by such a scaling.

The admittance functions, $|\chi_z|^2$ and $|\chi_\theta|^2$ exhibit a fairly constant magnitude up to $fB/\bar{u} \approx 0.1$, from which point both functions start to decay. The roll-off for reduced frequencies $fB/\bar{u} \geq 0.1$ appears to be slightly slower than $\propto f^{-1}$ predicted by the Liepmannâ ĂŹs approximation [117] to the Sears function. Within this reduced frequencies range, $|\chi_z|^2$ and $|\chi_\theta|^2$ are above the prediction computed for thin airfoils, i.e. the Sears function. This should not be surprising given the aspect ratio of the cross-section, which is clearly not associated with the aerodynamics of a body having fully attached flow, for which the linear theory of Sears [173] was derived. Deck-generated turbulence may also contribute to a certain extent within the higher range of reduced frequencies [98], especially for the aspect ratio of the cross-section studied herein. In fact, for a $B/D = 4.7$ cross-section, the relative contribution of body-generated turbulence and trailing edge surface pressures to the lift and moment is expected to be more significant than the one characterising a more streamlined cross-section. The value of $fB/\bar{u} \approx 0.1$ as "cut-off" frequency agrees well with the results by G. Larose [101; 98], namely the case of box girder bridge deck with $B/D = 5$ tested for $\mathscr{L}_w/B = 1.5$ and $I_w = 0.07$.

The cross-sectional aerodynamic admittance functions (AAF) are generally estimated in wind tunnels on a motionless section model to treat the wind buffeting forces separately from the motion-induced wind forces [100; 14; 101]. In a full-scale experiment, the motionless state cannot be attained and, thus, the heave and twisting motion of the girder may impact the estimated cross-sectional loads to a certain degree and, consequently, the estimate of the aerodynamic admittance function [208]. For $|\chi_z|^2$ for example, a reduced frequency of $fB/\bar{u} = 0.5$ corresponds to $f = 0.4\,\mathrm{Hz}$ when $\bar{u} = 10\,\mathrm{m\,s}^{-1}$. This frequency is in the range of VS2 ($f = 0.413\,\mathrm{Hz}$). Nevertheless, this argument should also take into account the concurrent effect of atmospheric turbulence, namely its intensity and length scale. Haan Jr and Kareem [55] investigated the turbulence effects on a vibrating $B/D = 6.7$ rectangular cylinder and highlighted a slight increase in the rms values and broad-banded wind buffeting loads. The increase in spectral levels was gener-

ally found for $fD/\bar{u} > 0.1$. Interestingly, an increase of only 2-3% in the rms values was found when I_w was increased to 10%, for the larger turbulence length scale tested. Thus, such experimental evidence supports the fact that the cross-sectional admittance functions shown in Figure 6.19 should not be significantly compromised by the motion-dependent contribution of the fluctuating wind forces.

Three further comments are noteworthy for the interpretation of the results shown in Figure 6.19:

(a) The atmospheric turbulence affects the buffeting wind loads in a three-dimensional way, that is the aerodynamic admittance and the span-wise coherence of these loads [101]. For a given cross-section, the unsteady gust loading at a sectional level strongly depends on the length scale of turbulence [101], e.g. $\mathscr{L}_w/B$, as well as the turbulence intensity [165]. An increase of the latter for grid-generated turbulence is usually associated with a decrease in the magnitude of the aerodynamic admittance [165; 100], an effect that is more significant for bluffer rectangular cylinders [165].

(b) The yaw angle is $\beta = 23°$ for the case studied. It can be speculated that a non-zero yaw angle may favour an increased span-wise coherence of forces, due to the augmented cross-flow between neighbouring chords, together with a decrease in aerodynamic admittance relative to the $\beta = 0°$ case. This interpretation is primarily inspired by the seminal work of Larose [101, 103]; Larose et al. [99] about gust loading on streamlined bridge decks for normal incidence of the flow.

(c) The aerodynamic admittance functions are computed based on a linearised framework for the buffeting load, see Equations (2.44) and (2.45). Specifically, cross-sectional buffeting forces are assumed linearly dependent on the incident velocity fluctuations, which holds for small oscillations of the relative angle of attack. A departure from the linearity assumption can be expected for high turbulence intensities like in the present example, where $I_w = 0.20$, which could be interpreted as an average dynamic angle of attack of $11.3°$. This value goes beyond the range of angles utilized to define C_L' and C_M'. Smaller average lift and moment derivatives with respect to the angle of attack would determine an increase in the magnitude of $|\chi_z|^2$ and $|\chi_\theta|^2$ shown in Figure 6.19.

Also, for $I_w = 0.20$, the corresponding relative angle of attack would occasionally be in the stalling region (see Figure B.2).

6.5.3 Span-wise co-coherence and cross-correlation of the cross-sectional wind forces

The co-coherence of the vertical force (F_z) and twisting moment (F_θ) is compared to the co-coherence of the vertical turbulence component w in Figure 6.20 as a function of $k \cdot dy$, where k is the wave number (Equation (2.16)) and dy is the span-wise separation. The co-coherence is shown for each considered dy separately. For the turbulence component w, the fitted co-coherence model (Equation (2.24)) is given in Figure 6.20 for the sake of clarity. The corresponding coefficients are estimated based on a single lateral separation using the pair H08E and H10E. The values are $c_{y1}^w = 4.9$ and $c_{y2}^w = 0.001$. Hence the range dy/B covered is different for wind velocities and forces.

Cross-sectional lift and twisting moment exhibit higher values of co-coherence across the entire band of the reduced frequencies, for the range of separation dy/B available. The higher correlation of the buffeting wind forces translates into values of $c_{y1}^{F_L} = 3.0$ and $c_{y1}^{F_M} = 3.3$ for lift and moment, respectively. The coefficients $c_{y2}^{F_L}$ and $c_{y2}^{F_M}$ are too small to be numerically significant for the case at hand. Note that due to the slopes of $\gamma_{F_L F_L}$ and $\gamma_{F_M F_M}$ for $k \cdot dy < 1$, the co-coherence model adopted for the wind turbulence (Equation (2.24)) fails to capture the observed behaviour of the wind loads. Identifying a suitable co-coherence model to describe the force correlation and their dependence on dy/B is out of the scope of the present work.

The relationship between the span-wise coherence of velocity fluctuations and unsteady gust loading is at the heart of the estimation of the buffeting response of line-like structures, dating back to A.G. Davenport in 1962 [34]. Figure 6.20 provides an original full-scale perspective on the potential limitations of the strip assumption for unsteady lift and moment, for a $B/D = 4.6$ bridge deck in the atmospheric turbulence. This observation is in overall agreement with the state-of-the-art knowledge of the generation of turbulence-driven loads on bridge decks. Different wind tunnel experiments have demonstrated that the unsteady lift and moment exhibit a span-wise correlation higher than the oncoming velocity fluctuations, for streamlined closed-box girders [100; 101; 78]. Other studies dealt with leading edge surface pressures on rectangular cylinders [166; 83]. The governing parameters
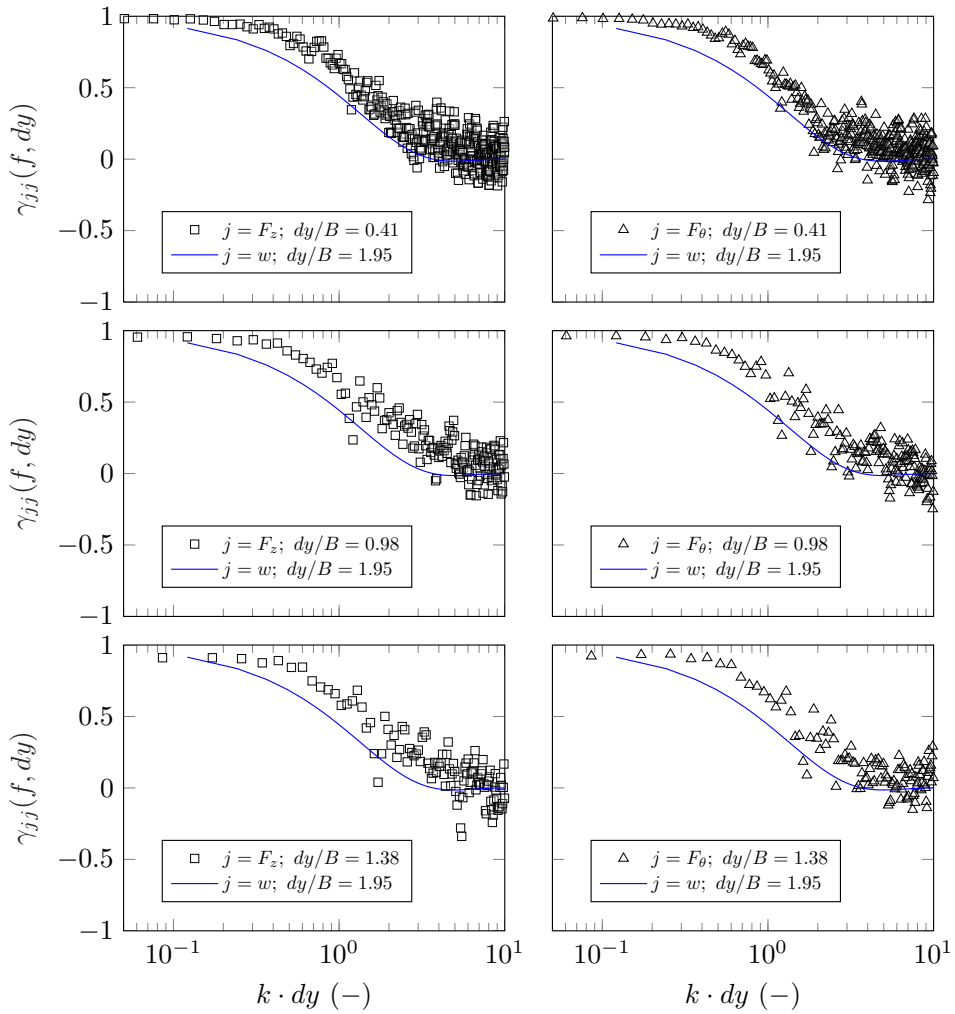
Figure 6.20: The span-wise co-coherence of vertical force (left panels) and overturning moment (right panels) compared to the co-coherence of the vertical velocity component w; the dataset is from 06/08/2021, from 18:30 to 19:30 UTC. $\mathscr{L}_w/B = 4$, $I_w = 0.20$ and $\beta = 25°$.

are [101]: (a) the ratio between characteristic length scale of the approaching turbulence over the deck width; (b) the deck width itself for a given geometry; (c) the geometry of the cross-section and its aspect ratio. The wind tunnel findings have also been supported by analytical calculations [98; 114; 115]. Full-scale evidence of higher correlation of forces [143; 5] or leading surface pressures [137], albeit rare, is also available. These are extremely valuable
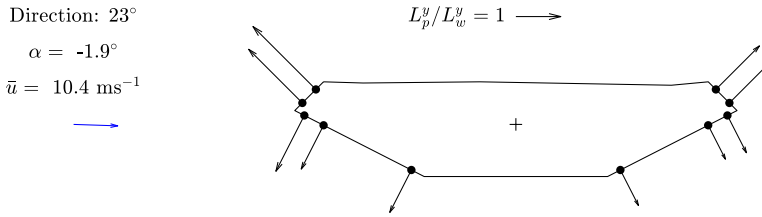
Figure 6.21: The ratio between the span-wise length scale of surface pressure over the span-wise length scale of w; the dataset is from 06/08/2021, from 18:30 to 19:30 UTC. $\mathscr{L}_w/B = 4$ and $I_w = 0.20$.

since full-scale measurements inherently deal with the natural relationship between the scale of atmospheric turbulence on-site and the bridge deck width. In addition, no issues stemming from potential Re number effects are of concern.

The span-wise correlation length associated with surface pressures (L_p^y) is compared to the correlation length of vertical velocity fluctuations (L_w^y) in Figure 6.21. Here, the quantity L_p^y/L_w^y is computed following Larose [101]:

$$L_p^y/L_w^y = \frac{\int_0^{+\infty} R_{pp}(\Delta y)dy}{\int_0^{+\infty} R_{ww}(\Delta y)dy} \qquad (6.8)$$

where $R_{pp}(\Delta y)$ and $R_{ww}(\Delta y)$ are the cross-correlation coefficients at given span-wise separations of the surface pressures and vertical velocity fluctuations, respectively. To approximate $R_{pp}(\Delta y)$ and $R_{ww}(\Delta y)$, an exponential decay function is employed.

The largest increase in span-wise length scale is found on the top leading edge of the cross-section, namely $L_p^y/L_w^y = 1.98$ at pressure tap A01. Below the deck nose, the correlation length gradually decreases moving towards the trailing edge of the cross-section. The minimum is reached at the tapping point A09, where $L_p^y/L_w^y = 0.85$. Eventually, an increase of correlation occurs for the surface pressures on the leeward top inclined panel.

Similar calculations in terms of correlation lengths are performed for the lift and twisting moment. Figure 6.22 reports the computed value of $L_{F_z}^y/L_w^y$ and $L_{F_\theta}^y/L_w^y$ as a function of $\mathscr{L}_w/B$, which was 4 for the case at hand. Additional correlation widths relevant for single closed-box girders tested in wind tunnels were included to provide a more comprehensive overview of the correlation distribution across different values of $\mathscr{L}_w/B$. Following Larose
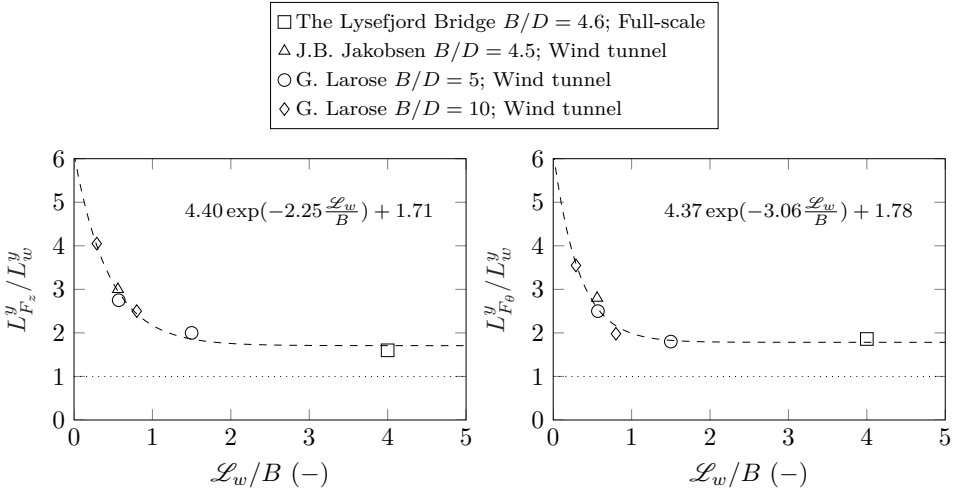
Figure 6.22: The ratio between the span-wise length scale of lift (left panel) and twisting moment (right panel) over the span-wise length scale of w; the full-scale data point is from 06/08/2021, from 18:30 to 19:30 UTC. ($\triangle$) Bogunovic Jakobsen [14]; ($\circ$) and ($\diamond$) Larose [101].

[101, 103], a simple exponential expression, which is fitted to the data points reported in Figure 6.22, describes adequately the correlation widths of lift and moment. As $\mathscr{L}_w/B$ increases, the correlation lengths of the buffeting forces should approach the correlation length of the velocity fluctuations, i.e. the strip assumption should be applicable. For the case at hand with $\mathscr{L}_w/B = 4$ and $I_w = 0.20$, $L_{F_z}^y/L_w^y = 1.60$ and $L_{F_\theta}^y/L_w^y = 1.86$.

6.6 Characteristics of vortex shedding

The section aims at complementing the discussion on vortex shedding outlined in Chapter 5, which is based on velocity measurements in the near wake of the deck. In particular, the emphasis is on: (a) the Strouhal number St; (b) the span-wise coherence of trailing edge surface pressures; (c) the significance of turbulence intensity I_w in the approaching wind flow and (d) the influence of the yaw angle β on the span-wise correlation of trailing edge surface pressures.

Throughout the section, the vortex shedding process is investigated by utilizing a series of selected records, the turbulence characteristics of which

Table 6.6: Overview of the wind characteristics of selected time series used to study the vortex shedding.

Date	14/06/2021	06/08/2021	27/08/2021	11/09/2021
Hour (UTC)	08:30 to 09:30	18:30 to 19:30	10:40 to 11:10	12:00 to 12:50
Sensor	H08Wb	H08E	H08E	H08Wb
Sector	SSW	NNE	NNE	SSW
β (°)	2	25	13	27
α (°)	2	-1.9	1	4
$\bar{u}$ (ms^{-1})	8.2	10.4	7.1	7
z/L	0.17	-0.01	1.21	0.38
I_u	0.12	0.28	0.09	0.10
I_v	0.10	0.25	0.09	0.10
I_w	0.07	0.20	0.07	0.07

are summarised in Table 6.6. Flows characterised by low levels of turbulence intensity are prioritized. All the chosen samples are associated with a stably stratified flow, except for the one recorded on 06/08/2021, which is addressed as a high TI case. It is not fully clarified if stable conditions of the atmosphere somehow modify the interaction between free-stream turbulence and the free shear layers, thereby influencing the vortex shedding process for the case at hand. On the one hand, fS_w typically peaks at higher reduced frequencies when $z/L > 0.1$ [79], suggesting an increased interaction between eddies of a suitable size and the free shear layers. On the other hand, for a stably stratified flow, turbulence mixing is partly inhibited compared to the case of $|z/L| \leq 0.1$. Anyway, the author did not find a significant variation of the estimated St number for increasing z/L.

6.6.1   A case study for low turbulence intensity

On 14/06/2021, from 08:30 to 09:30 UTC (see Table 6.6), the wind flow was blowing from SSW, with $\beta = 1°$, which is quite exceptional considering the wind conditions generally encountered on-site. Fortuitously, the flow was stably stratified and the turbulence intensities were fairly low, e.g. $I_w = 0.07$. These unique flow conditions provide an opportunity to analyse the vortex shedding without the expected suppression due to high TI levels, which are typical of complex terrain environments.
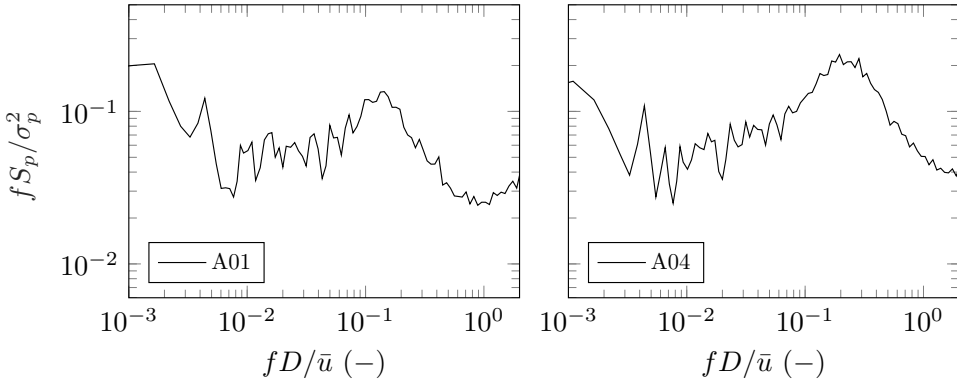
Figure 6.23: Normalized power spectral densities of surface pressures at the trailing edge, namely at points A01 (left panel) and A04 (right panel); dataset from 14/06/2021, from 08:30 to 09:30 UTC.

The normalized spectra of surface pressures at the trailing edge are given in Figure 6.23 as a function of the reduced frequency $fD/\bar{u}$. The corresponding standard deviation are $\sigma_{C_p} = 0.12$ and $\sigma_{C_p} = 0.15$ for A01 and A04, respectively. A signature of the background turbulence can be ascertained for $fD/\bar{u} < 0.01$. At higher reduced frequencies, both pressure spectra exhibit a spectral peak which represents vortex formation in the near-wake region of the deck. Interestingly, the spectral peaks appear detuned. On the top inclined edge (A01), the pressure spectrum reaches a local maximum at $fD/\bar{u} = 0.15$. Instead, below the deck nose (A04), the spectral peak is located at $fD/\bar{u} = 0.21$. Such difference could be ascribed to the asymmetry of the cross-section. Railings, including their partial blocking effects, may also contribute to a certain extent. Note that a similar behaviour was observed when examining the near wake velocity measurements undertaken in the wind tunnel (see Section 5.4), for smooth flow and $\beta = 0°$. Specifically, S_w exhibits a discernable "double peak" across different innermost points of the near wake (see Figure 5.22 for the details). At $B/2$ from the trailing edge, the (partly-detuned) vortex shedding, and subsequent entrainment, is still at an "early" stage. As a result, detection of its signature is still possible by inspecting S_w estimated in model scale. In turbulent flow, this behaviour can not be uncovered, partly because turbulence is known to increase the mixing and entrainment of the shear layers [96]. Given the asymmetry in the cross-section, it is likely that the free shear layer above the deck nose has different characteristics than the one forming downstream of the bottom

Figure 6.24: Co- (left panel) and quad-(right panel) coherence between surface pressures acquired on the trailing edge, i.e. tapping points A01 and A04; dataset from 14/06/2021, from 08:30 to 09:30 UTC.

knuckle lines. Thus, owing to this asymmetry, vortices can be expected to shed with a slightly different frequency.

The co- and quad-coherence between the two pressure signals is shown in Figure 6.24. The co-coherence peaks at around $fD/\bar{u} = 0.18$ with a magnitude of -0.4. Such a reduced frequency defines the *St* number for the case at hand. The negative values of co-coherence reflect the alternating shedding of vortices having opposite signs of vorticity. Noteworthy observations are: (a) the magnitude of the co-coherence at the shedding frequency is not negligible due to the favourable flow conditions, i.e. low TI and flow normal to the deck axis; (b) the negatively correlated components of the pressure signals are fairly broad-banded around the shedding frequency.

The span-wise correlation of the trailing edge surface pressures is studied in terms of co- and quad-coherence in Figure 6.25, for three different lateral separations. Tapping points 01 (top inclined panel) and 04 (bottom inclined panel, below the deck nose) are chosen. For $\Delta y/B = 0.41$ and $\Delta y/B = 0.98$, pressures at points 01 appear to be better correlated when $fD/\bar{u} < 0.1$. A signature of the vortex formation can be identified based on A01, in the range $0.15 \leq fD/\bar{u} \leq 0.20$, for all the span-wise separations considered. When $\Delta y/B = 0.41$, the fluctuations of surface pressures are in-phase around the *St* number due to the relatively modest separation of the pressure strips. As $\Delta y/B$ increases, the co-coherence exhibits negative values (around -0.4), thereby indicating out-of-phase fluctuations.

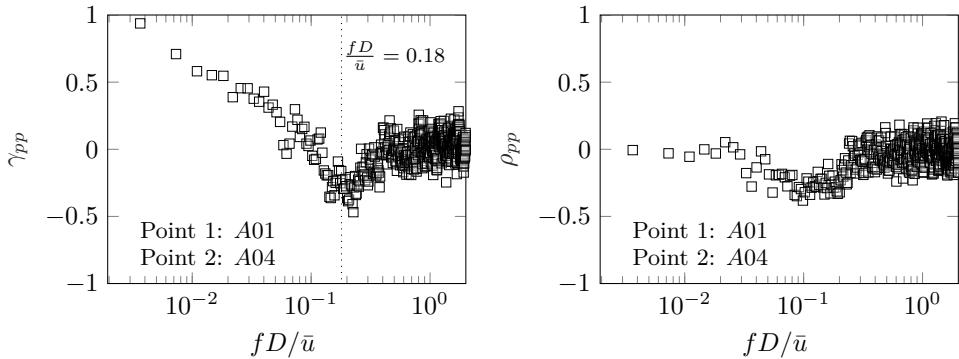Interestingly, the trailing edge surface pressures below the deck nose do
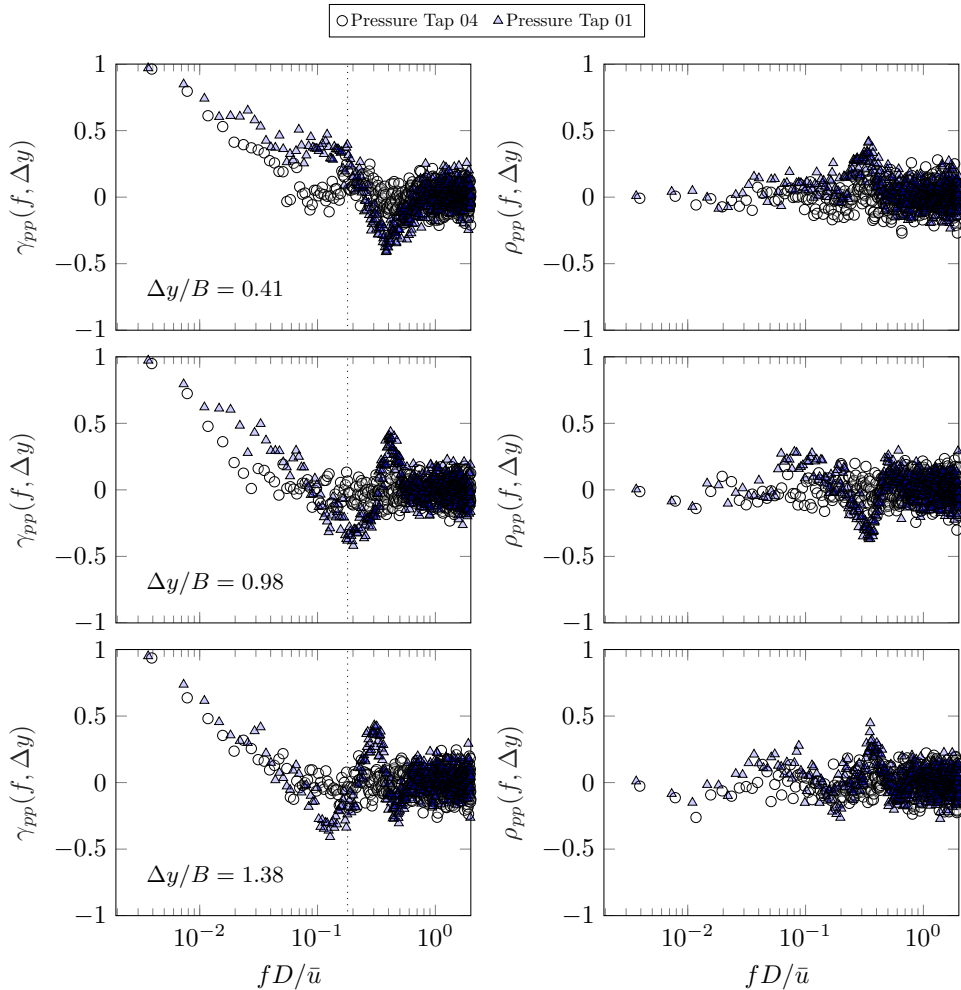
Figure 6.25: Span-wise co- (left panel) and quad-(right panel) coherence between surface pressures acquired on the trailing edge; dataset from 14/06/2021, from 08:30 to 09:30 UTC.

not exhibit clear evidence of a coherent, span-wise, vortex shedding process, except for the shortest separation $\Delta y/B = 0.41$, for which the co-coherence shows a slight increase in magnitude around $fD/\bar{u} = 0.20$ (Figure 6.25). The origin/cause of such a discrepancy is still unclear. Note that at tapping points A01 and A04, the surface pressure spectra (see fig. 6.23 for example) generally indicate the periodic formation of vortex structures.

At this stage of the discussion, the reader should naturally raise the following question: What is the estimated *St* number? And how does it compare

to the one estimated based on the near wake turbulence measurements? For the case at hand, the vertical velocity spectrum $f S_w$ predicts $St = 0.17$, which falls within the range estimated in Table 5.2. This value is bounded by the reduced frequencies at which the trailing pressure spectra have a peak, i.e. at $f D / \bar{u} = 0.15$ and $f D / \bar{u} = 0.21$ for A01 and A04, respectively (see Figure 6.23). This is in agreement with the corresponding co-coherence (see Figure 6.24), which was characterised by a fairly broad-banded peak between $f D / \bar{u} = 0.15$ and $f D / \bar{u} = 0.23$.

The lack of a significant narrow-banded correlation between the trailing edge surface pressures, both span-wise and at the same chord, may partly explain why the vortex-induced contribution to the (modal) lift is generally limited and, consequently, vortex-induced vibrations do not build up.

6.6.2   The significance of turbulence intensity levels

The wind turbulence affects the flow past a body. In particular, the characteristics of the vortex shedding process may vary at the cross-sectional level and in terms of span-wise correlation.

For example, Figure 6.26 illustrates the dramatic effects of the turbulence intensity on the trailing edge surface pressure based on two intervals during which a flow from NNE is blowing. The turbulence intensities are $I_w = 0.07$ and $I_w = 0.20$ for the low and high TI cases, respectively. An overview of the corresponding wind characteristics is given in Table 6.6. A significant
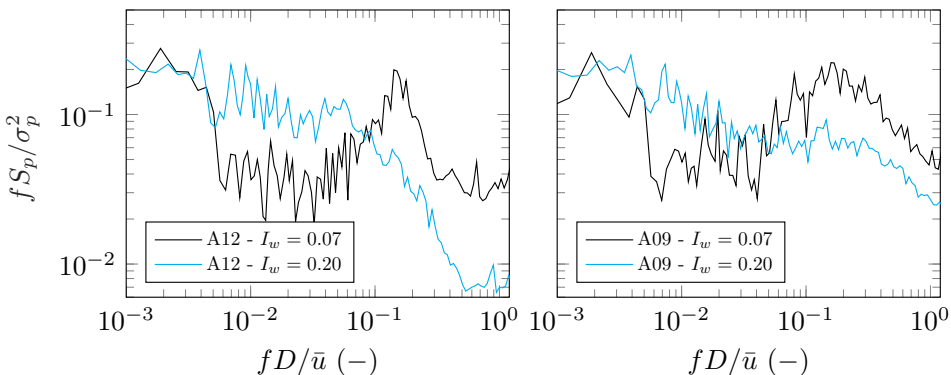
Figure 6.26: The influence of turbulence intensity on the normalized spectrum of the trailing edge surface pressures; dataset from 06/08/2021 and 27/08/2021, see Table 6.6.
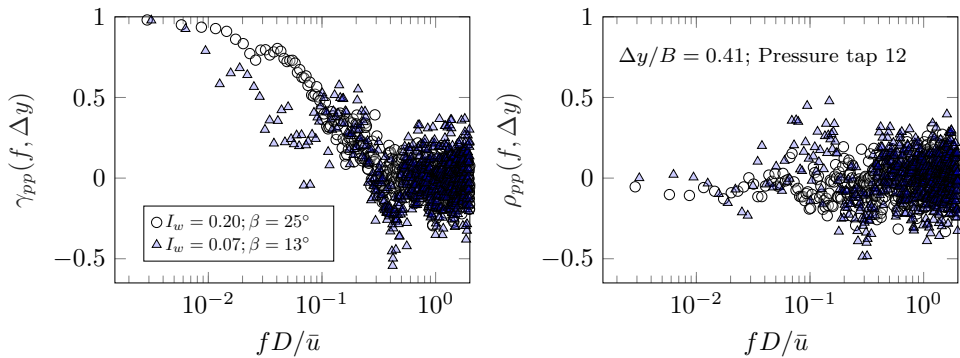
Figure 6.27: The influence of turbulence intensity on the span-wise coherence of the trailing edge surface pressures at the tapping point 12; dataset from 06/08/2021 and 27/08/2021, see Table 6.6.

turbulence intensity ($I_w = 0.20$) tends to suppress and/or overshadow the formation of coherent vortex structures. This effect appears to be more evident above the deck nose for the case at hand. In fact, at pressure tap 12, no increase in the spectral level around the Strouhal number cab be observed.

The impact of turbulence intensity levels on the span-wise correlation is quantified in terms of coherence in Figure 6.27 for the smaller lateral separation. It can be inferred that no significant increase in correlation can be detected in the range $0.15 \leq fD/\bar{u} \leq 0.20$ when $I_w = 0.20$, even if the separation along the bridge axis is only $5.04\,\text{m}$, e.g. $1.87 \cdot D$. Conversely, for $I_w = 0.07$, the co-coherence assumes values around 0.5 within $0.15 \leq fD/\bar{u} \leq 0.20$, which corresponds to the range of the non-dimensional shedding frequency for the case at hand. Note that the lateral coherence of the turbulence components u and w depends in general on the atmospheric stability, see e.g. Ropelewski et al. [161]. The potential impact of the thermal stratification of the atmosphere on the coherence of surface pressure fluctuations is still unclear.

6.6.3   Influence of the yaw angle

Based on the records analysed (Table 6.6), the yaw angle does not appear to distort significantly the spectral shape of the trailing edge surface pressures. Specifically, the width and prominence of the spectral peak at $fD/\bar{u} = St$ do not change drastically with the studied yaw angle. On the other hand,
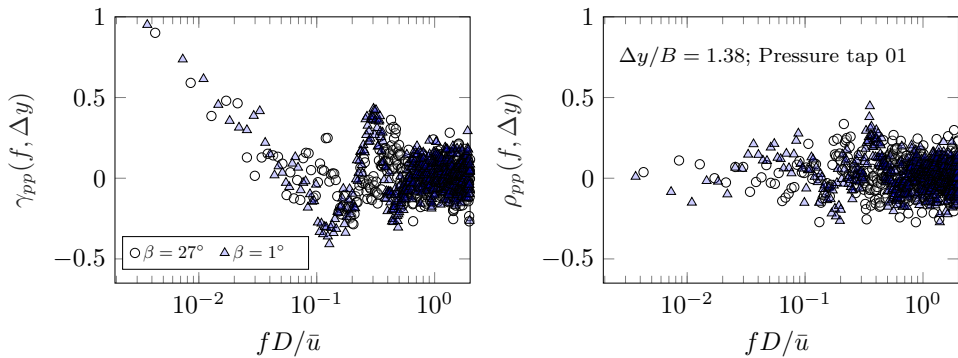
Figure 6.28: The influence of the yaw angle on the span-wise coherence of the trailing edge surface pressures at the tapping point 12, for $\Delta y/B = 1.38$; dataset from 14/06/2021 and 11/09/2021, see Table 6.6.

a non-zero yaw angle seems to affect the span-wise coherence of surface pressure on the upper inclined panel of the girder (A01), on the downwind side. Figure 6.28 reports the co-coherence and quad-coherence estimates for a span-wise separation of $\Delta y/B = 1.38$, considering two different yaw angles, i.e. $\beta = 1°$ and $\beta = 27°$. As expected, the co-coherence decreases, in absolute value, when the yaw angle increases for $0.15 \leq fD/\bar{u} \leq 0.20$. It can be speculated that the axial flow on the leeward side of the bridge deck, which is documented to develop as $\beta \geq 10°$ in full-scale (Section 5.3.1), may interact with the vortex shedding formation and its correlation along the bridge axis. Further research on this topic is deemed necessary for a more comprehensive understanding.

6.7   Summary

The chapter described specific aspects of the bridge deck aerodynamics using surface pressures monitored on the Lysefjord Bridge (Norway). The emphasis was on the gust loading and the vortex shedding process in the natural wind.

Assessing the validity of the strip assumption for the case at hand was central to this chapter, and perhaps, to the thesis. It was shown that the monitored lift and twisting moment were better correlated span-wise than the incident vertical velocity fluctuations. For $\mathscr{L}_w/B = 4$ and $I_w = 0.20$, the span-wise correlation lengths of the lift and moment were $1.60 L_w^y$ and $1.86 L_w^y$, respectively. This result contributes to an improved understanding of

the spatial structure of the gust loading on a bridge deck, corroborating the experimental wind tunnel investigations. In particular, its significance should be framed in the full-scale context of the measurements undertaken, see e.g. Figure 6.22.

An accurate estimation of the aerodynamic admittance function was challenging due to the limited number of pressure taps along the monitored chords. Note that the uncertainties mostly dealt with the magnitude of $|\chi_z(f_r)|^2$ and $|\chi_\theta(f_r)|^2$ rather than their shape. The magnitude of $|\chi_z(f_r)|^2$ is affected to a certain degree by the lack of monitored pressures on the top part of the deck. A certain dependence of the AAF on the level of turbulence in the incoming flow was noted. Specifically, the magnitude of the AAFs tends to increase slightly as the TI decreases. This aspect, together with the implication of large TI on the linearisation of the buffeting loads, should be studied further when a larger number of valuable data samples is available. Future analysis should also focus on the significance of the TI for the span-wise co-coherence of the forces, as the gust loading on a bridge deck is a three-dimensional process.

Records associated with stably stratified flows and relatively low TI ($I_w \approx 0.07$) were exploited to explore the vortex shedding process. Noteworthy observations were the following: (a) the non-dimensional vortex shedding frequency depends on the location of the pressure tap because the deck is asymmetric. For example, the Strouhal number is 0.15 (0.21) when estimated above (below) the bridge deck nose on the trailing edges. (b) the span-wise coherence at the vortex shedding frequency is stronger for the surface pressures on the upper inclined panel of the girder; (c) Increasing the turbulence level in the incident flow weakens significantly the formation of coherent vortex structures, both at the cross-sectional level and in terms of span-wise correlation.

Chapter 7

Conclusions

7.1 Concluding remarks

The thesis primarily explored innovative experimental approaches to study the fluid-structure interaction on a full-scale closed-box girder bridge deck. Specifically, the gust loading mechanism and the near-wake flow have been studied. The case study was the Lysefjord Bridge in Norway.

The experimental framework to investigate the aerodynamics of a bridge deck in full-scale was introduced. The emphasis was on the development of a bespoke pressure measuring system, consisting of three pressure strips, each with 12 tapping points, and pressure probes to monitor the atmospheric static pressure. The solution developed with the "strap-embedded pressure taps" installed on the deck outer surface, allows for flexible measurements at variable separations between the pressure strips, i.e. span-wise distances between the monitored deck cross-sections. Also, the pressure system can be expanded with additional tapping points. The measurement layout can be adapted for use on other bridges, without the need for drilling holes through the deck in a wind tunnel fashion. As such, it represents a valuable "backbone" of a more comprehensive pressure measuring system for future studies.

The pressure measuring system is complemented by sonic anemometry, both on the hangers above the girder where the flow is considered undisturbed, and at the deck level, in the near wake and stagnation zones. The full-scale experiment dealt with the simultaneous measurements of the incident wind turbulence within the stagnation and near-wake regions, the wind-induced surface pressures on the bridge girder and lastly, the deck motion. In that

respect, the experimental setup permits a detailed investigation on the trans-formation of the incident atmospheric turbulence into surface pressure around the bridge deck, a topic rarely investigated in full-scale. The challenging design and development of the pressure measuring system for the field study, and the joint deployment of all the different sensors represent an original contribution of the present work. Lastly, a complementary wind-tunnel study was designed, concentrating on mapping the near-wake past a stationary 1:50 section model of the bridge deck.

The first topic investigated in this work was the incident flow. Specif-ically, the wind turbulence monitored 2 m (0.74D) upstream of the bridge deck nose was compared to the one seen 6 m (2.22D) above the bridge deck, on the upwind side. Using velocity records associated with a near-neutral stratification of the atmosphere, the pronounced frequency-dependent dis-tortion of turbulence approaching the bridge deck nose was characterised in detail. The along-wind velocity component was found to be attenuated (e.g. σ_u was reduced by 9%) at $fz/\bar{u} < 3$ due to the blocking effect of the girder. Conversely, the vertical velocity fluctuations were significantly amplified for reduced frequencies $fz/\bar{u} < 3$: the spectral energy was augmented by a factor of ≈ 2.7 compared to the nominally undisturbed turbulence. The observed distortion of the larger eddies approaching the deck is understood to be associated with the increased span-wise coherence of lift and moment, compared to the span-wise coherence of the oncoming vertical turbulence component. Specifically, the observed amplification of S_w ahead of the body connects the incident flow characteristics and the generation of the resulting forces on a single chord-wise strip.

In agreement with wind tunnel investigations on stationary closed-box girder bridge decks, the estimated lift and twisting moment were found to be better correlated along the bridge span than the incident vertical velocity fluctuations. Full-scale investigations of this type, including not only the deck leading edge surface pressures, are a rarity. For the case at hand, the flow was characterised by a yaw angle of $25°$, $I_w = 0.20$ and $\mathscr{L}_w/B = 4$. The ratios between the correlation lengths were $L_{F_L}^y/L_w^y = 1.60$ and $L_{F_M}^y/L_w^y = 1.86$, for lift and moment, respectively. This result demonstrated the limits of the strip assumption, even at $\mathscr{L}_w/B = 4$, in the natural wind.

Lastly, the thesis attempted to provide an insight into potential Reynolds number effects on the Strouhal number for the studied bridge deck cross-section, which is an example of sharp-edged body. For this purpose, the

near-wake turbulence measurements in full-scale were complemented by hot-wire measurements undertaken in the wind tunnel, in both smooth and turbulent flows. In full-scale ($Re \approx 2 \cdot 10^6$), the median value of the Strouhal number was 0.20, with a variability primarily driven by the turbulence level of the oncoming flow (the larger the turbulence intensity, the larger the Strouhal number). In model-scale, with $Re = 3.6 \cdot 10^4$ and in turbulent flow with normal incidence, the estimated Strouhal number was 0.19. Overall, the bridge deck studied did not exhibit a significant Reynolds number sensitivity. Also, the three-dimensional characteristics of the near-wake flow were documented in the wind tunnel for skewed flow conditions, which prevailed on-site. Yet, the interaction between the vortex shedding process and the documented axial flow, developing on the leeward side of the deck for skewed winds, has not been fully clarified. Part of the reason is the lack of consistent full-scale data, including surface pressure measurements, especially for the reference case of wind normal to the bridge axis.

7.2 Future tasks

The primary thrust of this work was to obtain further insight into the aerodynamics of a bridge deck from a full-scale perspective. The challenging development of the pressure measuring system represents an integral part of the research activity. In particular, the surface pressure measurements are believed to represent an original feature of this work and should be relevant for future studies on wind load modelling for cable-supported bridges. The results discussed herein are considered to be indicative rather than fully conclusive, especially those revolving around surface pressures (Chapter 6) given the limited number of valuable samples currently available. Nevertheless, their significance should not be underestimated as they represent clues for the advancement of this type of research. In many ways, this study can be considered as a relevant initial step, that provides valuable insight into topics that should be studied further.

7.2.1 Areas of further research

Areas where further research is considered necessary are outlined as follows:

- The aerodynamic admittance functions and co-coherence of the lift and

moment were here estimated on a bridge deck undergoing a certain level of ambient vibrations. The impact of the structural motion on the surrounding flow shall be adequately quantified considering the concurrent effects of the turbulence intensities and scales of the incident flow, see e.g. Haan Jr and Kareem [55]; Haan Jr et al. [56]. Along these lines, the full-scale observations can be aided by wind tunnel tests on a stationary and oscillating section model of the Lysefjord Bridge, in a simulated turbulent flow. Including runs with a yawed deck section model would also be desirable.

- The effects of the turbulence intensity on the separating shear layers past the downwind knuckle lines should be investigated further for the case at hand. Complementary wind tunnel studies can be designed to investigate the significance of turbulence intensity and length scale.

- A larger data set of surface pressure signals and bridge deck accelerations could also be studied in terms of the motion-dependent forces for a range of reduced wind velocities.

- A denser array of pressure taps within a given chord would also enable a study of instantaneous fluctuating loads in relation to the underlying relative angles of attack, to investigate e.g. non-linearities in the gust loading process, associated with the high turbulence intensity commonly encountered near the Lysefjord for the NNE wind exposure.

7.2.2   Development of the pressure measuring system

The research and development of a pressure measuring system tailored for a full-scale long-span bridge represent the foundation of this thesis. The system is valuable for studying bridge deck aerodynamics. The following discussion addresses various topics and makes suggestions for improving the full-scale experiment setup presented and the related instrumentation.

Rainwater challenges the collection of high-quality pressure signals on the tapping points directly exposed to the rainfall. Also, a natural drainage of the waterlogged tubing may take several days, thereby limiting the full capabilities of the pressure measuring system. Future work needs to focus on the design and development of a pressure tap able to convey accurate pressure signals also in wet conditions. Note that the pressure taps, including

the corresponding tubing system, are expected to be located on the outer side of the girder for an installation that is non-damaging for the bridge, as in the case at hand.

Along these lines, the pressure measuring system may benefit from complementary short-duration pressure measurements on the top side of the bridge deck, including the area within traffic lanes, as done by Isaksen [76]; Andersen et al. [5]; Svend Ole Hansen ApS [188] on the Gjemnessund Bridge (Norway). A more detailed description of the wind buffeting forces could thus be achieved.

The pressure measuring system was designed to monitor primarily the fluctuating part of the pressure signals. Three-way solenoid valves connected to the reference pressure system may be implemented to provide timely a zero calibration for each differential pressure transducer. Such a system should allow for a suitably accurate estimate of the time-averaged pressure coefficients. Examples of such techniques in the field of building aerodynamics can be found in Hoxey and Richardson [69]; Levitan and Mehta [110]; Snæbjörnsson [179]. To improve the accuracy of the first-order statistics, a temperature probe could be installed inside the controlled air volume providing the backing reference pressure. Any drift in air temperature and, consequently inside pressure, within a given averaging time could be thus evaluated.

Further studies should assess in detail the minimum height above the bridge deck to monitor the atmospheric static pressure undistorted by the deck-induced pressure field. Comparative full- (see e.g. Hoxey and Richards [67]) and model-scale investigations should provide a sound estimate considering different angles of wind incidence.

Expanding the pressure measuring system can provide a more comprehensive picture of the gust loading process. Firstly, an additional pressure strip equipped with e.g. ≈ 24 tapping points could be employed to achieve a finer description of the pressure distribution along a chord. Its position along the bridge span could be chosen to increase the current largest span-wise separation (1.4B) up to 1.95B, which currently represents the minimum lateral separation (24 m) between sonic anemometers on the bridge. Secondly, individual pressure taps could be designed to be conveniently installed above the bridge deck nose, to aid in the description of the span-wise correlation of the leading edge surface pressures.

Appendix A

Static pressure probe testing

A.1   Introduction

To monitor the atmospheric static pressure, four static pressure probes as described in Moran and Hoxey [141], so-called Hoxey probes, were acquired on loan from the Wind Engineering research group at the University of Birmingham. To investigate the capabilities of this probe, wind tunnel tests were conducted at Svend Ole Hansen ApS (SOH), in København. The objective was to measure the first moment of the static pressure of the incoming airflow [187]. In particular, the sensitivity of the pressure probe to Re number, angle of wind incidence, yaw angle and turbulence intensity was of interest. The pressure probe is of shroud-type, with four 3 mm in diameter protected sensing holes, thereby allowing for omni-directional porting for a horizontal flow. The performance specifications of the pressure probe can be found in Moran and Hoxey [141]; Hoxey et al. [68].

A.2   Experimental setup

The experimental setup is described in Figures A.1 and A.2. The differential pressure between the static port of a wall-mounted Pitot static tube and the port of the static pressure probe [141] was measured with a sampling frequency of 3 Hz. The duration of each test run was 60 s. The wind dynamic pressure was estimated based on the wall-mounted Pitot static tube. The tests were performed in both smooth flow (residual along-wind turbulence intensity of $I_u \simeq 0.02$) and turbulent flow (spire-generated turbulence, $I_u \simeq 0.10$), using
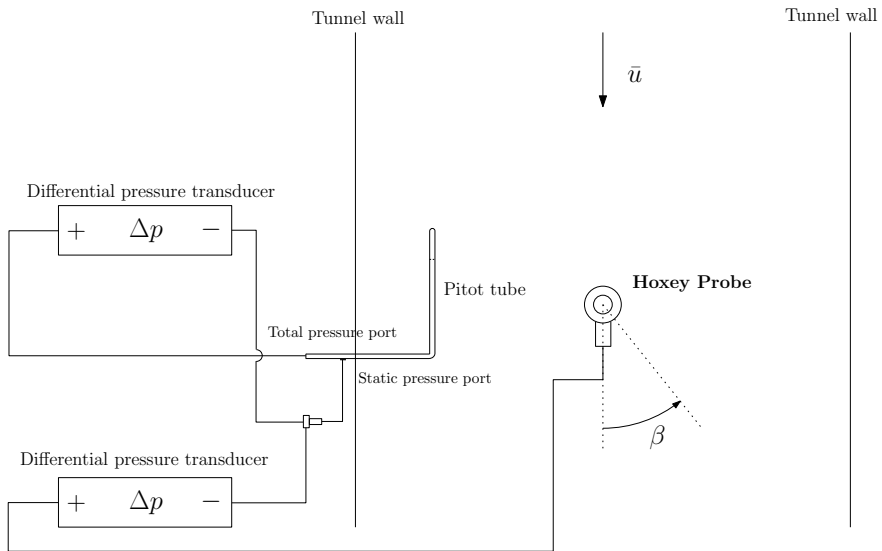
Figure A.1: Schematic diagram of the experimental setup utilized to test the static pressure probe [141] in the wind tunnel of Svend Ole Hansen ApS (SOH), København [187].
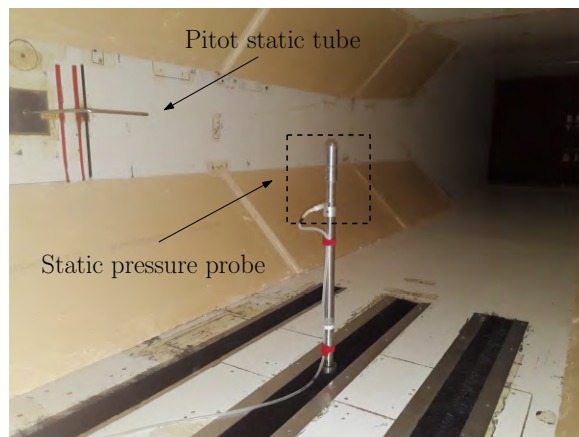

Figure A.2: A view of the static pressure probe [141] tested in the wind tunnel of Svend Ole Hansen ApS (SOH), København [187].

three different mean wind dynamic pressures ($\bar{q}$), with approximate values of 40, 80 and 150 Pa. The yaw angle β is defined as the angle between the pressure signal port of the probe and the mean wind direction in a horizontal plane (see Figure A.1), e.g. when the port is on the downwind side of the probe then $\beta = 0°$. The pitching angle α is positive when the sensor head is tilted towards the oncoming flow.

Prior to the actual testing of the probe, a mapping of the static pressure within the test section was undertaken to estimate the difference in static pressure at the location of the wall-mounted static Pitot tube and the location corresponding to the sensing ports of the probe. Such deviations of static pressure were generally lower than 0.9% of the tested wind dynamic pressure $\bar{q}$, for both smooth and turbulent flows.

A.3   Results

The static pressure probe designated as $P212$ was primarily tested. The shroud-collar gap of the probe [141] was 5.5 mm. The results are presented herein in terms of non-dimensional mean pressure coefficient $\overline{C_p}$, which, for the present application, is defined as follows:

$$\overline{C_p} = \frac{\Delta p_{static,\ probe} - \Delta p_{static,\ mapping}}{\bar{q}} \tag{A.1}$$

where $\Delta p_{static,\ probe}$ is the mean differential pressure (designated as DP1, see Figure A.1) between the static port of the wall-mounted static Pitot tube and the pressure sensed by the probe; $\Delta p_{static,\ mapping}$ is the differential pressure based on the static pressure mapping within the test section, which was carried out beforehand; $\bar{q}$ is the mean wind dynamic pressure.

For $\beta = 0°$ and $\alpha = 0°$, the repeatability of the measurements was investigated for different velocity pressures. The error estimated did not exceed a pressure coefficient of ± 0.01 and ± 0.005 for a smooth and turbulent flow, respectively.

The effects of the Reynolds number on the mean static pressure ($\overline{C_p}$) sensed by pressure probe [141] are summarised in Figure A.3, for the tested range of wind dynamic pressures, $\alpha = 0°$ and $\beta = 0°$. The mean pressure coefficient decreases with increasing wind dynamic pressure as described in the original calibration procedure of Moran and Hoxey [141], where the mean pressure coefficient associated with the pressure probe appeared to be linearly
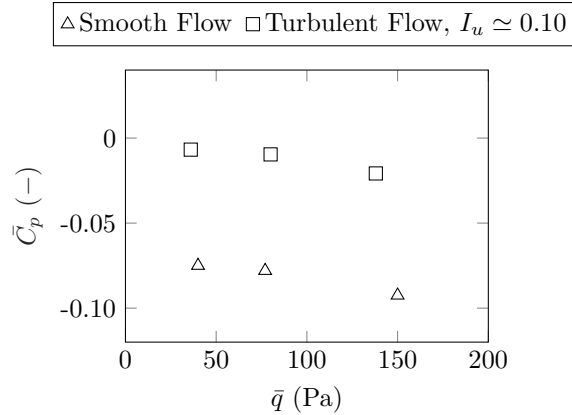
Figure A.3: Mean pressure coefficient ($\bar{C}_p$) measured by the static pressure probe [141], as a function of the dynamic wind pressure ($\bar{q}$), in both smooth and turbulent flow.

dependent on the wind dynamic pressure. Turbulence in the incoming air flow was proven to be beneficial in reducing, in absolute value, the estimated pressure coefficient $\overline{C_p}$, which did not exceed the range $-0.02 < \overline{C_p} < 0.00$, as shown in Figure A.3.

A.3.1 Sensitivity to yaw and pitching angle

The estimated sensitivity of the pressure probe to different yaw angles (β) as well as incidence angle (α) is documented in Figure A.4. Thanks to the omni-directional design of the probe, i.e. four pressure-sensing holes distributed around the sensing head [141], variations across the different pressure coefficients with the yaw angles are acceptably small. The difference between the mean pressure coefficient is lower than 0.015 and 0.013 in smooth and turbulent flow conditions, respectively.

For a turbulent flow and non-zero mean angle of incidence of the flow, the estimated pressure coefficient did not exceed the range ±0.03, based on the tested velocity pressure (Figure A.4). On the other hand, a larger dispersion of the pressure coefficient was found in nominally smooth flow conditions, across the different mean wind speeds tested (Figure A.4). However, for both flow conditions, the pressure probe response in α is not symmetrical about $\alpha = 0°$. This implies, in principle, that the fluctuations of wind angle of incidence for highly turbulent flow may introduce a bias, the sign of which
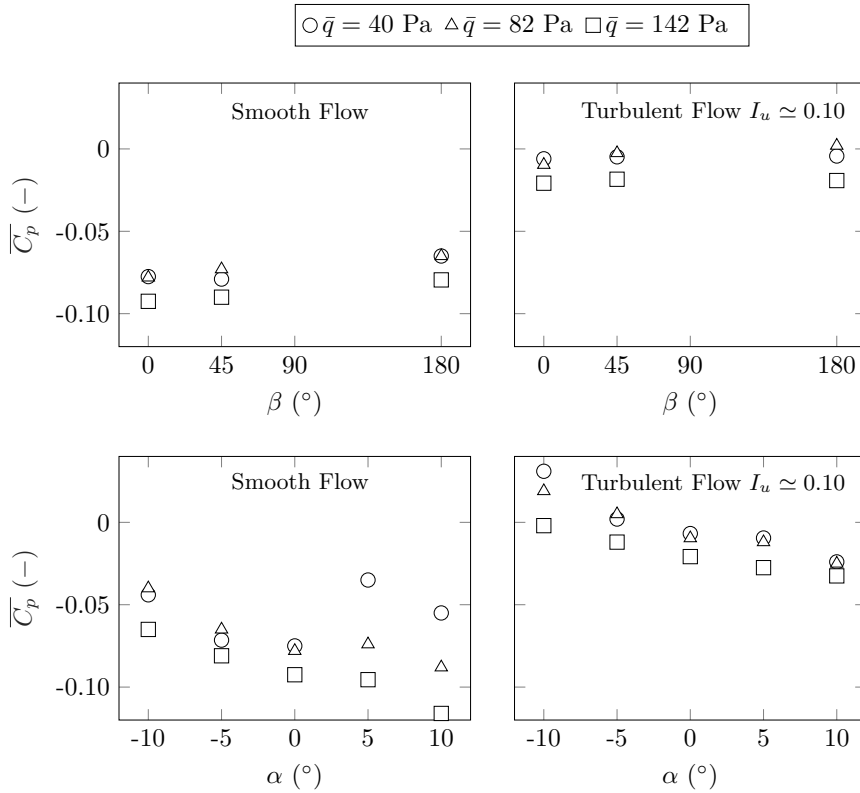
Figure A.4: Variation of the mean pressure coefficient ($\bar{C}_p$) with the yaw angle (β) and angle of wind incidence (α), for different dynamic wind pressures ($\bar{q}$), in both smooth and turbulent flow.

will depend on α and $\bar{q}$.

Considering the working range of conditions during the full-scale application of the pressure probe, namely atmospheric turbulence and an expected range of mean wind speed $6 \leq \bar{u} \leq 20\ \mathrm{m\,s^{-1}}$, the estimated errors associated with the first moment of the static pressure are considered to be sufficiently small.

Appendix B

Wind tunnel tests on a section model

B.1 Overview

Wind tunnel tests were conducted by SOH Wind Engineering LLC on a 1:50 scale rigid section model of the Lysefjord Bridge [181; 182]. The testing was performed in the wind tunnel of SOH Wind Engineering LLC (Williston, VT, USA). The working section is 3 m high × 3 m wide. The primary objective of the tests was to investigate the turbulent near wake for a stationary non-yawed and yawed section model as well as estimate the time-averaged force coefficients for a wide range of angles of wind incidence.

The rigid section model of the bridge was 2.4 m-long, which corresponds to a monitored length-to-width ratio of 9.76. The deck width and depth of the cross-section were 246.0 mm and 53.9 mm, respectively. The railings in model-scale were designed to fulfil the full-scale solidity ratio, considering a sub-critical flow regime at full-scale *Re* for all circular components. The eigenfrequency associated with the first bending mode of the structural system was 12.66 Hz. The section model was equipped with two end plates to minimize potential end effects and ensure the two-dimensionality of the flow within the monitored section. All the tests were performed with the cycle/pedestrian lane on the downwind side of the deck, which simulates a north-northeasterly flow in full-scale. A view of the section model during the wind tunnel testing is given in Figure B.1.

Time-averaged force coefficients were estimated in a turbulent flow. On

Figure B.1: A view of the Lysefjord Bridge section model during the static wind tunnel tests conducted by SOH Wind Engineering LLC [181].

Table B.1: One-point characteristics of spire-generated turbulence [180].

$\bar{u}$ (ms^{-1})	I_u	I_w	L_u^x (m)	L_w^x (m)
9.41	0.098	0.079	0.69	0.16

the other hand, wake velocity measurements downstream the stationary section model were performed in both smooth and turbulent flows. During all the test runs, the target mean wind speed, which was estimated at the shear centre height of the deck, was typically around $9.4\,\mathrm{m\,s}^{-1}$. The corresponding Reynolds number was thus $Re = 3.6 \cdot 10^4$ (based on the cross-wind dimension, D). Turbulent flow conditions were generated using a set of spires located 18.2 m upstream of the section model. The fundamental turbulence characteristics utilized during the wind tunnel experiment are reported in Table B.1. A complete documentation on the flow conditions can be found in SOH Wind Engineering LLC [180]. At section model height, the along-wind turbulence intensity was $I_u = 9.8\%$, with $\sigma_w/\sigma_u = 0.81$. The integral length scales were estimated based on the single-point velocity spectrum provided in the Eurocode [44], which was fitted to the measured normalized spectrum. For the tested 1:50 scale sectional model, the ratio L_w^x/B was 0.65.

In smooth flow conditions, the (residual) along-wind turbulence intensity at deck height was around 1%. The wind tunnel tests were generally conducted with a mean wind speed of around $9.4\,\mathrm{m\,s}^{-1}$. Thus, a Reynolds number of $Re = 3.6 \cdot 10^4$ (based on the cross-wind dimension, D) was achieved.

B.2 Time-averaged force coefficients

Time-averaged force coefficients of the section model were estimated in turbulent flow conditions (see Appendix B.1), spanning angles of wind incidence from $-25°$ to $+25°$ (positive "nose up"). The largest blockage ratio of the section model was 3.69% for the $\pm 25°$ configurations and, therefore, no blocking correction was undertaken. The overturning moment is defined as the moment around the shear centre of the cross-section, which is located 1.45 m (full-scale) from the bottom horizontal plate of the girder. The time-averaged force coefficients are defined as follows [41]:

$$C_D = \frac{F_D}{\frac{1}{2}\rho \bar{u}^2 D} \tag{B.1}$$

$$C_L = \frac{F_L}{\frac{1}{2}\rho \bar{u}^2 B} \tag{B.2}$$

$$C_M = \frac{F_M}{\frac{1}{2}\rho \bar{u}^2 B^2} \tag{B.3}$$

where C_D, C_L and C_M are the time-averaged drag, lift and moment coefficients, respectively. The variations of the static coefficients with the angle of wind incidence are reported in Figure B.2. The lift and moment derivatives with respect to the angle of attack, were estimated within the range $\pm 4°$, and are reported in Table B.2 along with the mean force coefficients at $0°$ angle of wind incidence. Based on thin airfoil theory, the ratio C_M'/C_L' suggests the location of the lift resultant at an upstream distance of 0.275B from the shear centre of the cross-section.

Table B.2: Time-averaged force coefficients for Lysefjord Bridge section model at $\alpha = 0°$, turbulent flow.

C_D (0°)	C_L (0°)	C_M (0°)	C_L' (0°)	C_M' (0°)
0.725	-0.128	0.027	4.696	1.293
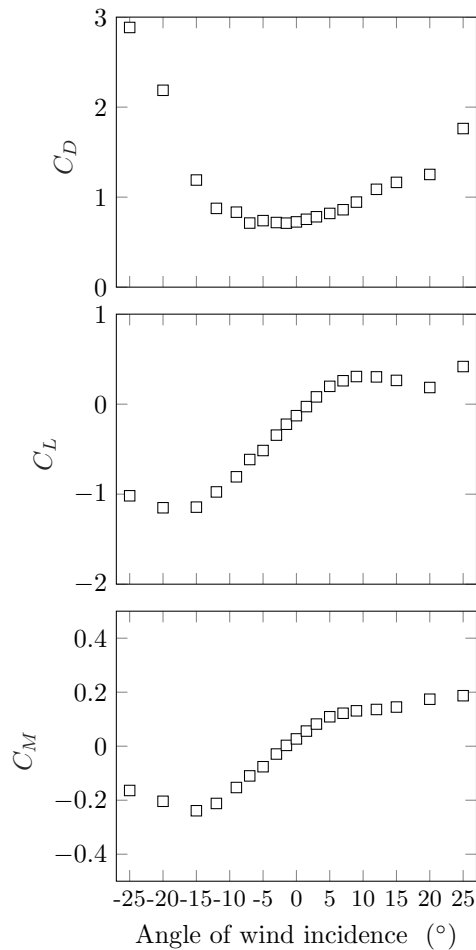
Figure B.2: Time-averaged force coefficients for the Lysefjord Bridge section model, for a turbulent flow ($I_u = 0.10$).

B.3   Velocity measurements in the near wake

Velocity measurements in the near wake of the section model were carried out in both smooth and turbulent flows (see Appendix B.1), testing two yaw angles, i.e. $\beta = 0°$ and $\beta = 25°$. The mean angle of wind incidence was set to $0°$. For each turbulence condition and yaw angle, velocity measurements were performed to study the variation of turbulence characteristics across the near wake along with the span-wise coherence of three velocity components.

The measurements stations were distributed along two vertical lines, i.e. across flow direction, located at a distance of B (4.6D) from the shear
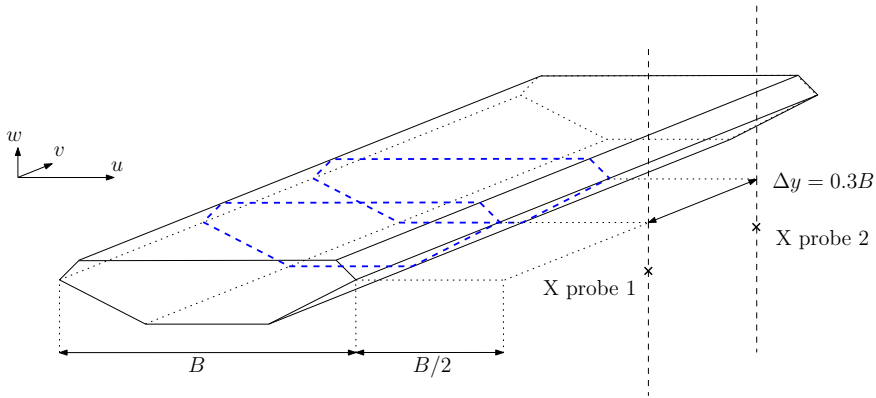
Figure B.3: Layout of the velocity measurements along two laterally separated verticals in the near wake of the bridge section model.

centre of the deck, i.e. B/2 from the trailing edge, as shown in Figure B.3. The adopted downstream location was an adequate trade-off between the interest in the near wake turbulence and the potential loss of accuracy in the velocity measurements stemming from the experimental setup. An array of two X-probes positioned at the same height were utilized with a span-wise separation of $\Delta y = 0.3B$, thereby providing simultaneous measurements of two velocity components and their correlation along the span for each run. Figure B.4 reports the location of the measurement points along the vertical line. Each measurement point is designated using the text string $V_{j,k}$, where $j = 1, 2$ identifies the X wire probe and $k = \{1, 2, ..., 7\}$ is associated with the corresponding measurement height. The order is sequential starting from the top outer station, as described in Figure B.4. The horizontal location of the X probe 1 is such that it is more "upstream" compared to X probe 2 during the runs with a yawed section model.

Velocity measurements were undertaken using constant temperature anemometry (CTA), namely MiniCTA 54T42 manufactured by Dantec Dynamics, and two dual sensors X wire probes, Type 55 manufactured by Dantec Dynamics. The setup of the X probes is such that either velocity fluctuations u and v or u and w can be simultaneously measured. The traverse system adopted for the hot-wire anemometry is shown in Figures B.5 and B.6. The traverse is mounted at 10 deck depths above the section model. For the yawed configuration, the ends of the section models were equipped with two elements having the same geometrical characteristics as the deck cross-section. This ensured that no additional flow distortion was induced by end effects. The alignment
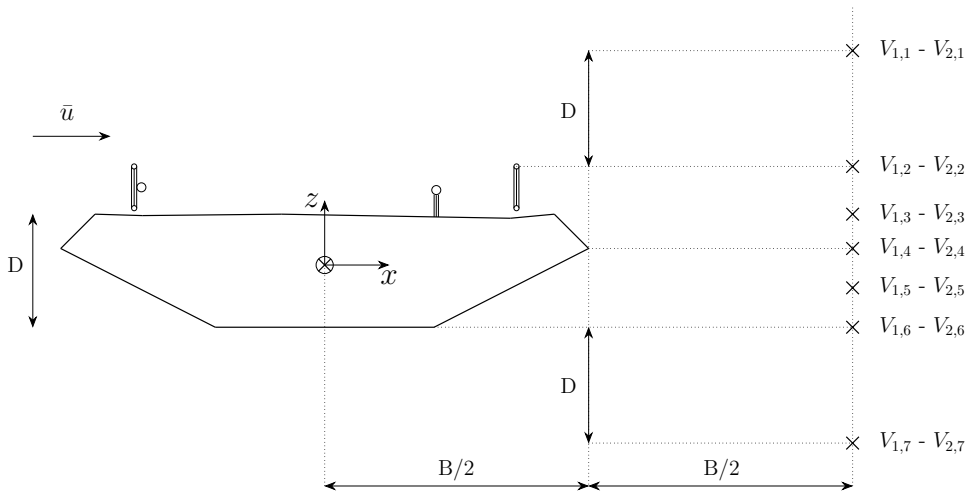
Figure B.4: Scheme of the vertical positions of the X probes for the velocity measurements in the near wake. Each ($\times$) indicates a pair of X probes performing simultaneous velocity measurements.

of the X-probes is based on the coordinate system of the incoming flow for both $\beta = 0°$ and $\beta = 25°$.

The sampling frequency was set to $1000\,\text{Hz}$ and the duration of the sampled records was $120\,\text{s}$. Considering a velocity scale of 1:1, e.g. $\bar{u} \simeq 10\,\text{m s}^{-1}$ in full-scale, the corresponding time scale is approximately 1:50. Thus, the sampling time corresponds to $100\,\text{min}$ in full-scale. During the tests, the minimum vortex shedding frequency was approximately $25\,\text{Hz}$ (for $\beta = 25°$). Thus, the number of cycles detected should be such that the random errors associated with the estimation of the St number are minimized.
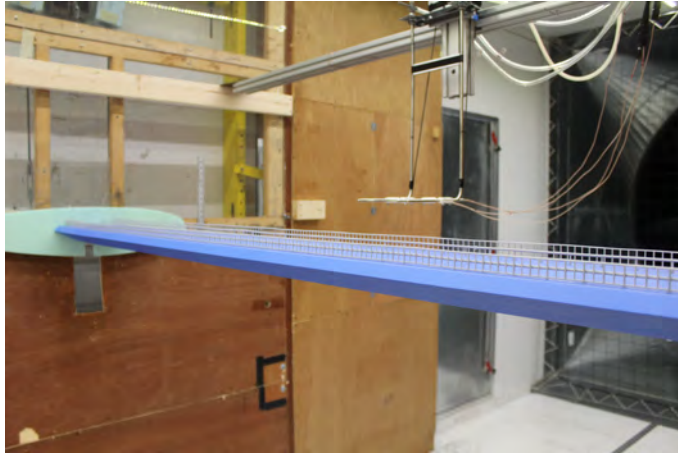
Figure B.5: A view of the setup utilized for velocity measurements in the near wake of the section model. The photo is from SOH Wind Engineering LLC [182].

Figure B.6: A view from downstream the section model of the X-probes configuration. The photo is from SOH Wind Engineering LLC [182].

Appendix C

Publications related to the thesis

Journal papers

1. Daniotti, N., Jakobsen, J.B., Snæbjörnsson, J., Cheynet, E. and Wang, J., 2021. Observations of bridge stay cable vibrations in dry and wet conditions: A case study. *Journal of Sound and Vibration*, 503, p.116106. https://doi.org/10.1016/j.jsv.2021.116106

2. Cheynet, E., Daniotti, N., Jakobsen, J.B. and Snæbjörnsson, J. and Wang, J., 2021. Unfrozen turbulence generation in skewed flow for wind loading on structures. *Submitted to Probabilistic Engineering Mechanics*.

3. Cheynet, E., Daniotti, N., Jakobsen, J.B. and Snæbjörnsson, J., 2020. Improved long-span bridge modeling using data-driven identification of vehicle-induced vibrations. *Structural Control and Health Monitoring*, 27(9), p.e2574. https://doi.org/10.1002/stc.2574

Conference papers

1. Daniotti, N., Jakobsen, J.B., Snæbjörnsson, J., Cheynet, E. and Wang, J., 2021. Full-scale observations of bridge stay cable vibrations in a wet state. *Proceedings of the second international symposium on dynamics and aerodynamics of cables - ISDAC 2021, 16-17 September 2021, Stavanger, Norway*.

2. Daniotti, N., Jakobsen, J.B., Snæbjörnsson, J. and Cheynet, E., 2021. Observations of the turbulent near wake of a bridge deck. *6th American Association for Wind Engineering Workshop (online); Clemson University, Clemson, SC, USA; May 12-14, 2021.*

3. Daniotti, N., Cheynet, E., Jakobsen, J.B. and Snæbjörnsson, J., 2019. Analysing wind-induced vibrations of a suspension bridge using GNSS data. *The 15th International Conference on Wind Engineering; September 1-6, 2019, Beijing, China.*

4. Daniotti, N., Cheynet, E., Jakobsen, J.B. and Snæbjörnsson, J., 2019. Damping estimation from full-scale traffic-induced vibrations of a suspension bridge. In *Computing in Civil Engineering 2019: Smart Cities, Sustainability, and Resilience* (pp. 171-179). Reston, VA: American Society of Civil Engineers. https://doi.org/10.1061/9780784482445.022

Bibliography

[1] Achenbach, E. and E. Heinecke (1981). On vortex shedding from smooth and rough cylinders in the range of reynolds numbers 6×10^3 to 5×10^6. *Journal of Fluid Mechanics 109*, 239–251. 18

[2] Albertson, J. D., G. G. Katul, M. B. Parlange, and W. E. Eichinger (1998). Spectral scaling of static pressure fluctuations in the atmospheric surface layer: The interaction between large and small scales. *Physics of Fluids 10*(7), 1725–1732. 128

[3] Andersen, M. S. (2021). Operational fluid modal analysis of full-scale pressure and wake flow measurements on the Gjemnessund Bridge. *Engineering Structures 249*, 113295. 9, 24, 112

[4] Andersen, M. S. and N. S. Bossen (2021). Modal decomposition of the pressure field on a bridge deck under vortex shedding using POD, DMD and ERA with correlation functions as Markov parameters. *Journal of Wind Engineering and Industrial Aerodynamics 215*, 104699. 9, 112, 132

[5] Andersen, M. S., B. Isaksen, and S. O. Hansen (2021). Full-scale monitoring of the wind field, surface pressures and structural response of Gjemnessund suspension bridge. *Structural Engineering International*. 7, 9, 68, 81, 117, 132, 133, 134, 146, 161

[6] Argentini, T., D. Rocchi, and C. Somaschini (2020). Effect of the low-frequency turbulence on the aeroelastic response of a long-span bridge in wind tunnel. *Journal of Wind Engineering and Industrial Aerodynamics 197*, 104072. 30

[7] Bastos, F. (2015). *Aerodynamic Behaviour of Long Span Structures. Numerical Analysis and Experimental Validation based on Full-Scale Measurements*. Ph. D. thesis. 9

[8] Batchelor, G. K. (1953). *The theory of homogeneous turbulence*. Cambridge University Press. 128

[9] Bearman, P. (1965). Investigation of the flow behind a two-dimensional model with a blunt trailing edge and fitted with splitter plates. *Journal of Fluid Mechanics 21*(2), 241–255. 100

[10] Bearman, P. (1971). An investigation of the forces on flat plates normal to a turbulent flow. *Journal of Fluid Mechanics 46*(1), 177–198. 70, 72, 73

[11] Bearman, P. (1972). Some measurements of the distortion of turbulence approaching a two-dimensional bluff body. *Journal of Fluid Mechanics 53*(3), 451–467. 67, 70, 72, 73

[12] Bergh, H. and H. Tijdeman (1965). Theoretical and experimental results for the dynamic response of pressure measuring systems. Technical report. NLR-TR F.238. 50, 56, 119, 120, 121

[13] Bietry, J., D. Delaunay, and E. Conti (1995). Comparison of full-scale measurement and computation of wind effects on a cable-stayed bridge. *Journal of Wind Engineering and Industrial Aerodynamics 57*(2-3), 225–235. 7, 67

[14] Bogunovic Jakobsen, J. (1995). Fluctuating wind load and response of a line-like engineering structure with emphasis on motion-induced wind forces. *Doktor ingenioravhandling, Institutt for Konstruksjonsteknikk, Trondheim 62*. 98, 143, 148

[15] Bowen, A., R. Flay, and H. Panofsky (1983). Vertical coherence and phase delay between wind components in strong winds below 20 m. *Boundary-Layer Meteorology 26*(4), 313–324. 78

[16] Britter, R., J. Hunt, and J. Mumford (1979). The distortion of turbulence by a circular cylinder. *Journal of Fluid Mechanics 92*(2), 269–301. 70

[17] Brownjohn, J., M. Bocciolone, A. Curami, M. Falco, and A. Zasso (1994). Humber bridge full-scale measurement campaigns 1990–1991. *Journal of Wind Engineering and Industrial Aerodynamics 52*, 185–218. 67

[18] Bursnall, W. J. and L. K. Loftin Jr (1951). Experimental investigation of the pressure distribution about a yawed circular cylinder in the critical reynolds number range. Technical report, National Aeronautics And Space Administration Washington DC. 26

[19] Busch, N. E. and H. A. Panofsky (1968). Recent spectra of atmospheric turbulence. *Quarterly Journal of the Royal Meteorological Society 94*(400), 132–148. 13, 93

[20] Chamecki, M. and N. Dias (2004). The local isotropy hypothesis and the turbulent kinetic energy dissipation rate in the atmospheric surface layer. *Quarterly Journal of the Royal Meteorological Society: A journal of the atmospheric sciences, applied meteorology and physical oceanography 130*(603), 2733–2752. 87, 95

[21] Cheung, J. and W. Melbourne (1983). Turbulence effects on some aerodynamic parameters of a circular cylinder at supercritical numbers. *Journal of Wind Engineering and Industrial Aerodynamics 14*(1-3), 399–410. 18, 22, 110

[22] Cheynet, E. (2016). *Wind-induced vibrations of a suspension bridge: A case study in full-scale*. Ph. D. thesis, University of Stavanger, Norway. 3, 29, 30

[23] Cheynet, E. (2020). Personal Communication. 71, 87, 90

[24] Cheynet, E., N. Daniotti, J. B. Jakobsen, and J. Snæbjörnsson (2020). Improved long-span bridge modeling using data-driven identification of vehicle-induced vibrations. *Structural Control and Health Monitoring 27*(9), e2574. 3, 114

[25] Cheynet, E., J. B. Jakobsen, and J. Snæbjörnsson (2016). Buffeting response of a suspension bridge in complex terrain. *Engineering Structures 128*, 474–487. 3, 7, 30, 35, 48, 62

[26] Cheynet, E., J. B. Jakobsen, and J. Snæbjörnsson (2019). Flow distortion recorded by sonic anemometers on a long-span bridge: Towards a better modelling of the dynamic wind load in full-scale. *Journal of Sound and Vibration 450*, 214–230. 7, 13, 29, 35, 36, 37, 40, 61, 62, 63, 64, 65, 67, 68, 82, 88, 123, 124, 126, 131, 142

[27] Cheynet, E., J. B. Jakobsen, J. Snæbjörnsson, N. Angelou, T. Mikkelsen, M. Sjöholm, and B. Svardal (2017). Full-scale observation of the flow downstream of a suspension bridge deck. *Journal of Wind Engineering and Industrial Aerodynamics 171*, 261–272. 8, 63, 81, 83, 89, 101

[28] Cheynet, E., J. B. Jakobsen, J. Snæbjörnsson, T. Mikkelsen, M. Sjöholm, J. Mann, P. Hansen, N. Angelou, and B. Svardal (2016). Application of short-range dual-doppler lidars to evaluate the coherence of turbulence. *Experiments in Fluids 57*(12), 1–17. 61, 129

[29] Cheynet, E., S. Liu, M. C. Ong, J. B. Jakobsen, J. Snæbjörnsson, and I. Gatin (2020). The influence of terrain on the mean wind flow characteristics in a fjord. *Journal of Wind Engineering and Industrial Aerodynamics 205*, 104331. 62, 63

[30] Dalley, S. and G. Richardson (1992). Reference static pressure measurements in wind tunnels. *Journal of Wind Engineering and Industrial Aerodynamics 42*(1-3), 909–920. 56

[31] Davenport, A. G. (1961a). The application of statistical concepts to the wind loading of structures. *Proceedings of the Institution of Civil Engineers 19*(4), 449–472. 7

[32] Davenport, A. G. (1961b). The spectrum of horizontal gustiness near the ground in high winds. *Quarterly Journal of the Royal Meteorological Society 87*(372), 194–211. 8, 17

[33] Davenport, A. G. (1962a). Buffetting of a suspension bridge by storm winds. *Journal of the Structural Division 88*(3), 233–270. 27, 31, 33

[34] Davenport, A. G. (1962b). The response of slender, line-like structures to a gusty wind. *Proceedings of the Institution of Civil Engineers 23*(3), 389–408. 16, 27, 29, 31, 61, 76, 117, 145

[35] Davenport, A. G. (1975). Perspectives on the full-scale measurement of wind effects. *Journal of Wind Engineering and Industrial Aerodynamics 1*, 23–54. 1

[36] D'Errico, J. (2020). inpaint_nans. http://www.mathworks.com/matlabcentral/fileexchange/4551-inpaint{_}nans. MATLAB Central File Exchange, Retrieved: July 01, 2020. 65, 88

[37] Diana, G., S. Bruni, A. Cigada, and E. Zappa (2002). Complex aero-dynamic admittance function role in buffeting response of a bridge deck. *Journal of Wind Engineering and Industrial Aerodynamics 90*(12-15), 2057–2072. 30, 31

[38] Diana, G., M. Falco, S. Bruni, A. Cigada, G. L. Larose, A. Darnsgaard, and A. Collina (1995). Comparisons between wind tunnel tests on a full aeroelastic model of the proposed bridge over Stretto di Messina and numerical results. *Journal of Wind Engineering and Industrial Aerodynamics 54*, 101–113. 29

[39] Diana, G. and S. Omarini (2020). A non-linear method to compute the buffeting response of a bridge validation of the model through wind tunnel tests. *Journal of Wind Engineering and Industrial Aerodynamics 201*, 104163. 30

[40] Diana, G., F. Resta, A. Zasso, M. Belloli, and D. Rocchi (2004). Effects of the yaw angle on the aerodynamic behaviour of the Messina multi-box girder deck section. *Wind & Structures 7*(1), 41–54. 99

[41] Dyrbye, C. and S. O. Hansen (1997). *Wind loads on structures*. Wiley. 27, 171

[42] Elliott, J. (1972a). Instrumentation for measuring static pressure fluctu-ations within the atmospheric boundary layer. *Boundary-Layer Meteorol-ogy 2*(4), 476–495. 128

[43] Elliott, J. A. (1972b). Microscale pressure fluctuations measured within the lower atmospheric boundary layer. *Journal of Fluid Mechanics 53*(2), 351–384. 125, 128, 131

[44] En, B. et al. (1991). Eurocode 1: Actions on structuresâĂŤpart 1–4: General actionsâĂŤwind actions. *NA to BS EN, Brussels, Belgium.* 170

[45] ESDU 86010 (2001). Characteristics of atmospheric turbulence near the ground Part III: Variations in space and time for strong winds (neutral atmosphere). 129

[46] Fabris, G. (1983). Higher-order statistics of turbulent fluctuations in the plane wake. *The Physics of Fluids 26*(6), 1437–1445. 103

[47] Fenerci, A., O. Øiseth, and A. Rønnquist (2017). Long-term monitoring of wind field characteristics and dynamic response of a long-span suspension bridge in complex terrain. *Engineering Structures 147*, 269–284. 7, 61, 67

[48] Ferre, J. A. and F. Giralt (1989). Pattern-recognition analysis of the velocity field in plane turbulent wakes. *Journal of Fluid Mechanics 198*, 27–64. 98

[49] Frandsen, J. (2001). Simultaneous pressures and accelerations measured full-scale on the Great Belt East suspension bridge. *Journal of Wind Engineering and Industrial Aerodynamics 89*(1), 95–129. 8, 10, 23, 81

[50] George, W. K., P. D. Beuther, and R. E. Arndt (1984). Pressure spectra in turbulent free shear flows. *Journal of Fluid Mechanics 148*, 155–191. 128

[51] Gill Instruments, . (2019). KN1508. improvements to the WindMaster product range. WindMaster and WindMaster Pro. Technical report. 65

[52] Graham, J. (1970). Lifting surface theory for the problem of an arbitrarily yawed sinusoidal gust incident on a thin aerofoil in incompressible flow. *The Aeronautical Quarterly 21*(2), 182–198. 33

[53] Graham, J. (1971). A lifting-surface theory for the rectangular wing in non-stationary flow. *The Aeronautical Quarterly 22*(1), 83–100. 33

[54] Gutmark, E., M. Wolfshtein, and I. Wygnanski (1978). The plane turbulent impinging jet. *Journal of Fluid Mechanics 88*(4), 737–756. 74

[55] Haan Jr, F. and A. Kareem (2009). Anatomy of turbulence effects on the aerodynamics of an oscillating prism. *Journal of Engineering Mechanics 135*(9), 987–999. 143, 160

[56] Haan Jr, F. L., T. Wu, and A. Kareem (2016). Correlation structures of pressure field and integrated forces on oscillating prism in turbulent flows. *Journal of Engineering Mechanics 142*(5), 04016017. 9, 160

[57] Hansen, E. H. (1988). Wind engineering–lecture notes. 7

[58] Hansen, S. O., R. G. Srouji, B. Isaksen, and K. Berntsen (2015). Vortex-induced vibrations of streamlined single box girder bridge decks. In *14th International Conference on Wind Engineering*. 23, 24

[59] Hanson, A. (1966). Vortex shedding from yawed cylinders. *AIAA Journal 4*(4), 738–740. 26, 109

[60] Hejlesen, M. M., J. T. Rasmussen, A. Larsen, and J. H. Walther (2015). On estimating the aerodynamic admittance of bridge sections by a mesh-free vortex method. *Journal of Wind Engineering and Industrial Aerodynamics 146*, 117–127. 30

[61] Hillier, R. and N. Cherry (1981). The effects of stream turbulence on separation bubbles. *Journal of Wind Engineering and Industrial Aerodynamics 8*(1-2), 49–58. 136

[62] Hjorth-Hansen, E., A. Jakobsen, and E. Strømmen (1992). Wind buffeting of a rectangular box girder bridge. *Journal of Wind Engineering and Industrial Aerodynamics 42*(1-3), 1215–1226. 17

[63] Holmes, J. (1984). Effect of frequency response on peak pressure measurements. *Journal of Wind Engineering and Industrial Aerodynamics 17*(1), 1–9. 119

[64] Holmes, J. and R. Lewis (1987). Optimization of dynamic-pressure-measurement systems. I. single point measurements. *Journal of Wind Engineering and Industrial Aerodynamics 25*(3), 249–273. 119

[65] Hoxey, R. and P. Moran (1983). A full-scale study of the geometric parameters that influence wind loads on low rise buildings. *Journal of Wind Engineering and Industrial Aerodynamics 13*(1-3), 277–288. 56

[66] Hoxey, R., A. Reynolds, G. Richardson, A. Robertson, and J. Short (1998). Observations of reynolds number sensitivity in the separated flow region on a bluff body. *Journal of Wind Engineering and Industrial Aerodynamics 73*(3), 231–249. 2, 24, 81

[67] Hoxey, R. and P. Richards (1993). Flow patterns and pressure field around a full-scale building. *Journal of Wind Engineering and Industrial Aerodynamics 50*, 203–212. 53, 56, 161

[68] Hoxey, R., P. Richards, A. Quinn, A. Robertson, and H. Gough (2021). Measurements of the static pressure near the surface in the atmospheric boundary layer. *Journal of Wind Engineering and Industrial Aerodynamics 209*, 104487. 53, 56, 127, 128, 163

[69] Hoxey, R. and G. Richardson (1984). Measurements of wind loads on full-scale film plastic clad greenhouses. *Journal of Wind Engineering and Industrial Aerodynamics 16*(1), 57–83. 53, 161

[70] Hunt, J. (1973). A theory of turbulent flow round two-dimensional bluff bodies. *Journal of Fluid Mechanics 61*(4), 625–706. 69, 70, 72

[71] Hussain, A. F. and M. Hayakawa (1987). Eduction of large-scale organized structures in a turbulent plane wake. *Journal of Fluid Mechanics 180*, 193–229. 92

[72] Irwin, H. (1979). Cross-spectra of turbulence velocities in isotropic turbulence. *Boundary-Layer Meteorology 16*(3), 237–243. 17, 77

[73] Irwin, H., K. Cooper, and R. Girard (1979). Correction of distortion effects caused by tubing systems in measurements of fluctuating pressures. *Journal of Wind Engineering and Industrial Aerodynamics 5*(1-2), 93–107. 50, 56, 119, 120, 121

[74] Irwin, H. P. A. (1977). Wind tunnel and analytical investigations of the response of Lions' Gate Bridge to a turbulent wind. *National Research Council Canada*. 28

[75] Irwin, P. (1998). The role of wind tunnel modeling in the prediction of wind effects on bridges. In *Proc. of the international symposium on advances in bridge aerodynamics, Copenhagen, Denmark*, pp. 99–117. 23, 113

[76] Isaksen, B. (2008). *Experimental Investigations of Wind Loading on a Suspension Bridge Girder*. Ph. D. thesis, Fakultet for ingeniørvitenskap og teknologi. 9, 52, 119, 132, 161

[77] Isaksen, B., E. Strømmen, and K. Gjerding-Smith (2001). Suppression of vortex shedding vibrations at osterøy suspension bridge. In *Proceedings of the forth Symposium on Strait Crossings*, pp. 99–105. 23

[78] Jakobsen, J. B. (1997). Span-wise structure of lift and overturning moment on a motionless bridge girder. *Journal of Wind Engineering and Industrial Aerodynamics 69*, 795–805. 17, 32, 33, 117, 145

[79] Kaimal, J. C. and J. J. Finnigan (1994). *Atmospheric boundary layer flows: their structure and measurement*. Oxford University Press. 10, 12, 14, 65, 76, 83, 87, 95, 149

[80] Kaimal, J. C., J. Wyngaard, Y. Izumi, and O. Coté (1972). Spectral characteristics of surface-layer turbulence. *Quarterly Journal of the Royal Meteorological Society 98*(417), 563–589. 13, 14

[81] Kaspersen, J. and P.-Å. Krogstad (1993). The effect of transition to turbulent flow in tubing networks for fluctuating pressure measurement. *Journal of Wind Engineering and Industrial Aerodynamics 48*(1), 1–11. 50, 119

[82] Katul, G. G., J. D. Albertson, M. B. Parlange, C.-I. Hsieh, P. S. Conklin, J. T. Sigmon, and K. R. Knoerr (1996). The âĂIJinactiveâĂİ eddy motion and the large-scale turbulent pressure fluctuations in the dynamic sublayer. *Journal of the atmospheric sciences 53*(17), 2512–2524. 125, 128

[83] Kimura, K., Y. Fujino, S. Nakato, and H. Tamura (1997). Characteristics of buffeting forces on flat cylinders. *Journal of Wind Engineering and Industrial Aerodynamics 69*, 365–374. 33, 145

[84] Kimura, K. and H. Tanaka (1992). Bridge buffeting due to wind with yaw angles. *Journal of Wind Engineering and Industrial Aerodynamics 42*(1-3), 1309–1320. 12

[85] Kiya, M. and M. Matsumura (1985). Turbulence structure in intermediate wake of a circular cylinder. *Bulletin of JSME 28*(245), 2617–2624. 81, 92, 93, 102

[86] Kleissl, K. and C. Georgakis (2012). Comparison of the aerodynamics of bridge cables with helical fillets and a pattern-indented surface. *Journal of Wind Engineering and Industrial Aerodynamics 104*, 166–175. 27

[87] Kolmogorov, A. N. (1941). The local structure of turbulence in incompressible viscous fluid for very large reynolds numbers. *Cr Acad. Sci. URSS 30*, 301–305. 14, 72, 74, 95, 104, 128

[88] Kovaerk, M., L. Amatucci, K. A. Gillis, F. A. Potra, J. Ratino, M. L. Levitan, D. Yeo, et al. (1994). Calibration of dynamic pressure in a tubing system and optimized design of tube configuration: A numerical and experimental study. Technical report. NIST Technical Note. 119, 120

[89] Kozakiewicz, A., J. Fredsee, and B. M. Sumer (1995). Forces on pipelines in oblique attack: steady current and waves. In *The fifth international offshore and polar engineering conference*. 26, 67, 109

[90] Krenk, S. (1996). Wind field coherence and dynamic wind forces. In *IUTAM symposium on advances in nonlinear stochastic mechanics*, pp. 269–278. Springer. 17

[91] Kristensen, L. and N. Jensen (1979). Lateral coherence in isotropic turbulence and in the natural wind. *Boundary-Layer Meteorology 17*(3), 353–373. 17, 61, 67, 77

[92] Kristensen, L., H. A. Panofsky, and S. D. Smith (1981). Lateral coherence of longitudinal wind components in strong winds. *Boundary-Layer Meteorology 21*(2), 199–205. 78

[93] Kubo, Y., Y. Niihara, R. Nakano, and K. Hayashida (1997a). Full scale measurement of wind pressure on a deck of a concrete cable-stayed bridge part 1 mean and fluctuating pressure coefficient. *Wind Engineers, JAWE 1997*(72), 47–58. 8, 68

[94] Kubo, Y., Y. Niihara, R. Nakano, and K. Hayashida (1997b). Full scale measurement of wind pressure on a deck of a concrete cable-stayed bridge part 2 spectra of fluctuating pressure and reynolds number effect. *Wind Engineers, JAWE 1997*(73), 25–34. 8, 24, 112

[95] Kwok, K. C. (1986). Turbulence effect on flow around circular cylinder. *Journal of Engineering Mechanics 112*(11), 1181–1197. 18, 22, 110

[96] Laneville, A., I. Gartshore, and G. Parkinson (1975). An explanation of some effects of turbulence on bluff bodies. In *Proc. of 4th Int'l Conference on Buildings and Structures, London, England*. Cambridge Univ. Press. 22, 113, 150

[97] Larose, G. and A. DâĂŹauteuil (2006). On the Reynolds number sensitivity of the aerodynamics of bluff bodies with sharp edges. *Journal*

of Wind Engineering and Industrial Aerodynamics 94(5), 365–376. 2, 24, 26, 81, 93, 111, 112

[98] Larose, G. and J. Mann (1998). Gust loading on streamlined bridge decks. *Journal of Fluids and Structures 12*(5), 511–536. 30, 33, 34, 47, 143, 146

[99] Larose, G., H. Tanaka, N. Gimsing, and C. Dyrbye (1998). Direct measurements of buffeting wind forces on bridge decks. *Journal of Wind Engineering and Industrial Aerodynamics 74*, 809–818. 33, 47, 144

[100] Larose, G. L. (1992). The response of a suspension bridge deck to turbulent wind: the taut strip model approach. Master's thesis, The University of Western Ontario. 30, 32, 33, 117, 143, 144, 145

[101] Larose, G. L. (1997). *The dynamic action of gusty winds on long-span bridges*. Ph. D. thesis, Technical University of Denmark. 14, 15, 19, 29, 30, 31, 32, 34, 47, 73, 76, 80, 117, 143, 144, 145, 146, 147, 148

[102] Larose, G. L. (1999). Experimental determination of the aerodynamic admittance of a bridge deck segment. *Journal of Fluids and Structures 13*(7-8), 1029–1040. 33

[103] Larose, G. L. (2003). The spatial distribution of unsteady loading due to gusts on bridge decks. *Journal of Wind Engineering and Industrial Aerodynamics 91*(12-15), 1431–1443. 142, 144, 148

[104] Larsen, A., S. Esdahl, J. E. Andersen, and T. Vejrum (2000). Storebælt suspension bridge–vortex shedding excitation and mitigation by guide vanes. *Journal of Wind Engineering and Industrial Aerodynamics 88*(2-3), 283–296. 23

[105] Larsen, A. and G. L. Larose (2015). Dynamic wind effects on suspension and cable-stayed bridges. *Journal of Sound and Vibration 334*, 2–28. 1, 9

[106] Larsen, A. and A. Wall (2012). Shaping of bridge box girders to avoid vortex shedding response. *Journal of Wind Engineering and Industrial Aerodynamics 104*, 159–165. 23

[107] Lenschow, D., J. Mann, and L. Kristensen (1994). How long is long enough when measuring fluxes and other turbulence statistics? *Journal of Atmospheric and Oceanic Technology 11*(3), 661–673. 12

[108] Letchford, C., P. Sandri, M. Levitan, and K. Mehta (1992). Frequency response requirements for fluctuating wind pressure measurements. *Journal of Wind Engineering and Industrial Aerodynamics 40*(3), 263–276. 119

[109] Levitan, M. L. (1993). *Analysis of reference pressure systems used in field measurements of wind loads*. Ph. D. thesis, Texas Tech University. 50, 53, 55, 56

[110] Levitan, M. L. and K. C. Mehta (1992). Texas Tech field experiments for wind loads part 1: building and pressure measuring system. *Journal of Wind Engineering and Industrial Aerodynamics 43*(1-3), 1565–1576. 53, 161

[111] Levitan, M. L., K. C. Mehta, W. Vann, and J. Holmes (1991). Field measurements of pressures on the Texas Tech building. *Journal of Wind Engineering and Industrial Aerodynamics 38*(2-3), 227–234. 53

[112] Li, H., S. Laima, J. Ou, X. Zhao, W. Zhou, Y. Yu, N. Li, and Z. Liu (2011). Investigation of vortex-induced vibration of a suspension bridge with two separated steel box girders based on field measurements. *Engineering Structures 33*(6), 1894–1907. 8, 81

[113] Li, H., S. Laima, Q. Zhang, N. Li, and Z. Liu (2014). Field monitoring and validation of vortex-induced vibrations of a long-span suspension bridge. *Journal of Wind Engineering and Industrial Aerodynamics 124*, 54–67. 8, 112

[114] Li, S. and M. Li (2017). Spectral analysis and coherence of aerodynamic lift on rectangular cylinders in turbulent flow. *Journal of Fluid Mechanics 830*, 408–438. 146

[115] Li, S., M. Li, and G. L. Larose (2018). Aerodynamic admittance of streamlined bridge decks. *Journal of Fluids and Structures 78*, 1–23. 30, 33, 34, 117, 146

[116] Li, S., M. Li, and H. Liao (2015). The lift on an aerofoil in grid-generated turbulence. *Journal of Fluid Mechanics 771*, 16–35. 30, 33, 34

[117] Liepmann, H. W. (1952). On the application of statistical concepts to the buffeting problem. *Journal of the Aeronautical Sciences 19*(12), 793–800. 27, 29, 33, 133, 142, 143

[118] Liepmann, H. W. (1955). Extension of the statistical approach to buffeting and gust response of wings of finite span. *Journal of the Aeronautical Sciences 22*(3), 197–200. 33

[119] Lim, H. C., I. P. Castro, and R. P. Hoxey (2007). Bluff bodies in deep turbulent boundary layers: Reynolds-number issues. *Journal of Fluid Mechanics 571*, 97–118. 2, 24

[120] Lou, X., T. Zhou, Y. Zhou, H. Wang, and L. Cheng (2016). Experimental investigation on wake characteristics behind a yawed square cylinder. *Journal of Fluids and Structures 61*, 274–294. 26, 90

[121] Lumley, J. (1965). Interpretation of time spectra measured in high-intensity shear flows. *The Physics of Fluids 8*(6), 1056–1062. 87

[122] Lyons, G. W. (2016). *Statistical Scaling of Turbulent Surface Pressure in the Atmospheric Boundary Layer*. Ph. D. thesis, University of Mississippi. 128

[123] Ma, C., Q. Duan, Q. Li, H. Liao, and Q. Tao (2019). Aerodynamic characteristics of a long-span cable-stayed bridge under construction. *Engineering Structures 184*, 232–246. 8, 10, 30, 68

[124] Ma, C., C. Pei, H.-l. Liao, M. Liu, and M. Li (2020). Field measurement and wind tunnel study of aerodynamic characteristics of twin-box girder. *Journal of Wind Engineering and Industrial Aerodynamics 202*, 104209. 8, 30

[125] Ma, X., G.-S. Karamanos, and G. Karniadakis (2000). Dynamics and low-dimensionality of a turbulent near wake. *Journal of Fluid Mechanics 410*, 29–65. 95

[126] Macdonald, J. H., P. A. Irwin, and M. S. Fletcher (2002). Vortex-induced vibrations of the Second Severn Crossing cable-stayed bridge - full-scale and wind tunnel measurements. *Proceedings of the Institution of Civil Engineers-Structures and Buildings 152*(2), 123–134. 7, 22, 23, 113, 114

[127] Mannini, C., A. M. Marra, L. Pigolotti, and G. Bartoli (2017). The effects of free-stream turbulence and angle of attack on the aerodynamics of a cylinder with rectangular 5:1 cross section. *Journal of Wind Engineering and Industrial Aerodynamics 161*, 42–58. 98, 103, 109, 110, 137, 139

[128] Marshall, J. (2003). Wake dynamics of a yawed cylinder. *J. Fluids Eng. 125*(1), 97–103. 90, 99, 109

[129] Matsuda, K., K. Cooper, H. Tanaka, M. Tokushige, and T. Iwasaki (2001). An investigation of Reynolds number effects on the steady and unsteady aerodynamic forces on a 1:10 scale bridge deck section model. *Journal of Wind Engineering and Industrial Aerodynamics 89*(7-8), 619–632. 113

[130] Matsumoto, M. (1998). Observed behavior of prototype cable vibrationn and its generation mechanism. In *Proc. of the international symposium on advances in bridge aerodynamics, Copenhagen, Denmark*, pp. 189–211. 27, 90

[131] Matsumoto, M., N. Shiraishi, M. Kitazawa, C. Knisely, H. Shirato, Y. Kim, and M. Tsujii (1990). Aerodynamic behavior of inclined circular cylinders-cable aerodynamics. *Journal of Wind Engineering and Industrial Aerodynamics 33*(1-2), 63–72. 27, 88, 90

[132] Matsumoto, M., N. Shiraishi, H. Shirato, S. Stoyanoff, and T. Yagi (1993). Mechanism of, and turbulence effect on vortex-induced oscillations for bridge box girders. *Journal of Wind Engineering and Industrial Aerodynamics 49*(1-3), 467–476. 23

[133] Matsumoto, M., T. Yagi, H. Hatsuda, T. Shima, M. Tanaka, and H. Naito (2010). Dry galloping characteristics and its mechanism of inclined/yawed cables. *Journal of Wind Engineering and Industrial Aerodynamics 98*(6-7), 317–327. 23, 27, 82, 88, 90, 91

[134] Mauder, M. and M. J. Zeeman (2018). Field intercomparison of pre-vailing sonic anemometers. *Atmospheric Measurement Techniques 11*(1), 249–263. 42

[135] McBean, G. and J. Elliott (1975). The vertical transports of kinetic energy by turbulence and pressure in the boundary layer. *Journal of Atmospheric Sciences 32*(4), 753–766. 124, 131

[136] McCoy, E. J., A. T. Walden, and D. B. Percival (1998). Multitaper spectral estimation of power law processes. *IEEE Transactions on Signal Processing 46*(3), 655–668. 66

[137] Melbourne, W. (1982). Comparison of model and full-scale tests of a bridge and chimney stack. In *Proc. of Int'l Workshop on Wind Tunnel Modelling, Maryland, USA*, pp. 637–653. 8, 117, 146

[138] Midjiyawa, Z., E. Cheynet, J. Reuder, H. Ágústsson, and T. Kvamsdal (2021a). Potential and challenges of wind measurements using met-masts in complex topography for bridge design: Part I–integral flow character-istics. *Journal of Wind Engineering and Industrial Aerodynamics 211*, 104584. 13, 61

[139] Midjiyawa, Z., E. Cheynet, J. Reuder, H. Ágústsson, and T. Kvamsdal (2021b). Potential and challenges of wind measurements using met-masts in complex topography for bridge design: Part II–spectral flow character-istics. *Journal of Wind Engineering and Industrial Aerodynamics 211*, 104585. 61

[140] Moore, C. J. (1986). Frequency response corrections for eddy correla-tion systems. *Boundary-Layer Meteorology 37*(1), 17–35. 17

[141] Moran, P. and R. Hoxey (1979). A probe for sensing static pressure in two-dimensional flow. *Journal of Physics E: Scientific Instruments 12*(8), 752. 45, 46, 56, 57, 163, 164, 165, 166

[142] Mugridge, B. (1971). Gust loading on a thin aerofoil. *Aeronautical Quarterly 22*(3), 301–310. 33

[143] Niihara, Y., R. Nakano, K. Hayashida, and Y. Kubo (1998). Full-scale measurements of wind pressures acting on the deck cross-section

of a cable-stayed bridge. In *Wind Engineering into the 21st Century*, pp. 1005–1012. Balkema Rotterdam. 8, 10, 117, 146

[144] Nishiyama, R. T. and A. J. Bedard Jr (1991). A "Quad-Disc" static pressure probe for measurement in adverse atmospheres: With a comparative review of static pressure probe designs. *Review of scientific instruments 62*(9), 2193–2204. 56

[145] Norberg, C. and B. Sunden (1987). Turbulence and Reynolds number effects on the flow and fluid forces on a single cylinder in cross flow. *Journal of Fluids and Structures 1*(3), 337–357. 18

[146] Novak, M. and H. Tanaka (1977). Pressure correlations on a vibrating cylinder. In *Proc. 4th Int. Conf. on Wind Effects on Buildings and Structures, Heathrow, U.K.*, pp. 227–232. 22, 23

[147] Øiseth, O., A. Rönnquist, and R. Sigbjörnsson (2013). Effects of co-spectral densities of atmospheric turbulence on the dynamic response of cable-supported bridges: a case study. *Journal of Wind Engineering and Industrial Aerodynamics 116*, 83–93. 29

[148] Olesen, H., S. E. Larsen, and J. Højstrup (1984). Modelling velocity spectra in the lower part of the planetary boundary layer. *Boundary-Layer Meteorology 29*(3), 285–312. 13

[149] Ong, L. and J. Wallace (1996). The velocity field of the turbulent very near wake of a circular cylinder. *Experiments in Fluids 20*(6), 441–453. 93, 95, 102, 103

[150] Panofsky, H., D. Larko, R. Lipschut, G. Stone, E. Bradley, A. J. Bowen, and J. Højstrup (1982). Spectra of velocity components over complex terrain. *Quarterly Journal of the Royal Meteorological Society 108*(455), 215–230. 69

[151] Peña, A., E. Dellwik, and J. Mann (2019). A method to assess the accuracy of sonic anemometer measurements. *Atmospheric Measurement Techniques 12*(1), 237–252. 65, 74

[152] Quinn, A., M. Hayward, C. Baker, F. Schmid, J. Priest, and W. Powrie (2010). A full-scale experimental and modelling study of ballast flight

under high-speed trains. *Proceedings of the Institution of Mechanical Engineers, Part F: Journal of Rail and Rapid Transit 224*(2), 61–74. 56

[153] Ramberg, S. E. (1983). The effects of yaw and finite length upon the vortex wakes of stationary and vibrating circular cylinders. *Journal of Fluid Mechanics 128*, 81–107. 18, 26, 99, 109

[154] Rasmussen, J. T., M. M. Hejlesen, A. Larsen, and J. H. Walther (2010). Discrete vortex method simulations of the aerodynamic admittance in bridge aerodynamics. *Journal of Wind Engineering and Industrial Aerodynamics 98*(12), 754–766. 30

[155] Raspet, R., J. Yu, and J. Webster (2008). Low frequency wind noise contributions in measurement microphones. *The Journal of the Acoustical Society of America 123*(3), 1260–1269. 128

[156] Richards, P. and R. Hoxey (2012). Pressures on a cubic buildingâĂŤ-part 1: Full-scale results. *Journal of Wind Engineering and Industrial Aerodynamics 102*, 72–86. 121

[157] Richards, P., R. Hoxey, B. Connell, and D. Lander (2007). Wind-tunnel modelling of the Silsoe Cube. *Journal of Wind Engineering and Industrial Aerodynamics 95*(9-11), 1384–1399. 113

[158] Richards, P., R. Hoxey, and J. Short (2000). Spectral models for the neutral atmospheric surface layer. *Journal of Wind Engineering and Industrial Aerodynamics 87*(2-3), 167–185. 13

[159] Richardson, G. and D. Surry (1992). The Silsoe Building: a comparison of pressure coefficients and spectra at model and full-scale. *Journal of Wind Engineering and Industrial Aerodynamics 43*(1-3), 1653–1664. 53, 56

[160] Robertson, A. and A. Glass (1988). *The Silsoe Structures Building: Its design, instrumentation and research facilities*. AFRC Institute of Engineering Research Silsoe, Bedford, England. 56

[161] Ropelewski, C. F., H. Tennekes, and H. Panofsky (1973). Horizontal coherence of wind fluctuations. *Boundary-Layer Meteorology 5*(3), 353–363. 16, 154

[162] Roshko, A. (1961). Experiments on the flow past a circular cylinder at very high Reynolds number. *Journal of Fluid Mechanics 10*(3), 345–356. 24

[163] Saathoff, P. and W. Melbourne (1989). The generation of peak pressures in separated/reattaching flows. *Journal of Wind Engineering and Industrial Aerodynamics 32*(1-2), 121–134. 113, 136

[164] Sacré, C. and D. Delaunay (1992). Structure spatiale de la turbulence au cours de vents forts sur differents sites. *Journal of Wind Engineering and Industrial Aerodynamics 41*(1-3), 295–303. 67, 78

[165] Sankaran, R. and E. Jancauskas (1992). Direct measurement of the aerodynamic admittance of two-dimensional rectangular cylinders in smooth and turbulent flows. *Journal of Wind Engineering and Industrial Aerodynamics 41*(1-3), 601–611. 30, 144

[166] Sankaran, R. and E. Jancauskas (1993). Measurements of cross-correlation in separated flows around bluff cylinders. *Journal of Wind Engineering and Industrial Aerodynamics 49*(1-3), 279–288. 33, 145

[167] Saranyasoontorn, K., L. Manuel, and P. S. Veers (2004). A comparison of standard coherence models for inflow turbulence with estimates from field measurements. *J. Sol. Energy Eng. 126*(4), 1069–1082. 77

[168] Scanlan, R. (1978). The action of flexible bridges under wind, II: Buffeting theory. *Journal of Sound and Vibration 60*(2), 201–211. 7, 27, 33

[169] Schaefer, J. W. and S. Eskinazi (1959). An analysis of the vortex street generated in a viscous fluid. *Journal of Fluid Mechanics 6*(2), 241–260. 100

[170] Schewe, G. (2001). Reynolds-number effects in flow around more-or-less bluff bodies. *Journal of Wind Engineering and Industrial Aerodynamics 89*(14-15), 1267–1289. 2, 19, 24, 25, 81, 111

[171] Schewe, G. (2013). Reynolds-number-effects in flow around a rectangular cylinder with aspect ratio 1:5. *Journal of Fluids and Structures 39*, 15–26. 2, 24, 81, 93, 110, 111, 113

[172] Schewe, G. and A. Larsen (1998). Reynolds number effects in the flow around a bluff bridge deck cross section. *Journal of Wind Engineering and Industrial Aerodynamics 74*, 829–838. 2, 24, 25, 111

[173] Sears, W. R. (1941). Some aspects of non-stationary airfoil theory and its practical application. *Journal of the Aeronautical Sciences 8*(3), 104–108. 33, 142, 143

[174] Shiraishi, N. and M. Matsumoto (1983). On classification of vortex-induced oscillation and its application for bridge structures. *Journal of Wind Engineering and Industrial Aerodynamics 14*(1-3), 419–430. 22, 23

[175] Shirakashi, M., A. Hasegawa, and S. Wakiya (1986). Effect of the secondary flow on Karman vortex shedding from a yawed cylinder. *Bulletin of JSME 29*(250), 1124–1128. 27, 67, 90

[176] Sill, B., N. Cook, and C. Fang (1992). The Aylesbury comparative experiment: a final report. *Journal of Wind Engineering and Industrial Aerodynamics 43*(1-3), 1553–1564. 53

[177] Simiu, E. and R. H. Scanlan (1978). *Wind effects on structures.* Wiley. 27

[178] Snæbjörnsson, J., J. Jakobsen, E. Cheynet, and J. Wang (2017). Full-scale monitoring of wind and suspension bridge response. In *IOP Conference Series: Materials Science and Engineering*, Volume 276, pp. 012007. IOP Publishing. 36, 45

[179] Snæbjörnsson, J. T. (2002). *Full-and model scale study of wind effects on a medium-rise building in a built up area.* Ph. D. thesis, NTNU. 53, 56, 161

[180] SOH Wind Engineering LLC (2021a). Lysefjord Bridge, Norway. Flow properties of njord 1 wind tunnel (Revision 0). 170

[181] SOH Wind Engineering LLC (2021b). Lysefjord Bridge, Norway. Static wind tunnel tests (Revision 1). 169, 170

[182] SOH Wind Engineering LLC (2021c). Lysefjord Bridge, Norway. Wake flow measurements (Revision 1). 100, 169, 175

[183] Solari, G. and G. Piccardo (2001). Probabilistic 3-D turbulence modeling for gust buffeting of structures. *Probabilistic Engineering Mechanics 16*(1), 73–86. 68

[184] Soper, D., C. Baker, A. Jackson, D. Milne, L. Le Pen, G. Watson, and W. Powrie (2017). Full scale measurements of train underbody flows and track forces. *Journal of Wind Engineering and Industrial Aerodynamics 169*, 251–264. 56

[185] Strouhal, V. (1878). Über eine besondere art der tonerregung. In *Annalen der Physik, Feb. 16. 1878. Presented at der physikalische-medicininischen Gesellschaft in WÃijrzburg, 16, February 1878.* 21

[186] Surry, J. and D. Surry (1967). The effect of inclination on the strouhal number and other wake properties of circular cylinders at subcritical reynolds numbers. Technical report, Toronto Univ (Ontario) Inst For Aerospace Studies. 26, 109

[187] Svend Ole Hansen ApS (2020). Hoxey probe for measuring the static pressure component. Wind tunnel tests (Revision 0). 163, 164

[188] Svend Ole Hansen ApS (2021). Personal Communication. 10, 161

[189] Taylor, G. I. (1938). The spectrum of turbulence. *Proceedings of the Royal Society of London. Series A-Mathematical and Physical Sciences 164*(919), 476–490. 14, 17, 124, 129

[190] Thakur, A., X. Liu, and J. Marshall (2004). Wake flow of single and multiple yawed cylinders. *J. Fluids Eng. 126*(5), 861–870. 99

[191] Thomson, D. J. (1982). Spectrum estimation and harmonic analysis. *Proceedings of the IEEE 70*(9), 1055–1096. 66, 94

[192] Tieleman, H. W. (1995). Universality of velocity spectra. *Journal of Wind Engineering and Industrial Aerodynamics 56*(1), 55–69. 13, 14, 15

[193] Tieleman, H. W. (2003). Wind tunnel simulation of wind loading on low-rise structures: a review. *Journal of Wind Engineering and Industrial Aerodynamics 91*(12-15), 1627–1649. 113

[194] Tsuji, Y., J. H. Fransson, P. H. Alfredsson, and A. V. Johansson (2007). Pressure statistics and their scaling in high-Reynolds-number turbulent boundary layers. *Journal of Fluid Mechanics 585*, 1–40. 125

[195] Van Atta, C. (1968). Experiments on vortex shedding from yawed circular cylinders. *AIAA Journal 6*(5), 931–933. 26, 109

[196] Vickers, D. and L. Mahrt (1997). Quality control and flux sampling problems for tower and aircraft data. *Journal of atmospheric and oceanic technology 14*(3), 512–526. 65

[197] Vickery, B. (1966). Fluctuating lift and drag on a long cylinder of square cross-section in a smooth and in a turbulent stream. *Journal of Fluid Mechanics 25*(3), 481–494. 33

[198] Vickery, B. and R. Basu (1983). Across-wind vibrations of structures of circular cross-section. Part I. development of a mathematical model for two-dimensional conditions. *Journal of Wind Engineering and Industrial Aerodynamics 12*(1), 49–73. 22, 96

[199] Wang, H., S. M. Razali, T. Zhou, Y. Zhou, and L. Cheng (2011). Streamwise evolution of an inclined cylinder wake. *Experiments in fluids 51*(2), 553–570. 99

[200] Weber, R. O. (1999). Remarks on the definition and estimation of friction velocity. *Boundary-Layer Meteorology 93*(2), 197–209. 12

[201] Welch, P. (1967). The use of fast fourier transform for the estimation of power spectra: a method based on time averaging over short, modified periodograms. *IEEE Transactions on audio and electroacoustics 15*(2), 70–73. 77

[202] Wilczak, J., S. Oncley, and A. Bedard Jr (1992). Turbulent pressure fluctuations in the atmospheric surface layer. In *Tenth Symposium on Turbulence and Diffusion*, pp. 167–170. 128

[203] Wilczak, J. M., S. P. Oncley, and S. A. Stage (2001). Sonic anemometer tilt correction algorithms. *Boundary-Layer Meteorology 99*(1), 127–150. 10, 65

[204] Wyngaard, J., A. Siegel, and J. Wilczak (1994). On the response of a turbulent-pressure probe and the measurement of pressure transport. *Boundary-Layer Meteorology 69*(4), 379–396. 131

[205] Xie, J., H. Tanaka, R. Wardlaw, and M. Savage (1991). Buffeting analysis of long span bridges to turbulent wind with yaw angle. *Journal of Wind Engineering and Industrial Aerodynamics 37*(1), 65–77. 12

[206] Xu, Y. L. and Y. Xia (2019). *Structural health monitoring of long-span suspension bridges*. CRC Press. 7

[207] Xu, Y. L. and L. Zhu (2005). Buffeting response of long-span cable-supported bridges under skew winds. Part 2: Case study. *Journal of Sound and Vibration 281*(3-5), 675–697. 68

[208] Yan, L., X. H. He, R. G. Flay, et al. (2019). Experimental determination of aerodynamic admittance functions of a bridge deck considering oscillation effect. *Journal of Wind Engineering and Industrial Aerodynamics 190*, 83–97. 143

[209] Zdravkovich, M. M. (1997a). *Flow around circular cylinders: Volume 1: Fundamentals*, Volume 1. Oxford University Press. 2, 18, 19, 20, 82

[210] Zdravkovich, M. M. (1997b). *Flow around circular cylinders: Volume 2: Applications*, Volume 2. Oxford University Press. 2, 18, 23, 26

[211] Zhao, M., L. Cheng, and T. Zhou (2009). Direct numerical simulation of three-dimensional flow past a yawed circular cylinder of infinite length. *Journal of Fluids and Structures 25*(5), 831–847. 88, 90

[212] Zhou, T., S. M. Razali, Y. Zhou, L. Chua, and L. Cheng (2009). Dependence of the wake on inclination of a stationary cylinder. *Experiments in fluids 46*(6), 1125–1138. 88, 90, 99, 101, 109

[213] Zhu, L., Y. L. Xu, F. Zhang, and H. Xiang (2002). Tsing Ma Bridge deck under skew winds − Part I: Aerodynamic coefficients. *Journal of Wind Engineering and Industrial Aerodynamics 90*(7), 781–805. 99